# Catalyst Layers in Polymer Electrolyte Membrane Fuel Cells: Formation, Characterization and Performance

BY

Jian Zhao

A thesis
presented to the University of Waterloo
in fulfillment of the
thesis requirement for the degree of
Doctor of Philosophy
in
Mechanical and Mechatronics Engineering

Waterloo, Ontario, Canada, 2019
© Jian Zhao 2019

# Examining Committee Membership

The following served on the Examining Committee for this thesis. The decision of the Examining Committee is by majority vote.


External Examiner                     Dr. Biao Zhou
                                      Professor, Ph.D., P.Eng.
                                      University of Windsor


Supervisor                            Dr. Xianguo Li
                                      Professor, Ph.D., P.Eng., FCAE, FEIC,
                                      FCSME, University Research Chair


Internal Member                       Dr. John Z. Wen
                                      Professor, Ph.D., P.Eng.

                                      Dr. Mary Wells
                                      Professor, Ph.D., P.Eng., Dean of
                                      Engineering, Physical Sciences at the
                                      University of Guelph


Internal-external Member              Dr. Eric Croiset
                                      Professor, Ph.D., P.Eng., Chair at the
                                      Department of Chemical Engineering


Other Member(s)                       N/A

# Author's Declaration

I hereby declare that I am the sole author of this thesis. This is a true copy of the thesis, including any required final revisions, as accepted by my examiners.

I understand that my thesis may be made electronically available to the public.

# Abstract

The structure of the catalyst layers (CLs) has a decisive impact on the performance, durability, and cost of polymer electrolyte membrane (PEM) fuel cells – these are the main technical challenges to the commercialization of PEM fuel cells. The porous CL conventionally consists of carbon-based platinum (Pt/C) and ionomer (Nafion polymer). An ideal CL should maintain the desired structure with sufficient gas diffusion and water removal channels (pores), proton transport media (ionomer), electron travel pathways (catalyst particles), and optimal three-phase boundaries (TPBs) where electrochemical reaction occurs (reaction sites). Practically, the CL is formed during the fabrication process which determines the physical structures, often represented by porosity, mean pore size, pore size distribution (PSD) and specific surface area. The physical structures, in turn, determine the effective transport properties such as effective mass diffusion coefficient and permeability for the reactant in the CLs. However, there is still no clear understanding of what is the optimal structure for the CLs.

To investigate the structure of CLs, three aspects are studied in the present thesis work: (i) the effect of fabrication process on the resulting structure, (ii) the effect of the CL structure on its macro-properties, and (iii) the effect of the structure and macro-properties on the mass transport phenomena and the associated cell performance. Many factors including fabrication techniques and CL compositions have a significant impact on the structure formation of CLs. However, how these factors affect the structure is still unclear. Additionally, there lacks experimental characterization of the structure such as porosity, PSD, specific surface area, mean pore size, and surface fractal dimension, as well as mass transport properties such as effective diffusion coefficient and gas permeability for the CLs in literature. With the experimentally determined structural and mass transport parameters of the CLs and the associated electrodes, the mass transport phenomena in PEM fuel cells can be quantitatively analyzed.

In the present thesis work, the CL pore structure is experimentally characterized by the method of standard porosimetry (MSP), which is established based on the phenomenon of capillary equilibrium in the wetted porous materials. By

the means of MSP, a comprehensive characterization of the structure in terms of porosity, PSD, specific surface area, mean pore size, and surface fractal dimension is obtained. In addition, the effective diffusion coefficient of the CL is studied by the modified Loschmidt Cell, built based on the Fick's law of diffusion. The parameters including effective diffusion coefficient, diffusion resistivity, and its relation with the porosity and mean pore size is investigated. Further, the permeability is measured based on Darcy's law via a custom-engineered apparatus developed in my thesis work. The effect of Pt loading, temperature, flow rate, and gas species is explored in this thesis study. With the experimentally determined pore structure characterization and mass transport properties, a numerical study is performed for the better understanding of the mass transport mechanisms in the porous electrodes. The cell performance conducted in our lab is also reported in the present thesis for a better understanding of the *ex-situ* experiment and a comparison with the numerical modeling.

The experimental and numerical studies presented in the present thesis work is of great significance to (i) understand the structure of the CLs, (ii) to understand the relation between the structure and the mass transport properties such as the effective diffusion coefficient and permeability, and (iii) to understand the effect of the structural parameters and mass transport properties on the mass transport phenomena and hence the cell performance in the PEM fuel cells.

# Acknowledgments

I would like to express my deepest gratitude to my supervisor, Dr. Xianguo Li, for his invaluable guidance, steady encouragement, inspiration and support throughout my Ph.D. studies. I have learned a lot from Dr. Li, which will benefit throughout my career and life. I would also like to thank my committee members, Dr. Biao Zhou, Dr. John Wen, Dr. Mary Wells, and Dr. Eric Croiset for taking the time to scrutinize my thesis. Their comments significantly improved my thesis, which is very much appreciated.

# Table of Contents

# List of Figures

xi

xiii

xiv

# List of Tables

# List of Abbreviations

| | |
|---|---|
| ACL | Anode catalyst layer |
| AFM | Atomic force microscopy |
| CCL | Cathode catalyst layer |
| CCM | Catalyst coated on membrane |
| CCS (CCGDL) | Catalyst coated on substrate (i.e., GDL) |
| CL | Catalyst layer |
| DI | Deionized |
| DOE | U.S. Department of Energy |
| DTM | Decal transfer method |
| ECSA | Electrochemical surface area |
| GDL | Gas diffusion layer |
| HOR | Hydrogen oxidation reaction |
| IPA | Isopropyl alcohol |
| IUPAC | International Union of Pure and Applied Chemistry |
| MEA | Membrane electrode assembly |
| MPL | Microporous layer |
| MPS | Mean pore size |
| MSP | Method of standard porosimetry |
| OCV | Open circuit voltage |
| ORR | Oxygen reduction reaction |
| PEM | Polymer electrolyte (or proton exchange) membrane |
| PSD | Pore size distribution |
| Pt/C | Carbon supported platinum |
| PTFE | Polytetrafluoroethylene |
| RMS | Root mean square |
| RSS | Root sum square |
| SCCM | Standard cubic centimeters per minute |
| SEM | Scanning electron microscopy |
| SLPM | Standard liter per minute |
| SSA | Specific surface area |
| TEM | Transmission electron microscopy |
| TPB | Tree-phase boundary |

# List of Symbols

| | |
|---|---|
| $a$ | Water activity |
| $A$ | Area [$m^2$] |
| $c$ | Molar concentration [$mol \cdot m^{-3}$] |
| $c_p$ | Specific heat [$J \cdot kg^{-1} \cdot K$] |
| $d$ | Diameter or characteristic length of water diffusion [m] |
| $D$ | Diffusion coefficient of species [$m^2 \cdot s^{-1}$] |
| $E$ | Voltage [V] |
| $EW$ | Equivalent weight of membrane [$kg \cdot kmol^{-1}$] |
| $f$ | Mean free path [m] |
| $FD$ | Fractal dimension |
| $I$ | Current density [$A \cdot cm^{-2}$] |
| $j$ | Volumetric reaction rate [$A \cdot m^{-3}$] |
| $j_0$ | Volumetric exchange current density [$A \cdot m^{-3}$] |
| $J$ | Molar mass flux [$kmol \cdot m^{-2} \cdot s^{-1}$] |
| $J_m$ | Mass flux [$kg \cdot m^{-2} \cdot s^{-1}$] |
| $k$ | Thermal conductivity [$W \cdot m^{-1} \cdot K^{-1}$] |
| $k_B$ | Boltzmann's constant = $1,3807 \times 10^{-23}$ [$J \cdot K^{-1}$] |
| $K$ | Permeability [$m^2$] |
| $K_c$ | Kozeny constant |
| $K_n$ | Knudsen number |
| $l$ | Characteristic length [m] |
| $m$ | Mass [g] |
| $\dot{m}$ | Mass flow rate [$kg \cdot s^{-1}$] |
| $M$ | Molecular weight [$kg \cdot kmol^{-1}$] |
| $n_d$ | Electro-osmotic drag coefficient [$H_2O$ per $H^+$] |
| $N_A$ | Avogadro number = $6.022 \times 10^{23}$ [$mol^{-1}$] |
| $p$ | Pressure [Pa] |
| $Q$ | Volumetric flow rate [$m^3 \cdot s^{-1}$] |
| $r$ | Radius [m] |
| $R$ | Diffusion resistance [$s \cdot m^{-3}$] |
| $R_h$ | Relative humidity |
| $R_u$ | The universal gas constant = 8314 [$J \cdot kmol^{-1} \cdot K^{-1}$] |
| $S$ | Surface area [$m^2$], or source terms in governing equations |

| | |
|---|---|
| $t$ | Time [s] |
| $T$ | Temperature [K] |
| $T_0$ | Operation temperature [K] |
| $u$ | Superficial velocity [m·s$^{-1}$] |
| $U$ | Uncertainty |
| $V$ | Volume [m$^3$] |
| $X$ | Molar fraction |
| $Y$ | Mass fraction |

**Greek letter**

| | |
|---|---|
| $\alpha$ | Transfer coefficient |
| $\beta$ | Diffusibility |
| $\delta$ | Thickness [m] |
| $\varepsilon$ | Porosity |
| $\zeta$ | Water transfer rate [s$^{-1}$] |
| $\eta$ | Over potential [V] |
| $\theta$ | Contact angle [$^{\circ}$] |
| $\kappa$ | Electrical conductivity [S·m$^{-1}$] |
| $\lambda$ | Water content in ionomer |
| $\mu$ | Dynamic viscosity [N·s·m$^{-2}$] |
| $v$ | Kinetic viscosity [m$^2$·s$^{-1}$] |
| $\rho$ | Density [kg·m$^{-3}$] |
| $\sigma$ | Surface tension [N·m$^{-1}$] |
| $\tau$ | Tortuosity |
| $\varphi$ | Potential [V] |
| $\Phi$ | Volume fraction |
| $\omega$ | Volume fraction of ionomer in catalyst layer |

**Subscript and superscript**

| | |
|---|---|
| a | Anode |
| act | Activation |
| bot | Bottom |
| bp | Bipolar plate |
| bulk | Bulk property |
| c | Cathode |
| ca | Capillary |
| cl | Catalyst layer |
| cond | Condensation |
| conv | Convection |
| d | Dissolved water |

| | |
|---|---|
| diff | Diffusion |
| dry | Dry |
| d-v | Dissolved water to vapor |
| eff | Effective |
| ele | Electronic |
| eod | Electro-osmotic drag |
| eq | Equivalent |
| equil | Equilibrium |
| evap | Evaporation |
| fl | Fluid phase |
| g | Gas phase |
| gdl | Gas diffusion layer |
| $H_2$ | Hydrogen |
| $H_2O$ | Water |
| i, j | The $i^{th}$ and $j^{th}$ components |
| in | Inlet |
| ion | Ionic |
| Kn | Knudsen |
| l | Liquid water |
| m | Mass (for source term) |
| mem | Membrane |
| out | Outlet |
| $O_2$ | Oxygen |
| pore | Pore |
| r | Reversible condition |
| ref | Reference state |
| s | Standard sample |
| sat | Saturation |
| sl | Solid phase |
| sub | Substrate property |
| t | Test sample |
| th | Thermo-neutral |
| top | Top |
| T | Energy (for source term) |
| u | Momentum (for source term) |
| v | Water vapor |
| v-l | Vapor to liquid water |

# Chapter 1
# Introduction

## 1.1 Background

A fuel cell is an electrochemical device that directly converts the chemical energy stored in fuels and oxidants into electric energy [1]. A polymer electrolyte membrane (PEM) fuel cell utilizes a solid membrane to transport protons from the anode to the cathode. The PEM fuel cell is becoming a promising alternative power source, especially suitable for portable and vehicular applications, due to its unique advantages, such as quiet working process, low operating temperature, high energy conversion efficiency, and low exhaust emission [2–12].

However, the cost reduction, performance improvement, and durability enhancement are the major challenges to the commercialization of the PEM fuel cells. According to the DOE report in 2017 [13], the fabrication of catalyst layers (CLs) costs as much as 41% of the PEM fuel cell stack for large-volume fabrication techniques. Two technical pathways to reduce the cost of the CLs are (i) enhancing performance and durability and (ii) reducing the use of expensive catalysts. However, these two pathways are often in a trade-off relation, which is highly related to the CL fabrication process.

Many efforts have been devoted to the optimization of the CL fabrication, which is still far away from the commercial stage. However, it is still unclear why the final structure of the CLs varies considerably with different fabrication methods and how the structure affects the CL macro-properties and performance. Therefore, the present thesis studies are mainly concentrated on (i) the characterization of the CL structure resulted from different fabrication methods with various materials and compositions and (ii) the investigation of how the CL structure influences its macro-properties and the cell performance.

## 1.2 Principle of PEM Fuel Cells

The major components of a PEM fuel cell unit include a solid membrane, two electrodes, two flow channels, and two distribution plates as shown in **Fig. 1**. Each electrode consists of one CL, where the electrochemical reaction occurs, and one gas diffusion layer (GDL), which is used to support the mechanically weak CL. At the anode, hydrogen gas is introduced to the anode electrode through flow channels and then diffuses into the anode CLs via GDLs. At the anode CL, hydrogen molecules break into protons (or hydrogen ions) and electrons. The generated protons are transported to the cathode side by the membrane; however, the electrons are rejected by the membrane due to its enormous electric resistance and are forced to travel through an external circuit to the cathode side. Meanwhile, on the cathode side, oxygen gas is supplied in the cathode flow channels. Oxygen gas from the flow channels arrives at the cathode CL through the GDLs. At the cathode CLs, protons from the membrane, electrons from the external circuit, and oxygen molecules from outer supply are combined, thus generating electricity and producing water and heat simultaneously.

On the anode side, the chemical reaction, in which molecular hydrogen breaks into protons and electrons, is called the hydrogen oxidation reaction (HOR). The HOR, which is also known as the anode half-cell reaction, is shown below,

$$H_2 \rightarrow 2H^+ + 2e^-$$
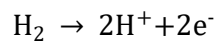
On the cathode side, the chemical reaction, in which the protons, electrons, and external oxygen molecules are combined to form water, is called oxygen reduction reaction (ORR). The ORR, which is also known as the cathode half-cell reaction, is shown as follows,

$$\frac{1}{2}O_2 + 2H^+ + 2e^- \rightarrow H_2O$$
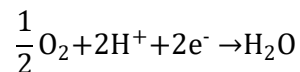
Base on the above analysis, the overall chemical reaction in a PEM fuel cell is

$$H_2 + \frac{1}{2}O_2 \rightarrow H_2O + Heat + Electricity$$
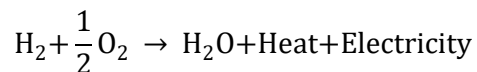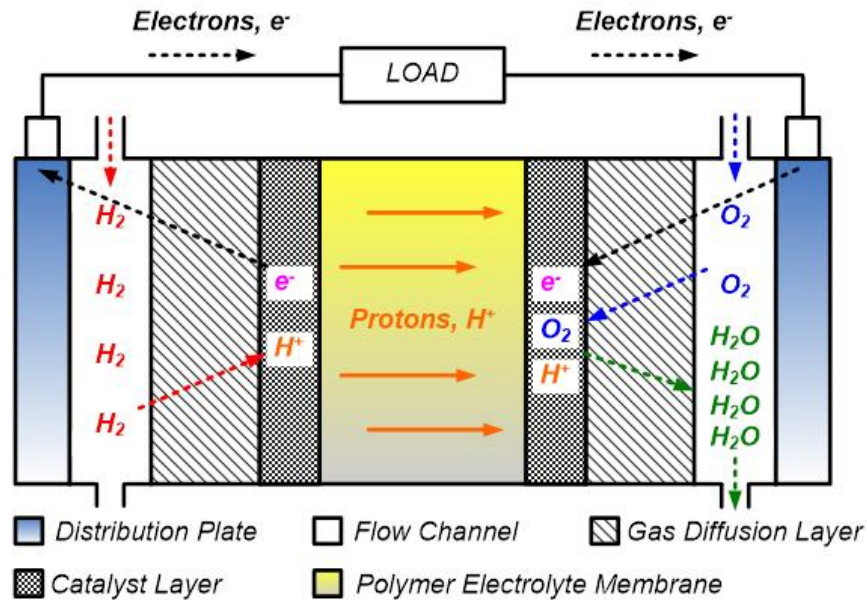
**Fig. 1.** Schematic of polymer electrolyte membrane (PEM) fuel cells.

The reaction product water appears at the three-phase boundary (TPB) area, which is the interface of solid catalyst (carbon supported platinum, Pt/C) phase, ionomer phase, and void region, in the cathode CLs. The chemical reaction occurs efficiently unless all active catalyst sites are accessible to the reactants, protons, and electrons, and are able to repel water product efficiently. Otherwise, the accumulation of an excess amount of water on the cathode side would occupy the reaction sites and lead to water flooding which is detrimental to the PEM fuel cell performance. Thus, the understanding of the CL structure is necessary to manage water effectively. However, no sufficient quantitative data on the pore structure of the CLs are available in literature. In other words, the thin CL involves complicated processes of reactant supply, chemical reactions, electron and proton transport, and product management.

## 1.3 Catalyst Layers of PEM Fuel Cells

The major components in PEM fuel cells are summarized in this section including the membrane, GDLs, bipolar plates, and with a focus on the CLs. The associated component functions, materials, geometric dimensions, and other requirements are discussed below.

The membrane is used to transport positive ions from the anode to the cathode, to insulate negative electrons and to separate reactants ($H_2$ and $O_2$). Therefore, the membrane should be a good conductor for protons, a good insulator for electrons, and

mechanically and chemically strong [14–17]. At the present stage, the most commonly used membranes are perfluorosulfonic acid (PSFA) membranes such as Nafion$^{®}$ (Dupont$^{TM}$), Gore-Select$^{®}$ (Gore$^{TM}$), and Aciplex$^{®}$ and Flemion$^{®}$ (Asahi$^{TM}$) [18]. The Nafion material, a polymer created by the DuPont company with a structure that resembles Teflon, has a long-term stability in oxidative or reductive environments [19]. More importantly, the Nafion polymer is prevalent due to its relatively lower cost and ease of fabrication. A thicker Nafion membrane shows better electric insulation and better mechanical and chemical strength but larger protonic resistance, and vice versa [11]. Therefore, the thickness of solid membranes should be optimized in practical application to achieve optimal performance, and the typical range of the thickness is approximately 25-175 μm. In addition, the protonic conductivity of the PEM increases with its water content, as the water can ionize the acid groups of the membrane material. Thus, the humidification of the reactants on both the anode and cathode sides is necessary to reduce protonic resistance. However, excessive humidification can lead to liquid water flooding, thus blocking the reactant gasses from moving to reaction sites and significantly lowering the performance of the PEM fuel cells. Therefore, water management is a significant issue in PEM fuel cells, and the amount of water in PEM fuel cells needs to be balanced so that insufficient humidify and water flooding can be avoided. In this thesis work, Nafion 211 with a typical thickness of 25.4 μm is selected to study the performance of CLs considering its low protonic resistance.

GDLs are usually used to support and protect the mechanically weak CLs, to transport chemical reactants, to conduct generated electrons, and to remove the produced liquid water efficiently [20–31]. As the physical support of the membranes and CLs, the GDLs are attached to the outside of the CLs. Current commercially available GDLs consist of two carbon-based porous layers. One is a macroporous carbon fiber paper (or cloth) substrate with a thickness of 100-300 μm, and the other one is a thinner micro-porous layer (MPL) consisting of carbon black powders and hydrophobic agents to increase the ability to expel excess water from CLs to the exhaust channels. In this study, a commercially available GDL (i.e., AvCarb GDS3250), which is composed of an AvCarb's proprietary carbon fiber paper, a PTFE treatment, and an MPL coating, is utilized.

Bipolar plates (a.k.a. flow field plates or distribution plates) are used to collect electrons and to insulate reactants between different cell units. Flow channels, cutting

on both sides of the bipolar plates, are used to transport chemical reactants (hydrogen and oxygen gasses) from an external supply to the surface of electrodes. The collected electrons then travel through an external circuit thereby powering the electrical load. In the present study, the flow channels are only cut on one side of the plates as only one cell unit is studied, and the plates are referred to as the distribution plates throughout the thesis for consistency.

Two CLs are tightly attached on both sides of the PEM and covered by the two GDLs. The functions of the CLs are to provide a platform for electrochemical reactions, to provide a flow pathway for reactants supply and products removal, and to transport the electrons and protons [1,19,32–37]. The catalyst is the most critical issue for the present PEM fuel cell research. Although the reaction of oxygen and hydrogen to form water can generate electricity and heat spontaneously, the reaction rate is extremely slow under normal conditions. Therefore, the catalyst is required to promote the electrochemical reactions under a relatively low temperature of 60-80 $^{\circ}$C, under which the membranes are well-hydrated and exhibits the best performance.

The present CLs typically consist of catalyst particles (e.g., Pt/C), binding materials (e.g., Nafion), and void regions. Electrocatalysts in PEM fuel cells including Pt and binary, ternary, or even quaternary Pt-transition metal alloys, such as PtCo, Pt-Cr-Ni, and Pt-Ru-Ir-Sn, have been proposed and implemented in many studies [18]. At the present stage, the most popular catalyst used in PEM fuel cells is platinum (Pt), although the above substitutes are currently under active research. Pt is widely used to enhance the reaction rate and selectivity of a particular reaction and to lower the Gibbs function of activation by providing more active areas for adsorption and dissociation of the reactants and products. During the practical CL fabrication, Pt is often supported by high-surface-area carbon materials, such as Vulcan-XC 72, Ketjen black, or Black pearls BP2000 [18]. Carbon serves as an essential medium to transport the generated electrons to the GDLs during electrochemical reactions. Meanwhile, the carbon supported platinum must have a good contact with ionomers to stabilize the catalyst particles and to transport protons from the catalyst sites to the membrane thus ionomer is often added not only to work as a binder but also to improve the protonic conductivity of the CLs. Therefore, to achieve an acceptable reaction rate, the CLs must ensure sufficient three-phase interfaces of catalysts, ionomers, and reactant gasses. The electrochemical reactions only occur at the interfaces: reaction gasses accumulate at the TPB through the void region, electrons

travel through carbon particles between the TPB and GDLs, and protons travel through ionomers between the TPB and membranes. In addition, the generated water product should be repelled promptly to avoid water flooding problem, although a proper amount of water should be maintained in order to avoid the membrane being over dried.

Therefore, the structure of the CLs should be carefully controlled to obtain a better cell performance, and the optimized balance among the three phases is crucial since each phase may dramatically limit the electrochemical reaction rate. Due to the complex processes of electrochemical reaction, heat generation, and electron and proton transport, the CLs should be comprehensively optimized although the CLs are the thinnest components in PEM fuel cells.

## 1.4 Objectives and Scope of the Thesis

Enormous effort has been made by the researchers to achieve a high-performance, long-lasting, and low-cost CL; however, the optimization of the CLs still needs to be improved. Many factors including coating techniques, catalyst ink composition, and fabrication conditions have a huge impact on the optimization of the CLs. Unfortunately, these factors are still not fully understood because how they affect the structure of the CLs and how the structure affects the CL macro-properties as well as the cell performance, are still unclear.

Therefore, the objectives of this thesis study are (i) to experimentally investigate how the CL fabrication process affects the CL structure, (ii) to experimentally study how the CL structure affects the CL macro-properties, and (iii) to understand how the CL macro-properties influence the mass transport phenomena and cell performance.

The scope of the thesis study is shown in **Fig. 2**. In this thesis, the structure of the CLs in the PEM fuel cells is investigated by experimental techniques to develop a fundamental understanding of the structure formation, the structure characterization, and the associated mass transport properties including the effective diffusion coefficient and permeability. Numerical techniques are employed to investigate the mass transport phenomena in PEM fuel cells based on the experimentally determined structural and mass transport properties of the porous media including CLs, and the numerical results are validated by the experimentally determined cell performance.
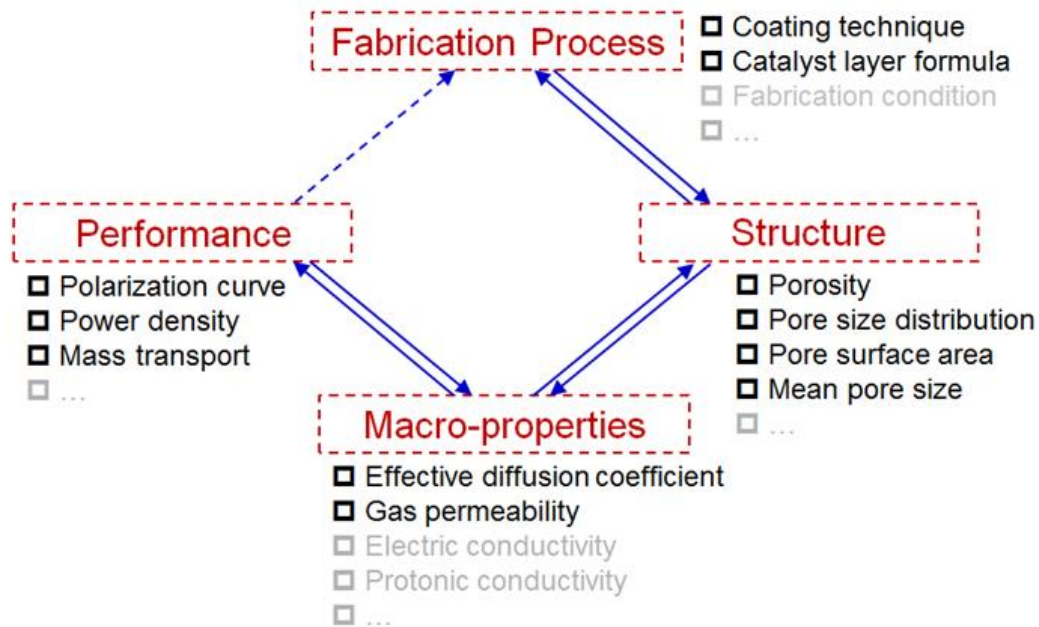
**Fig. 2.** Objectives and scope of the thesis work.

This thesis is divided into seven chapters. In chapter one, an introduction to the research problem, background information, working principles of PEM fuel cells and CLs, and objectives and scope are presented. A detailed literature review is put forward in chapter two. In chapter three, the details of the experiment development are given, while in chapter four the experimental results are analyzed. Based on the experimental results, a numerical model is developed and the corresponding numerical results are presented in chapter five and six. Finally, chapter seven gives a summary of the conclusions and the recommendations for future work.

# Chapter 2
# Literature Review

In this chapter, a comprehensive literature review is conducted with a focus on (i) the effect of the CL fabrication process on the CL structure, (ii) the effect of the CL structure on the CL macro-properties, and (iii) the effect of the CL macro-properties on the cell performance.

## 2.1 Effect of Fabrication Process on Structure

### 2.1.1 Fabrication Techniques

In this section, the CL fabrication techniques are comprehensively reviewed, and the corresponding advantages and disadvantages are discussed. According to the materials and catalyst loading employed, these CL fabrication methods are classified into three generations, and a comparison of these methods is presented in **Table 1**.

**Table 1**. Comparison of different fabrication methods of catalyst layers

| Fabrication method | 1st generation | 2nd generation | 3rd generation |
|---|---|---|---|
| Catalyst | Pt black | Pt/C | Pt |
| Binder | PTFE | Ionomer | N/A |
| Solvent | Organic fluid/water | Organic fluid/water | N/A |
| Pt loading (mg·cm$^{-2}$) | 4 | 0.4 | <0.1 |
| Thickness | 5~30 μm | 5~30 μm | ~1 μm |
| Durability | High | Medium | Low |
| Material cost | High | Medium | Low |
| Equipment cost | Low | Low | High |
| Catalyst Utilization | ~20% | ~40% | N/A |

Note: thickness depends on the Pt loading applied.

The first-generation CLs were developed in 1967 and made of PTFE-bounded Pt black catalysts with a typical catalyst loading of 4 mg·cm$^{-2}$ [38,39]. The function of

the PTFE material in the CLs is to act as a binder to stabilize the catalyst particles and to improve the hydrophobicity of the CLs. However, the amount of PTFE in the catalyst ink needs to be optimized as a high PTFE content may cause the catalyst particles being wrapped in the final deposition, thereby reducing the oxygen permeability, protonic conductivity, and catalyst utilization [38]. The optimal PTFE content is 10-40% for this type of catalyst ink. To improve the ionic conductivity, the first-generation CLs are typically impregnated with Nafion polymer by brushing or spraying. However, the catalyst utilization of these CLs remains as low as 20%. The low catalyst utilization may result in an extremely high cost, although these CLs exhibit an excellent long-term performance [39].

To reduce the Pt loading in the CLs, Ticianelli et al. [40] first substituted carbon supported platinum (Pt/C) for the Pt black particles in 1983. Additionally, Wilson et al. [38] replaced the hydrophobic PTFE material with hydrophilic Nafion polymer, which is the same as the membrane material. The Pt loading was thus reduced to ~0.4 mg·cm$^{-2}$ with an equivalent cell performance in comparison with the first-generation methods. The replacement of Nafion polymer helped increase the power density to twice of that in the PTFE-bounded CLs. This replacement enhanced the active reaction area from 22% (first-generation fabrication methods) to 45.4% (second-generation fabrication methods, a.k.a. thin-film methods). It should be noticed that the value of 45.4% implies that there is still sufficient room to improve and optimize the second-generation method [8,11,33,41]. The thickness of the second-generation CLs is typically less than 30 μm (depending on the catalyst loadings), and this helps reduce the resistance of mass transport, thus inhibiting the polarization and improving the cell performance. This thin-film method is most commonly used in the industry due to the CLs' good performance, high durability, and relatively low cost for the material and fabrication.

To further increase the utilization of the catalysts, direct Pt depositions without carbon support are employed on the GDLs with Nafion polymer partially covered. By this method, the CL can be made ultra-thin at the thickness level of ~1 μm with an ultra-low platinum loading of <0.1 mg·cm$^{-2}$. These ultra-thin film methods are actively investigated recently including sputtering deposition [42] and ion-beam [43]. However, since the Pt loading is extremely low, the ultra-thin CLs may have an extremely low durability, even though it reduces the cost dramatically.

In summary, the first-generation methods have the best long-term performance; however, the extremely high cost made this method less prevalent in the industry. Vice versa, the third generation methods reduce the cost dramatically; however, these methods are still impractical for the mass production due to their complex fabrication equipment and unverified long-term performance [39]. The second-generation method shows a good balance of the long-term performance and fabrication cost; however, there is still sufficient room to improve the performance by optimizing the CL structure. Therefore, the second-generation method will be studied the thesis work to achieve a better understanding of the CL structure.

## 2.1.2 Fabrication vs. Structure Formation

Although extensive studies are focused on the structural changes in the CLs during a long-term operation [44,45], less attention has been paid to the initial structure formation, which determines the macro-properties and the associated CL performance. Many factors, including catalyst ink composition, ink preparation, and ink coating processes, determine the structure of a fresh CL [46–48], as shown in **Fig. 3**.

Currently, the CL conventionally consists of carbon-supported platinum (e.g., Pt/C) and ionomer (e.g., Nafion polymer) with a comprehensively optimized ratio. A good design of the CLs should be able to maintain the desired structure with sufficient gas diffusion and water removal channels (void regions), electron travel pathways (catalyst particles), proton transport media (ionomer), and most importantly, optimal three-phase boundaries (TPBs) where electrochemical reactions occur [19]. The optimized ratio determines the performance of the CLs, and some of the published data are summarized in **Table 2**. It can be seen that the optimized ratio varies significantly for different cases even though the same Pt loading and similar fabrication techniques are applied [35,46,48–58]. The causes of this variation remain unclear and are probably because of the rarely reported fabrication conditions performed by different researchers.

Additionally, the ink preparation procedures, including ingredients mixing and ultrasonic conditions, are also extensively studied. Especially, the ultrasonic conditions should be optimized to enhance the catalyst ink activity and the uniform distribution of catalyst particles; however, an extended irradiation might be harmful to its composition and morphology due to the cavitation and sonolysis phenomena [47]. Bruno and Jonathan [47] applied an ultrasonic machine with a frequency of 40 kHz to the catalyst

inks. They claim that aggressive ultrasonic treatment, e.g., more than 2-3 hours, might lead to a reduction in electrochemical surface area (ECSA) due to the possible ablation, agglomeration, and dissolution of Pt nanoparticles. In this study, a 40 kHz ultrasonic bath is utilized to disperse the catalyst inks, and the ultra-sonication duration remains one hour to achieve a good dispersion and to avoid material degradation.

Furthermore, the fabrication methods are also influenced by the resulted CL structure. Three most prevalent modes for the second-generation methods are catalyst coated on GDL substrate (CCS, also called CCGDL in some studies), catalyst coated on membrane (CCM) and decal transfer methods (DTM) [14]. Different fabrication methods exhibit various cell performances; however, it is almost impossible to identify which methods are more efficient from the literature review [14].
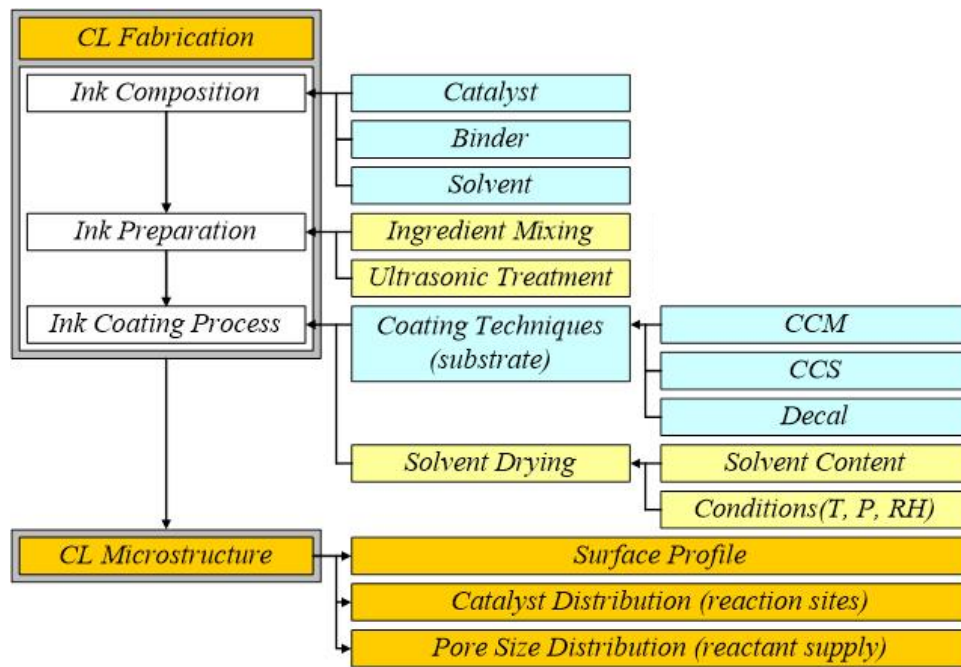


**Fig. 3.** Factors determining the structure of the catalyst layers.

**Table 2.** Optimal parameters of catalyst layers in literature

| Optimal Ink Composition | | | Solid Content | Ink Application | Pt loading (mg cm$^{-2}$) | References |
|---|---|---|---|---|---|---|
| Pt/C | Nafion | Solvent | | | | |
| 75% | 25% | IPA/glycerol | N/A | CCM, printing | 0.04 | Saha et al. [52] |
| 64% | 36% | IPA | ~4% | CCM, spraying | 0.10 | Gode et al. [46] |
| 70% | 30% | DI water | N/A | CCM, painting | 0.10 | Xiong and Manthiram [51] |
| 43% | 57% | Aliphatic alcohol | N/A | CCM, rolling | 0.40 | Lee et al. [53] |
| 67% | 33% | Glycerol/ethanol | N/A | CCS, spraying | 0.10 | Passalacqua et al. [35] |
| 67% | 33% | N/A | N/A | CCS, painting/printing | 0.20 | Gamburzev and Appleby [54] |
| 70% | 30% | Water | N/A | CCS, spraying | 0.20 | Qi and Kaufman [55] |
| 60% | 40% | Glycerol/IPA/ethanol | N/A | CCS, brushing | 0.20 | Antolini et al. [57] |
| 75% | 25% | IPA | 23% | CCS, air-brushing | N/A | Barrio et al. [58] |
| 70% | 30% | N/A | N/A | N/A | N/A | Hongsirikarn et al. [49] |
| 65% | 35% | 1-heptanol/ethylene glycol | 33.67% | CCS, screen printing | 0.40 | Bonifácio et al. [48] |
| 71% | 29% | 2-propanol | N/A | CCS, casting | 0.40 | Song et al. [50] |
| 50% | 50% | IPA | | | 0.10 | |
| 60% | 40% | IPA | N/A | CCS, brushing | 0.25 | Sasikumar et al. [56] |
| 80% | 20% | IPA | | | 0.50 | |

Note:
1. Pt/C is 20 wt. % Platinum on Vulcan XC-72, from E-TEK Division of De Nora, Inc., USA;
2. Nafion content comes from Nafion solution (5 wt. %, DuPont);
3. Solvent includes isopropyl alcohol (IPA) and deionized (DI) water;
4. CCM means catalyst coated on membranes;
5. CCS means catalyst coated on gas diffusion layers (substrate).

## 2.2 Effect of Structure on Macro-property

### 2.2.1 Structure vs. Macro-property

Many factors, including catalyst particles distribution, ionomer content, and pore structure, determine the macro-properties (e.g., electronic conductivity, protonic conductivity, effective diffusion coefficient, and permeability) of the CLs [18,59]; however, these factors are primarily affected by the structure of the CLs. As shown in **Fig. 4**, the heterogeneous structure of the CL consists of the essentially non-uniform distribution of reaction sites, void regions, and surface profile [60]. Uneven reactions sites and void regions may lead to a non-uniform chemical reaction rate, causing uneven water production, uneven heat production, uneven electricity generation and uneven distribution of radical species at discrete regions in the CLs. The local excess water may occupy the reaction sites, reduce the porosity, and worsen the diffusion and convection of the reactants in the CLs, thereby deteriorating the reactant supply at discrete regions [61]. Additionally, if water is insufficiently supplied at some reaction sites due to local overheat or high gas resistance, the electrochemical reaction cannot be proceeded successfully [1]. Similarly, if the generated heat is not removed efficiently, 'hot spots' may occur at the corresponding reaction sites and cause the cracks and delamination of the CL and membrane, further increasing the ionic resistance and causing malfunction of the CL and membrane [34,44]. Moreover, uneven distribution of radical species and current density may worsen the temperature distribution and cause various chemical degradation, including carbon corrosion, Pt sintering and dissolution, and ionomer resolving [45,59,62], therefore leading to a poor catalyst utilization. Material degradation will also cause pinholes in CLs and with the help of mechanical and thermal stress cycling due to uneven surface profile and temperature distribution [7], and these pinholes may propagate to cracks and delamination which would cause malfunction of the CLs.

Furthermore, Pt and carbon degradation will decrease the electronic conductivity, and ionomer resolving will reduce the protonic conductivity of the CLs. The material degradation and stress cycling will change the pore structure of the CLs, and the effective diffusion coefficient and permeability will be reduced accordingly. As a result, the structure of the CLs determines the macro-properties of CLs especially for

effective diffusion coefficient and permeability, thus degrading the performance at high current density region.

However, there lacks experimental data on the pore structure, effective diffusion coefficient, and permeability for the CLs. It is still unclear how the fabrication process affects the pore structure and how the pore structure influences the effective diffusion coefficient and permeability.
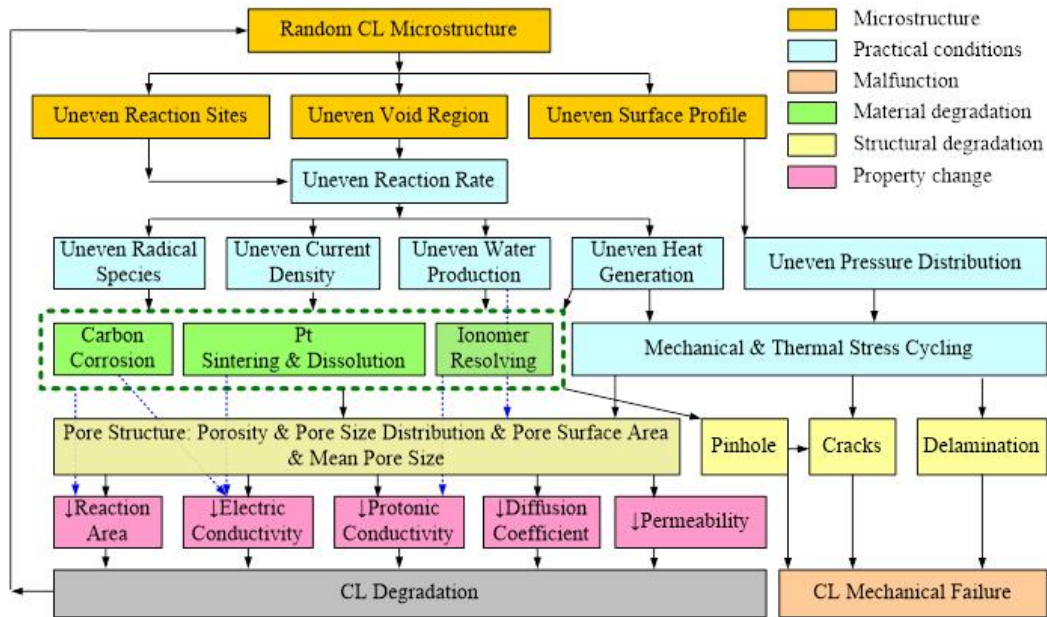


**Fig. 4.** Relation between the catalyst layer structure and macro-properties.

## 2.2.2 Pore Structure

The pore structure of the CL determines its macro-properties including electrical conductivity, protonic conductivity, effective diffusion coefficient, and permeability. Especially, at high current density regions, the performance of the PEM fuel cells is limited by the reactant and product transportation, which means that the effective diffusion coefficient and permeability of the CLs should be optimized accordingly to enhance the mass transport and cell performance of the PEM fuel cells. Therefore, it is of great importance to understand the CL structure; however, the data on the porosity and pore size distribution (PSD) of the CLs are very limited in literature, and a comprehensive understanding of the CL structure requires more characterization parameters such as pore surface area, mean pore size, etc. For a better clarification,

the basic concepts of the pore structure and the methods to determine the PSD are reviewed in this chapter.

### 2.2.2.1 Basic Concepts of Pore Structure

**(1) Pore Size Classification**

Most materials are more or less porous; actually, it is tough to achieve a solid material that does not contain any pores. Some physical properties of the CLs such as bulk density, thermal conductivity and the ability to transport reactant gas and water depend on the porous structure, thus the control of the porosity and PSD is of great importance for CL fabrication. The pores are often ideally considered in a shape of cylinders, cavities, slits, and spheres [63]. According to the International Union of Pure and Applied Chemistry (IUPAC) [63], the pores in the CLs are often assumed to be in the cylindrical shape of different diameters for the PSD measurement. The pore size is classified into three categories based on the diameter of the cylindrical pores: micropores (<2nm), mesopores (2nm~50nm) and macropores (>50nm) according to IUPAC, as shown in **Fig. 5**.

Pore Diameter

| micropore | mesopore | macropore |

2 nm        50 nm
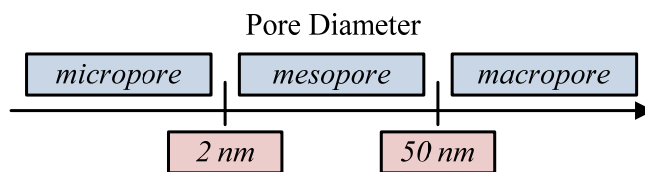
**Fig. 5.** Pore size classification based on different diameters.

**(2) Porosity**

The porosity is defined as the volumetric ratio of the pores to the total (bulk) volume of a sample. According to the definition, the values of porosity lie between 0 and 1, or as a percentage between 0% and 100%.

**(3) Pore Size Distribution**

PSD is another important parameter to evaluate a porous material [64]. The PSD commonly refers to the volumetric ratio of the pores with a particular radius to the total void volume of the sample. For a given porous sample, the fraction of the pores in a certain size range, e.g., with the radius of 10~20 nm, can be determined by

reading the PSD curve. The detailed calculation of these structural parameters is available elsewhere in **Chapter 3.2**.

### 2.2.2.2 Experimental Methods for Pore Size Distribution

Traditional methods to measure the porosity and PSD of a sample include mercury porosimetry [3,6,65–74], gas adsorption [75–77], capillary condensation [76], displacement method [78], liquid extrusion [79], low-angle X-ray scatting [80], optical microscopy and electron microscopy [46]. However, each of these methods has its disadvantages and limitations [71,72,75,76,79]. The method of mercury porosimetry may deform the test samples due to the high pressure of mercury. The gas adsorption and capillary condensation methods are suitable for only a small range of pore size. The centrifugal porosimetry and displacement methods work well only to measure the large pores. The liquid extrusion method is unable to detect micro-pores. The small-angle X-ray scattering can be used only for limited pore radius and may often output unreliable results. The experimental results of optical microscopy, scanning electron microscopy, transmission electron microscopy, and atomic force microscopy rely on the data-processing algorithm, and the PSD is calculated mostly from CL surface images. Therefore, a method of standard porosimetry (MSP) is employed in this study, because it not only eliminates most of the above disadvantages and limitations (e.g., no damage to soft and frail materials) but also can detect a broad range of pore sizes (0.3nm-300μm) as shown in **Fig. 6**.
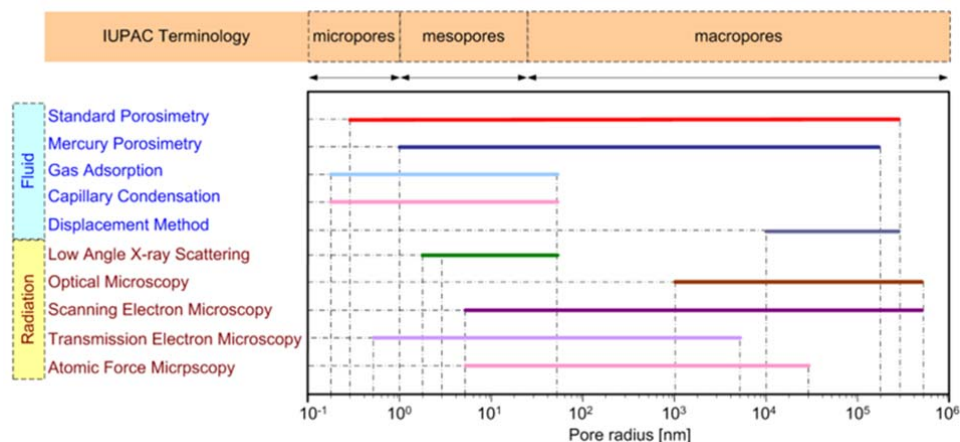


**Fig. 6.** Comparison of the pore size ranges that different methods can be used to determine the pore structure of porous media.

The MSP is established based on the capillary equilibrium between two wet porous media which are closed touched [67–69]. During the experiment, the test samples are completely submerged in octane for a sufficiently long time. Subsequently, the wet samples are dried in a heating station, and a small portion of the liquid evaporates from the wet samples. The mass of the evaporated liquid can be calculated by contrasting the sample mass difference before and after the evaporation, which can be transferred to the pore volume. In comparison with the standard sample, the relation between the pore volume and pore size can be established.

## 2.2.3 Effective Diffusion Coefficient

### 2.2.3.1 Fick's Law of Diffusion

Diffusion is often referred to as the net motion of molecules from one location to another as a result of random molecular motion [3,81–85]. The diffusion process can be driven by a pressure gradient, temperature gradient, external force field, and concentration gradient [86]. In this study, only the concentration diffusion is considered. The bulk diffusion coefficient is the measure of the diffusion process between two species driven by the collisions between molecules without the interference by any objects. Fick (1855) first applied the equation of heat conduction derived by Fourier (1822) to the diffusion of mass [87] with the assumption that the mass flux due to diffusion is proportional to the concentration gradient [81].

$$J = -D\frac{\partial c}{\partial x} \tag{2.1}$$

where $J$ is the molar mass flux in $kmol \cdot m^{-2} \cdot s^{-1}$, $c$ is the concentration of the diffusion substance in $kmol \cdot m^{-3}$, $x$ is the space coordinate in m, and $D$ is the diffusion coefficient in $m^2 \cdot s^{-1}$.

For the mass transfer due to diffusion in porous GDLs and CLs, the molar flux of a species is governed by the Fick's law of diffusion with the assumption of isotropic materials.

$$J_A = -D_{eff}\frac{\partial c_A}{\partial x} \tag{2.2}$$

where $J_A$ is the molar flux of species A (e.g., $O_2$ in this study) in $kmol \cdot m^{-2} \cdot s^{-1}$, $c_A$ is the concentration of the species A in $kmol \cdot m^{-3}$, and $D_{eff}$ is the effective diffusion coefficient in $m^2 \cdot s^{-1}$. The effective diffusion coefficient is theoretically smaller than

the bulk diffusion coefficient since the presence of the solid material makes the species harder to travel through a limited void region. In practice, the value of $D_{eff}$ is usually determined via experimental methods.

The diffusibility, $\beta$, is defined as its effective diffusion coefficient, $D_{eff}$, divided by the bulk diffusion coefficient, $D_{bulk}$ [3,66,88,89]. This parameter is also often studied in literature as a function of only the pore structure.

$$\beta = \frac{D_{eff}}{D_{bulk}} \qquad (2.3)$$

**2.2.3.2 Experimental Methods for Diffusion Coefficients**

Many experimental methods are used to determine the diffusion coefficient as summarized in **Fig. 7** [90], including close-tube, two-bulb, evaporation-tube, open-tube, capillary leak, and diffusion-bridge methods. However, each method has its disadvantages and limitations.
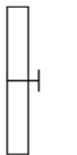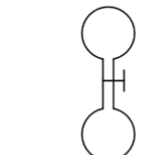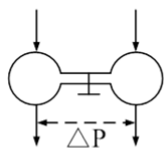


**Fig. 7.** Principal experimental methods for diffusion coefficients.

The closed-tube method developed by Loschmidt in 1870 was used to measure the binary diffusion coefficients experimentally for ten gas pairs at a temperature of 252 to 293 K [90]. This experiment utilized a long tube closed at both ends and an metal plate at the middle of the tube to control the diffusion process. A sensor controlled by a computer helps to record the composition changes as a function of time after a definite period of diffusion. This method is reliable, and the relative uncertainty for bulk diffusion coefficient measurement can be as small as 1-3%. Many

researchers modified this method to determine the effective diffusion coefficients of the porous media based on resistance network theory [91,92].

The two-bulb method established by Ney and Armistead in 1947 [90] utilizes two bulbs connected via a narrow tube, where the diffusion occurs. After an short period since the diffusion process starts, the concentration of the gas species in the bulbs varies exponentially with time and the diffusion coefficient can be found with the help of the relaxation time. The uncertainty and sources of uncertainty are similar to those of the closed-tube method. This method is less affected by convention flux due to the narrowness of the connecting tube; however, the Knudsen effects might introduce uncertainties to the results and a numerical constant depending on the geometrical configuration should be determined. Besides, this method is tough to be modified to measure the effective diffusion coefficient of the CLs.

The evaporation tube method developed by Stefan in 1873 [90] is suitable to determine the diffusion coefficients of the vapor-gas mixtures. This method utilizes an open tube partially filled with a liquid, and the evaporation rate of this liquid is affected by diffusion through an inert gas and by vapor removal at the tube outlet. The rate of the liquid loss is observed over extended periods of time (about half a day) so that the diffusion coefficient can be determined. The main disadvantages of this method are the long experimental time, the extreme sensitivity of the temperature and pressure measurements, and the existence of impurities. The uncertainty of this method is larger than 7.5% which is worse than the closed-tube and two-bulb methods.

The open-tube method utilizes a gas container filled with a gas [90]. At a given moment, the top of this container is open, and the gas will diffuse into the ambient atmosphere. Thus the diffusion coefficient can be calculated by analyzing the remaining gas composition after a known time. Reducing the effect of convective and controlling the temperature and pressure would be significant challenges for this method.

The diffusion-bridge method (Bendt in 1958) is a steady-state method for diffusion coefficient measurement by analyzing two steady gas streams flowing across a hollow capillary tube [90]. The flow rates of the two gas streams can be controlled to generate any desirable pressure difference across the capillary. This method works good for a large range of temperature, but requires calibration of the porosity of the system and is less frequently used to measure the diffusion coefficients in reality.

Of all the above methods, the closed tube method is most commonly used to determine the diffusion coefficients of the gas pairs because of its feasibility of modification for the porous media, high accuracy, short experimental time, ease of operation, and simple experimental configuration. In this study, the Loschmidt Cell method is modified to measure the effective diffusion coefficients of the CLs based on resistance network theory.

### 2.2.3.3 Correlation of Pore Structure and Effective Diffusion Coefficient

Three mechanisms drive the diffusion in pores including bulk diffusion (a.k.a. ordinary or Fickian diffusion), Knudsen diffusion, and surface diffusion [93,94]. In this study, surface diffusion is negligible in this study as it involves the motion of gas molecules at the solid material surfaces. Bulk diffusion is mainly driven by the collisions between molecules while Knudsen diffusion is driven by the collisions between molecules and pore walls when the pore diameter is comparable to or smaller than the mean free path of the gas molecules [94,95]. Knudsen number is used to determine the diffusion mechanism that dominates in pores of various pore diameters. Knudsen number, $K_n$, is calculated through the following equation.

$$K_n = \frac{f}{l} \tag{2.4}$$

where $f$ in m is the mean free path of gas molecules, and $l$ in m is the characteristic length scale of the medium (e.g., pore diameter in this study). The mean-free path of a gas species can be determined by the following equation assuming ideal gas and Maxwellian motion in all directions [96]:

$$f = \frac{k_B T}{\sqrt{2} p \pi d^2} \tag{2.5}$$

where $k_B$ is Boltzmann constant in J·K$^{-1}$, $T$ is the absolute temperature in K, $p$ is the pressure in Pa, and $d$ is the collision diameter in m. For $N_2$ and $O_2$ gasses in this study, the mean free path at standard temperature and pressure is around 70 nm [97]. When $K_n \ll 0.1$, the diffusion occurs in a continuum regime and bulk diffusion dominates in this regime; when $K_n \gg 10$, the mass transfer is dominated by Knudsen diffusion.

For porous media of sufficiently large pore size (e.g., GDLs with typical pore size larger than 1 μm), the diffusion is mainly driven by the collisions between molecules and thus the effects of collisions between the molecules and the walls are negligible. The effective diffusion coefficient in this type of materials is mainly

related to the volume fraction of the void region (i.e., porosity, $\varepsilon$) and the length fraction of the tortuous flow path to the straight line length (i.e., tortuosity, $\tau$) [92]. The effective diffusion coefficient of porous media is described using the following equation [92].

$$D_{\text{eff}} = \frac{\varepsilon D_{\text{bulk}}}{\tau} \qquad (2.6)$$

For unconsolidated material, the tortuosity ranges from 1.5 to 2.0 [95]; however, tortuosity is an unknown value for most porous media. Thus, the effective diffusion coefficients of porous materials are mostly determined by experiments.

For simplicity, many other empirical models are established to predict the effective diffusion coefficients of porous materials as a function of only porosity, including Bruggeman approximation [98,99], Neale and Nader model [100], Tomadakis and Sotirchos model [101], Mezedur model [102], Zamel model [88] and Das model [30] as shown in **Table 3**.

**Table 3.** Models to predict the effective diffusion coefficient of porous materials

| Model | Effective Diffusion Coefficient | Note | Source | Eq. # |
|---|---|---|---|---|
| Bruggeman (1937) | $D_{\text{eff}} = \varepsilon^{1.5} D_{\text{bulk}}$ | Spherical particles | [89,103] | (2.7) |
| Neale and Nader (1973) | $D_{\text{eff}} = [2\varepsilon/(3 - \varepsilon)]D_{\text{bulk}}$ | Spherical particles | [100] | (2.8) |
| Tomadakis and Sotirchos (1993) | $D_{\text{eff}} = \varepsilon[(\varepsilon - 0.037)/0.963]^{0.661} D_{\text{bulk}}$ | Fibers | [101] | (2.9) |
| Mezedur et al. (2002) | $D_{\text{eff}} = [1 - (1 - \varepsilon)^{0.46}]D_{\text{bulk}}$ $(0 \leq \varepsilon \leq 0.65)$ | Tetragonal network | [102] | (2.10) |
| Zamel et al. (2009) | $D_{\text{eff}} = \left\{1 - 2.76\varepsilon\cosh(3\varepsilon - 1.92)\left[\frac{3(1 - \varepsilon)}{3 - \varepsilon}\right]\right\} D_{\text{bulk}}$ $(0.33 \leq \varepsilon \leq 1)$ | Fibers | [88] | (2.11) |
| Das et al. (2010) | $D_{\text{eff}} = D_{\text{bulk}} - \dfrac{3(1 - \varepsilon)D_{\text{bulk}}}{\dfrac{3D_{\text{bulk}}}{D_{\text{bulk}} - \dfrac{2\omega D_{\text{mem}}}{3 - \omega}} - \varepsilon}$ | Catalyst layers | [30] | (2.12) |

Note: $D_{\text{mem}}$ is the diffusivity in ionomer, and $\omega$ is the volume fraction of ionomer in catalyst layers.

However, for porous media of tiny pore size (e.g., in CLs with typical size less than 100 nm), the effect of the collisions between the molecules and pore walls (often

refers to Knudsen diffusion) should be taken into consideration. The above mentioned empirical models over-predicted the effective diffusion coefficient of the CLs since a significant portion of the pores have a diameter less than the mean free path of gas molecules. Thus, the measurement of the PSD of this kind of material is of great importance.

In a single cylindrical pore, the effective diffusion coefficient is calculated by Bosanquet's formula [104] taking both Fickian diffusion and Knudsen diffusion into consideration (when neither Fickian nor Knudsen diffusion is fully dominant in the void region):

$$\frac{1}{D_{eff,pore}} = \frac{1}{D_{Kn}} + \frac{1}{D_{bulk}} \tag{2.13}$$

where $D_{eff,pore}$ is the effective diffusion coefficient in a single pore, $D_{Kn}$ is the Knudsen diffusion coefficient, and $D_b$ is the bulk diffusion coefficient.

The Knudsen diffusion coefficient is calculated by the following equation:

$$D_{Kn} = \frac{4}{3} d_{pore} \sqrt{\frac{R_u T}{2\pi M}} \tag{2.14}$$

where $D_{Kn}$ is the Knudsen diffusion coefficient in $m^2 \cdot s^{-1}$, $d_{pore}$ is the pore diameter in m, $R_u$ is the universal gas constant in $J \cdot kmol^{-1} \cdot K^{-1}$, $T$ is the temperature in K, and $M$ is the molecular weight of the gas species in $kg \cdot kmol^{-1}$.

There are also many models to predict the bulk diffusion coefficient, of which Marrero and Mason's model is widely used in literature because the uncertainty of this model is ~3% [90]. The bulk diffusion coefficient for oxygen and nitrogen gas pair can be calculated using the following equation [90]:

$$ln(p \cdot D_{bulk}) = ln(1.13 \times 10^{-5}) + 1.724 \cdot ln(T) \tag{2.15}$$

where $D_{bulk}$ is the bulk diffusion coefficient for species $O_2$ and $N_2$ in $cm^2 \cdot s^{-1}$, $p$ is the total pressure in atm, and $T$ is the temperature in K for the range of 285K ~ $10^4$ K.

## 2.2.4 Gas Permeability

### 2.2.4.1 Darcy's Law

The gas permeability of the GDLs and CLs is usually determined by using Darcy's law. It should be noted that Darcy's law is valid only for a slow flow, while a modified version of Darcy's law (i.e., Forchheimer Equation) must be considered for high-velocity flows (with high Reynolds numbers greater than 1-100 for packed

particles [105]). This is because the inertial effect becomes significant [93,106]. However, the pore Reynolds number for air in the PEM fuel cell electrodes is in the order of $10^{-4}$ [107], and it is also true in the current experimental setup. The small pore Reynold number indicates that the inertial effect is negligible and Darcy's law is valid for this study.

The general form of Darcy's law is express as,

$$u = -\frac{K}{\mu}\nabla p \qquad (2.16)$$

where $u$ is the superficial velocity of the fluid passing through the porous media in $m \cdot s^{-1}$, $K$ is the permeability coefficient in $m^2$, $\mu$ is the gas viscosity in Pa·s, and $p$ is the pressure in Pa.

### 2.2.4.2 Experimental Methods for Permeability

The permeability of the porous layers of PEM fuel cells is commonly determined based on Darcy's law by measuring the pressure drop at a specific flow rate across the samples [20,83,107–114]. **Table 4** summarizes some experimental data on the permeability for the GDLs in PEM fuel cells. It suggests that the permeability of the carbon paper/cloth is in the order of $6\text{-}70\times10^{-12}\,m^2$, and that of the GDL (i.e., carbon paper/cloth + MPL) is in the range of $0.3\text{-}1.1\times10^{-12}\,m^2$. However, the experimental data on the gas permeability of the CLs or the entire (or catalyzed) electrodes of PEM fuel cells is unavailable in literature. Further, it must be noticed that the experimental data in **Table 4** are obtained under room conditions.

**Table 4.** Experimental data on the gas permeability of the porous media in polymer electrolyte membrane (PEM) fuel cells.

| Porous Media | Type | PTFE Treated | MPL | Thickness [μm] | Working Fluid | In-plane Permeability $[10^{-12}\,m^2]$ | Through-plane Permeability $[10^{-12}\,m^2]$ | Source |
|---|---|---|---|---|---|---|---|---|
| TGP-H-060 | Paper | No | No | 190* | | 12.6 | 20.8 | |
| TGP-H-090 | Paper | No | No | 280* | | 12.2 | 14.4 | |
| TGP-H-120 | Paper | No | No | 370* | Air | 14.7 | 11.3 | [107] |
| E-Tek | Cloth | No | No | N/A | | 63.8 | 36.7 | |
| E-Tek ELAT | Cloth | Yes | Yes | 454* | Dry air / Humidified air | N/A | 0.47-1.11 / 0.36-0.73 | [20] |

| | | | | | | | | |
|---|---|---|---|---|---|---|---|---|
| SGL 34BA | Paper | 5 wt% | No | 251-255** | | N/A | 25.0-27.4 | |
| SGL 34BC | Paper | 5 wt% | Yes | 314-317** | Oxygen | N/A | 0.66-0.67 | [106] |
| MPL | N/A | N/A | N/A | 61-64** | | N/A | 0.13-0.14 | |
| SGL 10BA | Paper | 5 wt% | No | 400** | | N/A | 37.4 | |
| SGL 24BA | Paper | 5 wt% | No | 195** | | N/A | 14.5 | |
| SGL 34BA | Paper | 5 wt% | No | 285** | | N/A | 16.3 | |
| AvCarb P75 | Paper | No | No | 210** | Air | N/A | 5.70 | [115] |
| TGP-H-090 | Paper | No | No | 290** | | N/A | 8.99 | |
| E-Tek | Cloth | No | No | 360** | | N/A | 69.4 | |
| TGP-H-120 | Paper | No | Yes | 434** | | N/A | 0.295 | |
| TGP-H-120 | Paper | 20 wt% | Yes | 388** | | N/A | 0.436 | |
| TGP-H-120 | Paper | 20 wt% | Yes | 434** | Air | N/A | 0.336 | [116] |
| TGP-H-120 | Paper | 20 wt% | Yes | 486** | | N/A | 0.202 | |
| TGP-H-120 | Paper | 40 wt% | Yes | 434** | | N/A | 0.085 | |
| SGL 10AA | Paper | No | No | 390** | | N/A | 24.2 | |
| SGL 10BA | Paper | 5 wt% | No | 400** | | N/A | 27.2 | |
| SGL 10CA | Paper | 10 wt% | No | 400** | | N/A | 22.2 | |
| SGL 10DA | Paper | 20 wt% | No | 400** | Air | N/A | 21.9 | [108] |
| SGL 10EA | Paper | 30 wt% | No | 374** | | N/A | 23.9 | |
| EP 40 | Paper | No | No | 200** | | N/A | 7.20 | |

Note: 1. Experimental data on permeability are collected at room conditions;

2. MPL refers to the microporous layer;

3. PTFE represents polytetrafluoroethylene or Teflon;

4. * denotes the data taken from the manufacturer, and ** denotes the data taken from literature.

It is evident that despite its importance, the effect of CL on the permeability of the entire electrode of PEM fuel cells has not been investigated adequately. Therefore, one of the sub-objectives of the present study is to measure the permeability of the GDL with and without CL and the CL through ex-situ experiments such that the measured permeability values can be useful for modeling and simulation studies.

### 2.2.4.3 Correlation of Pore Structure and Permeability

The gas permeability of the electrode (i.e., GDL and CL combined) is controlled by its overall porous structure. Many models have been developed based on the pore structure to predict the gas permeability of different porous layers in PEM fuel cells. **Table 5** summarizes the most commonly used models for the porous layers in PEM fuel cells [93,101,109,117–120]. These models are widely employed for the porous media consisting of either spherical particles or fibers. Tomadakis et al. [101,109,117,118] developed different models based on fibrous materials with various structures. These models indicated that the permeability of the fibrous materials is significantly affected by the fiber diameter, porosity, and fiber direction. The other models are established based on spherical particles [93,119,120], and these models showed that the permeability is dependent on the spherical particles' diameters and porosity. A considerable amount of effort has been devoted to developing a general formula to estimate the permeability of different porous layer structures [109,120]; however, such a general formula does not exist yet because the permeability depends on the fiber/particle shape, size distribution, and their packing structure [93,120,121]. In PEM fuel cells, the porous electrode is a combination of the carbon fibers, carbon particles, Pt/C particles, PTFE, and ionomers, and its complex structure makes these models fail to predict the permeability of the electrode accurately. Further, the gas permeability also can be affected by many other factors. Klinkenberg (1941) pointed out that the gas permeability also depends on the gas properties, and the experimental results indicated that the air permeability of the Jena glass filter can be 28% smaller than hydrogen permeability in the same materials [112]. Zamora et al. (2015) also proved that the permeability of the MPL made of Vulcan XC72 particles for hydrogen is about 20% higher than that for the oxygen and air [122]. This observation implies that the hydrogen is easier to pass through the GDL and CL than the air in operating PEM fuel cells. In addition, the mean pressure of the gases in the porous samples also influences the permeability of gases because the mean free path of the gas varies with pressure [112].

**Table 5.** Models to predict the gas permeability of the porous media in polymer electrolyte membrane (PEM) fuel cells.

| Model | Material | Note | Reference | Eq. # |
|---|---|---|---|---|

| | | $\varepsilon$ –porosity | | |
|---|---|---|---|---|
| $$K = \frac{\varepsilon}{K_c}\left(\frac{V_{\text{pore}}}{S_{\text{pore}}}\right)^2$$ | General porous media | $K_c$ –Kozeny constant<br>$V_{\text{pore}}$ –pore volume<br>$S_{\text{pore}}$ –pore surface | [109] | (2.17) |
| $$K = \frac{r^2\varepsilon}{4K_c(\ln\varepsilon)^2}$$ | Random overlapping fiber structures | $r$ – fiber radius<br>$\varepsilon$ –porosity<br>$K_c$ –Kozeny constant | [109,117] | (2.18) |
| $$K = \frac{r^2\varepsilon^3}{4K_c(1-\varepsilon)^2}$$ | Random non-overlapping fiber structures | $r$ – fiber radius<br>$\varepsilon$ – porosity<br>$K_c$ –Kozeny constant | [109,118] | (2.19) |
| $$K = r^2\frac{\varepsilon(\varepsilon-0.11)^{\alpha+2}}{8(ln\varepsilon)^2\,(1-\varepsilon)^\alpha[(\alpha+1)\varepsilon-0.11]^2}$$ | Fibrous material | $r$ – fiber radius<br>$\varepsilon$ –porosity<br>$\alpha$ –0.785 through-plane<br>0.521 in-plane | [101,109] | (2.20) |
| $$K = \frac{d^2\varepsilon^3}{150(1-\varepsilon)^2}$$ | Spherical particles | $d$ –particle diameter<br>$\varepsilon$ –porosity | [93,119] | (2.21) |
| $$K = \frac{d^2\varepsilon^{5.5}}{5.88}\ \ (0.35 < \varepsilon < 0.7)$$ | Spherical particles | $d$ –particle diameter<br>$\varepsilon$ –porosity | [93,120] | (2.22) |

Note: Kozeny constant is an unknown parameter for most porous materials.

Due to its unique structure of the limited small dimensions in thickness and the presence of electrical current, it is challenging to conduct *in-situ* experimental measurement of various properties in an operating PEM fuel cell, and numerical models and simulations have been instrumental in providing an understanding of PEM fuel cell operation and performance [123,124]. PEM fuel cell operation and performance are essentially determined by the balance between the mass transport of gases through GDL and CL and the electrochemical reactions occurring on the catalyst surface. It is hence well known that in PEM fuel cells the mass transport of gases through GDL and CL is very significant factors affecting their performance [11]. However, due to the lack of experimental data in literature, many modeling and simulation studies, even some recent ones, either take the permeability values of the CLs or electrodes from another modeling and simulation study in literature, or simply assume some guessed values [123,125,126], and the value used in the modeling and simulation studies varies by many orders of magnitude, for example, from $10^{-15}$ to $10^{-12}$ m$^2$ [123–126]. Some other modeling and simulation studies may just estimate the

permeability values from some theoretical models as shown in **Table 5**. But as discussed earlier, these models in **Table 5** may not be suitable for the catalyzed electrodes or CLs because of their uniquely different compositions and structures. Therefore, ex-situ experimental study to measure gas permeability of GDLs, CLs and catalyzed electrodes is urgently required for the modeling and simulation as well as the design calculation of PEM fuel cells.

## 2.3 Effect of Macro-Property on Performance

The performance of the PEM fuel cells is usually characterized by a polarization curve which is a plot of the cell potential versus current output [1]. The current output is normalized by the area of fuel cells in a unit of $A \cdot cm^{-2}$ to provide comparable performance with other fuel cells of different types and sizes. The polarization curve is a critical indicator of the PEM fuel cell performance. As shown in **Fig. 8**, a sample polarization curve demonstrates various energy losses (or voltage drops) in a PEM fuel cell.

For a single PEM fuel cell, the thermo-neutral voltage is defined as the voltage a PEM fuel cell would have if all chemical energy stored in $H_2$ and $O_2$ is converted to electricity. It is impossible for PEM fuel cells to maintain the voltage at such a high level due to unavoidable heat generation during PEM fuel cell operation. Theoretically, there exists a maximum achievable voltage which is called reversible voltage, and the cell can only operate at the reversible cell potential under the thermodynamically reversible condition. However, in a practical PEM fuel cell, the cell voltage decreases as the increase of current due to four major types of irreversible losses: the losses due to fuel crossover and internal currents, activation loss, ohmic loss, as well as concentration loss.

Fuel crossover and internal currents are associated with the waste of fuels and electrons passing through the electrolyte [1]. Ideally, the electrolyte only transports protons and insulates fuel gasses for PEM fuel cells; however, a small amount of fuel and electrons passing through the membranes as the diffusion is always possible. The diffusion does have a remarkable impact on the open circuit voltage (OCV). Thus, this OCV is always lower than the reversible voltage. This type of energy loss decreases considerably and even diminishes when the current density increases.

Additionally, the nature of the PEM dominates this kind of energy loss which is beyond the scope of this research [1].

Activation loss arises from the slow rate of electrochemical reactions on the electrode surface, and a portion of energy is consumed to speed up the electrochemical reactions so that the demanded current can be achieved. Electrons and protons do not participate in the reactions immediately when they are released. The reactions only proceed when a certain amount of electrons and protons accumulates on the surface of the electrodes. The activation loss leads to a rapid voltage drop at the small current density region as shown in **Fig. 8**. The nature of catalysts and the structure of CLs determine the activation loss. Currently, Pt shows the best performance to minimize activation loss of PEM fuel cells due to its excellent activity, selectivity, and stability [127], and a higher surface area which is determined by the structure of CLs is also believed to be able to lower the activation loss. However, the activation loss only dominates when the current is small and does not increase too much as current increases [1]. In practice, PEM fuel cells operate at a higher current density region to obtain a larger power output where ohmic and concentration losses dominate.

Ohmic loss arises due to electrical resistance in the cell, including the ionic resistance to the ion flows in the electrolyte and electric resistance to the electron flows in the rest of the cell components [1]. The ohmic loss leads to a linear drop of voltage against the increasing cell current. This ohmic loss is represented by the linear fall in voltage in the middle of the polarization curve as shown in **Fig. 8**. For a well-designed and properly-established PEM fuel cell, the ohmic resistance mainly comes from the membrane. The Ohmic loss is also significantly affected by the electric and protonic conductivities of the CLs. However, a poor design of CLs could also significantly influence the ionic, electronic, and interfacial resistance for the whole fuel cell. The

Concentration loss is important at high current density due to the mass transfer rate from channels to the catalyst layers. The limited transfer rate results in the depletion of reactants near the reaction sites, and the mass transfer can be further restricted by the over-accumulated reaction products, blocking the reactants from approaching the reaction sites [1]. Three principal components significantly contribute to the concentration loss, including flow channels, GDLs and CLs. The concentration loss is affected by the effective diffusion coefficient and permeability of the GDLs

and CLs. Extensive numerical and experimental studies have been made to investigate the effect of flow channels and GDLs on the concentration losses [1,61,92]; however, the effect of CLs is still unclear, and the experimental data are rarely available in literature.

Recently, industry trends to operate the PEM fuel cell at the high current density region to obtain a higher performance (voltage and power); thus, the mass transport limitations are paramount. Therefore, the micro-porous structure and transport coefficient of different components, especially for the CLs, should be accurately measured to improve the numerical models and understand the fabrication and optimization of the CLs.
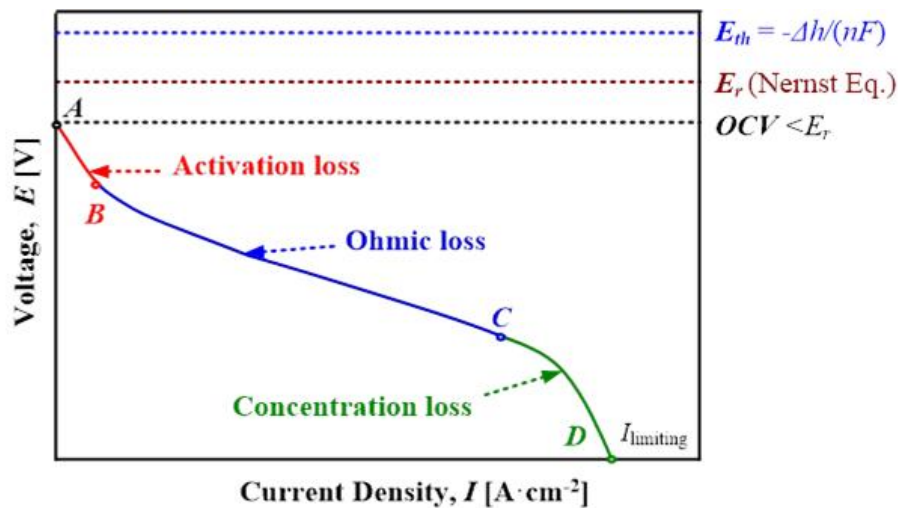


**Fig. 8.** A typical polarization curve of a single polymer electrolyte membrane (PEM) fuel cell (OCV denotes the open circuit voltage, $E_r$ is the reversible voltage, and $E_{th}$ is the thermo-neutral voltage).

## 2.3.1 Experimental

Mass transport limitation is recognized as the major obstacle that prevents the PEM fuel cells from achieving a high current density, which is crucial to improving the cell performance. Typically, the mass transport involves the effective transport of oxygen, hydrogen, product water (both liquid and vapor phase), electrons, and protons. The oxygen transport is more significant than hydrogen due to its low kinetics, and the existence of both liquid and vapor water makes the oxygen supply at the reaction sites even more complicated. In practice, humidified air is often used as the cathode

reactant gas, and the oxygen transport through the porous electrode is regarded as the most challenging technical difficulties, which is dominated by two major mechanisms: convection (driven by pressure gradient) and diffusion (driven by concentration gradient) [3,5,7,128].

The porous media's capability of transporting reactant gas through convection is characterized by permeability [5]. Higher gas permeability indicates that the gas species are easier to be transported through the porous layers under a given pressure difference. The permeability value is usually experimentally determined by Darcy's law which describes the relation between the flow rate and pressure gradient across the porous media [5,20,83,107]. Zhao et al.[5]'s work indicated that the Pt loading and Pt/C ratio are significant factors that affect the permeability of the porous media. Their results also exhibited that the thickness variation due to different design parameters of the CLs also affects the diffusion rate dramatically. For a specific porous layer with a constant gas permeability and thickness, the gas flow rate is determined by the gas pressure difference on both sides of the porous media. However, in PEM fuel cells, the measurement of the tiny pressure difference over the distance of a few microns is almost impossible.

The ability of the gas diffusion in porous media is measured by the effective diffusion coefficient [3,9]. The effective diffusion coefficient is commonly determined through Fick's law of diffusion, by measuring the gas concentration changes over time at a specific point in a binary diffusion system [66,90,91]. The pore structure, including porosity, pore size, and tortuosity, has a significant impact on the values of the effective diffusion coefficients. In addition, the thickness of the porous layer also dramatically affects the diffusion process. For a specific porous layer with a constant effective diffusion coefficient and thickness, the species transport rate is determined by the gas concentration difference between both sides of the porous layer; however, it is almost impossible to experimentally monitor the species concentration inside the PEM fuel cell porous media.

The mass transport properties are highly dependent on the pore structure of the GDLs and CLs. However, the pore structure including porosity, pore size, tortuosity, and other parameters varies significantly from the fabrication of the CLs as well as the materials applied. The values of CL porosity, for instance, varies from 30%-60% in literature [98,125,129–131], and this variation results in a significant difference in mass transport as well as cell performance. In addition, the liquid water due to

reaction and phase change will exist in the porous media in PEM fuel cells, which may dramatically reduce the effective porosity, blocking the reactant supply.

In addition to the structure of the porous media, the working conditions also have a significant impact on the mass transport mechanisms and processes [6,8,132]. At the cathode side of the PEM fuel cells, the oxygen is usually supplied from the air in the flow channels. Oxygen passes through the GDLs and arrives at CLs, where oxygen reacts with protons, generating water. The oxygen is continuously consumed at the cathode CL, thus generating a pressure and concentration gradient. However, it is extremely difficult to accurately measure the pressure and oxygen concentration inside the extremely thin porous GDLs and CLs, which necessitates the simulation of mass transport with actual component dimensions and mass transport properties of the porous electrodes for the understanding of mass transport phenomena in PEM fuel cells.

## 2.3.2 Numerical

With the development of PEM fuel cell technology in recent years, numerical simulation is becoming more important to investigate the mass transport, electrochemical reaction, and heat and water management in PEM fuel cells, which are difficult to be studied by experimental methods. The transport phenomena inside the PEM fuel cells are complex, and many uncertainties are related to the mass transport properties such as effective diffusibility and permeability of the porous GDLs and CLs. The effective diffusibility, representing the ability of the gas species to transport within porous media by diffusion, may vary from 0.01~0.9 as predicted by the models in **Table 3**; the permeability value, representing the degree of the convection in GDLs and CLs, may vary from $10^{-14}$~$10^{-10}$ $m^2$ as shown in **Table 4**. The significant variations in mass transport properties may result in many uncertainties in the simulation results, which highlighted the importance of the accurate determination of the mass transport properties, and it will improve the simulation based on these experimental data.

There are various modeling studies focusing on water transport through the membrane and the two-phase water transport in the GDLs and CLs. For the water transport in membranes, three major approaches, such as diffusive approach, convective (or hydraulic) approach, and chemical potential approach, are available in literature [32,61,121,133–141]. The proton concentration in the membrane is assumed

to be constant in the first two approaches, and the electric potential in the membrane is dominated by Ohm's law. However, the third approach assumes that the proton concentration varies with the water content. It should be noted that all these approaches are only valid in certain situations due to many simplifications, and many parameters or correlations, especially the third approach, remain unknown and requires further exploration. For the two-phase water transport in the GDLs and CLs, another three approaches are widely employed in many studies, including the mixture approach, the two-fluid approach, and the volume-of-fluid approach [98,125,128,131,134,135,142,143]. Among these three approaches, the two-fluid approach solves the governing equations for both phases separately, and specifically, in the PEM fuel cell modeling, this approach is often simplified by integrating the continuity with the momentum equation via Darcy's law and porous media's capillary pressure function. Sohn et al. [128] numerically investigated the hydrogen and oxygen transport mechanisms using COMSOL Multi-physics by separating the total reactant flux into convective and diffusive flux components based on the dimensional and mass transport parameters taken from literature. Their results indicated that the oxygen diffusion dominates in cathode GDL, while hydrogen convection and diffusion are equally important in anode GDL [128]. However, which mechanism dominates in different porous layers, e.g., GDLs or CLs, is still unclear.

**Table 6.** Mass transport parameters in PEM fuel cell modeling.

| Reference | Dimension | Porosity | Permeability | Diffusibility | Validation |
|---|---|---|---|---|---|
| S. Um et al. (2000) [98] | *$L$=7.112 cm<br>*$\delta_{gdl}$=254 μm<br>*$\delta_{cl}$=28.4 μm<br>*$\delta_{mem}$=230 μm<br>*$H_{cha}$=76.2 μm | *$\varepsilon_{GDL}$ = 0.4 | *$K_{GDL}$=1.76×10$^{-11}$$m^2$ | Bruggeman's correlation | Experimental data from literature |
| Z. Wang et al. (2001) [125] | *$L$=2 cm<br>*$\delta_{electrode}$=500 μm<br>*$H_{cha}$=700 μm | ***$\varepsilon$ = 0.3 | **$K$=10$^{-13}$$m^2$ | From literature | N/A |
| L. Wang et al. (2003) [17] | N/A | N/A | N/A | Bruggeman's correlation | Experimental data |
| U. Pasaogullari et al. (2004) [129] | *$\delta_{gdl}$=300 μm | *$\varepsilon_{GDL}$ = 0.5 | *$K_{GDL}$=5×10$^{-13}$$m^2$ | Bruggeman's correlation | N/A |
| Q. Ye et al. (2007) [130] | *$L$=20 cm<br>*$H_{cha}$=0.5 mm<br>*$W_{cha}$=1 mm<br>*$W_{rib}$=1 mm<br>*$\delta_{gdl}$=180 μm<br>*$\delta_{mem}$=50 μm | *$\varepsilon_{GDL}$ = 0.7<br>*$\varepsilon_{CL}$ = 0.2 | *$K_{GDL}$=3.0 ×10$^{-12}$$m^2$<br>*$K_{CL}$=3.0 ×10$^{-14}$$m^2$ | Bruggeman's correlation | N/A |

| | | | | | |
|---|---|---|---|---|---|
| Y. Jiang et al. (2018) [141] | *$H_{cha}$=1 mm<br>*$W_{cha}$=1 mm<br>*$W_{rib}$=0.5 mm<br>*$\delta_{gdl}$=300 μm<br>*$\delta_{mem}$=10 μm | *$\varepsilon_{GDL}$ = 0.6<br>*$\varepsilon_{CL}$ = 0.3 | *$K_{GDL}$=1.0 ×10$^{-11}$$m^2$<br>*$K_{CL}$=1.0 ×10$^{-13}$$m^2$ | Bruggeman's correlation | Experimental data from literature |
| Present Study | Measured | Measured | Measured | Measured | Experimental data |

Note:　　*　　　　Sources not specified

　　　　　**　　　　Assumed values

　　　　　***　　　Data taken from the publications

**Table 6** summarizes the major component structure and mass transport properties in literature. It is found that most of the models assume equal thickness for the anode and cathode CLs; however, practically, due to the various Pt loadings applied at the anode and cathode, a difference in thickness is always expected [3,6,7,10,11]. The varied thicknesses in the anode and cathode CLs should be introduced into the numerical models as the thickness of the CLs has a significant impact on the effective diffusion and permeation resistivity [3,5,11], which has been paid less attention in literature. The porosity of the GDL and CL, which is important for the reactant and water transport, also varies greatly from 0.3 to 0.7 in previous numerical studies as shown in **Table 6** [17,98,125,129–131]. However, these porosity values are taken from either unknown sources or other published experimental data. In addition, the permeability of the electrode is also varied significantly from ~10$^{-11}$ *to* ~10$^{-14}$$m^2$, and these data are difficult to be measured and often assumed or taken from the published data [17,98,125,129–131]. The diffusibility is often taken from the empirical correlations or literature [17,98,125,129–131], which may not be suitable for the CLs or catalyzed electrodes as the structure of the CLs is complicated due to the presence of the catalysts and ionomers [3,6]. Therefore, the experimental measurements of the component structure and mass transport properties are essential, and the validation with the corresponding *in-situ* experiment is necessary.


## 2.4 Summary

Extensive work has been done to optimize the CLs of PEM fuel cells in literature. However, much of this work is trial and error experiment in general and lacks understanding of the structure of the CLs. The literature review indicates that the

fabrication processes strongly affect the structure of the CLs, further influencing the macro-properties of the CLs and the cell performance. Therefore, understanding the structure of the CLs is of great significance for the optimization of the PEM fuel cells.

This present study is important since PEM fuel cells are considered to be a viable alternative power source and further research is needed to promote its commercialization. Macro-properties of the CLs, e.g., effective diffusion coefficient and permeability, are the limiting factors of the reaction rate at high current density regions, thus a better understanding of the CL structure is urgent. This thesis study is focused on the development of a comprehensive understanding of the relation among fabrication, structure, macro-property, and performance of the CLs. By completing this research, the following contributions to the science will be made:

(1) Understanding how the CL fabrication process determines the structure of the CLs. the In this thesis study, the experimental data on the pore structure characterization such as the porosity, PSD, pore surface area, mean pore size are investigated, and the effect of the fabrication process especially the materials and fabrication methods are studied;

(2) Understanding the impact of the structure of the CLs on their macro-properties. The structure affects the macro-properties, e.g., the effective diffusion coefficient and permeability, and the mechanisms remain unclear. Some studies focus on correlating the porosity with the effective diffusion coefficient and permeability of the porous materials, but these models over predict the effective diffusion coefficient and permeability of the CLs, as they failed to consider the Knudsen effects when the CLs contain micropores and mesopores of which the diameters are too small (<50 nm). This thesis study aims to provide the experimental data on the effective diffusion coefficient and permeability of the CLs, and to investigate the relation between the pore structure and the mass transport properties;

(3) Understanding how the macro-properties of the CLs, e.g., effective diffusion coefficient and permeability, affects the mass transport and hence the cell performance. Due to the lack of experimental means for the investigation of mass transport inside the cells during the cell operation, the mass transport inside the PEM fuel cells under various operating conditions has to be simulated numerically.

# Chapter 3
# Experiment Development

The experimental methods employed in this thesis work consist of five major components: fabrication of CLs, characterization of pore structure, measurements of the effective diffusion coefficient, determination of permeability, and test of cell performance. The pore structure, effective diffusion coefficient, and permeability are measured based on *ex-situ* methods, which can characterize CLs individually. The cell performance is characterized based on *in-situ* methods using a commercially available cell performance test station. The uncertainty of each experimental method is identified and quantified accordingly considering both bias and precision errors, and all uncertainties are studied within 95% confidential intervals unless otherwise specified. Some of the explanations for the experimental apparatus and experimental development are based on the journal articles [2,3,5,6].

## 3.1 Fabrication of Catalyst Layers

The thin-film methods (or the second-generation methods defined in the previous chapters) are employed in the present thesis work due to its unique advantages, such as the balance among the performance, durability, and cost, in comparison with the first- (a.k.a. PTFE-bound method) and third-generation methods (a.k.a. ultra-thin-film method). Additionally, the thin-film methods demonstrate a great space for further improvements by optimizing the structure of the CLs. The fabrication of the CLs using the thin-film methods in this research involves two major processes: catalyst ink preparation and ink coating.

### 3.1.1 Catalyst Ink Preparation

The catalyst ink is prepared following a similar procedure to that in [3,6–8]. Specifically, the catalyst particles, Nafion solution, and solvent (Isopropanol and deionized water) are mixed following a procedure shown in **Fig. 9**. The ink preparation system consists of a digital balance, an ultrasonic machine, and several clean droppers

and vials. The amount of each material is weighted by a digital balance (Sartorius ALC-210.4, the capacity of 210g with a resolution to 0.0001 g). An ultrasonic bath (Fisher Scientific $^{TM}$, 9.5L) is used to make sure that all the substances in the catalyst ink are dispersed uniformly by keeping a constant ultrasonic power, frequency, duration, and temperature. The catalyst ink in the present study is prepared by mixing Pt/C particles (catalyst), Nafion solution (5% Nafion$^{®}$PFSA ionomer as a binder for catalyst particles), and the mixture of water and IPA (working as solvent) under ultrasonic conditions. The Pt/C particles, isopropanol, and water are firstly mixed in a vial. Isopropanol is the major component of solvent due to its fast evaporating rate and good dispersion of ionomer and catalyst particles [144]. Then the mixture is treated ultrasonically for 10 min to make the particles uniformly distributed in the solvent. Subsequently, an appropriate amount of Nafion solution is added to the above mixture. Finally, the ink solution is subject to 60 min of sonication to ensure each ingredient uniformly dispersed in this solution. The ultrasonic treatment duration should be carefully controlled. If the treating time is too short, the particles and ionomers are unable to be uniformly dispersed in the ink and lower the ink activity; otherwise, if too long, cavitation and sonolysis phenomena will be harmful to the composition and morphology of the CLs [47]. In this research, a 60 min ultrasonic treatment is sufficient to disperse the particles and to avoid material degradation problems [47].

┌─────────────────────────────────┐
│ *Set Target Ink Composition* │
└─────────────────────────────────┘

┌─────────────────────────────────┐
│ *Calculation:* │
│ *Weight of Pt/C* │
│ *Weight of Nafion Solution* │
│ *Weight of Isopropyl alcohol* │
│ *Weight of $H_2O(l)$* │
└─────────────────────────────────┘

┌─────────────────────────────────┐
│ *Mix Pt/C, isopropyl alcohol and $H_2O(l)$* │
└─────────────────────────────────┘

┌─────────────────────────────────┐
│ *Ultrasonic treatment for 10 mins* │
└─────────────────────────────────┘

┌─────────────────────────────────┐
│ *Drip Nafion Solution into the mixture* │
└─────────────────────────────────┘

┌─────────────────────────────────┐
│ *Ultrasonic treatment for 60 mins* │
└─────────────────────────────────┘

┌─────────────────────────────────┐
│ *Final prepared catalyst ink* │
└─────────────────────────────────┘
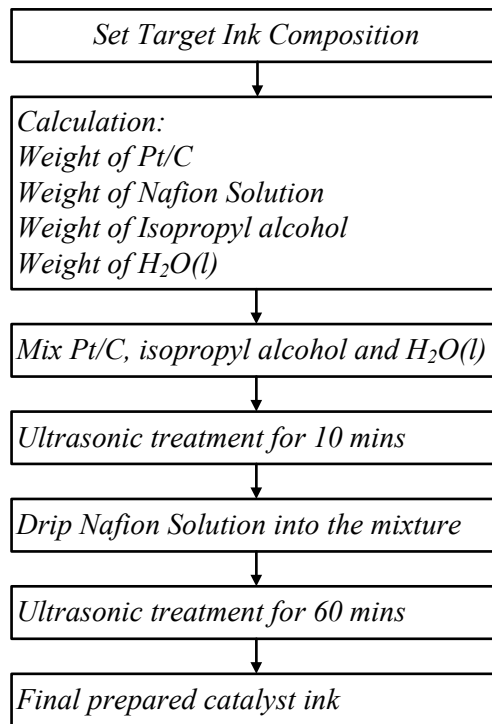
**Fig. 9.** Catalyst ink preparation procedures.

## 3.1.2 Catalyst Layer Fabrication Procedures

Three prevalent modes of the thin-film methods are widely employed in literature: catalyst coated on GDL substrate (CCS or CCGDL), catalyst coated on membrane (CCM), and decal transfer method (DTM) [1,5,11,14,19,52,144–153] as shown in **Fig. 10**. It should be noted that during the DTM, the catalyst is applied onto a nonporous decal substrate, followed by a hot pressing process. As this method has a risk of uneven and incomplete transfer of catalyst from the decal substrate to the membrane, this method may not be appropriate for the development of low-Pt-loading electrodes [145]. For these reasons, the present studies focus on the CCM and CCS methods.

In the present study, all catalyst inks are coated using an airbrush (Paasche TALON) by spraying the prepared ink onto the surface of substrates. The spraying method is advantageous in comparison with other techniques such as blading and brushing when the Pt loading is very low (e.g., 0.1 mg·cm$^{-2}$) as it is easier to for spraying to control the amount of ink applied while offering excellent surface properties [144]. For CCS methods, catalysts are coated on the surface of GDL and then the prepared electrodes (GDL+CL) are combined with a membrane in between to

fabricate the membrane electrode assembly (MEA). For CCM, catalysts are directly coated on the surface of membranes on both sides, then two pieces of GDLs are attached on the outer side of CLs. For each method, the catalyst inks are coated using spraying technique and then dried in a vacuum environment with the temperature of 60 $^{o}$C. The spraying and drying processes are repeated until the desired Pt loading is achieved.
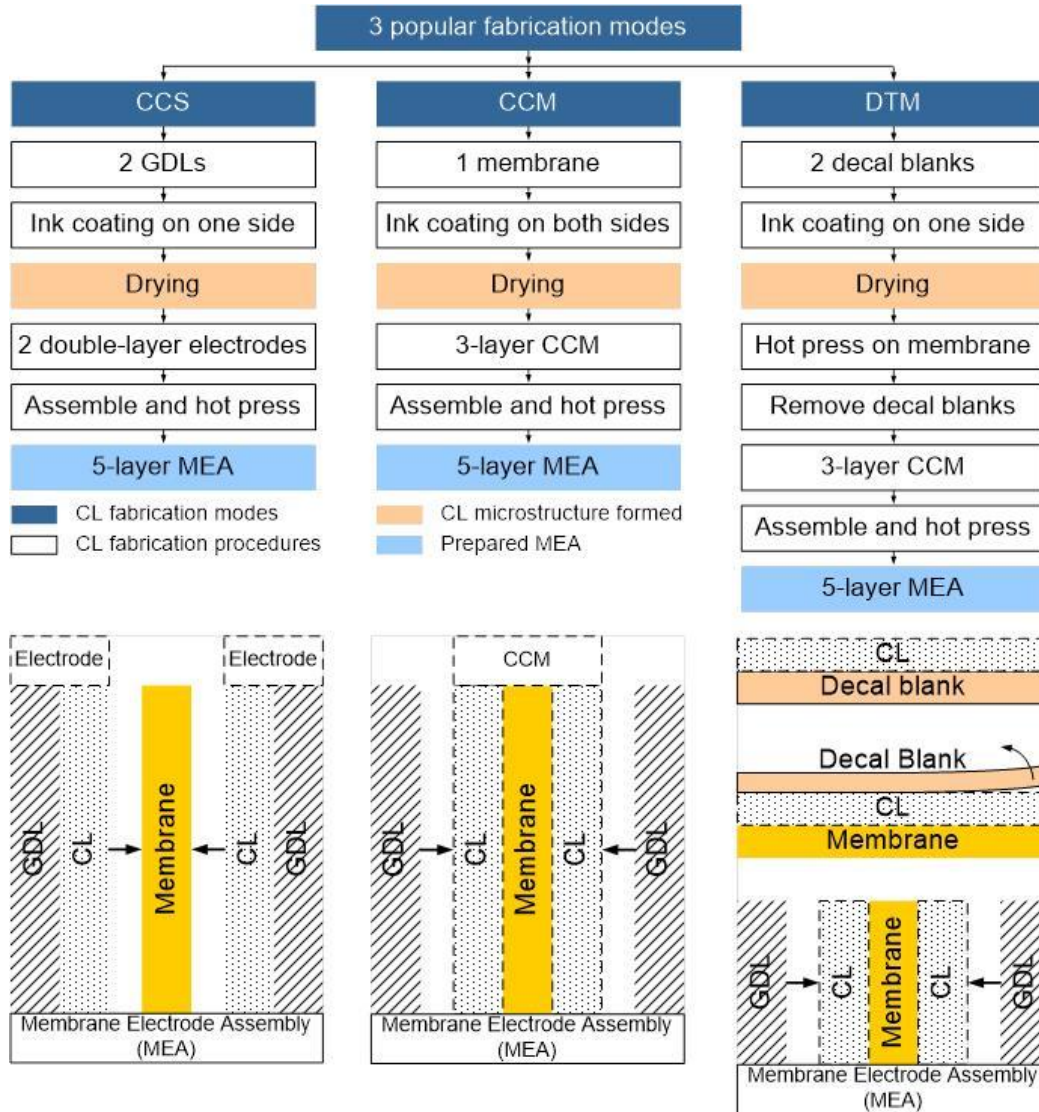


**Fig. 10.** Three major modes of the thin-film catalyst layer fabrication methods.

## 3.2 Pore Structure of Catalyst Layers

The method of standard porosimetry (MSP) is selected to measure the pore size distribution (PSD) of CLs due to its wide range of measurable pore size, no deformation to the tested porous samples, non-poisonous working liquid and good agreements with other methods. The Standard Porosimeter (SP) 3.1 manufactured by POROTECH is utilized to test the samples automatically.

### 3.2.1 Principle of Standard Porosimetry

The MSP is developed based on the phenomenon of capillary equilibrium [67,68,154], which means that if two or more porous materials stay together for a sufficiently long time in a wetting liquid, they will have the same capillary potentials (capillary pressure is one kind of the capillary potential):

$$p_{ca_1} = p_{ca_2} = p_{ca_i} = p_{ca} \tag{3.1}$$

where $p_{ca}$ is the capillary pressure of $i$ <sup>th</sup> layer of porous media.

The MSP experimentally determines the relationship between the liquid volume ($V_t$) in the test sample and the liquid volume ($V_s$) in the standard sample:

$$V_t = f_V(V_s) \tag{3.2}$$

The liquid distribution in the standard sample can be expressed as a function of $p_{ca}$ and is provided by the manufacturer as follows.

$$V_s = f_s(p_{ca}) \tag{3.3}$$

The liquid distribution in the tested samples regarding $p_{ca}$ is determined:

$$V_t = f_V[f_s(p_{ca})] \tag{3.4}$$

The capillary pressure, $p_{ca}$, can be expressed as the Young-Laplace equation [67]:

$$p_{ca} = -\frac{2\sigma\cos\theta}{r_{max}} \tag{3.5}$$

where $\sigma$ is the surface tension of the liquid, $\theta$ is the wetting angle, and $r_{max}$ is the maximum pore radius filled with liquid. Hence the function between $V_t$ and $r_{max}$ becomes:

$$V_t = f_V\left[f_s\left(-\frac{2\sigma\cos\theta}{r_{max}}\right)\right] = F(\theta, r_{max}) \tag{3.6}$$

For octane, the wetting angle is almost zero for all materials, thus **Eq. (3.6)** can be simplified to,

$$V_t = f_V \left[ f_s \left( -\frac{2\sigma}{r_{max}} \right) \right] = F(r_{max}) \tag{3.7}$$

On the other hand, the total pore volume, $V_{pore}$, of the test samples can be determined as follows:

$$V_{pore} = \frac{m_{sat} - m_{dry}}{\rho} \tag{3.8}$$

where $m_{sat}$ is the total mass of the saturated sample, $m_{dry}$ is the total mass of the dry sample, and $\rho$ is the density of the octane.

The bulk volume, $V_{bulk}$, can be calculated:

$$V_{bulk} = \frac{\pi d^2 \delta N}{4} \tag{3.9}$$

where $d$ is the diameter of the test sample, $\delta$ is the thickness of the sample and N is the number of the samples being tested together. In this case, $d = 23$ mm, and $N = 2$.

The porosity, $\varepsilon$, is defined as:

$$\varepsilon = \frac{V_{pore}}{V_{bulk}} \tag{3.10}$$

The pore surface area, $S_{pore}$, can be calculated from the integral pore radius distribution curve by using the following equation [65]:

$$S_{pore} = 2 \int_{r_{min}}^{r_{max}} \frac{1}{r} \frac{dV_t}{dr} dr \tag{3.11}$$

The specific surface area, SSA, is defined by the following equation in order to make a good comparison with other samples,

$$SSA = \frac{S_{pore}}{V_{bulk}} \tag{3.12}$$

The mean pore size, MPS, is defined as [3,6,93]:

$$MPS = \frac{4V_{pore}}{S_{pore}} \tag{3.13}$$

The fractal dimension, $FD$, can be determined based on the relation between the fractal surface area, $S_{pore}$, and the pore radius or "scale", $r$, used to measure the surface area, according to the following relation,

$$SSA = k_{FD} r^{2-FD} \tag{3.14}$$

where $k_{FD}$ is the constant that describes the shape of the solid elements in the porous media. The values of $k_{FD}$ and $FD$ can be determined by curve fitting of the pore surface area distribution using **Eq. (3.14)**.

The relation between the liquid content in the test sample and that in the standards can be determined by measuring the mass variation of each sample with a high-accuracy balance. Referring to the given PSD curve of the standard sample (provided by POROTECH, Ltd.), the pore volume and maximum pore size occupied by the liquid can be obtained.

**Fig. 11** represents the process of how the PSD is determined by the MSP method. On the left side, curve 2 shows the relationship between $V_s$ and $V_t$ which is measured by the MSP. On the right part of this figure, the pore volume of the standard sample presents a function of $log\ (r_{max})$. Curve 1 is the PSD curve for the standard sample given by the manufacturer. Curve 3 is the cumulative PSD of the tested samples which presents in the final results.
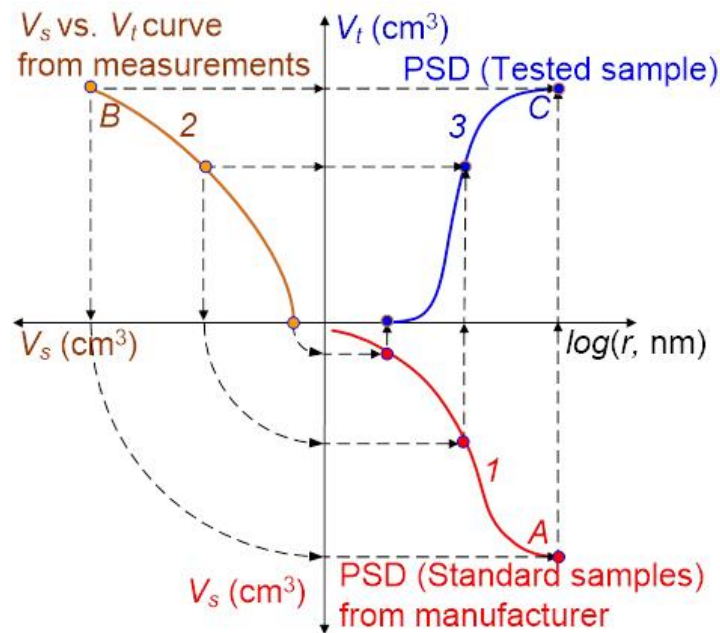


**Fig. 11.** Principles of the method of standard porosimetry: (1) Pore size distribution (PSD) curves for the standard sample; (2) $V_s$ vs. $V_t$; (3) PSD curves for the tested sample [67,68].

This experiment assumes that the wetting angles of the liquid octane for all contacted sample bodies are equal to zero. For a particular case of capillary

equilibrium, the $V_s$ and $V_t$ determine point B on curve 2. Then point A can be found as presented in **Fig. 11**, in which the maximum size of pores filled with the liquid in the standard sample can be determined. Due to capillary equilibrium, the maximum pore size of the test samples remains the same. By referring to point C in this figure, the relationship between $V_t$ and $r_{max}$ can be established. By repeating the evaporating and measuring procedures, more data points are collected to generate the PSD curve for the tested sample. The overall distribution curve 3 for the test sample is thus determined.

### 3.2.2 Experimental Setup

The experimental system setup is shown in **Fig. 12**. The experiment system consists of the following major components: (1) heating bottle, (2) vacuum pump, (3) clamping device, (4) digital balance, (5) standard porosimeter, (6) working liquid (octane), (7) sealed bottle, and (8) drying station.
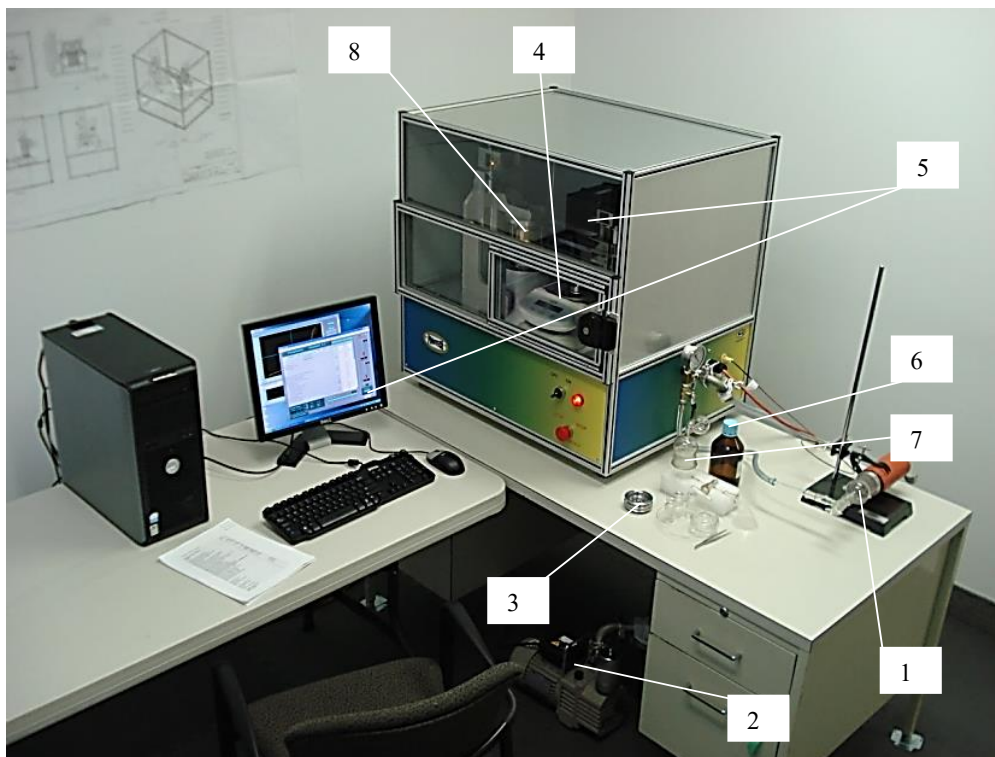


**Fig. 12.** Experiment system setup of the method of standard porosimetry (MSP): (1) heating bottle, (2) vacuum pump, (3) clamping device, (4) digital balance, (5) standard porosimeter (manufactured by Porotech, Ltd.), (6) working liquid (octane), (7) sealed bottle, and (8) drying station.

The heating bottle is used to heat the samples before each measurement, and the samples are totally dried after 30 mins. The vacuum pump is mainly used to create a vacuum environment so that the pores in the material are free of water vapor in the air. The clamping devices as shown in **Fig. 13** can fix the samples and slightly push them together. The stacked samples achieve capillary equilibrium after evaporating a small amount of octane. The digital balance with the high accuracy and resolution measures and records the mass change of these samples. The MSP automatically measures the mass of the samples with the help of the clamping devices. Octane is the working fluid since its wetting angle is almost zero degrees in all samples. The drying station is the place where the samples are dried at the temperature of 35 $^{\circ}$C. More detailed information about the experiment devices is shown in **Table 7**.
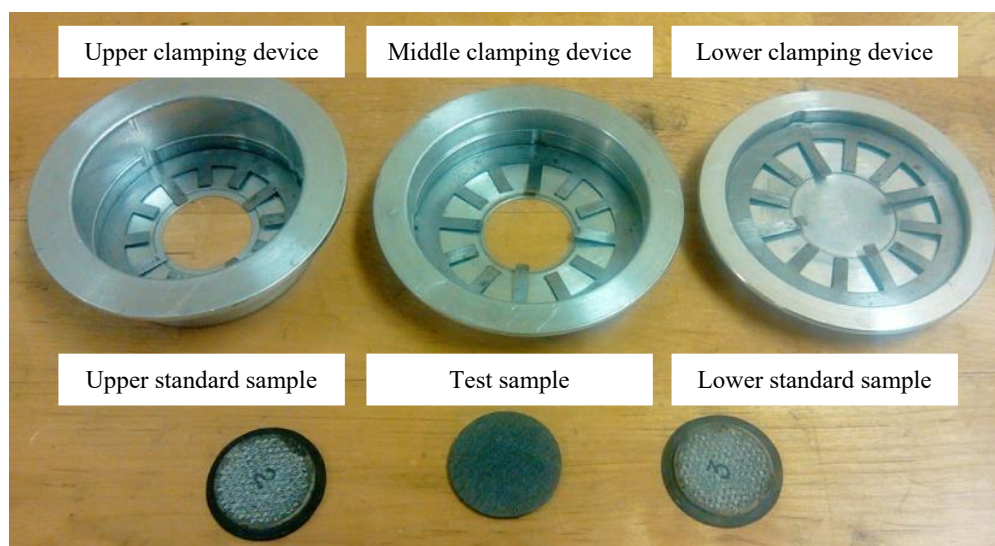


**Fig. 13.** Test samples, standard samples, and clamping devices.

**Table 7.** Major experimental devices for the method of standard porosimetry (MSP)

| Equipment | Specification | Manufacturer |
|---|---|---|
| Standard Porosimeter 3.1 | Dimensions: 840x800x660 mm(W-H-D) Mass: 85 kg (without a vacuum pump) AC 110V/60Hz Maximum power: 1 kW | POROTECH LTD. |
| Standard sample | Porous Teflon material in a disk-like shape Thickness: $\leq$ 1 mm Diameter: 20 mm | GORE$^{TM}$ |
| Digital Balance | Repeatability: $\pm$ 0.0001 g | Sartorius ALC-210.4 |

| (For automatic measurements) | Linearity: ± 0.0003 g<br>Resolution: 0.0001 g<br>Capacity: 210 g | |
|---|---|---|
| Digital Balance<br>(For manual<br>measurements) | Repeatability: ±0.000015 g<br>Linearity: ±0.00015 g<br>Resolution: 0.00001 g<br>Capacity: 60 g | Sartorius MSE125P |
| Vacuum Pump | 120V 3A | POROTECH LTD. |
| Heater | AC 110V | POROTECH LTD. |
| Electronic disk<br>micrometer | Accuracy: ±0.004 mm<br>Resolution: 0.001mm | The Fred V. Fowler<br>Company |
| n-Octane | Density of the octane: 702.2 kg·cm$^{-3}$<br>Surface Tension: 0.02175 N·m$^{-1}$<br>Wetting Angle: 0° | Sigma-Aldrich Co. LLC. |

## 3.2.3 Experimental Procedures

**(1) Test sample preparation**

The test samples are cut into a disk-like shape with a diameter of 2.3 cm using a die. 3~5 layers of samples are placed together as an individual test object so that the assembled test samples are thick enough to uptake sufficient liquid. Therefore, an adequate number of measurement points (e.g., ~100 points in this case) can be achieved to plot a relatively smooth PSD curve as shown in **Fig. 11.**

The geometrical sizes (thickness and diameter) of the samples are measured directly by the micrometer. Additionally, the compacted dry test samples and two dry standard samples are weighed separately by using the digital balance. Thus, the dry mass of the samples, $m_{dry}$, is determined

$$m_{dry} = m_1 - m_2 \qquad (3.15)$$

where $m_1$ is the total mass of the clean bottle and the test sample, and $m_2$ is the mass of the clean empty bottle.

**(2) Experimental Procedures**

After preparing the test specimens, this experiment is conducted in three major steps. First of all, the two standard samples and the test sample are dried in the heating bottle in a vacuum environment. The heating temperature keeps at 180 $^o$C (which can be adjusted according to the tested materials). After heating for 30 minutes, the samples are totally dried, which means that all pores in the samples are empty.

Secondly, a bottle seals the three totally dried samples under a vacuum environment. Subsequently, this bottle is filled with octane, and the samples are entirely immersed in the octane for 30 minutes. Thirdly, after the capillary equilibrium is achieved, the prepared samples are closely assembled in three individual clamping devices, which have been weighed ahead individually. Then the assembled samples and clamping devices are placed under the normal force of 6.86 N, under which the samples will not be damaged and can keep closely contacted. The samples achieve a new capillary equilibrium after a small portion of the liquid evaporating from these samples by heating at the temperature of 35 $^o$C for 1.5 minutes. Subsequently, a manipulation robot (as shown in **Fig. 14**) controlled by the computer program realizes the MSP automatically. The manipulation robot arm moves the clamping devices with samples from the drying station to the weighing station. The robot arm helps separate these clamping devices individually and measure the mass of each clamping device (upper, middle, and lower) with the corresponding sample, respectively (as shown in **Fig. 15**). Thus, the mass of the evaporated octane from each sample can be calculated by subtracting two adjacent measurements. This weighing process takes 1 minute. After the weighing process, these samples and clamping devices are reassembled, reheated and pressurized again. The above procedures are then repeated about 100 times until the samples are totally dried when the mass of the samples keeps unchanged. Thus the volume and weight of the liquid in these samples at different stages are estimated from the recorded data, which are collected and stored in the computer. The relation between the volume of the liquid in the porous test sample and that in the standard samples, together with known PSD curve of the standard sample provided by the manufacturer, gives a PSD curve for the sample under study [67,68]. Thus, the porosity and PSD of the tested material can be determined. Each type of materials is tested and measured at least three times to guarantee the accuracy and reduce the reading errors.

**Fig. 14.** Manipulation robot of the method of standard porosimetry (MSP).
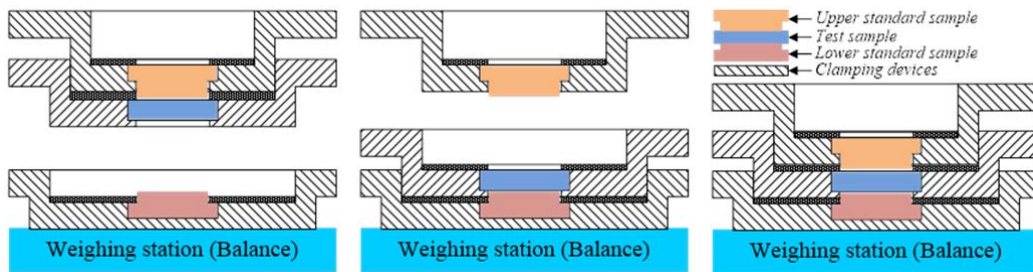


**Fig. 15.** Automatic weighing processes of the method of standard porosimetry (MSP).

Base on the above test procedures, the pore volume of the test samples can be determined as follows,

$$V_{\text{pore}} = \frac{(m_{\text{sat\_bs}} - m_{\text{b}}) - (m_{\text{dry\_bs}} - m_{\text{b}})}{\rho_{\text{octane}}} \qquad (3.16)$$

where $m_{\text{sat\_bs}}$ is the total mass of the saturated sample and clean bottle, $m_{\text{dry\_bs}}$ is the total mass of the dry sample and clean bottle, $m_{\text{b}}$ is the mass of the clean bottle, $\rho_{\text{octane}}$ is the density of the octane.

The effective area, $A$, of samples is calculated using the following equation,

$$A = \frac{1}{4}\pi d^2 \qquad (3.17)$$

where $d$ is the diameter of the samples.

The bulk density of the test samples can be calculated by the following,

$$\rho_{\text{bulk}} = \frac{m_{\text{dry\_bs}} - m_{\text{b}}}{\frac{1}{4}\pi d^2 \delta} \tag{3.18}$$

where $m_{\text{dry\_bs}}$ is the mass of clean bottle and dry test sample, and $m_{\text{b}}$ is the mass of the clean empty bottle, and $\delta$ is the thickness of the tested specimen.

The porosity, $\varepsilon$, of the test sample becomes,

$$\varepsilon = \frac{(m_{\text{sat\_bs}} - m_{\text{b}}) - (m_{\text{dry\_bs}} - m_{\text{b}})}{\frac{1}{4}\pi d^2 \delta \rho_{\text{octane}}} = \frac{m_{\text{sat\_bs}} - m_{\text{dry\_bs}}}{\frac{1}{4}\pi d^2 \delta \rho_{\text{octane}}} \tag{3.19}$$

## 3.2.4 Uncertainty Analysis

Based on the above analysis, the estimate of the uncertainty of the pore volume and porosity is a root sum square,

$$U_{\text{rss}} = \left[ \left( \frac{\partial f}{\partial x_1} U_1 \right)^2 + \left( \frac{\partial f}{\partial x_2} U_2 \right)^2 + \cdots + \left( \frac{\partial f}{\partial x_N} U_N \right)^2 \right]^{\frac{1}{2}} \tag{3.20}$$

where $f$ is the function of the pore-structural parameter, such as pore volume, porosity, and pore surface area, $x$ denotes the parameters, and $N$ is the number of these parameters.

Detailed calculation of measurement uncertainty is shown in **Appendix I**. The calculation results indicate that the maximum relative uncertainty of the pore volume and porosity, for example, occurs for the low-Pt-loading CLs, which is 5.1% and 7.3%, respectively. The CLs with a low Pt loading (0.1 mg cm$^{-2}$) has a small thickness of 9.7 μm, and the CL can only hold a small amount of liquid. Due to the limitation of the digital balance, a smaller mass of liquid always results in a less relative accuracy. Additionally, the relative measurement uncertainty of PSD also depends on the uncertainty of the standard sample which is < 1 % according to Volfkovich and Sakars [67]. Therefore, the MSP used in this study is suitable for the GDLs, CLs, and electrodes, and the measurement uncertainty is acceptable.

It should be pointed out that for ultra-low-Pt-loading CLs with thicknesses much smaller than 10 μm, the pore structure characterization using MSP should be carefully conducted. Improvements of the experimental equipment are required to further reduce the measurement uncertainty, e.g., by sample stacking and using a high-accuracy balance.

## 3.3 Effective Diffusion Coefficient of Catalyst Layers

The closed-tube method (a.k.a. Loschmidt Cell) is employed in this study to measure the effective diffusion coefficient of CLs due to its relatively high accuracy, easiness of operation, and feasibility of controlling experimental time. A Loschmidt Cell utilizes a long tube closed at both ends, and an opening mechanism separates the gas pair at the middle of the tube. Initially, the top and bottom chambers are filled with two gas species respectively, and when the mechanism opens, the diffusion starts. Subsequently, the concentration of one gas species is measured and recorded by a sensor. The composition change is a function of time after a definite period of diffusion. In this research, oxygen gas diffuses in nitrogen gas is studied by an oxygen sensor installed inside the nitrogen chamber.

### 3.3.1 Principle of Loshmidt Cell

The development of the diffusion theory is crucial to calculating the diffusion coefficient by analyzing the signals provided by the oxygen sensor in the Loschmidt Cell. The diffusion process in the chamber follows Fick's law of diffusion given below:

$$\frac{\partial c_i}{\partial t} = D\left(\frac{\partial^2 c_i}{\partial x^2} + \frac{\partial^2 c_i}{\partial y^2} + \frac{\partial^2 c_i}{\partial z^2}\right) \tag{3.21}$$

where $c_i$ is the concentration of species $i$ in mol·m$^{-3}$, $t$ is the diffusion time in s, $D$ is the diffusion coefficient in m$^2$·s$^{-1}$, and $x$, $y$, and $z$ are the spatial dimensions in m. $x$ and $y$ are the space dimensions along the diameter direction, and $z$ is the space dimension along the height of the chambers.

This problem can be simplified to be one-dimensional and along the height direction. This assumption is valid since the height is much longer than the diameter of the diffusion region. Thus, the governing equation is simplified and re-written as

$$\frac{\partial c_i}{\partial t} = D\frac{\partial^2 c_i}{\partial z^2} \tag{3.22}$$

According to the experimental setup and procedures, the initial conditions are,

$$c_i = \begin{cases} c_i^{top} & for\ (0 < z < \frac{L}{2}, t = 0) \\ c_i^{bot} & for\ (-\frac{L}{2} < z < 0, t = 0) \end{cases} \tag{3.23}$$

where $c_i^{top}$ and $c_i^{bot}$ in mol·m$^{-3}$ are the initial concentrations of species $i$ in the top and bottom chambers, respectively.

Since no gasses can escape from the chambers to the outside environment, the insulation boundary conditions are,

$$\frac{\partial c_i}{\partial z}\bigg|_{z=\pm L/2} = 0 \; for \; (t > 0) \tag{3.24}$$

Many analytical solutions of the above equation are developed based on specific initial and boundary conditions. A detailed derivation of these solutions is shown in **Appendix II**. The solution of the diffusion equation with space for a short period of time is provided by Crank [81],

$$c_i(z, t) = \frac{c_i^{bot}}{2} \text{erfc}\left(\frac{z}{2\sqrt{D_{eq}t}}\right) \tag{3.25}$$

This equation is developed based on semi-infinite-length model and the error compared to the general finite-length solution is negligible (See **Appendix II** for more information). Therefore, **Eq. (3.25)** is a valid approximation, and the semi-infinite-length solution is used in this experiment to process the oxygen concentration data to obtain the equivalent diffusion coefficient [91].
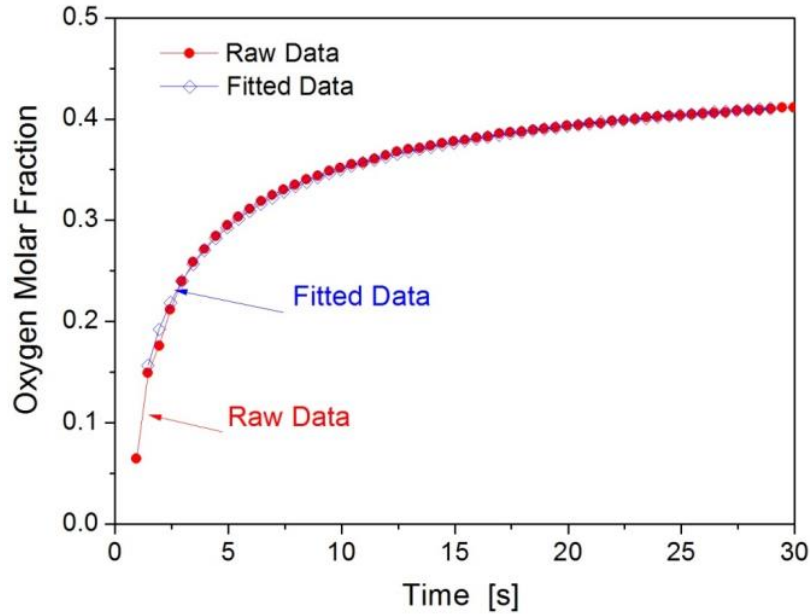


**Fig. 16.** The concentration evolution of $O_2$ in a binary gas mixture of nitrogen-oxygen at 20 $^o$C. The red line represents the experimental data, and the blue line is the curve fitting using **Eq. (3.25)**.

(1) For a single porous layer (i.e., the 'substrate' case)

The resistance network as shown in **Fig. 17** helps obtain the effective diffusion coefficient of the gas pair in the porous samples. The equivalent diffusion resistance is equal to the sum of the diffusion resistance in the chamber and that in the sample. Diffusion is the most dominant transport mechanism in these chambers, and advection effects are negligible. The fluid motion is considered to be tiny, in other words, the fluid is motionless.
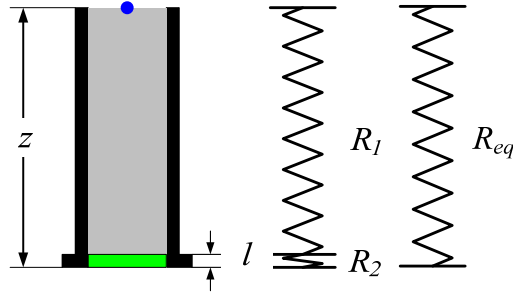


**Fig. 17.** Resistance network due to diffusion in the chamber and the sample – $R_{eq}$ is the equivalent resistance, $R_1$ is the resistance due to the diffusion in the chamber, and $R_2$ is the resistance due to the diffusion in the sample.

The equivalent diffusion resistance in the chamber is [3],

$$R_{eq} = \frac{z}{D_{eq}A_c}$$

(3.26)

where $R_{eq}$ in s·m$^{-3}$ is the equivalent resistance due to diffusion in the medium with the length $z$, $z$ in m is the diffusion distance in the diffusion direction, $D_{eq}$ in m$^2$·s$^{-1}$ is the equivalent diffusivity in the medium, and $A_c$ in m$^2$ is the cross-sectional area available for the diffusion. The equivalent diffusivity can be found by fitting **Eq. (3.25)** to the experimental data as shown in **Fig. 16**.

The resistance due to diffusion in the chamber is,

$$R_1 = \frac{z - l}{D_{bulk}A_c}$$

(3.27)

where $R_1$ is the resistance due to bulk diffusion in the chamber, and $D_{bulk}$ is the bulk diffusion coefficient.

The resistance due to diffusion in the porous samples is,

$$R_2 = \frac{l}{D_{eff}A_c}$$

(3.28)

where $R_2$ is the resistance due to diffusion in the sample, $l$ is the thickness of the samples and $D_{eff}$ is the effective diffusion coefficient.

According to the resistance network theory,

$$R_{eq} = R_1 + R_2 \tag{3.29}$$

The effective diffusion coefficient of the substrate (e.g., GDL) is,

$$D_{eff} = \frac{l}{\dfrac{z}{D_{eq}} - \dfrac{z-l}{D_{bulk}}} \tag{3.30}$$

The rewritten equation can be,

$$D_{eff,sub} = \frac{l_{sub}}{\dfrac{z}{D_{eq,sub}} - \dfrac{z-l_{sub}}{D_{bulk}}} \tag{3.31}$$

(2) For two porous layers (i.e., the 'substrate + CL' case)

In this study, the CL has to be supported by a relatively strong porous substrate since CLs are very thin and composed of unconsolidated particles. For CCS, the prepared samples can be directly tested by the Loschmidt Cell; however, for CCM and decal method, a substitute porous substrate has to be selected to replace the PEM or decal substrate. This substitute substrate should be carefully chosen to avoid blocking of pores of the substrate and maintaining the same structure of the original CCM or decal method. The algorithm to determine the effective diffusion coefficient of the CLs is shown in **Fig. 18**. The final equation to calculated $D_{eff}$ of the CL is given as follows by resistance network theory.

$$D_{eff,CL} = \frac{l_{CL}}{\dfrac{z}{D_{eq,total}} - \dfrac{z}{D_{eq,sub}} + \dfrac{l_{CL}}{D_{bulk}}} \tag{3.32}$$
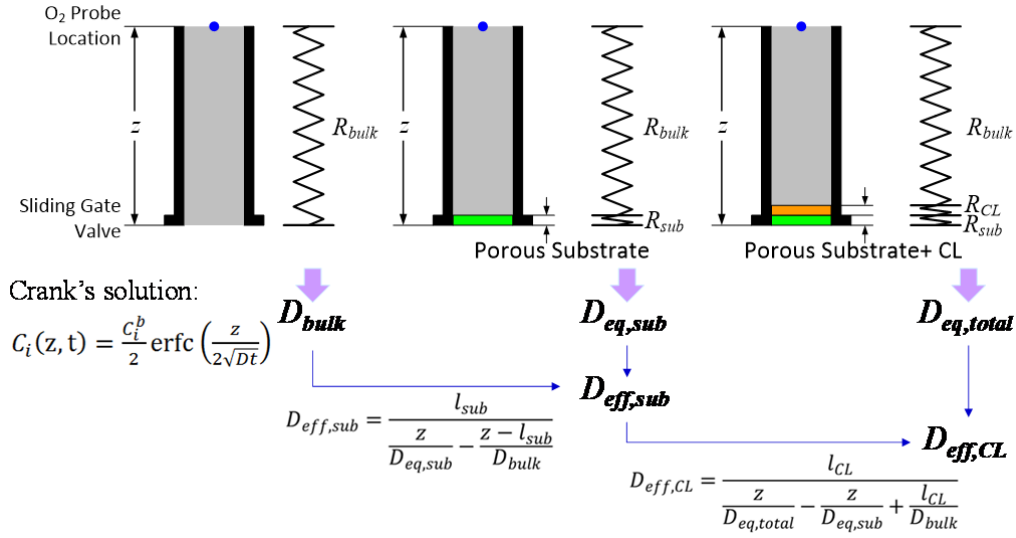
**Fig. 18.** Resistance network due to diffusion in the chambers, catalyst layer samples, and porous substrates.

## 3.3.2 Experimental Setup

A Loschmidt Cell consists of two chambers separated by a sliding gate as shown in **Fig. 19**. The top chamber and bottom chamber with an interior length and diameter of 42.5 cm and 3.8 cm are used to hold Nitrogen and Oxygen gasses, respectively. The $N_2$ and $O_2$ gasses can be separated or connected by the sliding gate made of a non-porous metal. Two mass flow controllers (Omega, Model FMA-5508) with a flow capacity of 0-500 SCCM are used to control the flow rate of $N_2$ and $O_2$ during the calibration and experimental processes. An oxygen sensor (Ocean Optics FOXY-AL300) is used to measure the oxygen concentration in the oxygen-nitrogen binary mixture. Its aluminum jacked optical fiber probe with a diameter of 300 μm is installed in the top chamber as shown in **Fig. 19**. Detailed specifications of the major experimental components can be found in **Table 8**.
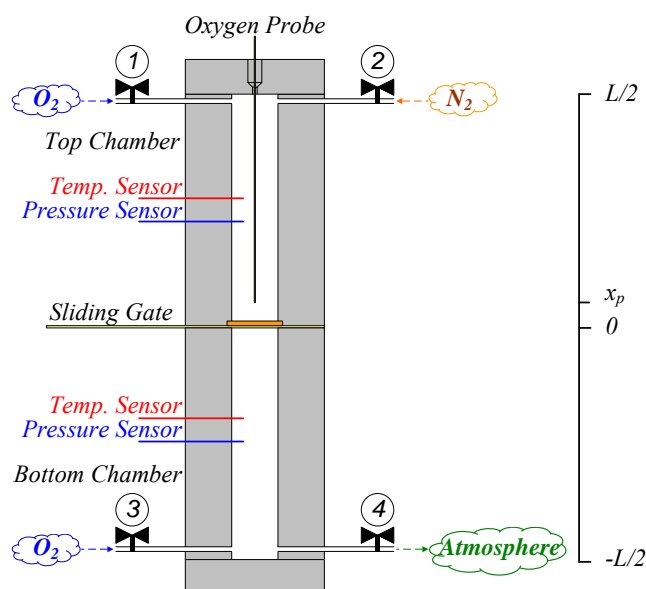
**Fig. 19.** Schematic diagram of the Loschmidt cell: (1) $O_2$ inlet, (2) $N_2$ inlet, (3) $O_2$ inlet, and (4) gas outlet.

**Table 8.** Specifications of major experimental components for the Loschmidt Cell

| Equipment | Specification | Manufacturer |
|---|---|---|
| Working Gasses | $N_2$-$O_2$ | ---- |
| Chambers | Diameter: 3.8125 cm ($1\frac{1}{2}$ in) | ---- |
| | Length: 42.5 cm ($16\frac{47}{64}$ in) | |
| Oxygen sensor | Accuracy: $\pm$ 0.02% $O_2$ @ 1% $O_2$ | Bare Fiber Oxygen |
| | $\pm$ 0.2% $O_2$ @ 20% $O_2$ | Sensors- Pyro Science |
| | Temperature range: 0 to 50°C (specified) | Item No. OXB50-HS |
| Thermocouple | Accuracy: $\pm$0.2 °C | OMEGA |
| Pressure sensor | Accuracy: $\pm$0.08 % FS | OMEGA, PX419-26BV |
| | Range: 26 to 32 inHg (i.e., | |
| | 88kPa~108kPa) | |
| Flow controller | Accuracy: $\pm$1.5% FS, including linearity | Omega, Model FMA- |
| | Repeatability: $\pm$0.5% FS | 5512 |
| Temperature | Electrical Requirements:115V, 60Hz | Thermo Fisher Scientific |
| Controller | Temperature Range: -25° to +100°C | |
| | Flow Rate (Metric): 20 L·min$^{-1}$ | |
| Electronic disk | Accuracy: $\pm$0.004 mm | The Fred V. Fowler |

| micrometer | Resolution: 0.001 mm | Company (IP54) |

Note: FS denotes the full scale.

### 3.3.3 Experimental Procedures

The typical calibration and experimental processes are shown in **Fig. 20**, and can be implemented by following eight steps as shown below:

1. Close Inlet 3, and open the sliding gate;
2. Inlet 1 and 2 is open and filled with $O_2$ and $N_2$ gasses respectively with a flow rate of 500 SCCM for 15 mins while outlet 4 is opened to expel the originally existed gas in the chambers (calibrate 50% $O_2$ point);
3. Close Inlet 1, and fill the chambers with $N_2$ gas through Inlet 2 for another 15 mins (calibrate 0% $O_2$ point);
4. Close the sliding gate, and open inlet 2 and inlet 3 to fill $N_2$ and $O_2$ gasses, respectively;
5. Purge gas in both chambers for 15 mins;
6. All valves are closed;
7. To keep the pressure inside the diffusion cell at atmosphere pressure, both outlet valve 1 and 4 are opened for 2 seconds and then closed (maintain the same pressure for both chambers);
8. Sliding gate is set to be opened smoothly so that the diffusion starts, and the temperature, pressure and $O_2$ concentration changes are monitored and measured with sensors and recorded by the computer automatically.
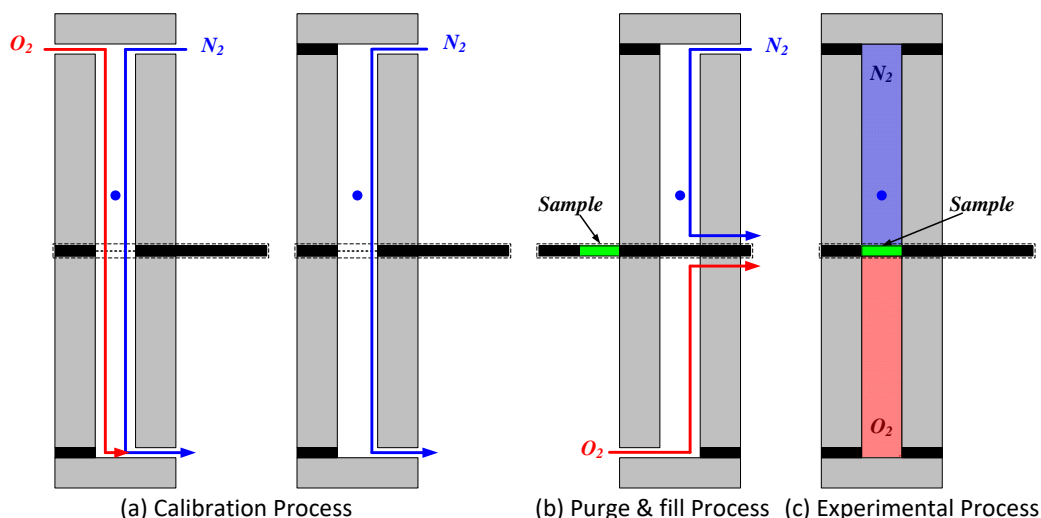
Fig. 20. Experimental procedures for the Loschmidt Cell.

### 3.3.4 Uncertainty Analysis

The uncertainty analysis for the measurement of the effective diffusion coefficient is discussed in **Appendix III.** The uncertainty analysis indicates that for a well-calibrated Loschmidt Cell, the uncertainty in the results is greatly affected by the experimental time (or the oxygen concentration range used to calculate $D_{eff}$), probe location, and numbers of samples stacked. To minimize the relative uncertainty (<10%), the probe location is set at 10 mm, four layers of samples are stacked for each measurement, and the data points with a concentration of 5-30% (usually experimental time within 1 min) are selected for the curve fitting.

It should be pointed out that for ultra-thin CLs (much less than 10 μm), the current experimental setup should be carefully improved to reduce the measurement uncertainty. Measures can be taken to further improve the experiment, such as optimization of sensor location, numbers of sample stacking, and selection of oxygen concentration and time range for data analysis.

## 3.4 Permeability of Catalyst Layers

### 3.4.1 Principle of Permeability Measurement

The gas permeability of the porous electrode is determined by using Darcy's law. It should be noted that Darcy's law is valid only for a slow flow, while a modified version of Darcy's law (i.e., Forchheimer Equation) must be considered for high-

velocity flows with high Reynolds numbers greater than 1-100 [5,105]. This is because the inertial effect becomes significant [93,106]. However, the pore Reynolds number for air in the PEM fuel cell electrodes is in the order of $10^{-4}$ [107], and it is also true in the current experimental setup. The small pore Reynold number indicates that the inertial effect is negligible and Darcy's law is valid for this study.

The general form of Darcy's law is,

$$u = -\frac{K}{\mu}\nabla p \tag{3.33}$$

where $u$ is the superficial velocity in m·s$^{-1}$, $K$ is the permeability in m$^2$, $\mu$ is the gas viscosity in Pa·s, and $p$ is the pressure in Pa.

The superficial velocity is defined as follows:

$$u = \frac{Q}{A} = \frac{\dot{m}R_{u}T}{AMp} \tag{3.34}$$

where $Q$ is the volumetric flow rate in m$^3$·s$^{-1}$, $\dot{m}$ is the mass flow rate in kg·s$^{-1}$, $R_{u}$ is the universal gas constant in J·kmol$^{-1}$·K$^{-1}$, $T$ is the temperature in K, $A$ is the cross-sectional area of the samples in m$^2$, and $M$ is the molecular weight of the gas in in kg·kmol$^{-1}$.

By substituting **Eq. (3.34)** into **Eq. (3.33)** and then integrating **Eq. (3.33)** from the inlet pressure, $p_{in}$, in Pa to the outlet pressure, $p_{out}$, in Pa across the thickness, $\delta$, in m of the test porous sample, Darcy's law yields [20,107]:

$$K = \frac{2\mu\delta RT\dot{m}}{AM(p_{in}^2 - p_{out}^2)} \tag{3.35}$$

The permeability tests are repeated five times under each condition, and the standard deviation is typically within 1-2% for the GDLs with and without the CLs, and still within 5% for the worst case when the CL permeability is determined.

### 3.4.2 Experimental Setup

**Fig. 21** shows the experimental setup used to measure the permeability of the electrode. The electrode samples are placed between two gas chambers. The interior length and diameter of the two chambers are 42.5 cm and 3.8 cm, respectively. The cross-sectional area of the tested samples is 11.3 cm$^2$. The nitrogen and oxygen gases with a purity level of 99.99% and the dried air are used as the test gas, respectively; and they are supplied by gas tanks separately. These gases are introduced into the top chamber through valve #1, forced to pass through the samples, and expelled to the

ambient atmosphere through valve #2. Two pressure sensors and thermocouples are installed in both chambers to measure the pressure and temperature of the gases, respectively. The flow meter is employed at the inlet in order to control the mass flow rates of the supplied gases.

In this study, the temperature at which the permeability is measured is controlled by a water loop as shown in **Fig. 21**. A thermal bath (Thermo Fisher Scientific) is used to maintain the desired temperature with an accuracy of 0.2 $^{\circ}$C. Thermocouples located in both chambers in order to ensure the temperature uniformity throughout during the test periods. In order to simulate the PEM fuel cell environment, the measurements are conducted over a range of temperatures (25, 37.5, 50, 62.5, and 75 $^{\circ}$C).
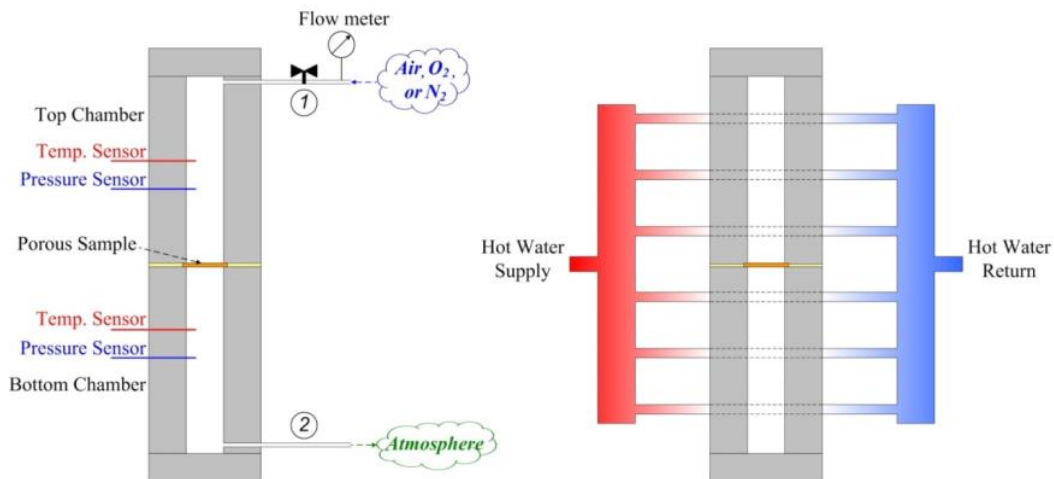


**Fig. 21**. Experimental setup for the gas permeability measurement. Air, oxygen, and nitrogen are used as the test gas, respectively, in the present study.

## 3.4.3 Experimental Procedures

A leak-check is performed before each experiment, and the experiment is conducted under predetermined operating conditions. The measurement procedure for each sample can be generalized into the following steps:

1. The temperature of both chambers is set to the desired value, e.g., 25 $^{\circ}$C.
2. The inlet valve is open and the entire chambers are filled with the gas, e.g., air.
3. The filling process lasts for more than 3 minutes with a flow rate of 500 SCCM.

4. After the flow is stabilized, the pressure and temperature of both the top and bottom chambers are recorded.

5. Change the flow rate to 400, 300, 200, and 100 SCCM, and repeat step 4 for each flow rate.

6. Change the gas species, e.g., oxygen and nitrogen, and repeat step 2-5.

7. Change the temperature to 37.5, 50, 62.5, and 75 $^{\circ}$C respectively, and repeat step 1-6 for each temperature.

The experimental procedure is continued with either the uncatalyzed GDL or the catalyzed GDLs (nine samples in total) being placed in the middle of the two connected chambers. Since in the PEM fuel cells, the mass transport of air or oxygen in the cathode is much slower than that of hydrogen in the anode, and cathode process is far more important in affecting the PEM fuel cell performance, only the permeability for air, oxygen, and nitrogen are measured in this study.

### 3.3.4 Uncertainty Analysis

The permeability, $K$, is a multiple-variable function. The uncertainty in a multi-variable function $K = func(x_1, x_2, \ldots x_N)$ due to uncertainties in variables $x_1, x_2, \ldots, x_N$ are evaluated by the root sum square product of the individual uncertainties computed to the first-order accuracy as [107]:

$$U_K = \left[ \sum_{i=1}^{N} \left( \frac{\partial K}{\partial x_i} U_{x_i} \right) \right]^{\frac{1}{2}} \tag{3.36}$$

where the partial derivative represents the sensitivity of $K$ to the $i^{th}$ variable $x_i$. $x_i$ represents the temperature, pressure, thickness, cross-sectional area, viscosity, and mass flow rate as indicated in **Eq. (3.35).** The uncertainties in independent variables are obtained either from the manufacturer's specifications for the instrument or from the measurement taken in the laboratory. In order to ensure the repeatability, each test is repeated three times on separate days.

It should be pointed out that for ultra-thin CLs (much thinner than 10 μm), the permeability measurement should be carefully improved for the reduction of measurement uncertainty. A high accuracy pressure sensor and a large-range flow rate controller can be employed for the experiment improvement.

# 3.5 Performance of Catalyst Layers

The performance of the CLs is tested by Fuel Cell Automated Test Station (FCATS, G20) which is manufactured by Greenlight Innovation.

## 3.5.1 Experimental Setup

The overall performance of PEM fuel cells depends on CLs where the chemical reaction occurs. The most common indicator of fuel cell performance is the current-voltage (I-V) curve (or polarization curve) by plotting the cell potential (V) against the current density ($A \cdot cm^{-2}$).

**(1) PEM Fuel Cell**

A single PEM fuel cell with an active area of 45 $cm^2$ is used to test the performance of the CLs. The PEM fuel cell consists of a Nafion 211 membrane, two CLs, two commercially available GDLs, two flow field plates with flow channels carved on one side, two current collectors, and two aluminum endplates. Detailed information is shown in **Table 9**.

**Table 9.** Summary of standard polymer electrolyte membrane (PEM) fuel cell stacks

| Cell Components | Properties | Value |
|---|---|---|
| Membrane | Membrane type | Nafion$^{TM}$ 211 |
| GDL (anode and cathode) | Thickness | 225 μm |
| | Porosity | 0.75 |
| Current collector | Material | Copper |
| Distribution plate | Material | Graphite |

**(2) Fuel Cell Automated Test Station (FCATS, G20)**

The fuel cell test station is manufactured by Greenlight Innovation and can be used to control the fuel cell relative humidity, temperature, pressure and stoichiometry of the reactant gasses on both anode and cathode sides. In this case, the above parameters are constant to make sure the CLs are tested under the same conditions. The operating parameters and conditions are controlled via software with the help of a computer-based control and data acquisition system.

The commercially available G20 test station requires the supply of hydrogen (fuel), air (oxidant), coolant water (temperature control), and nitrogen (used during the machine start-up and shut-down to purge out any reactant gasses that might be present inside the fuel cell). The reactant gasses are humidified by steam injection using deionized (DI) water; furthermore, the humidity level of the reactants is controlled by the adjusting the dew point temperature and inlet temperature. Backpressure is controlled by are backpressure regulator. The mass flow controller is connected to the computer system and located before the steam injection system. Load box is integrated into the FCATS and is used to measure the voltage and current response of fuel cell and to dissipate the power generated by the fuel cell.

## 3.5.2 Experimental Procedures

### (1) Gas Leakage Testing

Gas leakage is the major safety hazard for the experiment and may deteriorate the cell performance, further influencing the performance of the fuel cells. Principal sources of the gas leakage include inappropriate component design, seal failure, membrane degradation, electrode assembly failure, and insufficient pressure applied by the clamping force. Nitrogen is used to test leaking from both sides of the fuel cells, and the experiment is only safe for no warning signs.

### (2) Cell Performance Testing

After the leaking test, the anode and cathode inlets connect the hydrogen and air supplies, respectively. This machine controls the operating conditions including the stoichiometric ratio, back pressure, temperature (cell and reactants) and relative humidity. Then the current density varies from 0 to the maximum current density (where cell voltage ~0 V), and the FCATS records the corresponding voltage. The detailed experimental condition in the present study is shown in **Table 10**.

**Table 10.** PEM fuel cell test conditions in the present study

| Parameters | Values |
|---|---|
| Operating temperature | 75 $^o$C |
| Gas flow rates | Anode: 4.45 SLPM<br>Cathode: 9.00 SLPM |
| Humidified gases | Anode: 100%<br>Cathode: 100% |

| Outlet pressure | Anode: 35 kPag |
|---|---|
| | Cathode: 35 kPag |

## 3.6 Summary

The experimental methods employed in this thesis work consist of five major components: fabrication of CLs, characterization of pore structure, measurements of the effective diffusion coefficient, determination of permeability, and test of cell performance. Specifically, the pore structures of the prepared electrodes and CLs are investigated by the method of standard porosimetry (MSP) in terms of pore size distribution (PSD), porosity, pore surface area distribution, specific surface area (SSA), and mean pore size, and surface fractal dimension. The effective diffusion coefficient, diffusion diffusibility, and diffusion resistivity are measured based on Fick's law of diffusion via a modified Loschmidt Cell. The gas permeability and permeation resistivity of the porous materials are determined based on Darcy's law via a custom-engineered apparatus. The cell performance is tested using a commercially available test station. The corresponding experimental principles, apparatus, procedures, and uncertainty analysis are explained in details in this chapter.

# Chapter 4
# Experimental Results

In this chapter, the major experimental results are presented in four aspects: pore structure characterization, effective diffusion coefficient, permeability, and cell performance. Some of the results presented in this chapter are based on the journal articles [2,3,5–7].

## 4.1 Pore Structure Characterization

The pore structures of the catalyzed electrodes are investigated by the method of standard porosimetry (MSP) in terms of pore size distribution (PSD), porosity, pore surface area distribution, specific surface area (SSA), and mean pore size, and surface fractal dimension.

### 4.1.1 Pore Size Distribution (PSD)

PSD is the relative amount of each pore size in a representative volume of porous materials [155] and is usually represented by a probability density function indicating the pore volume at a given pore size. Since the pore shapes in natural objects are mostly irregular, the pore size is only meaningful when the equivalent pore shapes are assumed, and in the present study, the equivalent cylindrical pores are considered. In most of the porous media, the pore sizes are distributed over a wide range of values, and this parameter quantitatively describes the uniformity and complexity of the pore structure.

$\qquad$ **Fig. 22** (a) and (b) indicate the cumulative PSD of the electrodes containing two different types of catalysts with the Pt/C ratios of 30% and 60%, respectively. As can be seen, for the low Pt loading of 0.1 mg·cm$^{-2}$, the volume of the pores larger than 1 μm is decreased slightly for both two types of catalysts in comparison with the uncatalyzed GDL. This is likely due to the penetration of the small catalyst particles and ionomers into the GDLs; therefore, some large pores are occupied by the catalyst particles and ionomer, leading to a slight decrease in the volume of large pores.

However, as the Pt loading is increased to 0.4 mg·cm$^{-2}$, these two types of catalysts behave differently. For 30% Pt/C, the large pores (>1 μm) continue to reduce since the catalysts and ionomers trend to penetrate into and occupy more large pores; while for 60% Pt/C, more large pores are introduced by the thicker CLs. In other words, the pore volume and PSD of the electrodes can be changed by two means: reduced pore volume due to the material (catalyst particle and ionomer) penetration into GDLs and increased pore volume due to the presence of the deposited CLs. The combined effect of these two factors should be further determined based on other parameters, e.g., porosity.

**Fig. 22** (c) and (d) exhibit the differential PSD of the electrodes with two different types of catalyst, 30% and 60% Pt/C, respectively. The radii of the pores can be as large as 10 μm. It is seen that for the same type of catalyst, as the Pt loading is increased, the volume of the pores smaller than 100 nm increases (see **Fig. 22** (a) and (b)). This increase is likely due to the presence of more catalyst particles in the CLs with higher Pt loadings. For the constant Pt loading, the volume of pores smaller than 100 nm for 30% Pt/C (see **Fig. 22** (a)) is much higher than that for 60% Pt/C (see **Fig. 22** (b)). This implies that a lower Pt/C ratio requires more carbon particles in order to maintain the same Pt loading, and a larger amount of carbon particles leads to a significant increase in small pores, formed between the carbon particles with a diameter ranging from 30 to 50 nm.
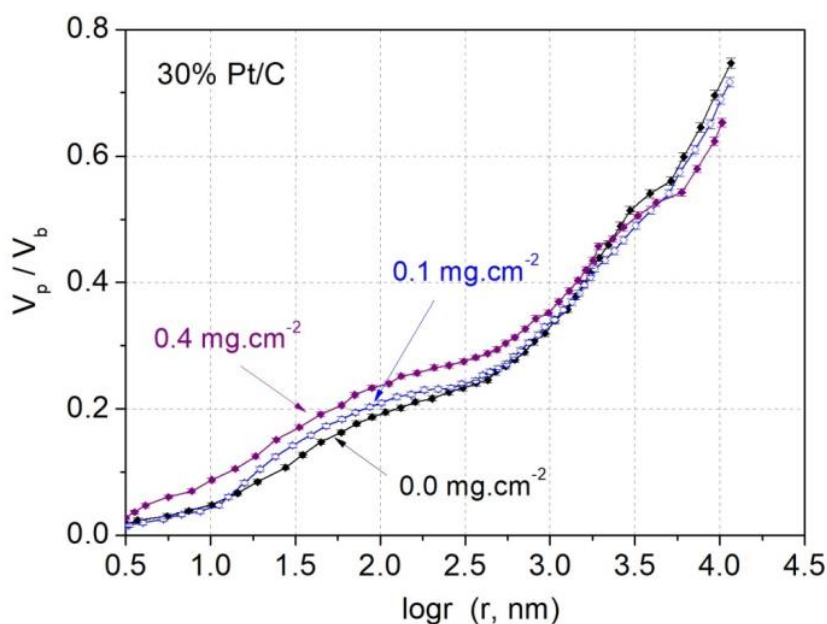


(a) Cumulative pore size distribution for 30% Pt/C.
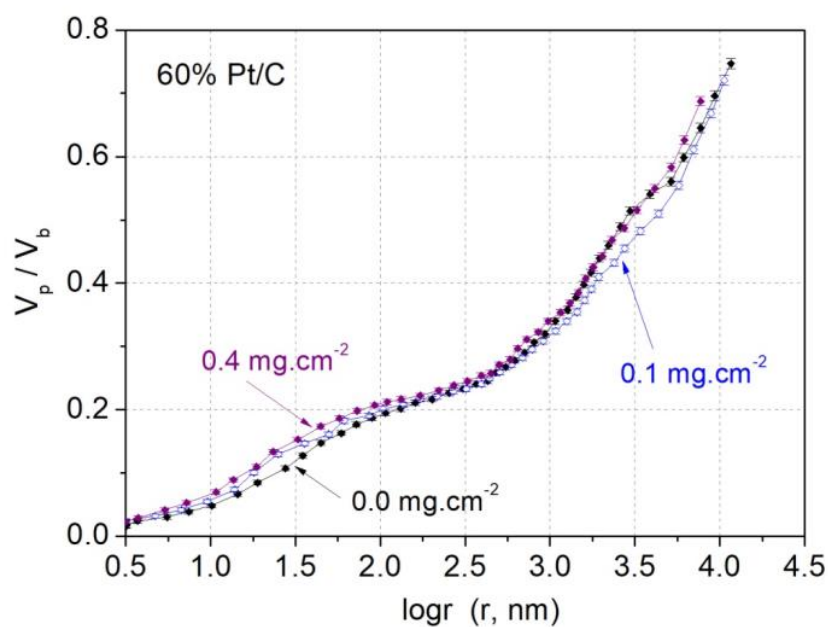
(b) Cumulative pore size distribution for 60% Pt/C.
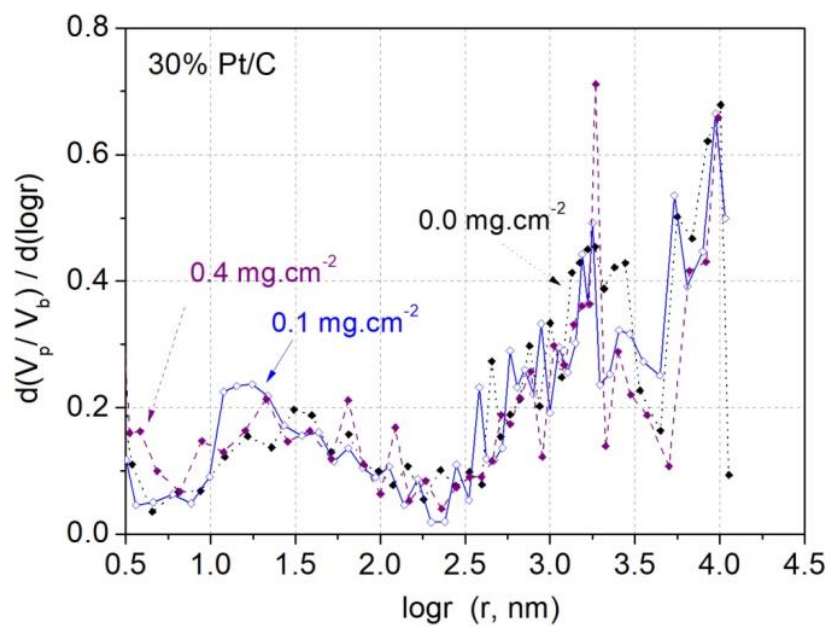


(c) Differential pore size distribution for 30% Pt/C.
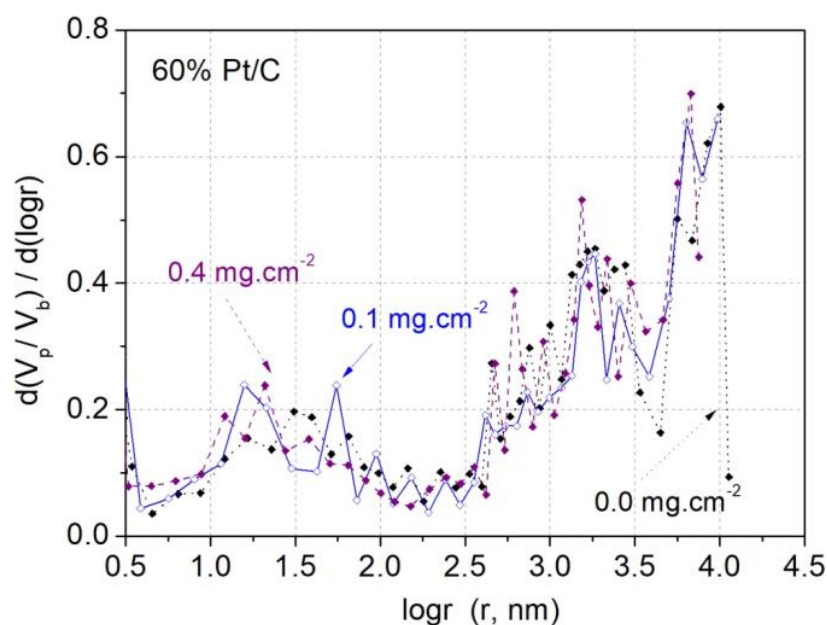
(d) Differential pore size distribution for 60% Pt/C.

**Fig. 22.** Pore size distribution (PSD) of the porous electrodes with the Pt loadings and catalyst types of (a) cumulative PSD for 30% Pt/C, (b) cumulative PSD for 60% Pt/C, (c) differential PSD for 30% Pt/C, and (d) differential PSD for 60% Pt/C ($V_{pore}$ is pore volume, $V_{bulk}$ is bulk volume, and $r$ is the pore radius).

## 4.1.2 Porosity

Porosity is a measure of the volumetric fraction of the pores in a porous medium. A larger porosity indicates that there are more void regions in the porous media which can be used for transporting oxygen, hydrogen, and water in PEM fuel cells, yielding a smaller mass transport resistance, hence a better cell performance. Therefore, to accurately measure the porosity is of great significance for the performance of the electrodes as well as the PEM fuel cells.

**Fig. 23** (a) and (b) present the relationships between the pore volume, bulk volume, and porosity for the electrodes with the two types of catalysts (30% and 60% Pt/C) studied, respectively. It can be observed that for a given type of Pt/C catalyst, the bulk volume presents a linear increase with the Pt loading since the amount of CL ingredients (Pt/C and ionomer) increases proportionally. This is because, for a given type of Pt/C catalyst, an increase in the Pt loading increases the thickness of the

electrode, as the cross-sectional area of the sample is fixed. For example, the electrode thickness increases from 221.6±2.1 μm (for the GDL investigated in the present study) to 243.0±2.1 μm for 30% Pt/C and to 231.0±2.1 μm for 60% Pt/C, respectively [5]. However, the pore volume of these electrodes does not change too much. As the porosity is defined as the ratio of pore volume to bulk volume, the porosity of the electrode for a higher Pt loading is decreased significantly. Similarly, for the same Pt loading, a higher Pt/C ratio requires fewer amounts of carbon and ionomer, thus resulting in a thinner electrode with a smaller bulk volume. Therefore, a Pt/C ratio of 30% results in a thicker and less porous electrode as compared to that of 60% Pt/C.
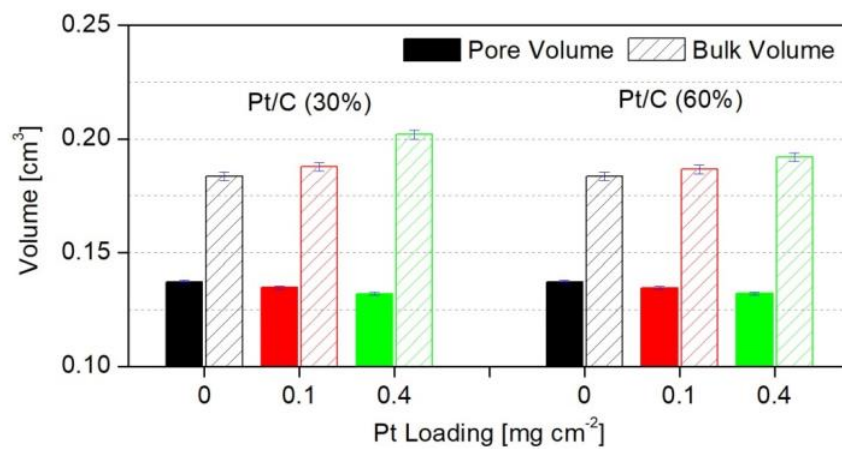


(a) Pore volume and bulk volume.
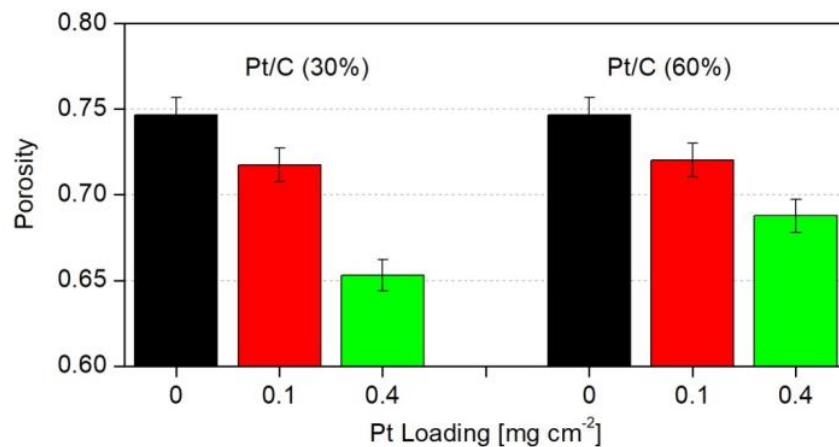


(b) Porosity.

**Fig. 23.** Pore volume and porosity of the electrodes with various Pt loadings and two types of catalysts of 30% and 60% Pt/C.

### 4.1.3 Pore Surface Area Distribution

Pore surface area distribution, similar to the PSD, is defined in this section as the probability density function of the amount of surface area at a given pore size. This parameter quantifies the surface area in either large or small pores and can be an indicator of the quantity of electrochemical reaction sites.

**Fig. 24** (a) and (b) indicate the cumulative surface area distribution of the pores from the maximum to minimum size for five types of prepared electrodes. The cumulative surface area shown represents the total pore surface area integrated from the maximum pore sizes to the given pore size, normalized by the total bulk volume of the sample involved. As can be seen, the surface area is greatly contributed by the small pores, e.g., 95.0%-96.5% for the pores with a radius smaller than 100 nm. In addition, for 60% Pt/C, 0.1 mg·cm$^{-2}$ Pt loading leads to a 1.2% increase in the specific surface area, while 0.4 mg·cm$^{-2}$ Pt loading causes a 24.0% increase. The rises of the pore surface area are contributed by the presence of small Pt/C particles, resulting in more chemical reaction sites. Further, for a smaller Pt/C ratio, more surface area can be observed with a constant Pt loading. The increase in surface area is due to the larger amount of carbon particles utilized. Meanwhile, only the pores larger than 3.2 nm is considered in order to study the pore surface area. This is because the pores with a range from 0 to 3.2 nm have negligible volumes as shown in **Fig. 23** (a) and (b), while the relative uncertainty in pore volume within this range can be as large as 100%. Therefore, the surface area calculated from the pores with a size range from 0 to 3.2 nm is unreliable, which is excluded from the pore surface area analysis in this study.
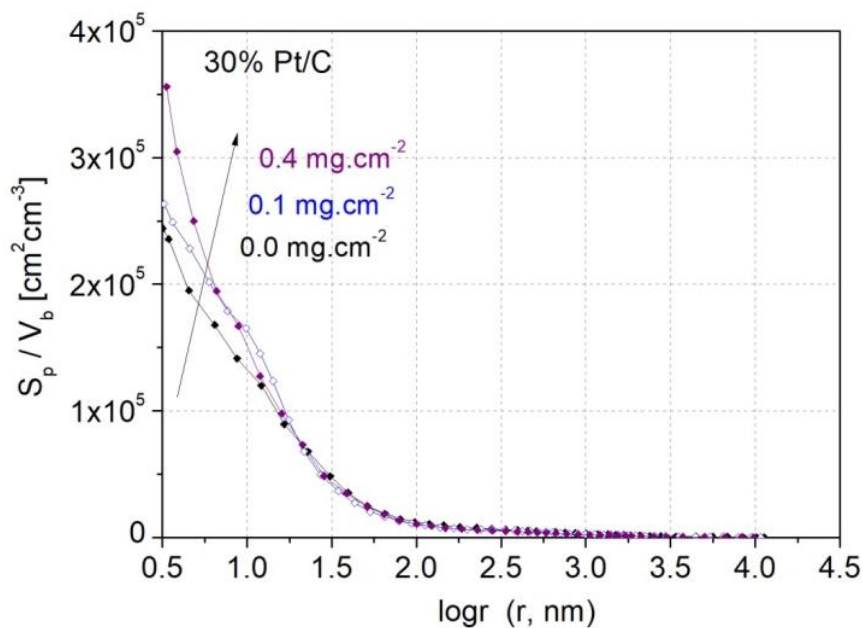
(a) Cumulative surface area distribution for 30% Pt/C.
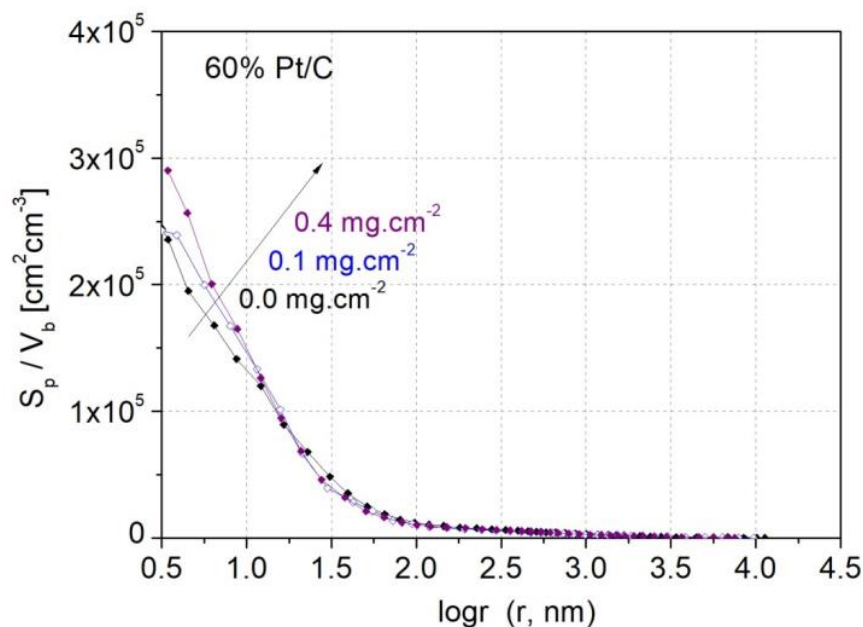


(b) Cumulative surface area distribution for 60% Pt/C.

**Fig. 24.** Cumulative surface area distribution of the porous electrodes with various Pt loadings and different types of catalysts: (a) 30% Pt/C and (b) 60% Pt/C.

## 4.1.4 Specific Surface Area (SSA)

The specific surface area is often defined as the total surface area of a porous medium per unit of bulk volume or mass. It has a particular importance for reaction rate,

permeability, and other physical properties. **Fig. 25** represents the volume-based specific surface area for the uncatalyzed and catalyzed electrodes considering the pores larger than 3.2 nm. As can be seen, as more catalysts are deposited on top of GDLs, the specific surface area increases significantly. For example, for 30% Pt/C, even though the thickness of the 0.4 mg cm$^{-2}$ is increased by only 7.5% in comparison with that of the 0.1 mg cm$^{-2}$, the specific surface area is increased by 35.2%. Similarly to the 60% Pt/C, the thickness increase is only 2.9%, while the SSA increase can be 19.4%. The increase in the surface area is contributed to by the small pores formed due to the presence of the catalyst particles.
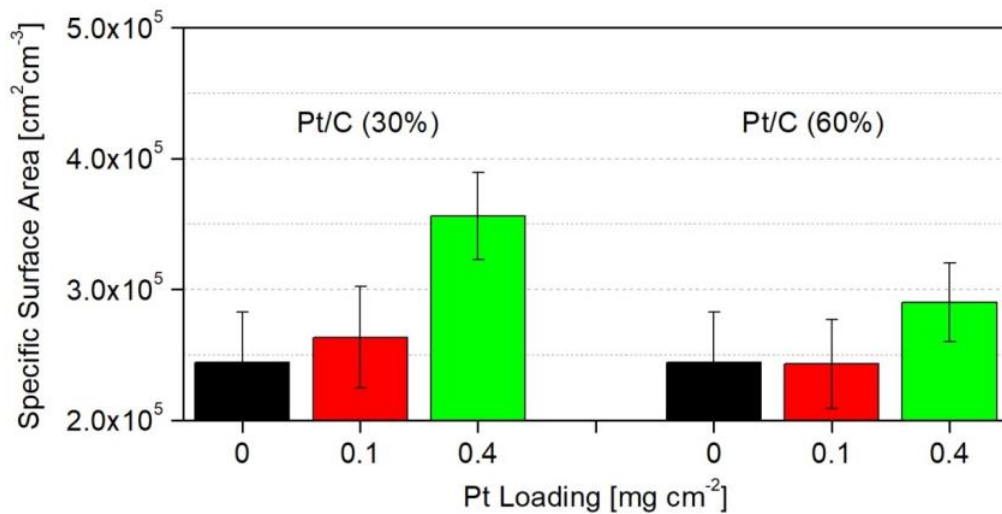


**Fig. 25.** Specific surface area of the porous electrodes with various Pt loadings and different types of catalysts.

## 4.1.5 Mean Pore Size

The mean pore size is defined as four times of the pore volume to the corresponding pore surface area. It represents the characteristic size of the pathways in the porous media, and a smaller mean pore size indicates that it is more difficult for reactant gases or liquid water to pass the media.

**Fig. 26** presents the mean pore size of the electrodes with various Pt loadings and different types of catalysts. For the same type of catalysts, as the Pt loading is increased to 0.4 mg·cm$^{-2}$, more Pt/C particles and ionomers are deposited on the GDLs. Because the CL is becoming thicker, the mean pore size decreases accordingly.

The mean pore size is equal to four times the ratio of pore volume to the pore surface area. A slight decrease in pore volume and a significant increase in pore surface area lead to the decrease in the mean pore size. In addition, for the constant Pt loading, reducing the Pt/C ratio leads to a significant drop in mean pore size. This is expected because a small Pt/C ratio results in more small pores in the electrode as discussed in previous sections.
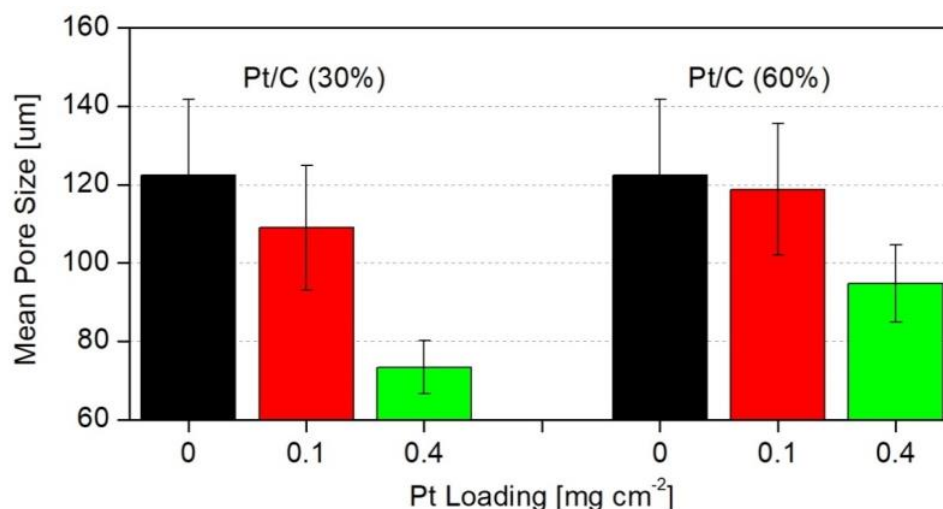


**Fig. 26.** Mean pore size of the porous electrodes with various Pt loadings and different types of catalysts.

## 4.1.6 Surface Fractal Dimension

Surface fractal dimension is a measure of the complexity of the porous structure. Normally, the Euclidean or topological dimension of a surface equals 2; however, the fractal dimension of the porous media, *FD*, as defined in **Eq. (3.14)**, can take a non-integer dimension between 2 and 3, and its value rises with the surface complexity or roughness [156,157]. When the fractal surface area is determined at different scale levels using various methods (e.g., gas adsorption [75], liquid extrusion [158], MSP [67–69], etc.), the fractal dimension can be calculated by fitting the data of the surface areas at different scale levels to **Eq. (3.14)**. The value of *k* is a measure of the shape of the solid elements, which is formed during the fabrication or formation of the porous materials, while *FD* is the fractal dimension which is a quantitative measure of the solid element distribution in space.

**Table 11** presents the fractal dimension and the corresponding constant (or shape factor of the solid element) calculated through curve fitting. The pore surface area is a function of the fractal dimension, *FD,* and the constant, $k_{FD}$. Using the least square curve fitting method as implemented in MATLAB's *lsqcurvefit* function [106], the experimental data on the surface area distribution are fitted to **Eq. (3.14)**, and the values of the fractal dimension, *FD,* and the constant, $k_{FD}$ are obtained for the best fit. As can be seen, the surface fractal dimensions of the uncatalyzed and catalyzed electrodes are within the range of 2.7-2.9. As the Pt loading is increased, the fractal dimension and shape factor increase. This indicates that the surface properties and pore structure of the porous media become more complicated due to the addition of more Pt, carbon, and ionomer. Similarly, when the catalyst is changed to 60% Pt/C, the fractal dimension, *FD*, and the shape constant, $k_{FD}$, are smaller in comparison with 30% Pt/C. This is because less carbon and ionomer are sprayed on the GDL when the Pt loading is constant and less carbon and ionomer means that the pore structure is less affected than that of 30% Pt/C. Therefore, the fractal dimension is a good indicator of the complexity of the pore structure of the electrodes.

**Table 11.** Fractal dimension of the uncatalyzed and catalyzed electrodes.

| Pt Loading [mg cm$^{-2}$] | GDL | GDL+CL (30% Pt/C) | | GDL+CL (60% Pt/C) | |
|---|---|---|---|---|---|
| | 0 | 0.1 | 0.4 | 0.1 | 0.4 |
| *FD* | 2.709 | 2.716 | 2.877 | 2.715 | 2.818 |
| $k_{FD}$ [×10$^6$] | 0.95 | 1.1 | 1.9 | 1.0 | 1.5 |
| $R^2$ (coefficient of correlation) | 0.9890 | 0.9724 | 0.9967 | 0.9750 | 0.9889 |

In order to further explore the fractal dimension theory, a BET surface area is measured for the electrode with 30% Pt/C and the Pt loading of 0.4 mg·cm$^{-2}$. The BET test is conducted by a Quantachrome Autosorb ASIQ-MP instrument, using nitrogen as the probing gas. The test sample is prepared in a square shape with a cross-sectional area of 0.85 cm$^2$. The sample is outgassed at 343K for 24h to remove any remaining moisture. The surface area is obtained through the analysis of the nitrogen adsorption at the temperature of 77K, in which the amount of nitrogen

adsorption onto the pore surface is correlated to the total geometric surface area. The BET method to derive the pore surface area from physisorption isotherm is based on the following BET equation [63].

$$\frac{p}{n(p_0 - p)} = \frac{1}{n_m C} + \frac{C - 1}{n_m C} \frac{p}{p_0} \tag{4.1}$$

where $n$ is the amount of adsorbed nitrogen in mole at the relative pressure $p/p_o$, $n_m$ is the monolayer capacity, and $C$ is the constant determined by isotherm shape. According to **Eq. (4.1)**, a linear correlation is established if $p/n(p_o-p)$ is plotted against $p/p_o$. The slope, $(C-1)/n_m C$, and the intercept value, $1/n_m C$, are determined from the linear plot so that the monolayer capacity $n_m$ is derived. The BET surface area, $A$(BET), can be determined using the following equation:

$$A(\text{BET}) = n_m N_A A_{N_2} \tag{4.2}$$

where $N_A$ is the Avogadro constant, and $A_{N2}$ is the cross-sectional area of a nitrogen molecule at 77K (0.162 nm$^2$). A detailed explanation of the BET method can be found in [63,77,159].

Fig. 27 (a) presents the PSD obtained from the BET method. The pore volume is divided by the cross-sectional area in order to provide a better comparison with the MSP data. As can be seen, the maximum pore size determined by the BET method is 251 nm (i.e., log(r)=2.4), which is inconsistent with the MSP method. The obvious difference between the BET and MSP methods indicate that the BET method is not suitable for the electrode material tested in this study, as the electrode has a wide range of pore size from 0 to 10 μm. Fig. 27 (c) compares the pore surface areas obtained via the MSP and BET methods. The pore surface area obtained from the MSP is calculated based on the specific PSD (marked as a black line in Fig. 27 (a).) with the assumption that all the pores are constant and have a cylindrical shape.

The BET surface area is calculated using Eqs. (4.1) and (4.2) by analyzing the nitrogen gas adsorption isotherm as shown in Fig. 27 (b). The surface area distribution (red line) indicates that if the minimum pore size is becoming smaller, the measured pore surface area will increase exponentially. The equivalent half size of the nitrogen molecule can be as small as 0.201 nm at the temperature of 77K, under which the BET method is conducted. Based on the fractal dimension theory, the calculated surface area of the pores larger than 0.201 nm will be 102,000 cm$^2$ per unit of cross-sectional area. The actual measured surface area based on the physical adsorption of nitrogen is around 83,000 cm$^2$, which is in the same order of the predicted value. The measured

value is about 17% smaller than the calculated value – this finding implies that the nitrogen molecules may not be able to access all the pores with a size of 0.201 nm. In addition, the BET method is not suitable for large pores, which could be another reason why the total surface area obtained by the BET method is relatively lower than the expected value. This interesting finding signifies the interrelation between these two independent techniques used for the characterization of porous media, and the theory of fractal dimension can be considered to be a bridge between these two methods.

The experimental results and fractal dimension also suggest that the actual geometric surface area of the pores for the whole size range is actually unmeasurable. The surface area is only meaningful when the minimum "scale" size is given. However, the fractal dimension theory provides a new and practical pathway to determine the surface area if the minimum pore size of interest is given.
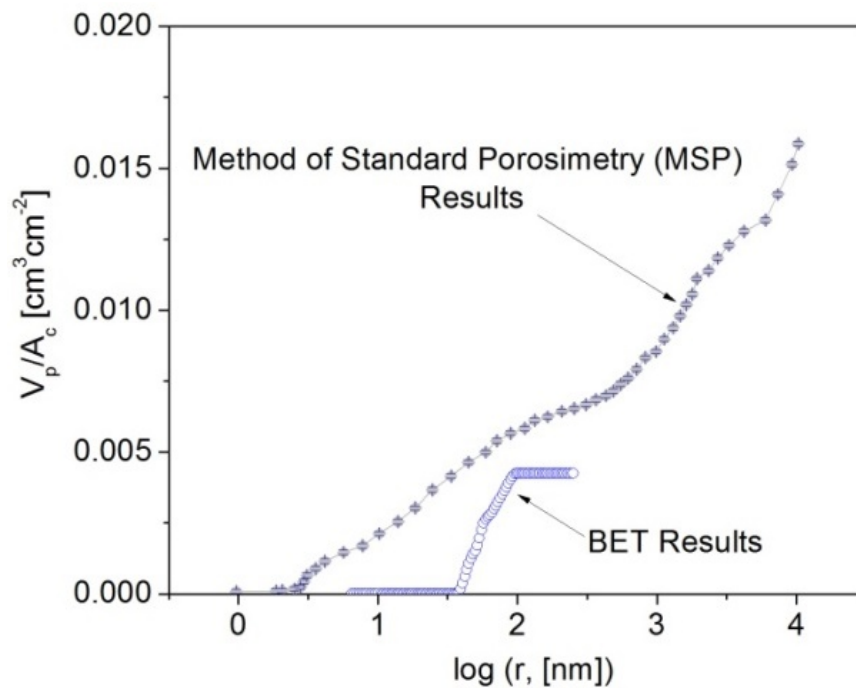


(a) Comparison of pore size distribution
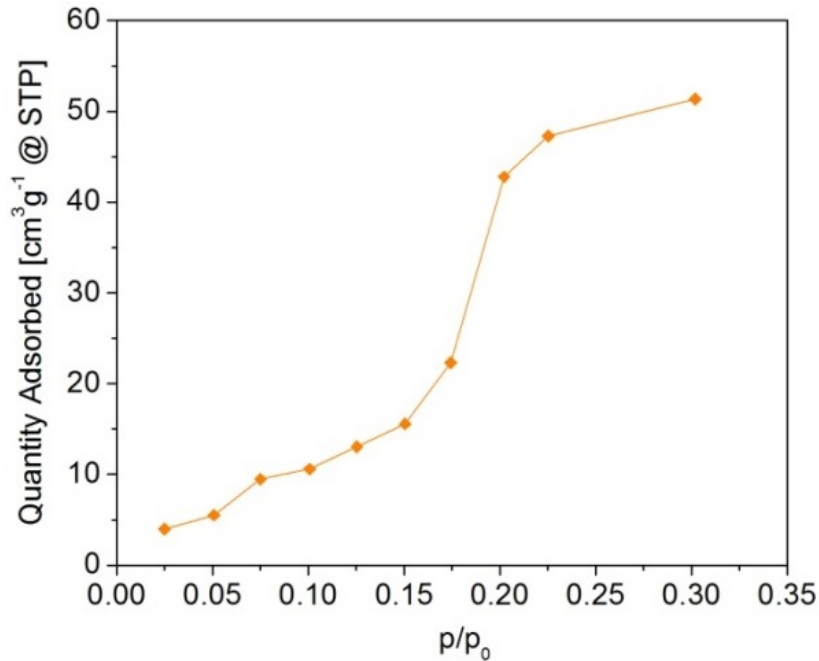
(b) Nitrogen gas adsorption isotherm
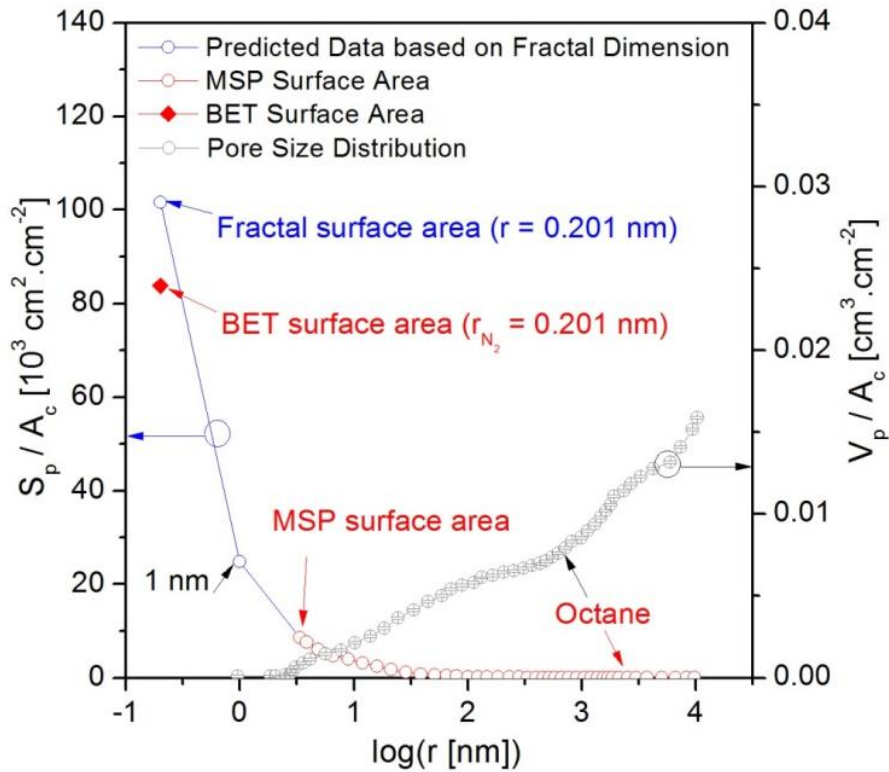


(c) Comparison of pore surface areas

**Fig. 27.** Characterization of the pore structure of the catalyzed electrode using the Brunauer-Emmett-Teller (BET) method: (a) Comparison of pore size distribution (PSD), (b) nitrogen gas adsorption isotherm, and (c) comparison of pore surface areas.

### 4.1.7 Comparison of Pore Structure between CCM and CCS Methods

In order to comprehensively compare the CCM and CCS methods, the electrode samples prepared by 60% Pt/C catalysts with the Pt loading of 0.1, 0.2, 0.3, and 0.4 mg·cm$^{-2}$ are compared in this section.

SEM is employed to demonstrate the impact of material penetration on the morphology and structure of the prepared CCS electrodes. It should be pointed out that the SEM imaging is only applied to the CCS electrodes since the effect of material penetration is relatively small for CCM methods as the catalyst is deposited on the membrane rather than highly porous GDLs. In addition, only the typical low- and high-Pt-loading electrodes (i.e., 0.1 and 0.4 mg·cm$^{-2}$) are selected and compared to the uncatalyzed GDL substrate by the SEM techniques.

**Fig. 28** shows the morphology and structure of the surface and cross-section of the reference GDL and electrodes. As can be seen, at the 100x magnification, there exist many noticeably large pores (20-50 μm) on the MPL surface, and the carbon fibers are completely underneath the MPL. After a small amount of catalyst ink is deposited (0.1 mg·cm$^{-2}$), the main macro-porous structure seems to remain almost the same – the pre-existing large pores are still clearly visible; however, the MPL morphology is altered and the fibers near the top surface can be clearly identified. However, as the catalyst loading is increased (from 0.1 to 0.4 mg·cm$^{-2}$), most of the large surface pores disappear, and the carbon fibers are no longer visible from the face view. Instead, some macro-scale cracks are observed to form throughout the CL surface during the drying process. With the identical composition of the catalyst ink, the catalyst loading (hence the CL thickness) has a significant impact on the morphology and structure of the low- and high-Pt-loading electrodes. It is also clear that as the catalyst loading is increased, the CL structure becomes comparatively denser, and this observation is reasonable as more CL materials including Pt, carbon carriers, and ionomer are deposited, resulting in a thicker CL architecture (see the images at 2,000x magnifications in **Fig. 28**). At 20,000x magnifications, it is clearly observed that the particle/agglomeration size of the CLs is much smaller than that of the MPLs, meaning that during the deposition process, some catalyst particles and ionomers will inevitably fall into the pores and cracks of the MPLs. This material penetration is likely to cause changes in the pore structures of the GDLs and CLs. It

should be noted that it is extremely difficult to distinguish the material penetration into GDL by only using cross-sectional SEM images, which necessitates the comparison the CCM and CCS electrodes through quantitative *ex-situ* and *in-situ* characterizations, such as thickness, porosity, surface area, diffusion resistivity, permeation resistivity, and cell performance.

| | Uncatalyzed GDL 0.0 mg·cm$^{-2}$ | Low-Pt-Loading Electrode 0.1 mg·cm$^{-2}$ | High-Pt-Loading Electrode 0.4 mg·cm$^{-2}$ |
|---|---|---|---|
| 100x | MPL Surface | CL Surface | CL Surface |
| 2,000x | MPL Surface / GDL Cross Section | CL Surface / MPL Cross Section | CL Surface / MPL Cross Section |
| 20,000x | MPL Surface | CL Surface | CL Surface |
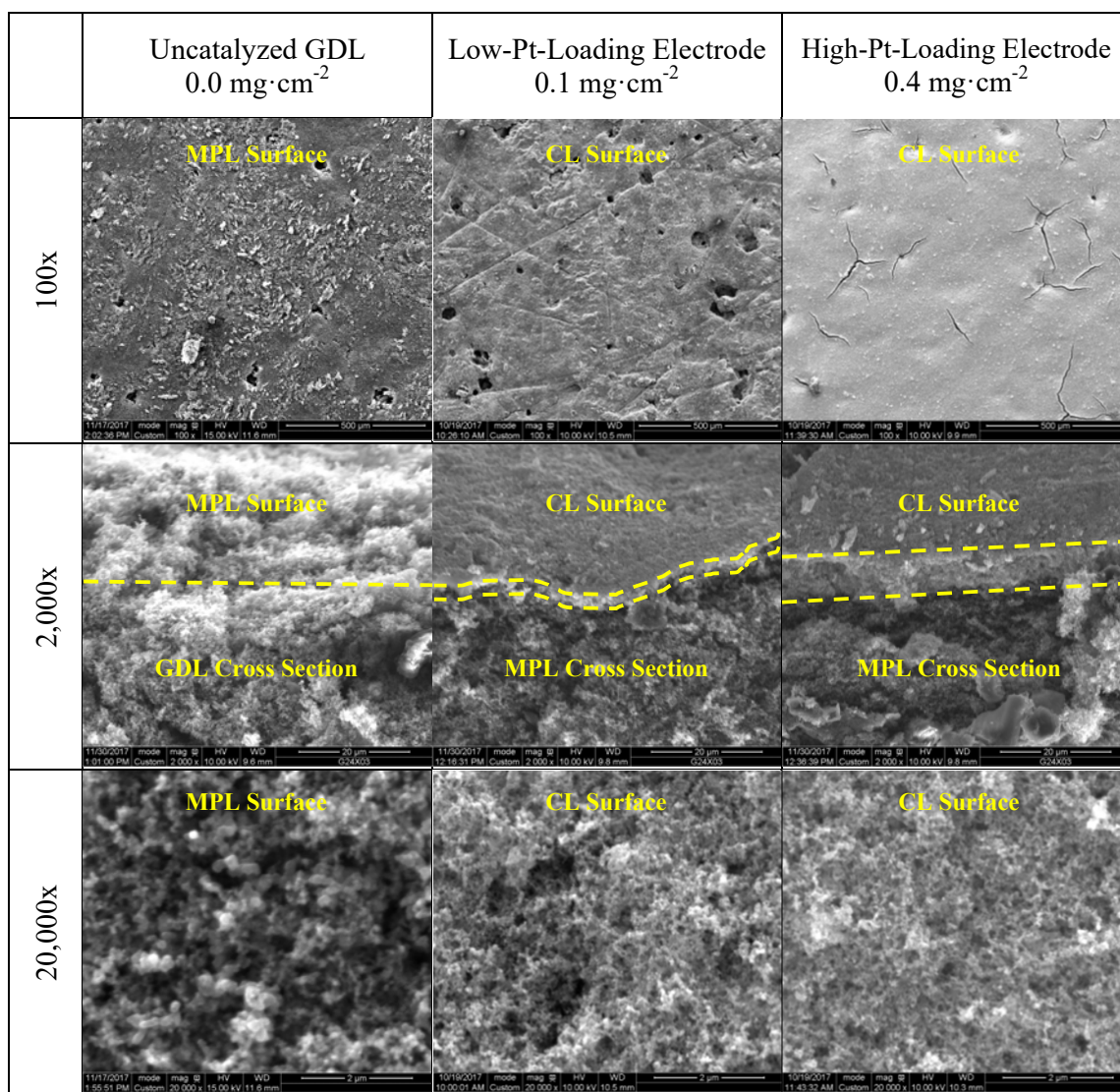
**Fig. 28.** Scanning electron micrographs of the CCS electrodes with low and high Pt loadings at various magnifications: Row 1 and 3 are the face view, and Row 2 is the cross-sectional view.

The structural parameters such as pore size, porosity, and pore surface area are of great significance because they have a significant impact on the mass transfer

resistance and reaction rate. In the present study, the MSP is utilized to directly measure the porous characteristics of GDLs, CCM CLs, and CCS electrodes. It should be noted that the pore structure of the CLs in CCS electrodes cannot be measured directly due to the penetration of material into GDLs during the fabrication process. In addition, the pore structure of the CCM electrodes can be determined indirectly from the pore structure of GDLs and CCM CLs using **Eq. (4.3)**.
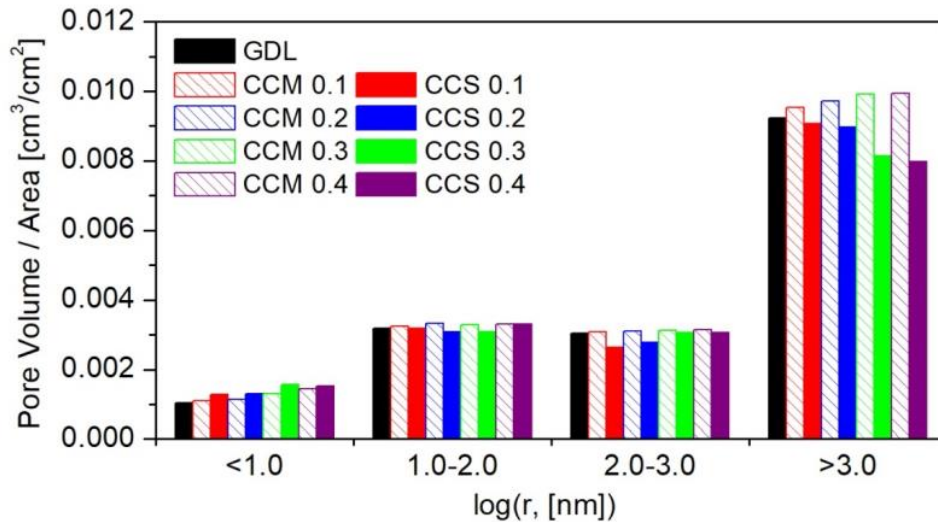


**Fig. 29.** Pore volume per unit of face view area of the electrodes prepared by the CCM and CCS methods with various Pt loadings from 0.1 to 0.4 mg·cm$^{-2}$.

**Fig. 29** exhibits the PSD of the CCM and CCS electrodes with various Pt loadings between 0.1 and 0.4 mg·cm$^{-2}$. The experimental results clearly demonstrate that the pore structure of the electrodes is significantly affected by the different catalyst deposition processes. For CCM electrodes, the volume of the large pores with the radius larger than 10 μm is found to increase with the catalyst loading. A higher Pt loading means more materials exist in the prepared CL, resulting in a thicker structure as shown in the SEM images (see **Fig. 28**). In CCM electrodes, the impact of material penetration may be negligible as the catalyst ink is unable to penetrate into membranes; therefore, the increased pore volume can be largely ascribed to the pore structure of the CLs. For CCS electrodes, the volume of the large pores with the radius larger than 10 μm decreases as Pt loading is increased. This is likely due to the particle penetration effect – when a certain amount of catalyst ink is deposited on top of the GDL, the ink penetrates into the GDL pore region, which means the catalyst

particles and ionomer will block large pores, causing a drop in the volume of the large pores. In this scenario, the decline in the volume of the large pores (>1 μm) resulted from material penetration can be as large as 24% at the Pt loading of 0.4 mg·cm$^{-2}$.

Similarly, both catalyst deposition methods generate more small pores in comparison to the reference GDL, but the mechanisms are slightly different. For the CCM electrode, the increase in the small pores (< 10 nm) is mainly due to the addition of the CLs since the material penetration during the deposition process is negligible. For the CCS electrode, the volume of the small pores (< 10 nm) is 6-20% larger than that of the CCM electrode, depending on the Pt loadings applied. This volume increase is not only caused by the existence of the CL but also contributed to by the penetration of the catalyst ink into the GDL pores, due to which the large pores in GDLs become smaller pores.
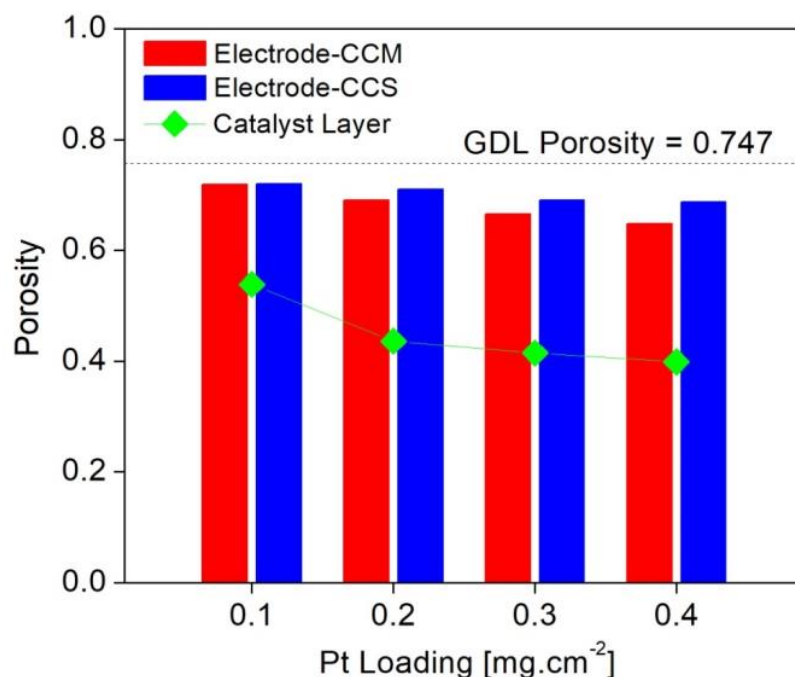


**Fig. 30.** Porosity of the electrodes prepared by the CCM and CCS methods with various Pt loadings from 0.1 to 0.4 mg·cm$^{-2}$.

**Fig. 30** demonstrates the porosity of the CCM and CCS electrodes with various Pt loadings from 0.1 to 0.4 mg·cm$^{-2}$. The porosity of the GDLs, CCS electrodes, and CCM CLs is directly measured through the MSP, while the effective

porosity of the CCM electrodes is calculated from the combination of the GDLs and CCM CLs using **Eq. (4.3)**.

$$\varepsilon_{\text{eff}} = \frac{V_{\text{p,GDL}} + V_{\text{p,CCM}} - V_{\text{p,membrane}}}{V_{\text{b,GDL}} + V_{\text{b,CCM}} - V_{\text{b,membrane}}} \tag{4.3}$$

where $V_{\text{p}}$ is the pore volume, and $V_{\text{b}}$ is the bulk volume of the corresponding components. It should be noted that the pore volume of the membrane is negligible in comparison with that of the CLs and GDLs. The neglected pore volume in membranes is carefully validated by immersing the membranes in octane under a vacuum condition for two hours, during which no observable changes in thickness and weight can be found.

It is found that the electrode porosity for both electrodes is slightly smaller than that of GDL substrates due to the deposition of the CLs, such that the porosity of the CLs is almost half of the GDLs demonstrating a much denser structure of CLs, consistent with the SEM images in **Fig. 28**. As the Pt loading is increased from 0.1 to 0.4 mg·cm$^{-2}$, the porosity of the entire electrodes is observed to become smaller gradually from 0.72 to 0.65 for the CCM and from 0.72 to 0.69 for the CCS electrodes since the pore structure becomes denser due to the deposition of the CLs. Further, with identical Pt loadings, the CCM electrode's porosity is found to be smaller than that of its CCS counterpart because CL thickness plays a predominant role in the entire electrode structure. The porosimetry results indicate that the material penetration into the GDL pores leads to a significant decrease in the pore volume while reducing the overall thickness and bulk volume. The combined effect of these two factors made the CCS electrode less porous than the reference GDL substrate, but more porous than the CCM electrode. This finding shows a good agreement with Reshetenko et al. [153]'s results.
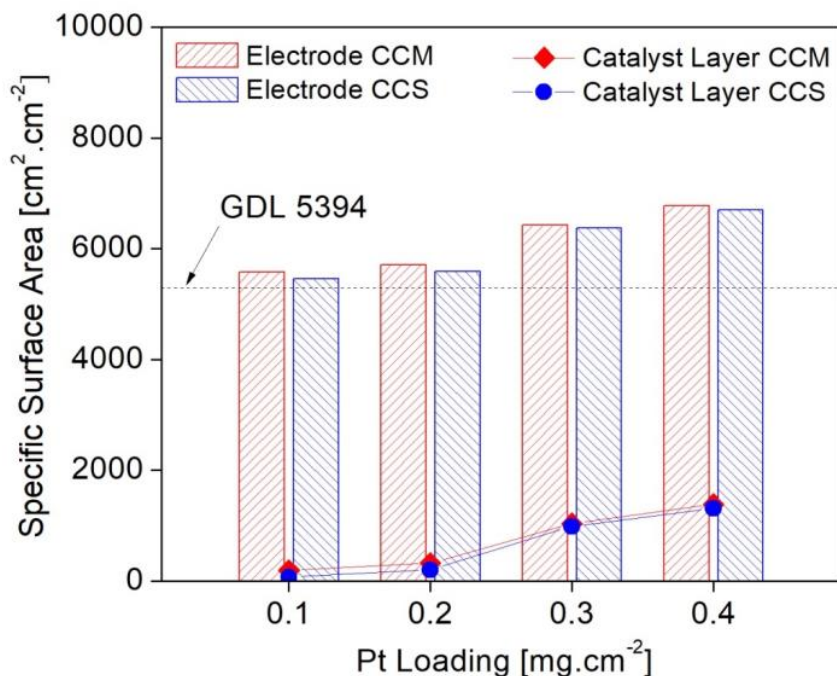
**Fig. 31.** Specific surface area of the electrodes prepared by CCM and CCS methods with various Pt loadings from 0.1 to 0.4 mg·cm$^{-2}$.

**Fig. 31** represents the specific surface areas of the CCM and CCS electrodes with the catalyst loadings between 0.1 and 0.4 mg·cm$^{-2}$. The surface area of the GDLs, CCS electrodes, and CCM CLs is calculated based on the measured PSD following a procedure that is similar to [6]. The surface area of CCM electrode is a combination of those of the GDLs and CCM CLs, while the surface area of CCS CLs is calculated by simply subtracting the surface area of GDLs from those of CCS electrodes for the purpose of comparison. It is found that all the electrodes have more surface area than GDLs, and as the Pt loading is increased, the specific surface area of the electrodes increases significantly. Moreover, the CCM electrodes possess larger surface areas than their CCS counterparts. By neglecting the penetration effect in CCM electrodes, the increase of surface area can be attributed to the addition of relatively thicker CLs in comparison with the CCS electrodes – this is reasonable, particularly considering the thickness differences between the CLs deposited onto membranes (8.6-34 μm) and GDLs (3.6-10 μm). Since the geometric surface is an indicator of the availability of the electrochemically active surface, the CCM electrodes are likely to provide superior electrochemical performance during cell operation.

## 4.2 Effective Diffusion Coefficient

The effective diffusion coefficients of the catalyzed electrodes and CLs made of 60% Pt/C catalysts with the Pt loading of 0.1, 0.2, 0.3, and 0.4 mg·cm$^{-2}$ are investigated in this section. In order to ensure the accuracy of the Loschmidt cell, the bulk diffusion coefficient is firstly measured under various temperatures from 25-60 $^{o}$C, and the results are compared with the classic Marrero and Mason's formula. The effective diffusion coefficients of the electrodes and CLs are measured under the temperature of the typical cell operation (i.e., 25 and 75 $^{o}$C), and their relationship with the porosity and pore size distribution are determined. Finally, the effect of the CCM and CCS fabrication methods on the effective diffusion resistivity, which considers both thickness and effective diffusion coefficient, are discussed.

### 4.2.1 Validation of Loschmidt Cell

**Table 12** compares the measured bulk diffusion coefficient of oxygen-nitrogen gases at different temperatures against the theoretical bulk diffusion coefficient obtained by Marrero and Mason's formula (i.e., **Eq. (4.4)**). It can be seen that the relative errors between the measured and theoretical values can be as small as 3.6%. According to Marrero and Mason [90,160], the bulk diffusion coefficients for the $O_2$-$N_2$ gas pair have sufficient accuracy (up to 3% error) using the following formula, This suggests that the experimental results are at an acceptable level of accuracy.

$$D_{bulk} = 1.13 \times 10^{-9} \frac{T^{1.724}}{p} \tag{4.4}$$

where $D_{bulk}$ is bulk diffusion coefficient in m$^2$·s$^{-1}$, $T$ is the gas temperature in K, and $p$ is the pressure in atm.

**Table 12.** Bulk diffusion coefficients of oxygen in nitrogen for different temperatures

| Temperature (°C) | Measured diffusion coefficient ($10^{-5}$ m$^2$·s$^{-1}$) | Marrero and Mason's formula [90] ($10^{-5}$ m$^2$·s$^{-1}$) | Relative Error (%) |
|---|---|---|---|
| 20 | 2.13±0.06 | 2.10 | 1.4 |
| 25 | 2.17±0.06 | 2.14 | 1.4 |
| 30 | 2.20±0.07 | 2.16 | 1.9 |
| 35 | 2.26±0.07 | 2.21 | 2.2 |

| 45 | 2.38±0.08 | 2.31 | 3.0 |
| 50 | 2.44±0.08 | 2.36 | 3.4 |
| 55 | 2.51±0.09 | 2.42 | 3.5 |
| 60 | 2.62±0.13 | 2.53 | 3.6 |

The bulk diffusion coefficient shown in **Table 12** is measured at the beginning of each measurement to make sure the experimental apparatus is functioning well. Additionally, to ensure the accuracy and repeatability of the measurements, three sets of measurements of diffusion coefficients for each parameter (e.g., temperature, Pt loading, and Ionomer ratio) are conducted. One set is carried out for the bulk region to make sure the machine is running well, one for the substrate, and another one for the combination of substrates and CLs. Each set consists of 3 measurements to ensure the repeatability.

## 4.2.2 Effective Diffusion Coefficient Measurement

**Fig. 32** (a) exhibits the effective diffusion coefficient of the electrodes with a range of Pt loadings from 0.0 to 0.4 mg·cm$^{-2}$ at the temperature of 25 and 75 $^{\circ}$C, respectively. As discussed earlier, a higher Pt loading can lead to a thicker CL, lower porosity, and smaller mean pore size. Thus, the effective diffusion coefficient of the electrode with a higher Pt loading becomes smaller as shown in **Fig. 32** (a). The corresponding diffusion resistivity equals the thickness divided by the effective diffusion coefficient. Due to the thicker electrode and its associated lower diffusion coefficient, the diffusion resistivity of the higher-Pt-loading electrode becomes larger as indicated in **Fig. 32** (b). It should be noted that a higher operating temperature will promote the diffusion of oxygen through the porous electrode, resulting in a lower mass transport resistance.
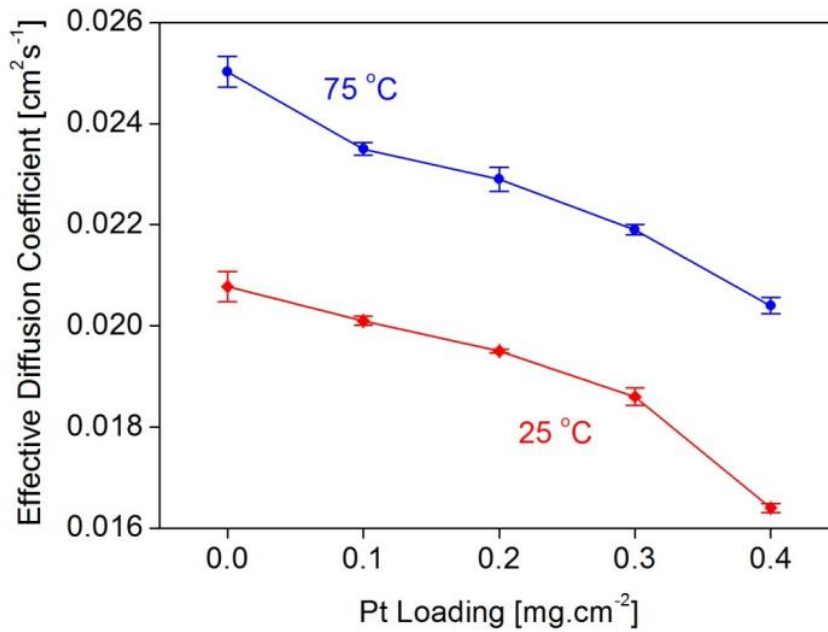
(a) Effective diffusion coefficient.
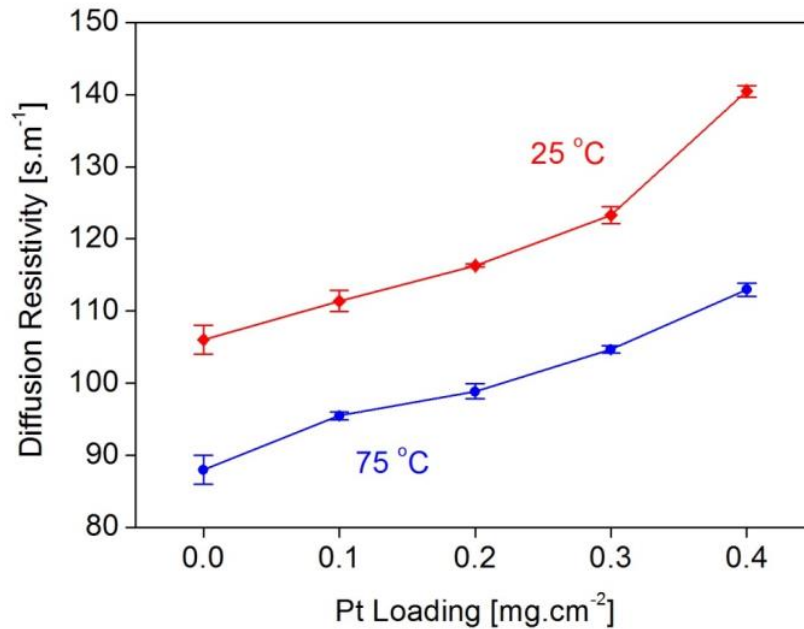


(b) Diffusion resistivity.

**Fig. 32.** Diffusion properties of the porous electrodes with different Pt loadings of 0.0, 0.1, 0.2, 0.3, and 0.4 mg·cm$^{-2}$ at the temperature of 25 and 75 $^{\circ}$C: (a) Effective diffusion coefficient and (b) diffusion resistivity.

In order to determine the effective diffusion coefficients of the CLs alone, the catalyzed and uncatalyzed GDLs are measured separately. From the effective

diffusion coefficients of the catalyzed and uncatalyzed GDLs shown in **Fig. 32**, the effective diffusion coefficients of the CLs can be calculated based on the resistance network theory [106] as follows:

$$D_{CL}^{eff} = \left(\delta_{GDL\_CL} - \delta_{GDL}\right)\left(\frac{\delta_{GDL\_CL}}{D_{GDL\_CL}} - \frac{\delta_{GDL}}{D_{GDL}}\right)^{-1} \tag{4.5}$$

where $\delta$ is the thickness of the corresponding component. The results determined are given in **Table 13**. The repeatability is within 8.3% for all cases. It is seen that the effective diffusion coefficients of the CLs are about one order of magnitude smaller than that of the uncatalyzed GDL measured in this study, and this observation is also consistent with the previous results as shown in Shen et al.'s work using $Al_2O_3$ as the substrate [91]. The average effective diffusion coefficients of the CLs are $(4.2\pm0.9) \times 10^{-7}$ and $(4.6\pm0.5) \times 10^{-7}$ $m^2 \cdot s^{-1}$ at 25 and 75 $^\circ$C, respectively. The current experimental data are slightly larger than those in Shen et al.'s work due to the different materials, composition, and fabrication methods employed, and the substrate selection might also contribute to the difference. It should be noted that this study utilizes a commercial GDL as the substrate, which means the results are more related to the practical PEM fuel cell operating conditions. It might be mentioned that the present study uses 60% Pt/C catalyst. If lower Pt/C catalyst is used, and for the same Pt loading for the electrode, more carbon and ionomer content will be present, resulting into a thicker CL [11], and also since the CL has smaller pore sizes and porosity than the uncatalyzed electrode [11], the entire catalyzed electrode will have lower porosity and lower effective diffusion coefficient as a result, which is undesirable for the mass transport. On the other hand, the effective catalyst surface area is increased for lower Pt/C catalyst with the same Pt loading. Therefore, the final cell performance will be a balance between the reduced mass transport and increased reactive surface area [11].

**Table 13.** Effective diffusion coefficient of the catalyst layers.

| Pt loading [mg·cm$^{-2}$] | Effective diffusion coefficient of catalyst layers [$10^{-7}$ m$^2$·s$^{-1}$] | | | |
|---|---|---|---|---|
| | 0.1 | 0.2 | 0.3 | 0.4 |
| 25 $^\circ$C | 4.9±0.3 | 4.6±0.1 | 4.4±0.3 | 2.8±0.1 |
| 75 $^\circ$C | 5.1±0.4 | 4.8±0.4 | 4.5±0.1 | 3.9±0.1 |

Note: the effective diffusion coefficients of the uncatalyzed GDL measured in this study is $20.8 \times 10^{-7}$ and $25.0 \times 10^{-7}$ $m^2 \cdot s^{-1}$ at 25 and 75 $^\circ$C, respectively.

## 4.2.3 Relation between Pore Structure and Effective Diffusion Coefficient

**Fig. 33** (a) and (b) illustrate the effect of porosity and mean pore size on the effective diffusion coefficients, respectively. Experimental results indicate that the effective diffusion coefficient is directly related to the porosity. Higher porosity has a positive impact on enhancing the effective diffusion coefficient. This trend is found to be in good agreement with the empirical correlation models shown in **Table 3**. Results suggest that mean pore size can also have a significant effect on the effective diffusion coefficients as shown in **Fig. 33** (b). The effective diffusion coefficients of the catalyzed electrodes present a clear increasing trend with the mean pore size. When the pore size is small, the gas molecules collide more frequently with the pore surface, resulting in a larger diffusion resistance (a.k.a. the Knudsen effect). The Knudsen diffusion coefficient, which is proportional to the pore diameter [91,161], indicates that the sample with a large mean pore size has a higher capability for diffusion. The Knudsen diffusion becomes significant when the pore size is less than one micrometer. As discussed earlier, the electrode with higher Pt loadings possesses a higher pore surface area and smaller mean pore size, thus leading to a lower effective diffusion coefficient.
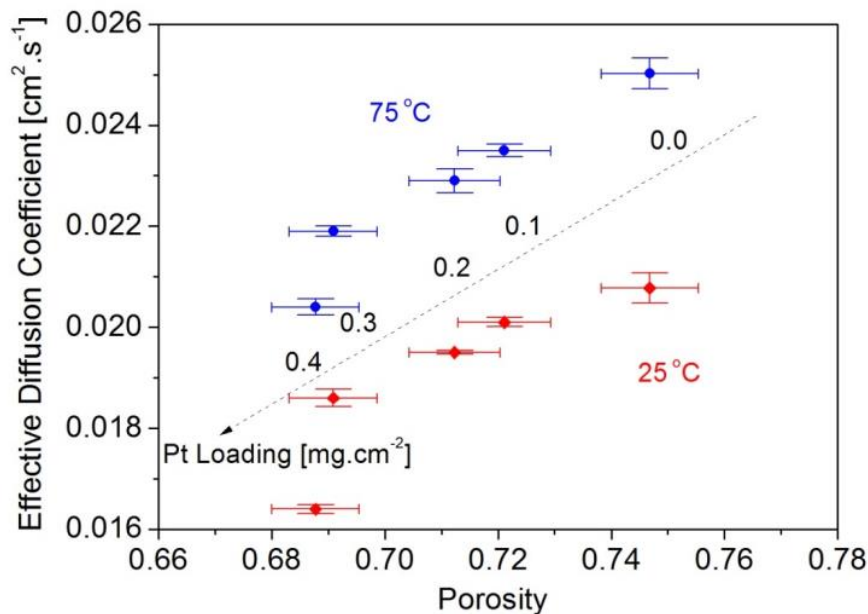


(a) Effective diffusion coefficient vs. Porosity.
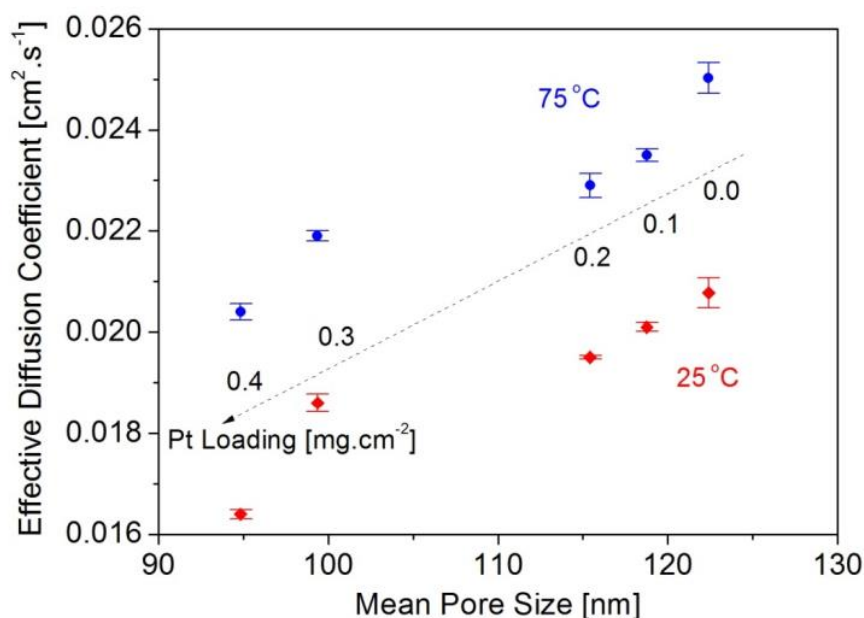
(b) Effective diffusion coefficient vs. Mean pore size.

**Fig. 33.** Relation between the diffusion coefficient of the porous electrodes and the pore structure in terms of (a) porosity and (b) mean pore size.

**Fig. 34** represents the comparison of the experimental data with the different models as a function of porosity. The description of these models is given in **Table 3**. It can be observed that the experimental data are much smaller than the predicted values. Among these models, Zamel et al.'s model is the closest to predict the effective diffusion coefficient of the porous electrode in PEM fuel cells. However, this model still over-estimates the effective diffusion coefficient of the electrode by almost 53% as shown in **Fig. 34**. This over-prediction is likely due to the presence of the CL and a microporous layer which results in a smaller mean pore size of the catalyzed electrode. The gas species experience higher diffusion resistances in smaller pores, and thus the effective diffusion coefficient is lower for the porous media with smaller pore sizes. This indicates that the Knudsen effect has to be considered for CLs and catalyzed electrodes. It should be noted that Das et al.' model is not included since the porosity of the CL only is required. This parameter cannot be measured in this study because the CLs are too thin and too delicate to be separated from the GDLs.
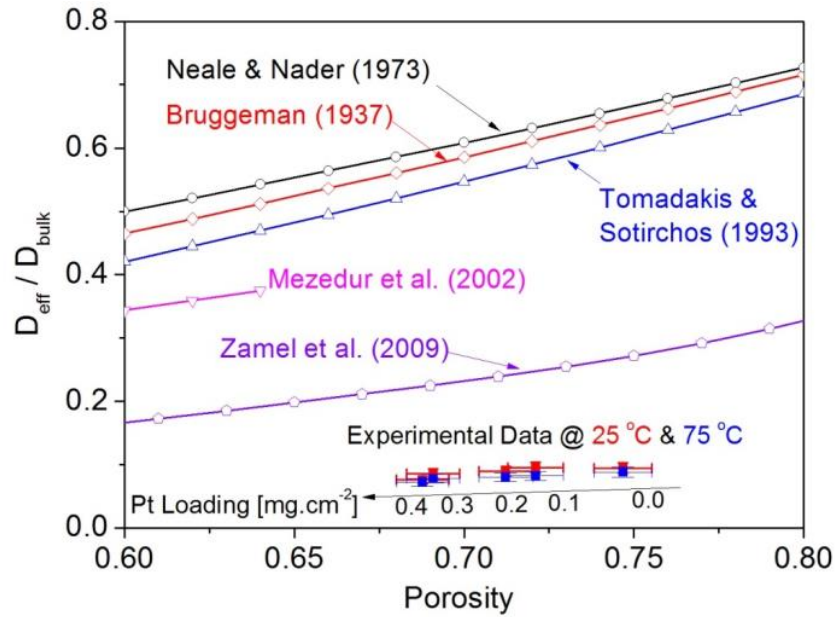
**Fig. 34.** Comparison of the experimental data with the empirical models.

## 4.2.4 Comparison of Diffusion Resistivity between CCM and CCS Methods

Diffusion resistivity, defined as the ratio of thickness to the diffusion coefficient, is a critical parameter that quantifies the easiness of oxygen, for example, to diffuse from the bulk channel to the reaction sites in CLs through the electrodes [3]. Physically, a thicker porous medium with a lower effective diffusion coefficient results in a higher diffusion resistance, which makes it more difficult to transport oxygen at the cathode electrode. The effective diffusion coefficient of the GDLs and CCS electrodes is measured directly using a modified Loschmidt Cell, during which the diffusion resistivity of the CLs is determined (see [3] for more details). The effective diffusion resistivity, $R_d$, which is defined as the diffusion distance over diffusion coefficient, is used to evaluate the easiness of the porous media to transport gasses by diffusion.

$$R_d = \frac{l}{D_{eff}} \tag{4.6}$$

where $l$ is the diffusion distance, and $D_{eff}$ is the effective diffusivity of the porous media. As the diffusion of oxygen in the cathode is much slower than that of hydrogen in the anode [3], only $O_2$-$N_2$ gas pair is studied for the diffusion resistivity of the electrodes. The determination of $D_{eff}$ is available in detail elsewhere [3].

**Fig. 35** presents the diffusion resistivity of the electrodes prepared by CCM and CCS methods with various Pt loadings from 0.1 to 0.4 mg·cm⁻². The results indicate that both the CCM and CCS electrodes have much higher diffusion resistivity than the GDLs. This is contributed to by the presence of CLs. Moreover, a thicker CL on the same GDL yields a larger diffusion resistance, thus the diffusion resistance of the CCM electrodes is much larger than that of CCS electrodes as the CLs in CCM electrodes are much thicker than those in CCS electrodes, which is discussed earlier. This finding also demonstrates that the CL plays a predominant role in gas diffusion throughout the entire electrode, which cannot be neglected in the studies of mass transport in PEM fuel cells even though the CL is very thin.
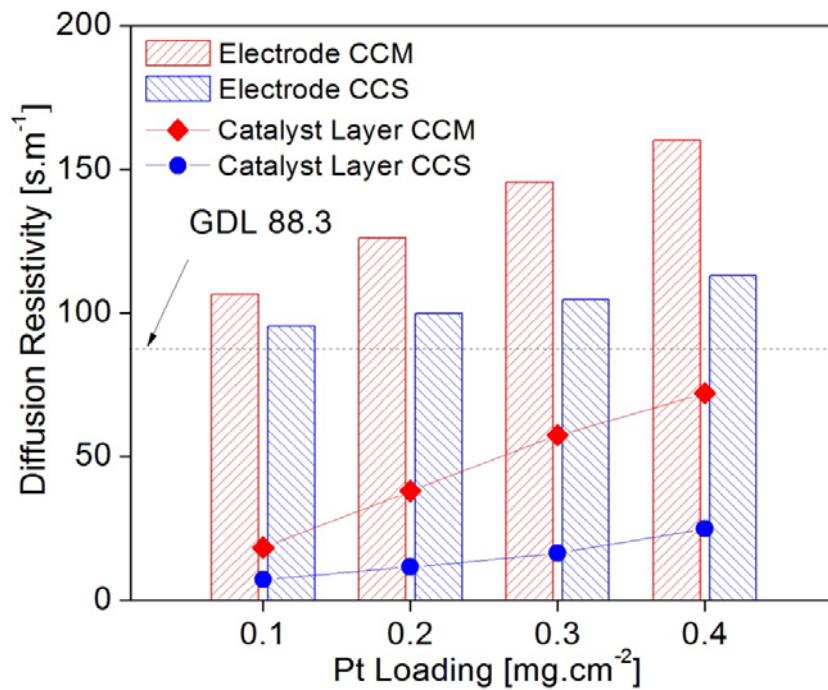


**Fig. 35.** Diffusion resistivity of the electrodes prepared by CCM and CCS methods with various Pt loadings from 0.1 to 0.4 mg·cm⁻².

## 4.3 Permeability

In order to investigate the effect of the CLs on the permeability of the porous electrode, nine groups of samples, including GDLs and catalyzed electrodes made of 30% and 60% Pt/C catalysts with the Pt loadings of 0.1, 0.2, 0.3, and 0.4 mg·cm⁻², are tested. **Table 14** summarizes the detailed information of the prepared electrodes and

is provided in this section for a better comparison. As can be seen, the thickness of the electrode increases almost linearly with the Pt loading for a given type of Pt/C catalyst, because more materials (Pt/C and ionomer) are deposited on the substrate surface for higher Pt loadings. Similarly, for the same Pt loading, a higher Pt/C ratio means less carbon and ionomer are utilized, resulting in a thinner electrode. On the other hand, the porosity for the entire electrodes tested reduces with an increase in the thickness of the entire electrodes.

**Table 14.** Thickness and porosity of the prepared electrodes.

| Pt loading [mg·cm$^{-2}$] | GDL | GDL+CL (30% Pt/C) | | | | GDL+CL (60% Pt/C) | | | |
|---|---|---|---|---|---|---|---|---|---|
| | 0.0 | 0.1 | 0.2 | 0.3 | 0.4 | 0.1 | 0.2 | 0.3 | 0.4 |
| Thickness [μm] | 221.6 ±2.1 | 226.0 ±2.1 | 233.1 ±2.1 | 239.0 ±2.1 | 243.0 ±2.1 | 224.6 ±2.1 | 226.4 ±2.1 | 229.2 ±2.1 | 231.0 ±2.1 |
| Porosity [%] | 74.7 ±1.0 | 71.4 ±1.0 | 67.9 ±1.0 | 66.1 ±0.9 | 65.3 ±0.9 | 72.0 ±1.0 | 71.0 ±1.0 | 69.1 ±1.0 | 68.8 ±1.0 |

Note: The thickness is measured using a micrometer, and the porosity is measured by the standard porosimetry using Octane. The GDL consists of a carbon paper and a micro-porous layer (MPL), and the catalyst layer is coated on top of the MPL.

The experimental results are presented below in three subsections: the effect of the Pt loading and Pt/C ratio, temperature, as well as gas species.

### 4.3.1 Effect of Pt loading and Pt/C ratio

The air permeability of the PEM fuel cell electrode with various Pt loadings of 0.1, 0.2, 0.3 and 0.4 mg·cm$^{-2}$ as well as two different Pt/C ratios of 30% and 60% are investigated at the controlled temperature of 25 $^{\circ}$C in this section. **Fig. 36** (a) and (b) present the relationships between the superficial velocities of air and their associated pressure gradients in the electrodes containing a CL made of 30% and 60% Pt/C catalyst, respectively. The air velocity in the electrode under a certain pressure gradient is governed by the porous structure, which explains the different slopes of the experimental data for different Pt loadings and Pt/C ratios as shown in **Fig. 36**. It can be observed that the gas velocity increases almost linearly with the pressure gradient following Darcy's law. For the same type of catalyst, it is found that a higher pressure

gradient is required to maintain the equivalent gas velocity for the higher Pt loading. This implies that a thicker CL resulting from a higher Pt loading can lead to a higher mass transport resistance. **Table 14** clearly indicates that a higher Pt/C ratio results in a thinner CL under the constant Pt loading, hence a smaller resistance to mass transport. This suggests that the flow rate of gases in the electrode of 60% Pt/C is larger than that of 30% Pt/C at the fixed pressure gradient. Error bars in **Fig. 36** correspond to the uncertainty in the calculated superficial velocity and pressure gradient, and the error bars are relatively small.
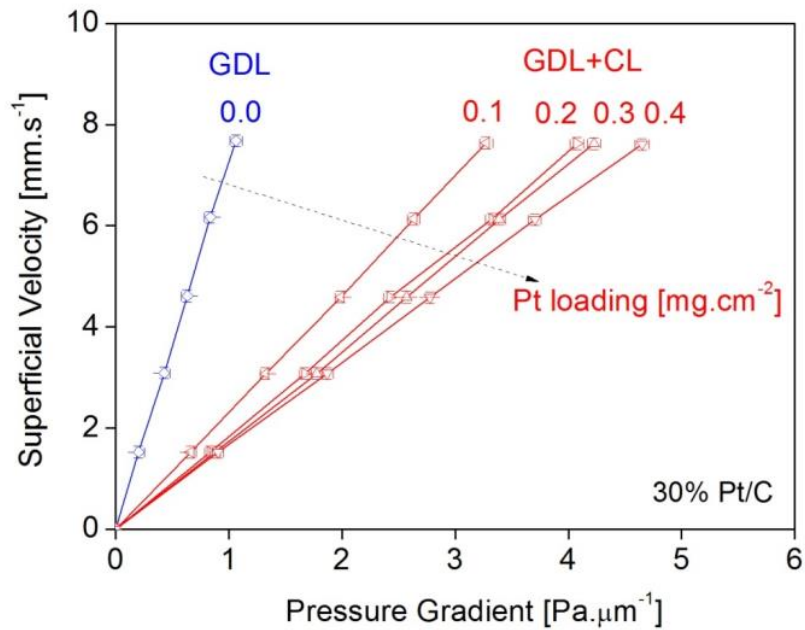


(a) 30% Pt/C
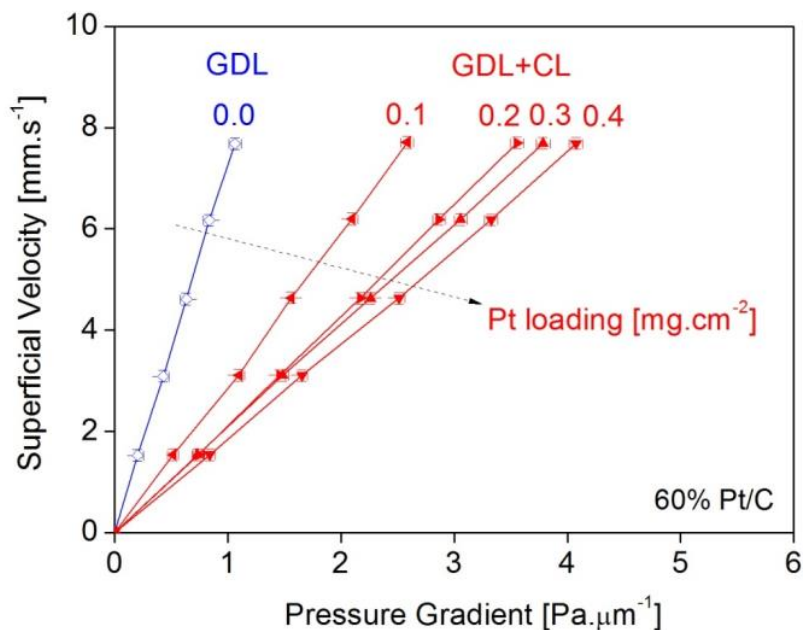
(b) 60% Pt/C

**Fig. 36.** Superficial velocity vs. pressure gradient for air at 25 $^{\circ}$C in uncatalyzed and catalyzed GDLs with various Pt loadings for different types of catalysts: (a) 30% Pt/C and (b) 60% Pt/C.

Further, the ratios of the permeability to the gas viscosity are presented by the slope of the lines in **Fig. 36**. Since all measurements are conducted at fixed temperatures, the slopes of the lines in **Fig. 36** are used to determine the permeability of the porous electrodes. In other words, the higher slopes indicate larger gas permeability values. **Fig. 36** clearly demonstrates that the uncatalyzed GDL (or 0.0 Pt loading) exhibits the highest slope among all the nine tested samples, yielding the highest permeability. This is because the uncatalyzed GDL has the smallest thickness and mass transport resistivity in comparison to the catalyzed GDLs with different Pt loadings, which is labeled as "GDL+CL" in the figure. When the Pt loading is increased from 0.0 to 0.4 mg·cm$^{-2}$, the thickness of the electrode is also increased noticeably in accordance due to the addition of Pt, carbon, and ionomer. The CL structure contains less void regions than the GDLs; therefore, it can be seen that the overall porosity of the electrode is reduced following the slope drops as the Pt loading is increased. In addition, increasing the Pt/C ratio from 30% to 60% with fixed Pt loadings results in a thinner CL because less carbon and ionomer are deposited. As a result, the corresponding mass transport resistivity is reduced with higher Pt/C ratios.
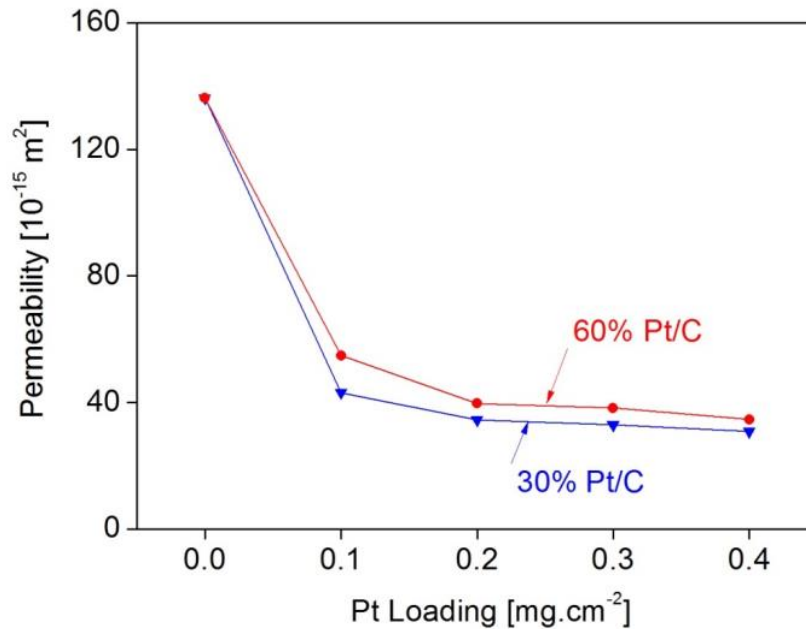
**Fig. 37.** Air permeability of the electrodes vs. Pt loadings at 25 °C for different types of catalysts (30% and 60% Pt/C).

**Fig. 37** shows the effect of different Pt loadings between 0.1 and 0.4 mg·cm$^{-2}$ on the air permeability. The results are obtained for Pt/C ratios of 30% and 60% at the fixed temperature of 25 °C. It reveals that the presence of the CL leads to a sharp reduction in the gas permeability by 58% - 77% in comparison to the uncatalyzed GDL, because of the increased thickness and reduced overall porosity of the electrode as shown in **Table 14**. Further, the gas permeability slightly drops as the Pt loading is increased, indicating a slower gas flow in the CL structures. In addition, a higher Pt/C ratio results in a higher permeability value because the electrode is thinner and more porous, thereby leading to a lower mass transport resistance. The experimental results also indicate that the CL can be considered as the main contributor to the mass transport limitations in PEM fuel cells. This is because the gas permeability of the catalyzed GDL is reduced by 2.3-4.5 times compared to the uncatalyzed GDL. In other words, the transport resistivity of the porous electrode increases due to the presence of the CL structure, which is further influenced by the amount of Pt loading and the type of the catalyst (Pt/C ratio) used.

From the permeability of the catalyzed and uncatalyzed GDLs shown in **Fig. 37**, the effective gas permeability of the CLs can be calculated based on the resistance network theory [106] as follows:

$$K_{CL}^{eff} = \left(\delta_{GDL\_CL} - \delta_{GDL}\right)\left(\frac{\delta_{GDL\_CL}}{K_{GDL\_CL}} - \frac{\delta_{GDL}}{K_{GDL}}\right)^{-1} \qquad (4.7)$$

where $L$ is the thickness of the corresponding component. The results so determined are given in **Table 15**. It is seen that the effective gas permeability of the CLs is about 2 orders of magnitude smaller than that of the uncatalyzed GDL measured in this study, and this observation is also consistent with the previous results as shown in **Table 4**. This is significant because in most of previous modeling and simulation studies of PEM fuel cells, the CL permeability is either entirely neglected, or simply guessed, as mentioned earlier in the introduction section, the two orders of magnitude smaller permeability value in the CL would pose a significant resistance to the transport of the reactant gas to reach the catalyst surface for electrochemical reaction. The permeability data reported here can be used for the modeling and simulation studies of PEM fuel cell operation and performance to improve the understanding of the physical processes involved in an operating PEM fuel cell and will be also useful for fuel cell industry in their design calculations of PEM fuel cells meeting specific performance targets.

**Table 15.** Effective gas permeability of catalyst layers.

| Catalyst Type | CL (30% Pt/C) | | | | CL (60% Pt/C) | | | |
|---|---|---|---|---|---|---|---|---|
| Pt loading $[\text{mg·cm}^{-2}]$ | 0.1 | 0.2 | 0.3 | 0.4 | 0.1 | 0.2 | 0.3 | 0.4 |
| Air Permeability $[10^{-15} \text{ m}^2]$ | 1.5 | 2.6 | 3.6 | 3.7 | 1.6 | 1.5 | 2.2 | 2.2 |

Note: effective gas permeability of the GDL measured in this study is $138.8 \times 10^{-15} \text{ m}^2$.

## 4.3.2 Effect of Temperature

The performance of the PEM fuel cells can be significantly affected by the operating temperatures, and the gas permeability of the electrodes is also influenced according to Darcy's law. Therefore, the air permeability of the PEM fuel cell electrodes is investigated at different temperatures of 25, 37.5, 50, 62.5, and 75 $^o$C.
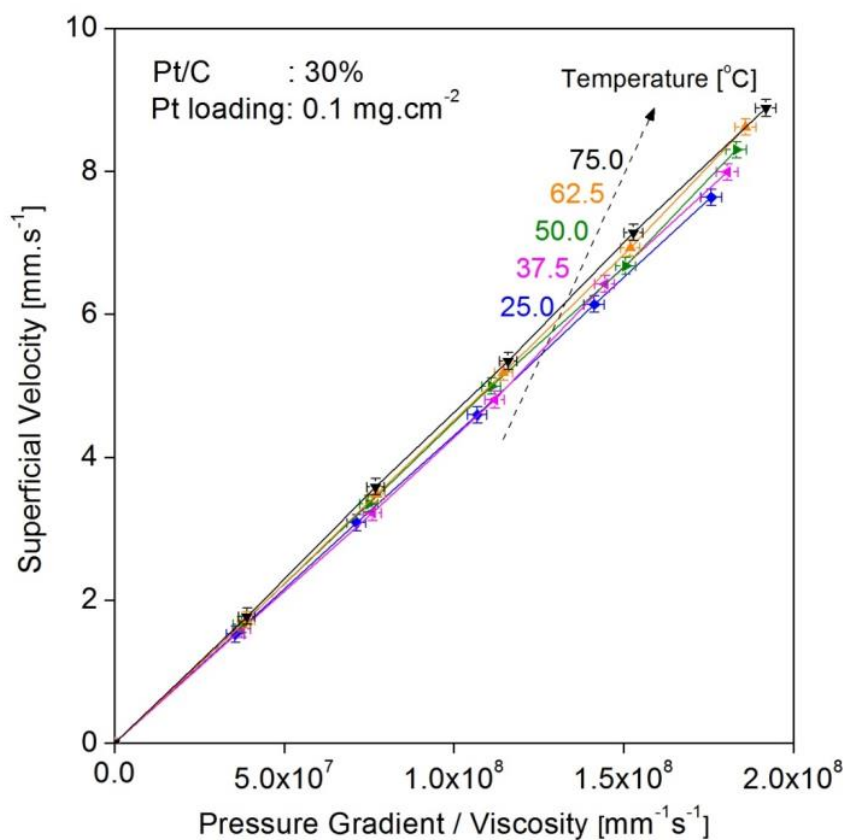
**Fig. 38**. Superficial velocity vs. pressure gradient/viscosity for air in catalyzed GDLs with Pt loadings of 0.1 mg·cm$^{-2}$ for 30% Pt/C at various temperatures.

Fig. 38 represents the results of the superficial velocity versus the ratio of the pressure gradient to viscosity for one specific sample (i.e., catalyzed GDL with 30% Pt/C under the Pt loading of 0.1 mg·cm$^{-2}$) at various temperatures. In this figure, the slope of each line equals the air permeability of the same sample at different temperatures. It can be observed that the slope of 25 $^{o}$C is the smallest, and increased as the temperature rises from 25 to 75 $^{o}$C. This indicates that the temperature does have an impact on the permeability of the gases; however, as the lines are relatively close to each other, the effect of the temperature may not be significant within the range of 25-75 $^{o}$C. It should be pointed out that similar trends can be found for all the samples at various temperatures not only for air but also for oxygen and nitrogen gases. For simplicity, only one sample is presented in this section.
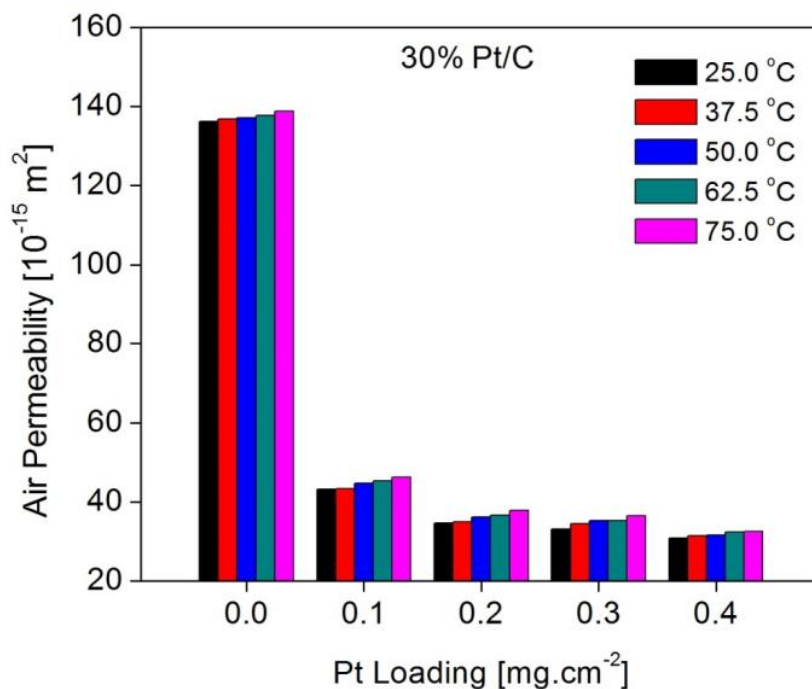
(a) 30% Pt/C
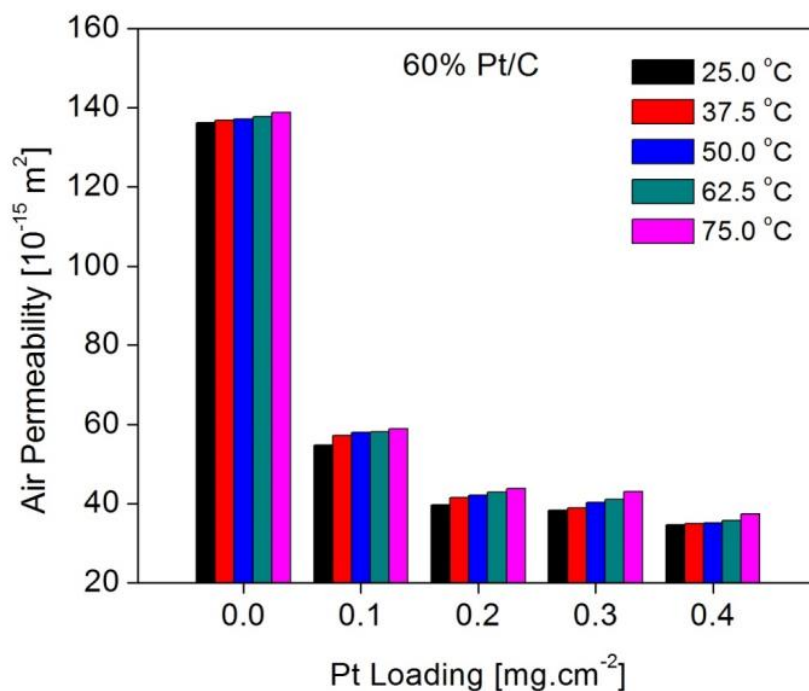


(b) 60% Pt/C

**Fig. 39.** The effect of temperature on the air permeability of the electrodes with five different Pt loadings of 0.0, 0.1, 0.2, 0.3 and 0.4 mg·cm$^{-2}$ and two different Pt/C ratios of (a) 30% and (b) 60%.

**Fig. 39** (a) and (b) demonstrate the effect of temperature on the air permeability for different Pt/C ratios of 30% and 60%, respectively. As can be seen, the gas permeability is increased slightly as the temperature is increased from 25 to 75 $^{o}$C for the same electrode. This implies that gases with higher temperatures possess better capabilities to penetrate the porous samples. However, it can be noted that the uncertainty margins at various temperatures are overlapped significantly for the tested cases. This suggests that the impact of the temperature on the air permeability will be marginal for PEM fuel cell electrodes in the temperature range between 25 and 75 $^{o}$C.

### 4.3.3 Effect of Gas Species

Since the air and oxygen are commonly used as oxidant reactants, the permeability of the electrodes in PEM fuel cells to these two gases is investigated. Further, nitrogen permeability is also measured because nitrogen is another major species in air.
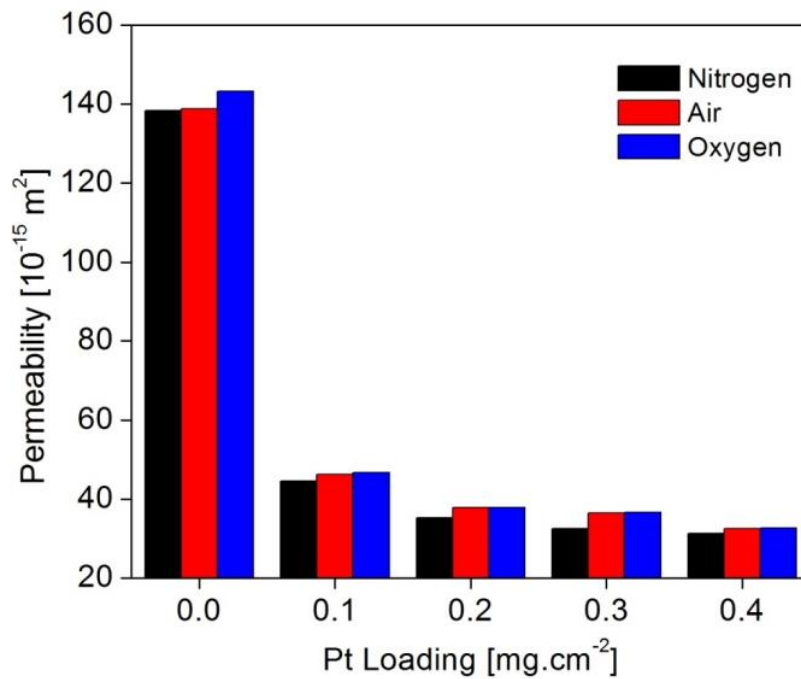


(a) 30% Pt/C
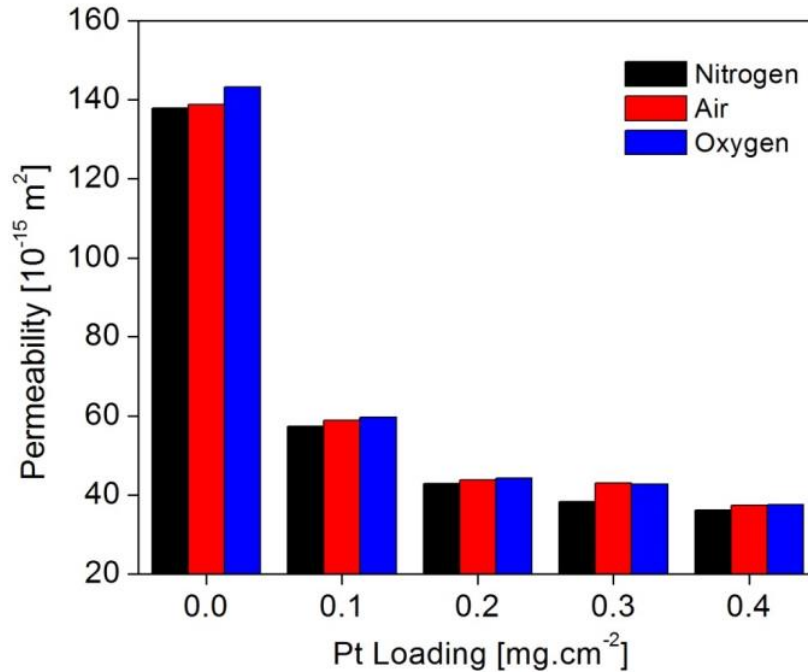
(b) 60% Pt/C

**Fig. 40.** Comparison of gas permeability of electrodes to air, oxygen, and nitrogen at 75 °C.

**Fig. 40** shows the permeability of the electrodes for oxygen, air, and nitrogen at a fixed temperature of 75 °C. The largest gas permeability corresponds to oxygen, closely followed by air. The lowest permeability is measured for nitrogen, the species with the smallest molecular weight of the three gases investigated. Similar trends can be found for all the electrodes under different temperatures. These variations in the permeability among the three gases can be related to the sizes of the gas molecules, which govern the capability of the gas species to flow through the micropores [112,122]. Moreover, for a given electrode, the difference in obtained permeability values for oxygen, air, and nitrogen is less than 5% and is within the range of the measurement uncertainties. This is because the oxygen, air, and nitrogen have a high similarity in terms of molecular weight, molecular diameter, and viscosity. The measured permeability values of the GDLs with MPLs are in good agreements with Tseng et al.'s work [116], while the permeability of the catalyzed GDLs is much smaller than that of the uncatalyzed GDLs.

## 4.3.4 Comparison of Permeation Resistivity between CCM and CCS Methods

Gas permeation resistivity is a parameter that represents the porous media's capability in mass transport, particularly when the pressure-driven convection is dominant [5]. The gas convection is affected by not only the cell operation but also the thickness and permeability of the porous components. In this study, gas permeation resistivity is defined as the thickness over permeability, indicating that a thicker porous medium with a lower permeability results in a higher resistance to the convection in porous media. The permeation resistivity of the GDLs, CCS electrodes, and CCS CLs is measured using a custom-built instrument based on Darcy's law, which is similar to the studies in [5]. The permeation resistivity (similar to the definition of diffusion resistivity), $R_p$, is defined as the thickness over permeability, representing the difficulty of the porous media to transport gases by the pressure-driven convection

$$R_p = \frac{l}{K} \tag{4.8}$$

where $K$ is the gas permeability.
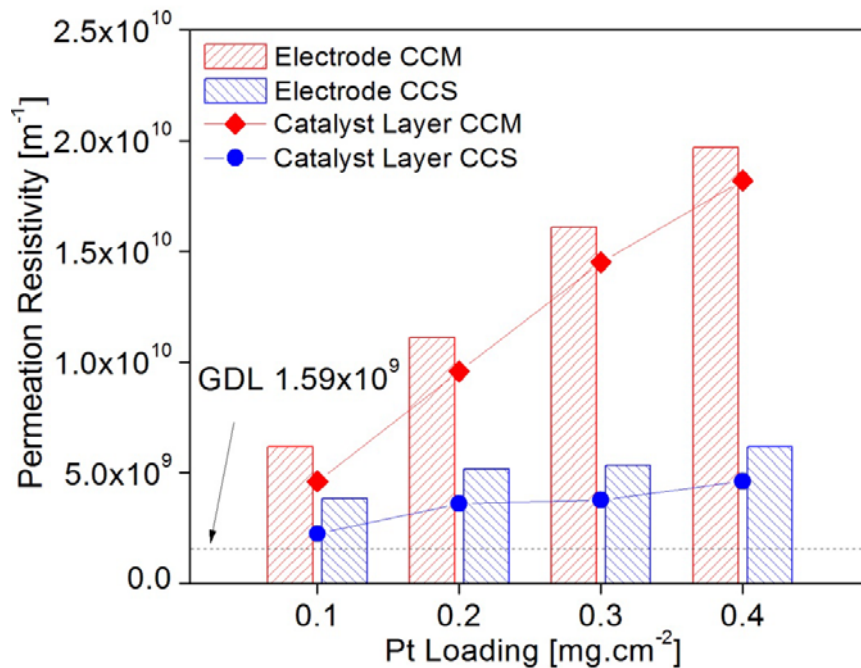


**Fig. 41.** Permeation resistivity of the electrodes prepared by CCM and CCS methods with various Pt loadings from 0.1 to 0.4 mg·cm$^{-2}$.

**Fig. 41** presents the permeation resistivity of the electrodes prepared by CCM and CCS methods with various Pt loadings from 0.1 to 0.4 mg·cm$^{-2}$. As can be seen, the permeation resistance in the prepared electrodes is much higher than that of the GDLs. Similar to the effective diffusion resistivity, a thicker CL on the same GDL yields a much higher permeation resistivity, representing the difficulty for the convection of gases in the CLs. At low Pt loadings (e.g., 0.1 mg·cm$^{-2}$), the permeation resistivity of CCM and CCS is $6.18 \times 10^9$ and $3.82 \times 10^9$ m$^{-1}$, respectively. As the Pt loading is increased to 0.4 mg·cm$^{-2}$, the permeation resistivity of CCM electrode is almost tripled ($1.97 \times 10^{10}$ m$^{-1}$), while that of the CCS electrode is increased by only 62%. The results indicate that the thickness of the CLs is crucial to the permeation resistivity in the entire electrode. The permeation resistivity together with the gas diffusion resistivity demonstrates that the mechanisms of mass transfer (especially for oxygen transport) can be significantly different in CLs and GDLs when different Pt loadings are applied to the entire electrodes.

## 4.4 Cell Performance

The polarization performances of the cathode electrodes prepared by CCS and CCM methods with the catalyst loadings of 0.1 and 0.4 mg·cm$^{-2}$ are investigated in a single fuel cell with an active area of 45 cm$^2$. In the present study, only the typical low- and high-Pt-loading electrodes are selected for the cell performance tests. The *in-situ* tests are performed under the same conditions: the temperature of 75°C, the backpressure of 35 kPag, and the anode and cathode flow rates of 4.45 and 9.00 SLPM for hydrogen and air, respectively. The relative humidity of hydrogen and air is maintained at 100%.

**Fig. 42** (a) demonstrates the cell potential versus current density of the four electrodes. Apparently, the high-Pt-loading CCM and CCS electrodes output almost identical voltages in the low current density regions (<0.15 A·cm$^{-2}$) where activation loss dominates. The similar OCV and activation-region performance observed clearly indicates that even though the CCM and CCS electrodes have different structure and mass transport resistivity, they can still perform comparably as the pore surface areas in the CCM and CCS CLs are almost identical when the Pt loading is 0.4 mg·cm$^{-2}$. In the medium current density region where ohmic loss dominates, the current density of the high-Pt-loading CCM electrode is about 1.27 A·cm$^{-2}$ at the cell voltage of 0.6 V,

while that of the CCS electrode is 1.19 A·cm$^{-2}$ – this corresponds to the performance difference of about 6.3%. The superior ohmic-polarization performance of the CCM electrode could be an indicator of relatively better interfacial characteristics between the CL and membrane achieved with the CCM method. Similarly, at high current density region where concentration loss dominates, the CCM electrode presents slightly better performance than its CCS counterpart. For example, at the current density of 1.90 A·cm$^{-2}$, the CCM electrode with the Pt loading of 0.4 mg·cm$^{-2}$ output the voltage of 0.48 V, while its CCS counterpart yields the voltage of 0.46 V – this corresponds to the performance improvement of about 4.2%. For high-Pt-loading CCM electrodes, the improved cell performance within the entire range of polarization curves can be attributed to the better interfacial contact between the CL and membrane resulted from the direct catalyst deposition onto the membrane. However, it is seen that the cell performances obtained for the high-Pt-loading CCM and CCS electrodes are still close to each other, clearly indicating that at high-Pt loadings (e.g., 0.4 mg·cm$^{-2}$), the penetration of materials into the GDL has a limited effect on the performance characteristics as the portion of inactive Pt nanoparticles is relatively small.

However, for low Pt loadings (e.g., 0.1 mg·cm$^{-2}$), the cell performance is significantly affected by the catalyst deposition locations, as presented in **Fig. 42** (a). It is found that the CCM and CCS electrode exhibits quite different cell performances in the activation, ohmic, and concentration polarization regions. For example, the CCM electrode is found to output a 4.4% higher OCV than its CCS counterpart, indicating that the CCS electrode provides relatively fewer reaction sites, consistent. As the current density is further increased, the performance difference between the CCM and CCS electrodes becomes even more obvious. For example, at the current density of 0.5 A·cm$^{-2}$, the output voltage of the CCM electrode is around 0.68 V, which is about 31% lower than that of CCS electrode (i.e., 0.47 V). The performance drop continues to enlarge at high current regions. For example, at the current density of 1.1 A·cm$^{-2}$, the voltage drop from CCM to CCS electrode can be as large as 88%.
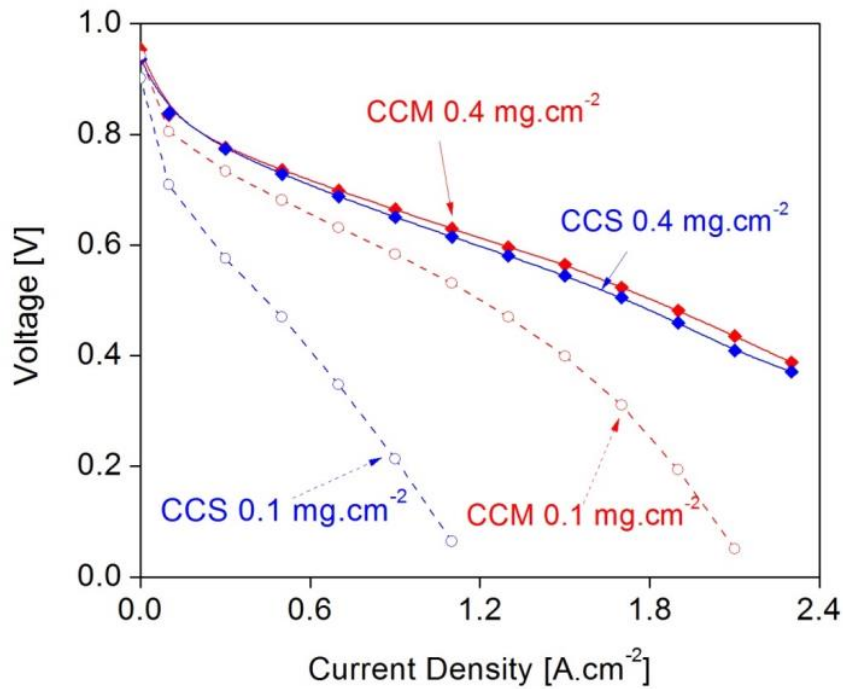
(a) Polarization curve
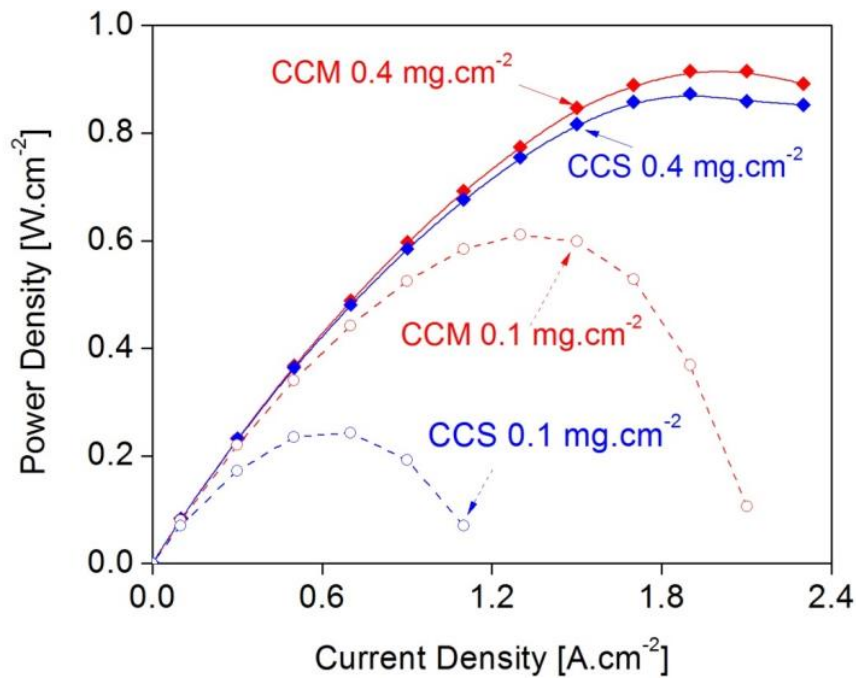


(b) Power density

**Fig. 42.** (a) Polarization curve and (b) power density of the cathode CCM and CCS electrodes with the Pt loadings of 0.1 and 0.4 mg·cm$^{-2}$. The ratio of cathode to anode Pt loading is set at 4:1. Test condition: cell temperature of 75$^o$C, cell backpressure of 35 kPag, and fully-humidified air and hydrogen of 9.00 and 4.45 SLPM.

The performance deterioration from CCM to CCS electrodes at various Pt loadings can also be clearly identified from the power density curves as shown in **Fig. 42** (b). For example, at high Pt loadings, the maximum power densities for CCM and CCS electrodes are 0.91 W·cm$^{-2}$ and 0.87 W·cm$^{-2}$, respectively - the difference is only 4.3%. However, when the Pt loading is decreased to 0.1 mg·cm$^{-2}$, the maximum power density for CCM and CCS electrodes decreases to 0.61 W·cm$^{-2}$ and 0.24 W·cm$^{-2}$, respectively. In other words, the maximum power density is decreased by 60% from CCM to CCS methods at the low catalyst loading of 0.1 mg·cm$^{-2}$. This dramatic performance deterioration is likely due to the material penetration into the GDLs during the catalyst deposition, causing some catalysts inactive in electrochemical reactions.

## 4.5 Summary

In this chapter, the major experimental results are presented in four aspects: pore structure characterization, effective diffusion coefficient measurement, permeability determination, and cell performance testing.

The pore structures of the prepared electrodes are investigated by the method of standard porosimetry (MSP) in terms of pore size distribution (PSD), porosity, pore surface area distribution, specific surface area (SSA), and mean pore size, and surface fractal dimension. It is observed that the presence of the CL is of great significance to the overall pore structure of the electrode. As the Pt loading is increased, the electrode porosity decreases. Specifically, for 30% Pt/C, the electrode porosity decreases from 75% of the uncatalyzed GDL to 65%; and for 60% Pt/C, the porosity is reduced to 69%. It is also seen that the pores smaller than 100 nm in all the catalyzed electrodes increase with the Pt loading in comparison with the uncatalyzed one. These pores significantly contribute to the formation of the specific pore surface area (SSA) such that 95.0-96.5% of the cumulative pore surface area is taken up by the pores smaller than 100 nm. For the constant Pt loading, the electrode made of a lower Pt/C ratio yields a thicker electrode, lower porosity, larger SSA, and smaller mean pore size. The surface fractal dimension of the electrode, between 2.709 and 2.877, is found to increase either with increasing Pt loading or decreasing Pt/C ratio, indicating more complex structure resulted from the fabrication of the CL on the electrode. Overall, this pore structure characterization highlights the importance of the CLs, hence its

design parameters, i.e., Pt loading and Pt/C ratio, on the pore structure of the entire electrode in PEM fuel cells.

The measurement of the effective diffusion coefficient is based on Fick's law of diffusion via a modified Loschmidt Cell. It is found that the effective diffusion coefficient decreases due to the smaller porosity and mean pore size for the higher-Pt-loading electrodes. In addition, a higher temperature enhances the effective diffusion coefficient by 15-25% from 25 $^o$C to 75 $^o$C, which are the typical operating temperatures of PEM fuel cells. Finally, the effective diffusion coefficient of the CL is about $4.6 \times 10^{-7}\,m^2 \cdot s^{-1}$ at 75 $^o$C. These results highlight the importance of CLs, with a focus on the impact of the Pt loading, in determining the overall mass transport in the porous electrode of PEM fuel cells.

The determination of permeability is based on Darcy's law via a custom-engineered apparatus. It is observed that the presence of the CL leads to a 58-77% drop in gas permeability in comparison with the uncatalyzed GDL. For consideration based on catalyst alone, the catalyst with a higher Pt/C ratio has higher gas permeability than the catalyst with a lower Pt/C ratio because of the thickness and porosity of the entire electrodes with a constant Pt loading. Similarly, for the electrodes made of the same type of catalyst, the permeability is larger for the electrode with a lower Pt loading, leading to better mass transport in the porous electrode. The effective gas permeability of the CLs is $(1.5-3.7) \times 10^{-15}\,m^2$, which is about two orders of magnitude smaller than that in the GDLs. In addition, a higher temperature results in a higher gas permeability value, although the enhancement is small within the temperature range tested (25-75$^o$C). Also, oxygen shows a slightly higher permeability value than air and nitrogen; however, the difference is within 5% for all cases because oxygen and nitrogen have similar molecular properties. These results highlight the importance of CLs, hence the Pt loading and Pt/C ratio, in determining mass transport in the porous media in PEM fuel cells. The permeability data reported can be used for the accurate modeling and simulation studies of PEM fuel cell operation and performance to improve the understanding of the physical processes involved in an operating PEM fuel cell, and will be also useful for fuel cell industry in their design calculations of PEM fuel cells meeting specific performance targets.

The cell performance is tested using a commercially available test station. At high Pt loadings (e.g., 0.4 mg·cm$^{-2}$), the CCM and CCS electrodes yield comparable

cell performance, while at low Pt loadings (e.g., 0.1 mg·cm$^{-2}$), the maximum power density of the CCS electrode deteriorates as much as 60% than that of CCM. This study provides practical insights into the effect of two extensively used catalyst deposition methods (CCM and CCS) on the morphological, structural, physical, and electrochemical characteristics of the fuel cell electrodes, reveals the main advantages of the CCM method over its CCS counterpart, and consequently indicates the possibility of further performance improvements through an effective catalyst deposition method.

In order to further investigate the mass transport phenomena in PEM fuel cells, the *ex-situ* experimental data on the pore structure, effective diffusion coefficient, and permeability can be introduced to the current numerical models, and the *in-situ* experimental data on the cell performance can be used to validate the numerical results. These results can be used to improve the understanding the mass transport in PEM fuel cells.

# Chapter 5
# Model Development

In this chapter, a three-dimensional numerical model has been developed based on the electrochemical reactions and transport processes inside the associated CLs, GDLs, and flow channels at the anode and cathode separated by the membrane. The model development has been discussed in three aspects: numerical formulation, boundary conditions, as well as grid independence and convergence criteria.

## 5.1 Numerical Formulation

A comprehensive PEM fuel cell model involves the electrochemical reaction kinetics and the transport of multi-component multi-phase species as well as electrons and protons. The PEM fuel cell in the present study has 36 straight flow channels in parallel for either anode or cathode. Therefore, a single channel pair is selected in the present numerical studies, and the computational domain is composed of nine components including a membrane, two CLs, two GDLs, two flow channels, and two distribution plates as shown in **Fig. 43**. Twelve conservation equations regarding the mass, momentum (x-, y- and z-components), gas species (oxygen, hydrogen, and water vapor), dissolved and liquid water, electronic and protonic potential, and energy are developed as shown in **Table 16** and **Table 17** [137,138]. For a better illustration, the x direction is referred to as the stream-wise direction hereafter, and the y and z directions are herein defined as the through-plane and in-plane directions, respectively.
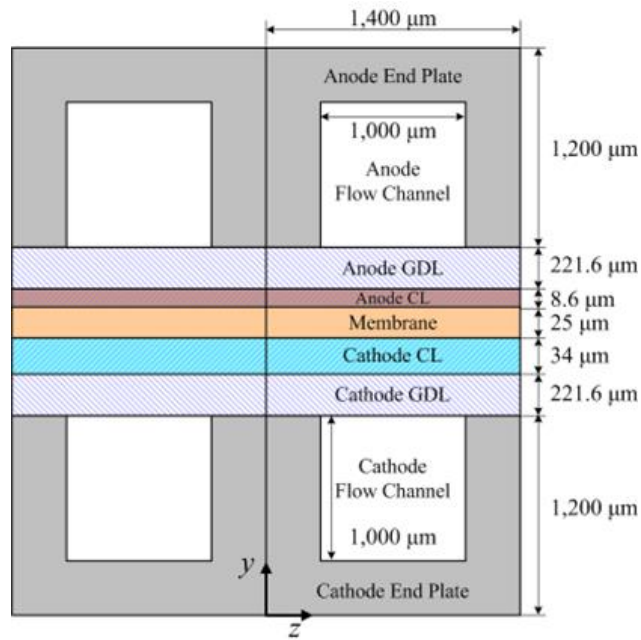
(a) Dimensions
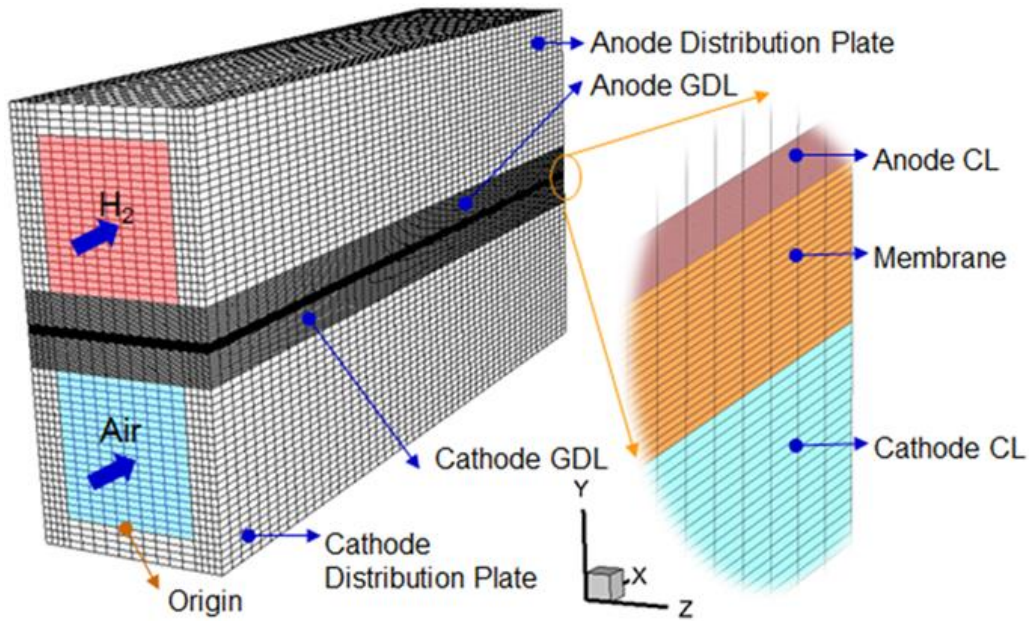


(b) Computational Domain and Meshes

**Fig. 43**. Computational domain for the simulation.

**Table 16.** Conservation equations.

| Property | Conservation equation | Domains solved in | Equation # |
|---|---|---|---|
| Mass | $\nabla \cdot (\rho_g \vec{u}_g) = S_m$ | Flow channel, GDL, CL | (5.1) |
| Momentum | $\nabla \cdot \left(\dfrac{\rho_g \vec{u}_g \vec{u}_g}{\varepsilon^2(1-\Phi_l)^2}\right) = -\nabla p_g + \mu_g \nabla \cdot \left(\left(\nabla\left(\dfrac{\vec{u}_g}{\varepsilon(1-\Phi_l)}\right)\right) + \nabla\left(\dfrac{\vec{u}_g^T}{\varepsilon(1-\Phi_l)}\right)\right) - \dfrac{2}{3}\mu_g \nabla\left(\nabla \cdot \left(\dfrac{\vec{u}_g}{\varepsilon(1-\Phi_l)}\right)\right) + S_u$ | Flow channel, GDL, CL | (5.2) |
| Gas species | $\nabla \cdot (\rho_g \vec{u}_g Y_i) = \nabla \cdot (\rho_g D_i^{\text{eff}} \nabla Y_i) + S_i$ | Flow channel, GDL, CL | (5.3) |
| Liquid water | $\nabla \cdot (f\rho_l \vec{u}_g) = \nabla \cdot (\rho_l D_l \nabla \Phi_l) + S_l$ | Flow channel, GDL, CL | (5.4) |
| Dissolved water | $0 = \dfrac{\rho_{\text{mem}}}{EW}\nabla \cdot (D_d^{\text{eff}}\nabla \lambda_d) + S_d$ | Membrane, CL | (5.5) |
| Ionic charge | $0 = \nabla \cdot (\kappa_{\text{ion}}^{\text{eff}}\nabla \varphi_{\text{ion}}) + S_{\text{ion}}$ | Membrane, CL | (5.6) |
| Electronic charge | $0 = \nabla \cdot (\kappa_{\text{ele}}^{\text{eff}}\nabla \varphi_{\text{ele}}) + S_{\text{ele}}$ | BP, GDL, CL | (5.7) |
| Energy | $\nabla \cdot \left((\rho c_p)_{\text{fl}}^{\text{eff}}\vec{u}_g T\right) = \nabla \cdot (k_{\text{fl,sl}}^{\text{eff}}\nabla T) + S_T$ | Entire cell components | (5.8) |

**Table 17.** Source terms of the governing equations.

| Cell Component | Source terms | | | | | | | |
|---|---|---|---|---|---|---|---|---|
| | $S_m$ | $S_u$ | $S_i$ | $S_l$ | $S_d$ | $S_{\text{ele}}$ | $S_{\text{ion}}$ | $S_T$ |
| | (kg·m⁻³·s⁻¹) | (kg·m⁻²·s⁻²) | (kg·m⁻³·s⁻¹) | (kg·m⁻³·s⁻¹) | (kmol·m⁻³·s⁻¹) | (A·m⁻³) | (A·m⁻³) | (W·m⁻³) |
| BP | 0 | 0 | 0 | 0 | 0 | 0 | 0 | $\|\nabla\varphi_{\text{ele}}\|^2 k_{\text{ele}}^{\text{eff}}$ |
| Channel | $S_v$ | 0 | $S_v = -S_{v\text{-}l}$ | 0 | 0 | 0 | 0 | 0 |
| GDL | $S_v$ | $-\dfrac{\mu_g}{K_g}\vec{u}_g$ | $S_v = -S_{v\text{-}l}$ | $S_{v\text{-}l}$ | 0 | 0 | 0 | $\|\nabla\varphi_{\text{ele}}\|^2 k_{\text{ele}}^{\text{eff}} + S_{\text{pc}}$ |
| Anode CL | $S_{H_2} + S_v$ | $-\dfrac{\mu_g}{K_g}\vec{u}_g$ | $S_{H_2} = -\dfrac{j_a}{2F}M_{H_2}$ $S_v = S_{d\text{-}v}M_{H_2O}-S_{v\text{-}l}$ | $S_{v\text{-}l}$ | $-S_{d\text{-}v} + S_{\text{eod}}$ | $-j_a$ | $j_a$ | $j_a|\eta_{\text{act}}| + \|\nabla\varphi_{\text{ele}}\|^2 k_{\text{ele}}^{\text{eff}} + \|\nabla\varphi_{\text{ion}}\|^2 k_{\text{ion}}^{\text{eff}} + S_{\text{pc}}$ |
| Cathode CL | $S_{O_2} + S_v$ | $-\dfrac{\mu_g}{K_g}\vec{u}_g$ | $S_{O_2} = -\dfrac{j_a}{4F}M_{O_2}$ $S_v = S_{d\text{-}v}M_{H_2O}-S_{v\text{-}l}$ | $S_{v\text{-}l}$ | $\dfrac{j_c}{2F} - S_{d\text{-}v} + S_{\text{eod}}$ | $j_c$ | $-j_c$ | $-\dfrac{j_c T\Delta s}{4F} + j_c|\eta_{\text{act}}| + S_{\text{pc}} + \|\nabla\varphi_{\text{ele}}\|^2 k_{\text{ele}}^{\text{eff}} + \|\nabla\varphi_{\text{ion}}\|^2 k_{\text{ion}}^{\text{eff}}$ |
| Membrane | 0 | 0 | 0 | 0 | 0 | 0 | 0 | $\|\nabla\varphi_{\text{ion}}\|^2 k_{\text{ion}}^{\text{eff}} + S_{\text{pc}}$ |

Note: BP, GDL, CL denote bipolar plate, gas diffusion layer, and catalyst layer, respectively.

Eqs. **(5.1)** and **(5.2)** are the conservation equations of mass and momentum for the gas mixtures, and **Eq. (5.3)** denotes the transport of various gas species, such as hydrogen, oxygen, and water vapor. The superficial velocity is employed in the present study to ensure the mass conservation at the channel-GDL interfaces. All the gas species involved in the present model are assumed to follow the ideal gas law, and the mixture density, $\rho_g$ in [kg·m$^{-3}$], is calculated as follows,

$$\rho_g = p_g \left( RT \sum_i \frac{Y_i}{M_i} \right)^{-1}$$

(5.9)

where $Y$ is the mass fraction of the gas species $i$ in the mixture.

The mixture dynamic viscosity in **Eq. (5.2)** is determined through the kinetic theory expressed as

$$\mu_g = \sum_i \frac{X_i \mu_i}{\sum_j X_j \psi_{ij}}$$

(5.10)

$$\psi_{ij} = \frac{\left[ 1 + \left( \frac{\mu_i}{\mu_j} \right)^{0.5} \left( \frac{M_j}{M_i} \right)^{0.25} \right]^2}{\left[ 8 \left( 1 + \frac{M_i}{M_j} \right) \right]^{0.5}}$$

(5.11)

where $X$ is the molar fraction of the gas species. The experimental correlations of the dynamic viscosity of a single species under various temperatures and pressures can be found in **Table 18**.

A source term due to the resistance to the gas convection in the porous media is introduced in the momentum equation (see **Eq. (5.2)** and **Table 17**). The convective gas transport is highly associated with the porous structure of the GDLs and CLs as well as the liquid water volume, which may block the pathways for gas transport. The pore structure determines the intrinsic permeability, $K_0$ in [m$^2$], of the porous media when liquid water is absent. This value may vary significantly from $10^{-15}$ to $10^{-12}$ [m$^2$] in various studies [98,125,129–131], which may introduce a large uncertainty when modeling the mass transport in GDLs and CLs. Thus the value of the intrinsic permeability is experimentally determined in the present study. The effect of water on the permeability of the gas and liquid phases is considered via modifying the permeability [129] using the following equations by considering the local volumetric fraction of the liquid water, $\Phi_l$

$$K_g = K_0 (1 - \Phi_l)^{3.0}$$

(5.12)

$$K_l = K_0 \Phi_l^{3.0} \tag{5.13}$$

The species transport is governed by **Eq. (5.3)** considering the convective and diffusive mass transport as well as species generation and consumption due to reactions. Many models are established to estimate the effective diffusivity based on the porosity of the porous media. These models assume the effective diffusivity as a function of the pore structure and bulk diffusivity. The bulk diffusivity is a function of pressure and temperature, while the effect of pore structure for a given porous media (fixed porosity and touristy) can be represented by a dimensionless constant, $\beta(\varepsilon, \tau)$, which is experimentally determined in the present study. The measured diffusibility is about one to two orders of magnitude lower than those predicted by the empirical models [3], and this will definitely affect the mass transport in the porous media significantly. It should be noted that the constant, $\beta(\varepsilon, \tau)$, is measured using the nitrogen-oxygen gas pair, and in the simulation work, this constant is applied to all the other gas species, such as hydrogen, oxygen, and water vapor, in GDLs and CLs. Similar to the permeability, the effective diffusivity can also be affected by the existence of liquid water in the electrode during the actual cell operation. Therefore, the effective diffusivity of the GDLs and CLs may be considered as [3,61,88]

$$D_i^{eff} = D_i \beta(\varepsilon, \tau)(1 - \Phi_l)^{1.5} \tag{5.14}$$

The total flux of the gas species i, $J_{m,i}^{total}$, can be calculated as the sum of the convective, $J_{m,i}^{conv}$, and diffusive components, $J_{m,i}^{diff}$ [128]:

$$J_{m,i}^{conv} = \rho_g \vec{u}_g Y_i \tag{5.15}$$

$$J_{m,i}^{diff} = -\rho_g D_i^{eff} \nabla Y_i \tag{5.16}$$

$$J_{m,i}^{total} = J_{m,i}^{conv} + J_{m,i}^{diff} \tag{5.17}$$

The liquid water is assumed to have a constant density as shown in **Table 18** since the changes in its density within the temperature and pressure range of the fuel cell operation are negligible. The transport of liquid water is expressed in **Eq. (5.4).** The interfacial drag coefficient, $f$, is calculated using the following equation [162].

$$f = \frac{K_l \mu_g}{K_g \mu_l} \tag{5.18}$$

The capillary diffusivity, $D_l$ in [m$^2$·s$^{-1}$], of the liquid water in GDLs and CLs are defined as

$$D_l = -\frac{K_l}{\mu_l}\frac{dp_{ca}}{d\Phi_l} \tag{5.19}$$

where the capillary pressure, $p_{ca}$, is determined via the Leverett function based on the surface tension, contact angle, intrinsic permeability, porosity, and volumetric fraction of liquid water [15,61]:

$$p_{ca} = \begin{cases} \sigma\cos\theta\left(\frac{\varepsilon}{K_0}\right)^{0.5}[1.42(1-\Phi_l)-2.12(1-\Phi_l)^2+1.26(1-\Phi_l)^3], & \theta < 90^{\circ} \\ \sigma\cos\theta\left(\frac{\varepsilon}{K_0}\right)^{0.5}[1.42\Phi_l-2.12\Phi_l{}^2+1.26\Phi_l{}^3], & \theta > 90^{\circ} \end{cases} \tag{5.20}$$

where the surface tension and contact angle are given in **Table 18**, and the intrinsic permeability and porosity of the GDLs and CLs are measured in the present study.

The water phase change between the vapor and liquid is

$$S_{v\text{-}l} = \begin{cases} A_{pore}\dfrac{S_{h\,cond}D_v}{d}\varepsilon(1-\Phi_l)(\rho_v-\rho_{sat}), & \text{if } \rho_v \geq \rho_{sat} \\[2mm] A_{pore}\dfrac{S_{h\,evap}D_v}{d}\varepsilon\Phi_l(\rho_v-\rho_{sat}), & \text{if } \rho_v < \rho_{sat} \end{cases} \tag{5.21}$$

where $S_{h\,cond}$ and $S_{h\,evap}$ are the dimensionless rates of phase transfer due to the condensation and evaporation (in the range of 0.00204 to 0.245) [61], $D_v$ is the diffusivity of the water vapor in [$m^2 \cdot s^{-1}$], $d$ is the chracteristic length of the water diffusion in [m], $\Phi_l$ is the liquid volume fraction, and $\rho_v$ and $\rho_{sat}$ are the densities of the actual water vapor and saturated water vapor in [$kg \cdot m^{-3}$], respectively. When the actual vapor density is higher than the saturated vapor, condensation occurs; Otherwise, evaporation occurs.

The transport of the dissolved water in the membrane is governed by **Eq. (5.5).** The water transfer between the vapor and dissolved phase in the membrane is expressed as

$$S_{d\text{-}v} = \zeta_{d\text{-}v}\frac{\rho_{mem}}{EW}(\lambda_d - \lambda_{equil})(1-\Phi_l) \tag{5.22}$$

where the water transfer rate between dissolved and vapor water, $\zeta_{d\text{-}v} = 1\ s^{-1}$, is taken in the present study [61,136].

The dissolved water content, $\lambda_d$, is defined as follows,

$$\lambda_d = \frac{EW}{\rho_{mem}}c_{H_2O} \tag{5.23}$$

In addition, the equilibrium dissolved water content, $\lambda_{equil}$, is expressed as [135,163],

$$\lambda_{equil} = 0.3 + 6a[1 - \tanh(a - 0.5)] + 3.9\sqrt{a}\left[1 + \tanh\left(\frac{a - 0.89}{0.23}\right)\right] \quad (5.24)$$

where $a$ denotes the water activity defined as,

$$a = \frac{X_v p_g}{p_{sat}} + 2\Phi_l \quad (5.25)$$

where $p_{sat}$ in [Pa] is the saturated vapor pressure determined by the following equation [98],

$$p_{sat} = 101325 \times 10^{-2.1794+0.02953(T-273)-9.1837\times10^{-5}(T-273)^2+1.4454\times10^{-7}(T-273)^3} \quad (5.26)$$

The diffusivity of the dissolved water in membranes, $D_d$ in $[m^2 \cdot s^{-1}]$, is calculated as [135,163],

$$D_d = 4.1 \times 10^{-10} \left(\frac{\lambda_d}{25}\right)^{0.15} \left[1 + \tanh\left(\frac{\lambda_d - 2.5}{1.4}\right)\right] \quad (5.27)$$

The water transport via the electro-osmotic drag (EOD), $S_{eod}$, from the anode to the cathode through the membrane is,

$$S_{eod} = \nabla \cdot \left(\frac{n_d}{F} \kappa_{ion}^{eff} \nabla \varphi_{ion}\right) \quad (5.28)$$

where $n_d$ is the EOD coefficient, indicating the number of water molecules traveling with each proton in ionomers, $\kappa_{ion}^{eff}$ is the effective ionic conductivity in $[S \cdot m^{-1}]$, $\varphi_{ion}$ is the ionic potential in [V]. The EOD coefficient, $n_d$, can be calculated using the following equation

$$n_d = \frac{2.5\lambda_d}{22} \quad (5.29)$$

The electronic and protonic potentials in the cell are governed by **Eqs. (5.6)** and **(5.7)**. The effective ionic conductivity, $\kappa_{ion}^{eff}$ in $[S \cdot m^{-1}]$, of the GDLs and CLs can be calculated via,

$$\kappa_{ion}^{eff} = \omega^{1.5} \kappa_{ion} \quad (5.30)$$

where $\omega$ is the volumetric ratio of the ionomer in the corresponding domain, and the ionic conductivity of the membrane, $\kappa_{ion}$ in $[S \cdot m^{-1}]$, is determined through the following expression [98]

$$\kappa_{\text{ion}} = (0.5139\lambda_{\text{d}} - 0.326)\exp\left[1268\left(\frac{1}{303.15} - \frac{1}{T}\right)\right] \qquad (5.31)$$

The effective electronic conductivity, $\kappa_{\text{ele}}^{\text{eff}}$ in [S·m$^{-1}$], of the GDLs and CLs is usually modified via the Bruggeman's correlation as follows

$$\kappa_{\text{ele}}^{\text{eff}} = (1 - \varepsilon - \omega)^{1.5}\kappa_{\text{ele}} \qquad (5.32)$$

The volumetric reaction rates in the anode and cathode CLs, $j_{\text{a}}$ and $j_{\text{c}}$ in [A·m$^{-3}$], are determined via the Butler-Volmer equations

$$j_{\text{a}} = (1 - \Phi_{\text{l}})j_{0,\text{a}}^{\text{ref}}\left(\frac{c_{\text{H}_2}}{c_{\text{H}_2}^{\text{ref}}}\right)^{0.5}\left[\exp\left(\frac{2F\alpha_{\text{a}}}{RT}\eta_{\text{act}}\right) - \exp\left(-\frac{2F\alpha_{\text{c}}}{RT}\eta_{\text{act}}\right)\right] \qquad (5.33)$$

$$j_{\text{c}} = (1 - \Phi_{\text{l}})j_{0,\text{c}}^{\text{ref}}\left(\frac{c_{\text{O}_2}}{c_{\text{O}_2}^{\text{ref}}}\right)\left[-\exp\left(\frac{4F\alpha_{\text{a}}}{RT}\eta_{\text{act}}\right) + \exp\left(-\frac{4F\alpha_{\text{c}}}{RT}\eta_{\text{act}}\right)\right] \qquad (5.34)$$

where $j_{0,\text{a}}^{\text{ref}}$ and $j_{0,\text{c}}^{\text{ref}}$ in [A·m$^{-3}$] are the reference volumetric current densities for the anode and cathode, respectively. $F$ is the Faraday's constant in [C·kmol$^{-1}$]. $\eta_{\text{act}}$ in [V] is the activation overpotential. The charge transfer coefficients for the anode and cathode $\alpha_{\text{a}}$ and $\alpha_{\text{c}}$ can be found in **Table 18**.

The energy conservation is expressed in **Eq. (5.8).** The effective volumetric heat capacities are calculated using the following equation,

$$\left(\rho c_{\text{p}}\right)_{\text{fl}}^{\text{eff}} = \varepsilon\left[\Phi_{\text{l}}\rho_{\text{l}}\left(c_{\text{p}}\right)_{\text{l}}\frac{K_{\text{l}}\mu_{\text{g}}}{K_{\text{g}}\mu_{\text{l}}} + (1 - \Phi_{\text{l}})\rho_{\text{g}}\left(c_{\text{p}}\right)_{\text{g}}\right] \qquad (5.35)$$

where $\left(c_{\text{p}}\right)_{\text{g}}$ is the mixture specific heat capacity in [J·kg$^{-1}$·K], which is calculated as $\left(c_{\text{p}}\right)_{\text{g}} = \Sigma_i Y_i\left(c_{\text{p}}\right)_i$. The volumetric effective thermal conductivity, $k$ in [W·m$^{-1}$·K$^{-1}$], is determined via **Eqs. (5.36)-(5.38).**

$$k_{\text{fl,sl}}^{\text{eff}} = \varepsilon\left[\Phi_{\text{l}}k_{\text{l}} + (1 - \Phi_{\text{l}})k_{\text{g}}\right] + (1 - \varepsilon - \omega)k_{\text{sl}} + \omega k_{\text{mem}} \qquad (5.36)$$

$$k_{\text{g}} = \sum_i \frac{X_i k_i}{\Sigma_j X_j \psi_{ij}} \qquad (5.37)$$

$$\psi_{ij} = \frac{\left[1 + \left(\frac{\mu_i}{\mu_j}\right)^{0.5}\left(\frac{M_j}{M_i}\right)^{0.25}\right]^2}{\left[8\left(1 + \frac{M_i}{M_j}\right)\right]^{0.5}} \qquad (5.38)$$

where the subscripts fl, sl, l, g, and mem denote fluid, solid, liquid, gas, and membrane, respectively. As the specific heat capacity and thermal conductivity of an

individual substance are almost independent of the temperature within the range from 0-100 °C, both of them are considered as constant in the modeling as summarized in **Table 18**.

The function of latent heat, $S_{pc}$, in [W·m$^{-3}$] is calculated below according to the rate of phase change and water transfer,

$$S_{pc} = \begin{cases} h_{cond}S_{v\text{-}l} & \text{(in GDL)} \\ h_{cond}(S_{v\text{-}l} - S_{d\text{-}v}M_{H_2O}) & \text{(in CL)} \end{cases} \tag{5.39}$$

where $h_{cond}$ in [J·kg$^{-1}$] is the latent heat of condensation, which strongly depends on temperature, $T$ in [K], and the following linear correlation is employed [139]

$$h_{cond} = -2438.5T + 3170700 \tag{5.40}$$

**Table 18**. Physical and electrochemical properties and correlations used in the present study.

| Parameter | Correlation |
|---|---|
| Hydrogen dynamic viscosity (kg·m$^{-1}$·s$^{-1}$) [139] | $\mu_{H_2} = 3.205 \times 10^{-3}(T/293.85)^{1.5}(T+72)^{-1.0}$ |
| Oxygen dynamic viscosity (kg·m$^{-1}$·s$^{-1}$) [139] | $\mu_{O_2} = 8.46 \times 10^{-3}(T/292.25)^{1.5}(T+127)^{-1.0}$ |
| Water vapor dynamic viscosity (kg·m$^{-1}$·s$^{-1}$) [139] | $\mu_v = 7.512 \times 10^{-3}(T/291.15)^{1.5}(T+120)^{-1.0}$ |
| Liquid water dynamic viscosity (kg·m$^{-1}$·s$^{-1}$) [139] | $\mu_l = 2.414 \times 10^{-5} \times 10^{247.8/(T-140)}$ |
| Hydrogen diffusivities (m$^2$·s$^{-1}$) [139] | $D_{H_2} = 1.055 \times 10^{-4}(T/333.15)^{1.5}(101325/p)$ |
| Oxygen diffusivities (m$^2$·s$^{-1}$) [139] | $D_{O_2} = 2.652 \times 10^{-5}(T/333.15)^{1.5}(101325/p)$ |
| Water vapor diffusivities in anode (m$^2$·s$^{-1}$) [139] | $D_v^a = 1.055 \times 10^{-4}(T/333.15)^{1.5}(101325/p)$ |
| Water vapor diffusivities in cathode (m$^2$·s$^{-1}$) [139] | $D_v^c = 2.982 \times 10^{-5}(T/333.15)^{1.5}(101325/p)$ |
| Specific heat capacities of H$_2$, O$_2$, vapor water, and liquid water [139] | $(c_p)_{H_2} = 14283 \quad (c_p)_{O_2} = 919.31$ <br> $(c_p)_v = 2014 \quad (c_p)_l = 4182$ |
| Thermal conductivities of H$_2$, O$_2$, vapor water, and liquid water [139] | $k_{H_2} = 0.1672 \quad k_{O_2} = 0.0264$ <br> $k_v = 0.0261 \quad k_l = 0.6$ |
| Entropy change of reaction (J·kmol$^{-1}$·K$^{-1}$) [139] | $\Delta s = -163110$ |
| Surface tension (N·m$^{-1}$) | $\sigma = -0.0001676T + 0.1218$ <br> $(273.15K \le T \le 373.15K)$ |
| Overpotential (V) [139] | $\eta_{act} = \varphi_{ele} - \varphi_{ion}$ |
| Transfer coefficient [139] | $\alpha_a = \alpha_c = 0.5$ |
| Volumetric reference exchange current density in anode (A·m$^{-3}$) [139] | $j_{0,a}^{ref} = j_{0,a}^{ref}\big|_{353.15K}\exp\left[-1400\left(\frac{1}{T} - \frac{1}{353.15}\right)\right]$ |
| Volumetric reference exchange current density in cathode (A·m$^{-3}$) [139] | $j_{0,c}^{ref} = j_{0,c}^{ref}\big|_{353.15K}\exp\left[-7900\left(\frac{1}{T} - \frac{1}{353.15}\right)\right]$ |

Note: $T$ in K, and $p$ in Pa.

## 5.2 Boundary Conditions

The boundary conditions in the modeling include the inlet reactant flow conditions, operating temperature, operating pressure and electric loads. The anode mass flow rate of the computational domain, $\dot{m}_a$, is 0.124 slpm, and at the cathode side, $\dot{m}_c = 0.25$ slpm, which is consistent with the experimental conditions. A constant outlet pressure is specified at the flow channel outlets (35 kPag). A constant temperature is defined at the anode and cathode flow channel inlets and the surrounding walls (348 K). The liquid water volume fraction in the channels is zero with the assumption that the liquid water can be effectively removed from the channels. The molar concentration of the $H_2$ and $O_2$ at the anode and cathode channel inlets are determined as follows:

$$c_{H_2} = \frac{\left(p_{g,out}^a + \Delta p_g^a - R_{h,a}p_{sat}\right)}{RT_{in}^a} \tag{5.41}$$

$$c_{O_2} = \frac{0.21\left(p_{g,out}^c + \Delta p_g^c - R_{h,c}p_{sat}\right)}{RT_{in}^c} \tag{5.42}$$

The pressure differences in **Eqs. (5.41)** and **(5.42)**, which can be estimated based on the average current density and the frictional pressure loss in the channel, are marginal in comparison with the absolute pressure in straight channels (this assumption is further confirmed by the numerical results that the pressure differences between the inlet and outlet for anode and cathode are about 0.08% and 0.25% of the absolute pressure, respectively), but this assumption should be carefully justified for large-scale stacks composed of multiple cells or serpentine channels [164,165]. The electric potential at the bottom of the cathode distribution plate as shown in **Fig. 43** is set at zero, while the electric potential at the top surface of the anode distribution plate is the difference between the reversible and operating cell voltages [61,98,135,136].

$$\begin{cases} \varphi_e^{a,top} = E_r - E_{cell} = \eta_{total} \\ \varphi_e^{c,bot} = 0 \end{cases} \tag{5.43}$$

where $V_{rev}$ is the reversible cell voltage, which is determined via the Nernst equation [135].

$$V_{rev} = \frac{\Delta g_{ref}}{2F} + \frac{\Delta s_{ref}}{2F}(T_0 - T_{ref}) + \frac{RT_0}{2F}\ln\left[\left(\frac{p_{H_2}^{in}}{p_{ref}}\right)\left(\frac{p_{O_2}^{in}}{p_{ref}}\right)^{1/2}\right] \tag{5.44}$$

## 5.3 Grid Independence and Convergence Criteria

The conservation equations are discretized via the second-order upwind method and are solved using FLUENT, a commercial software package, with user-defined functions based on finite volume methods. The SIMPLE algorithm is employed to couple the pressure and velocity field. A set of numerical tests have been performed to ensure the independence of the numerical solutions from the grid size. The grid numbers in x, y and z directions ($N^x$, $N^y$, and $N^z$) are determined separately by varying the grid number in only one direction while fixing the grid numbers in the other two directions. For instance, to determine the $N^x$, the grid numbers in the y and z directions are fixed at $N^y = 10$ and $N^z = 18$, respectively. The value of $N^x$ is varied from 10 to 70. The current density obtained by the high grid number of $N^x = 70$ is selected as the "exact solution", and the relative errors, $Err^x$ are defined as

$$Err^x = \left| \frac{\theta_{N^{70}} - \theta_{N^x}}{\theta_{N^{70}}} \right| \times 100\% \tag{5.45}$$

where $\theta$ denotes the variable to be compared (i.e., the average current density).

**Fig. 44** (a) demonstrates the effect of $N^x$ on the errors of the average current density due to various $N^x$ values applied. It is seen that the solution precision increases with the grid number. However, when the grid number $N^x$ is larger than 50, the changes in solution is almost negligible. Similar to $N^x$, the values of $N^y$ and $N^z$ are determined according to the following equations,

$$Err^y = \left| \frac{\theta_{N^{25}} - \theta_{N^y}}{\theta_{N^{25}}} \right| \times 100\% \tag{5.46}$$

$$Err^z = \left| \frac{\theta_{N^{20}} - \theta_{N^z}}{\theta_{N^{20}}} \right| \times 100\% \tag{5.47}$$

In this study, the values of $N^y$ varies from 5 to 25 while $N^x = 50$ and $N^z = 18$ are fixed. The values of $N^z$ varies from 12 to 20 at $N^x = 50$ and $N^y = 20$. **Fig. 44** (b) and (c) indicate that when $N^y \geq 20$ and $N^z \geq 18$, the errors in the average current density due to a further increase in grid numbers are negligible. Therefore, it is reasonable to assign the grid number in x, y and z directions to be 50, 20 and 18 as larger numbers of grids do not change the results much but increase the computational time exponentially.

Strict convergence criteria are carefully determined for the residue of all variables, and the effect of the residue value on the average current density is investigated by varying the residue from $10^{-3}$ to $10^{-9}$ while keeping the above-

determined grid numbers constant. The error is calculated by assuming $10^{-9}$ is the "exact solution" based on the following equation.

$$Err = \left| \frac{\theta_{N^{1e-9}} - \theta_{N^c}}{\theta_{N^{1e-9}}} \right| \times 100\% \qquad (5.48)$$

where $\theta$ is the variable to be compared (i.e., the average current density).

**Fig. 44** (d) indicates that the error becomes negligible when the residue value is smaller than $10^{-8}$, which exhibits a sufficient accuracy. Therefore, the residue of $10^{-8}$ is employed for the present study.

In addition, to make sure the physical properties are converged, the average current densities at the top and bottom surfaces of the corresponding anode and cathode distribution plates are sufficiently close to each other with an error smaller than 0.1%. Similar grid independence studies and convergence criteria are available elsewhere for the PEM fuel cell modeling [121,135,137,139].



(a) $N^x$    (b) $N^y$

(c) $N^z$    (d) Convergence Criteria
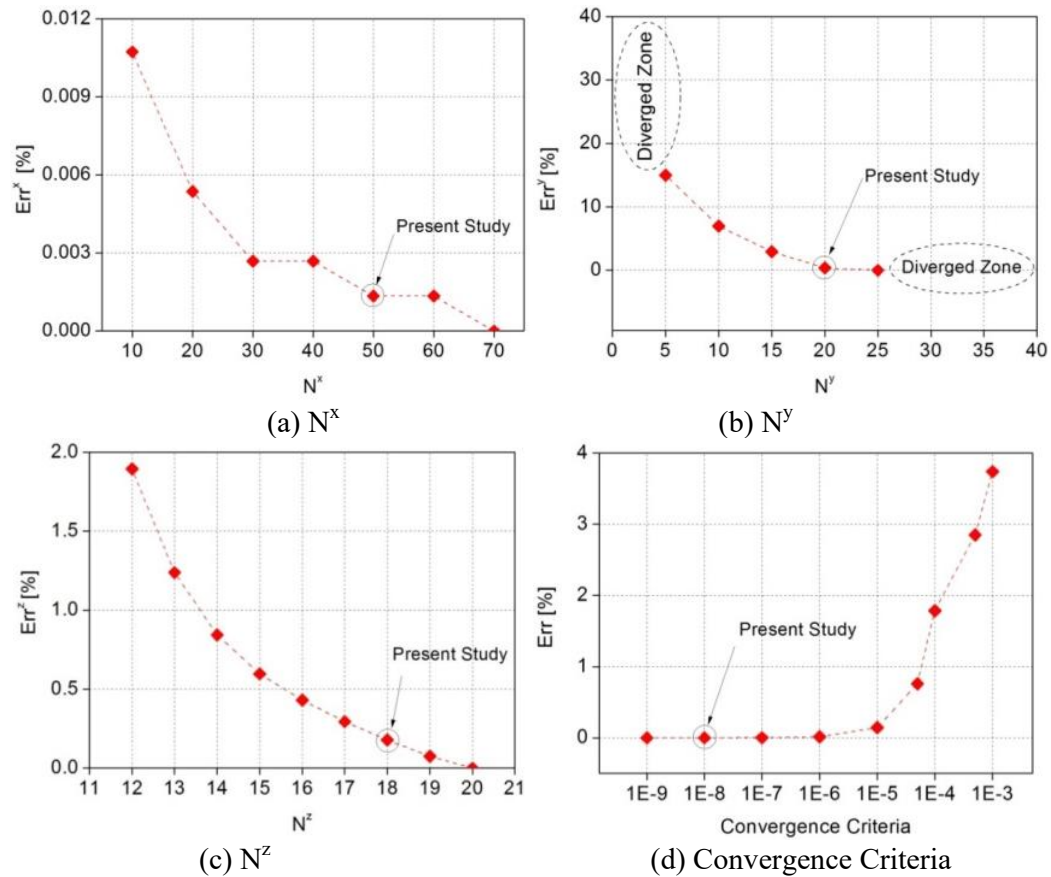
**Fig. 44**. Determination of the grid numbers and convergence criteria: (a), (b) and (c) are the number of the grids for each cell component in x, y, and z directions, respectively; (d) is the convergence criteria for the residue.

## 5.4 Summary

In the chapter, a three-dimensional numerical model has been developed based on the electrochemical reactions and transport processes inside the associated CLs, GDLs, and flow channels at the anode and cathode separated by the membrane. Governing equations of continuity, momentum, gas species transport, electronic and protonic potential, liquid and membrane water, and energy are coupled with chemical reaction kinetics by introducing various sources terms. The dimensions of the fuel cell components, the pore structure of the porous media (GDLs and CLs), and mass transport properties such as permeability and effective diffusibility are experimentally determined. These experimental parameters are introduced into the two-fluid model, and the simulation results are validated with the experimental current-voltage (I-V) curves (i.e., polarization curves). The work done in this chapter will make the numerical modeling more relevant to the actual PEM fuel cell operation.

# Chapter 6
# Comparison and Numerical Results

The experimental results in aspects of component dimensions, pore structure characterization, effective diffusibility, and permeability are incorporated into the modeling. The simulation results are presented in terms of convective and diffusive oxygen fluxes. The dimensions of the porous media are measured using a micrometer, the porosity is investigated by the MSP, the permeability is determined by a custom-engineered apparatus based on Darcy's law, and the effective diffusibility is studied by the modified Loschmidt Cell based on Fick's law of diffusion.

Table 19 summarizes the major parameters measured and then used for the present model simulation. It should be noted that the thicknesses of the anodic and cathodic CLs are 8.6 and 34.0 μm, respectively. The thickness varies significantly, as the Pt loading in the anode and cathode is 0.1 and 0.4 mg·cm$^{-2}$, respectively, resulting in a significant difference in thickness, which is more realistic than many other studies in which the anode and cathode CLs are assumed identical (e.g., [128,140,163]). The permeability of the GDLs and CLs in the present study is 1.39×10$^{-13}$ and 1.6-2.18×10$^{-15}$ m$^2$, respectively, which are about 1-2 orders of magnitude smaller than those reported in literature (e.g., [98,125,130,131]). The diffusibility of the GDLs and CLs is 0.094 and 0.015-0.019, which are much smaller than the values determined by the Bruggeman's correlation (widely used in the previous modeling studies) as a function of the porosity of each porous cell component.

Table 19. Experimental data on pore structure characterization and mass transport properties.

| Parameter | Value | Unit | Experimental method or theory |
|---|---|---|---|
| Thickness of membrane | 25.0 | μm | Micrometer |
| Thickness of anode CL | 8.6 | μm | Micrometer |

| | | | |
|---|---|---|---|
| Thickness of cathode CL | 34.0 | μm | Micrometer |
| Thickness of anode and cathode GDLs | 221.6 | μm | Micrometer |
| Length of channel | 9.0 | cm | Ruler |
| Height of channel | 1.0 | mm | Ruler |
| Width of channel | 1.0 | mm | Ruler |
| Porosity of anode CL | 0.54 | -- | Standard porosimetry |
| Porosity of cathode CL | 0.40 | -- | Standard porosimetry |
| Porosity of GDL | 0.75 | -- | Standard porosimetry |
| Permeability of anode CL | $1.6 \times 10^{-15}$ | $m^2$ | Darcy's law |
| Permeability of cathode CL | $2.18 \times 10^{-15}$ | $m^2$ | Darcy's law |
| Permeability of GDL | $1.39 \times 10^{-13}$ | $m^2$ | Darcy's law |
| Effective diffusibility of anode CL | 0.019 | -- | Loschmidt Cell (Fick's law) |
| Effective diffusibility of cathode CL | 0.015 | -- | Loschmidt Cell (Fick's law) |
| Effective diffusibility of GDL | 0.094 | -- | Loschmidt Cell (Fick's law) |

Note: CL and GDL denote the catalyst layer and gas diffusion layer, respectively.

## 6.1 Comparison with Experimental Results

With the above-determined mass transport properties, the current-density-voltage relation and power-density-voltage relation are simulated at various output voltages. **Fig. 45** compares the simulated polarization and power density curves with the experimental data under the identical operating conditions The *in-situ* experiment is conducted for the PEM fuel cell of an active area of 45 $cm^2$ with the cathode and anode Pt loadings of 0.4 and 0.1 mg·$cm^{-2}$, respectively. The cell performance is tested under the conditions: cell temperature of 75°C, cell backpressure of 35 kPag, and fully-humidified air and hydrogen with the flow rates of 9.00 and 4.45 slpm for the entire cell. The experimental data has been reported in our previous studies [11]. The simulated results exhibit a good agreement with the experimental data, which may be attributed to the experimentally determined pore structure characterization and mass transport properties, and indicates that the model is reasonably validated with good accuracy.
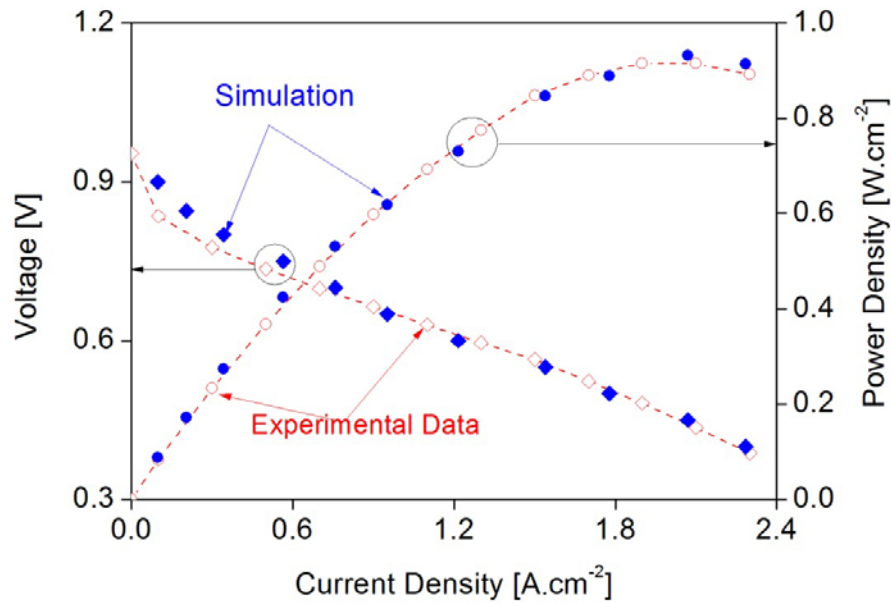
**Fig. 45.** Comparison of the simulation and experimental data on the polarization curve and power density. Cell temperature: 75°C; cell backpressure: 35 kPag; humidified air and hydrogen.

## 6.2 Local Oxygen Flux

The local oxygen flux in the fluid zones (i.e., the cathode channel, GDL, and CL) can be affected by various parameters such as the pressure gradient and oxygen concentration gradient, which are extremely difficult to be determined by experimental means.

### 6.2.1 Effect of Current Density

The average current density of the cell is associated with the electrochemical reaction rate, which determines the rates of the oxygen consumption as well as water production, thus influencing the internal pressure and oxygen distribution within the PEM fuel cells. Therefore, the current density may significantly affect the oxygen transport phenomena within the PEM fuel cells. The x- and y-direction oxygen mass fluxes along the central line in the cathode channel, GDL, and CL is discussed, while the z-component flux is ignored, as the z-component flux (smaller than $10^{-11}$ kg·m$^{-2}$·s$^{-1}$) is negligibly small, which is at least five to six orders of magnitude smaller than its x- and y-directional counterparts.

(a) Convective mass flux of oxygen        (b) Diffusive mass flux of oxygen
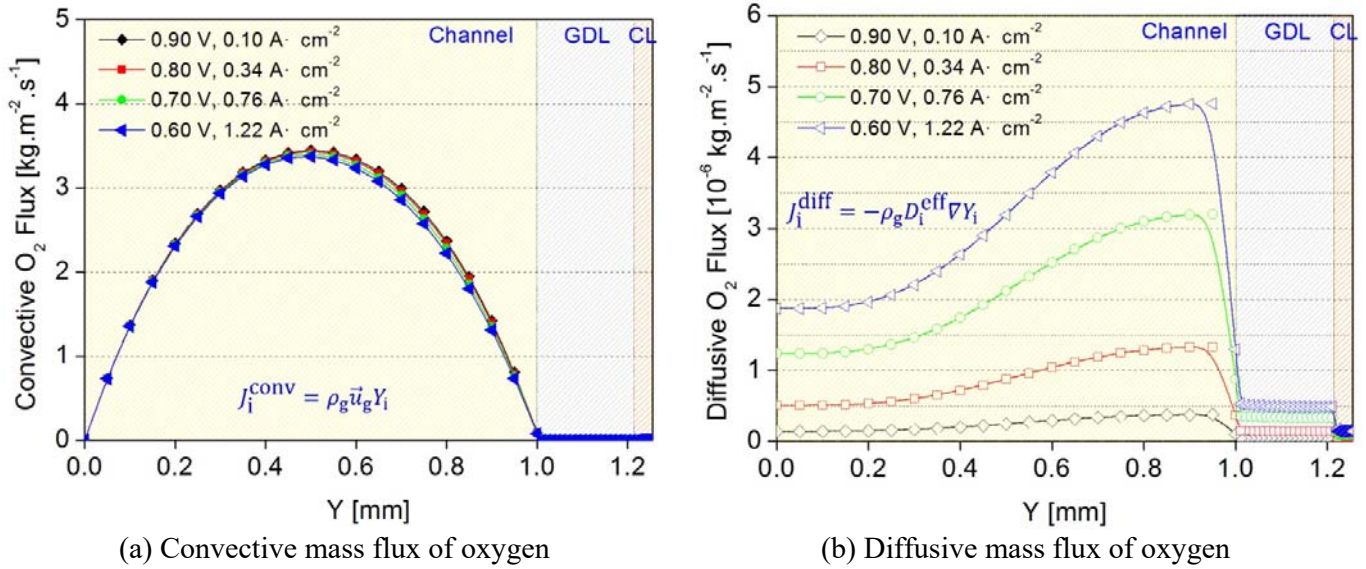
**Fig. 46.** Local (a) convective and (b) diffusive mass fluxes of oxygen in x direction (stream-wise direction) at the center (x = 50% channel length) of the cathode channel, gas diffusion layer and catalyst layer under the various average cell current densities corresponding to the various given cell voltages.

**Fig. 46** presents the local convective and diffusive mass fluxes of oxygen in the x direction (i.e., the stream-wise direction) at the center (x = 50% channel length) of the cathodic channel, GDL, and CL under various output voltages and current densities. It is found that the x-component diffusive oxygen flux is of the order of $10^{-6}$ kg·m$^{-2}$·s$^{-1}$, which is almost negligible in comparison with its convective counterpart, which is of the order of $10^{0}$ kg·m$^{-2}$·s$^{-1}$. In other words, the convective oxygen flux in stream-wise direction dominates in the cathodic flow channel.

(a) Convective mass flux of oxygen



(b) Diffusive mass flux of oxygen
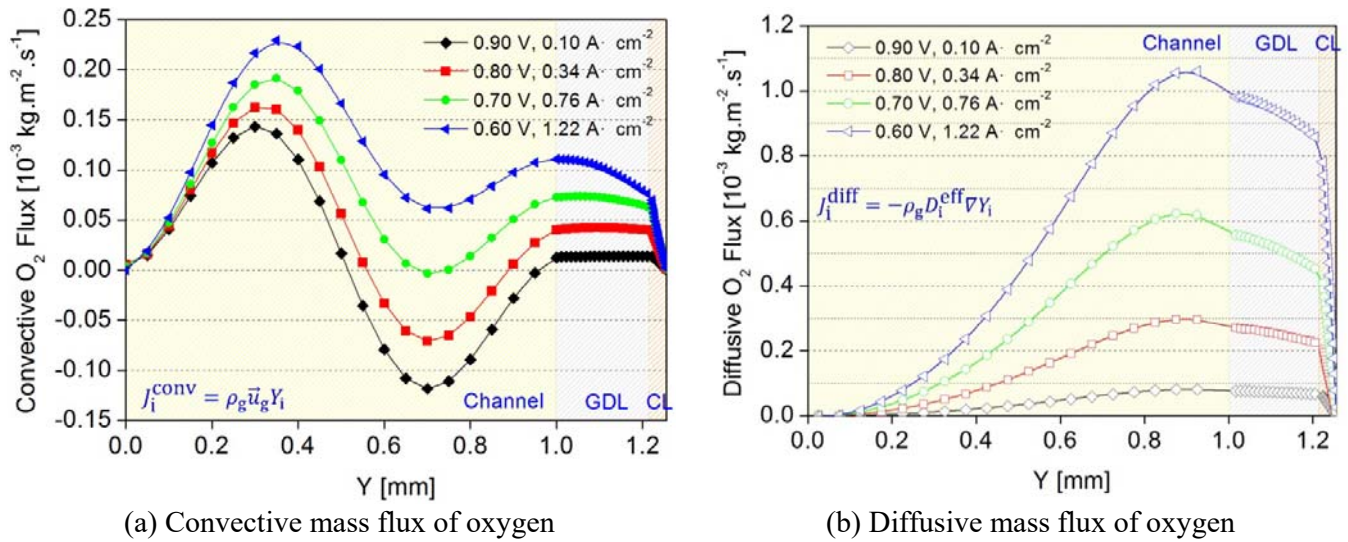
**Fig. 47.** Local (a) convective and (b) diffusive mass fluxes of oxygen in y (through-plane) direction at the center (x = 50% channel length) of the cathode for the various average cell current densities corresponding to the various given cell voltages.

**Fig. 47** indicates the local oxygen mass fluxes due to convection and diffusion in the y-direction (i.e., through-plane direction) at the shared central line (x = 50% channel length) of the cathode channel, GDL, and CL under various current densities. The y-component oxygen flux is of great significance in PEM fuel cells as it represents the amount of oxygen transported from the channel toward the reaction region (i.e., the CL) during the cell operation. Under small current densities (e.g., 0.10 and 0.34 A·cm$^{-2}$), a negative convective flux can be found in the channel (see **Fig. 47 (a)**), which indicates that the oxygen may be convectively carried from the GDL to the channel center due to the boundary layer effect. Under the high current density (e.g., 1.22 A·cm$^{-2}$), all convective fluxes are from the channel toward the CL, this is probably due to the resulted high rate of oxygen consumption, creating a lower pressure in the CL (see **Fig. 48 (a)** and **Fig. 49 (a)**), which drags the bulk air in. It can be seen that the boundary layer near the porous layer negatively affects the transport of the oxygen, and the effect of the boundary layer is more evident when the current density is small. The results also suggest that if measures can be taken to force the reactants to flow toward the CL, the mass transport can be likely improved [166].
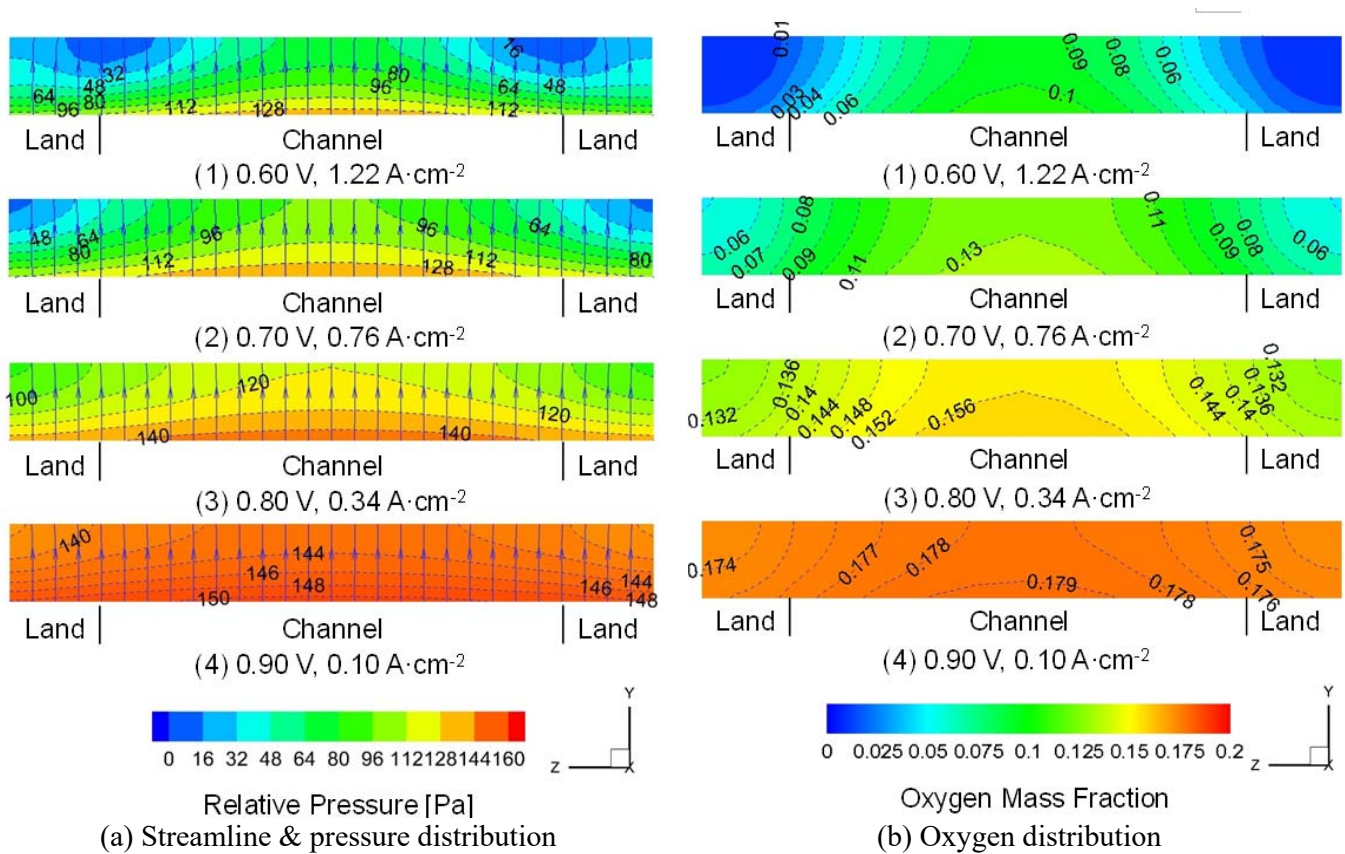
**Fig. 48.** (a) Streamline & pressure distribution and (b) oxygen distribution in the cathode catalyst layer at the various average cell current densities corresponding to the various given cell voltages: (cross-section parallel to the y-z plane at x = 50% channel length).

For the diffusive oxygen fluxes (see **Fig. 47 (b)**), the oxygen transport rate is the highest near the channel-GDL interface. Generally, the diffusive flux is increased with the increased current density, since a larger rate of electrochemical reactions indicates a higher rate of oxygen consumption, which causes a depletion of oxygen in the CL. Therefore, under high current densities, the oxygen concentration difference between the channel and CL is larger than that under smaller current densities as shown in **Fig. 48 (b)**. The large concentration difference thus results in a high diffusive oxygen flux under high-current-density operations as shown in **Fig. 47 (b)**. At constant current densities, the diffusive flux in the GDL decreases slightly as the oxygen approaches the CL. Further, the diffusive flux in the CL drops quickly as the oxygen travels toward the membrane interface. The rapid drop of the diffusive oxygen flux in the CL is attributed to the fast oxygen consumption during the cell operation

through electrochemical reactions. The rapid oxygen consumption causes the oxygen concentration to be maintained at a relatively low level (e.g., 1-10% under the current density of 0.10 A·cm⁻²) in the CL as shown in **Fig. 48 (b)**, generating a large oxygen concentration gradient in the CL (see **Fig. 48 (b)**) and GDL (see **Fig. 49 (b)**).



(a) Flow field & pressure distribution

(b) Oxygen distribution
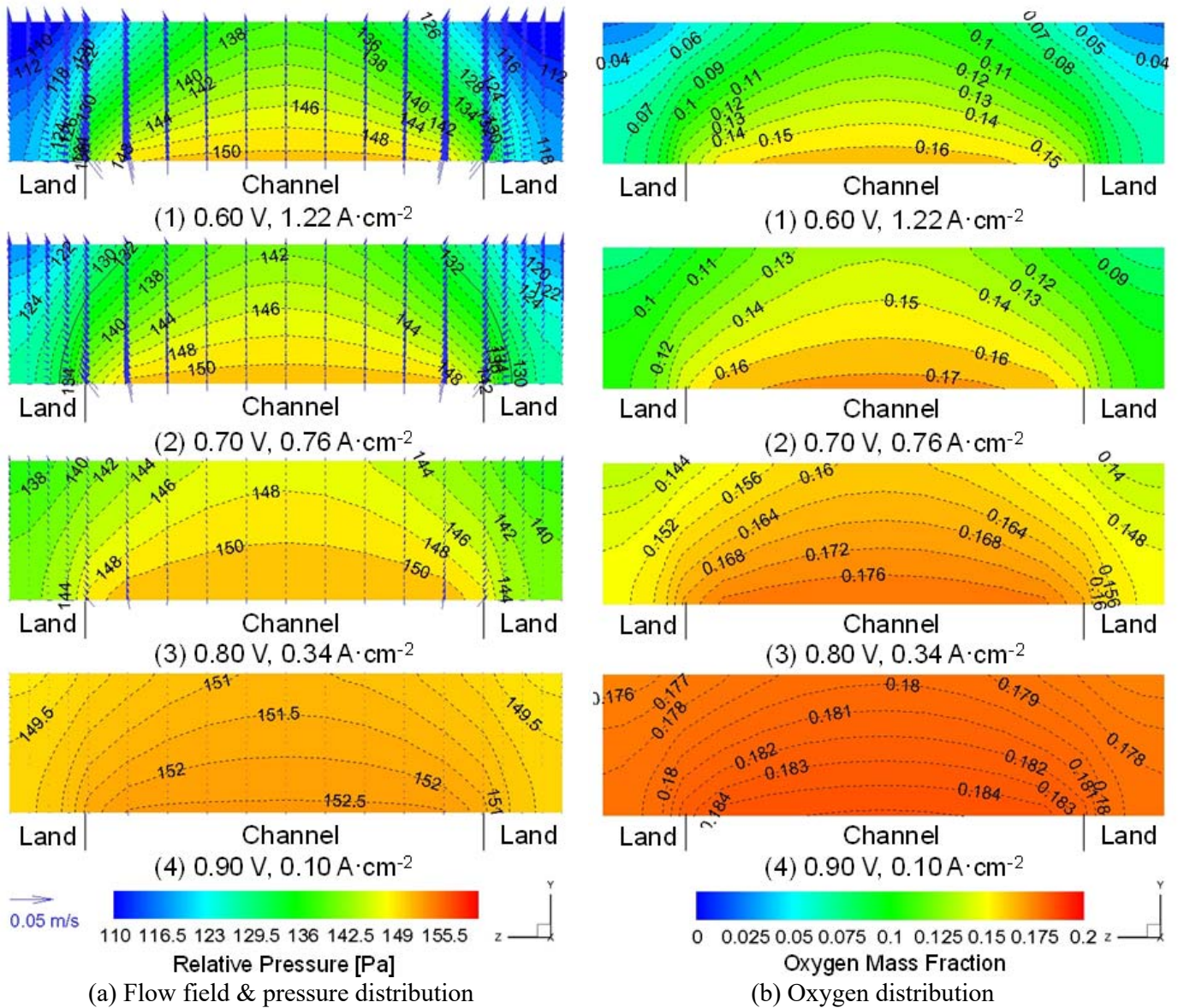
**Fig. 49.** (a) Velocity field & pressure distribution and (b) oxygen distribution in the cathode gas diffusion layer at the various average cell current densities corresponding to the various given cell voltages: (cross-section parallel to the y-z plane at x = 50% channel length).

## 6.2.2 Effect of Stream-wise Location

As the channel length is about 90 times longer than the channel width and height, the pressure and oxygen concentration at the different stream-wise locations may vary significantly due to the electrochemical reactions and pressure drop in the channel along the stream-wise direction. Therefore, it is necessary to study the effect of stream-wise locations on the mass transport phenomenon inside the PEM fuel cells. The case of 0.76 A·cm$^{-2}$ is presented as representative.



(a) Convective oxygen mass flux          (b) Diffusive oxygen mass flux
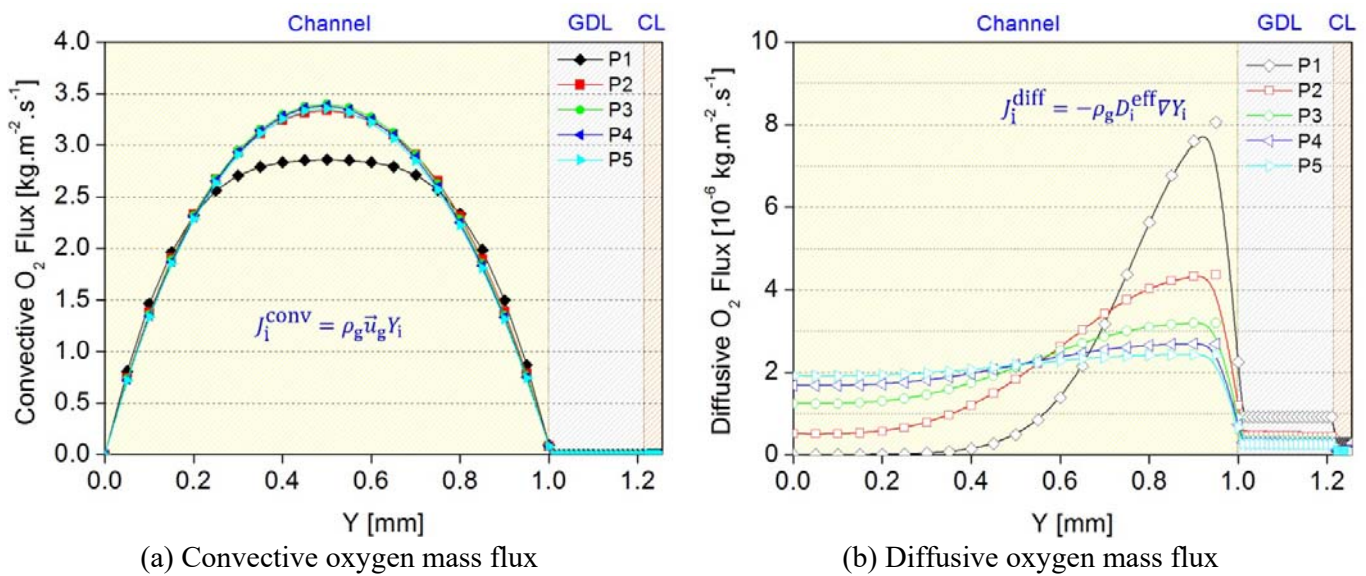
**Fig. 50.** Local convective (a) and diffusive (b) mass fluxes of oxygen in the x direction (stream-wise direction) at the different stream-wise locations in the cathode channel, gas diffusion layer and catalyst layer under the average cell current density of 0.76 A·cm$^{-2}$: P1-5 represent the locations of 10%, 30%, 50%, 70% and 90% of the channel length downstream of the channel inlet.

**Fig. 50 (a)** and **(b)** show the x-component convective and diffusive oxygen mass fluxes at the different stream-wise locations in the cathode channel, GDL, and CL under the current density of 0.76 A·cm$^{-2}$. It is seen that the diffusive oxygen flux is in the order of 10$^{-6}$ kg·m$^{-2}$·s$^{-1}$, which is much lower than its convective counterpart (in the order of 1 kg·m$^{-2}$·s$^{-1}$). Near the channel inlet, e.g., at the location P1 which is 10% of the channel length downstream of the inlet, the flow has not been fully developed, the x-directional (or stream-wise) convective mass flux near the channel

center is smaller than those at other locations as shown in **Fig. 50 (a)**. When the stream-wise location is sufficiently far away from the inlet, e.g., P2-5, the x-component oxygen flux, which is closely related to the x-direction velocity according to **Eq. (5.15),** exhibits almost the same profile as shown in **Fig. 50 (a)**. It is also observed that the convective flux in GDL and CL is almost negligible.



(a) Convective oxygen mass flux



(b) Diffusive oxygen mass flux
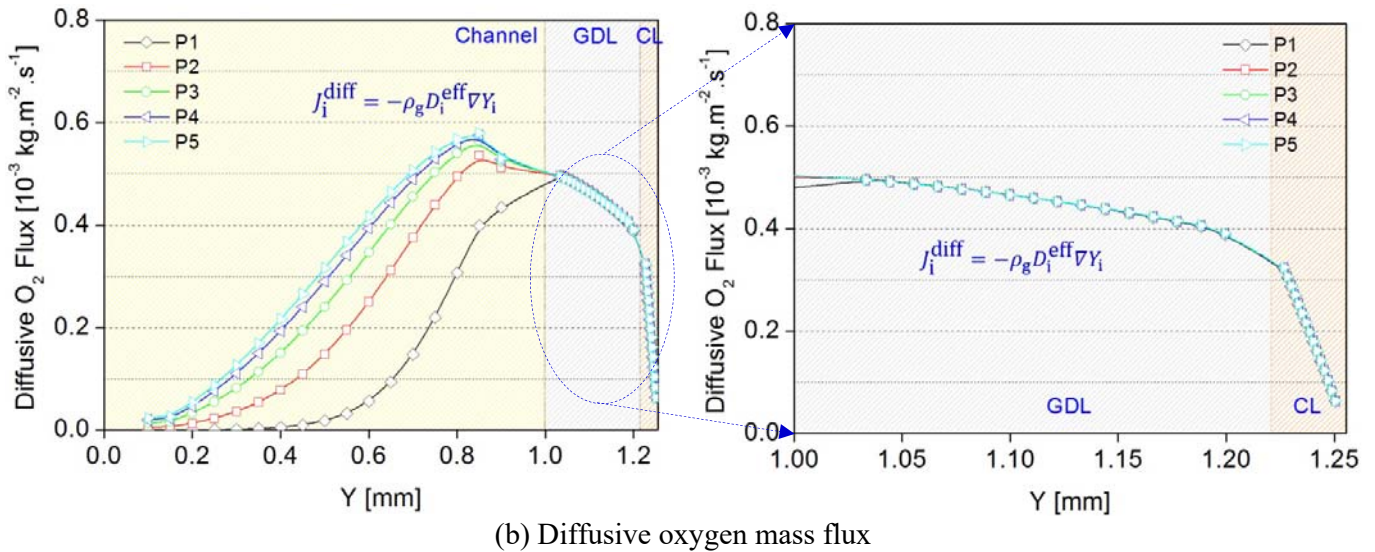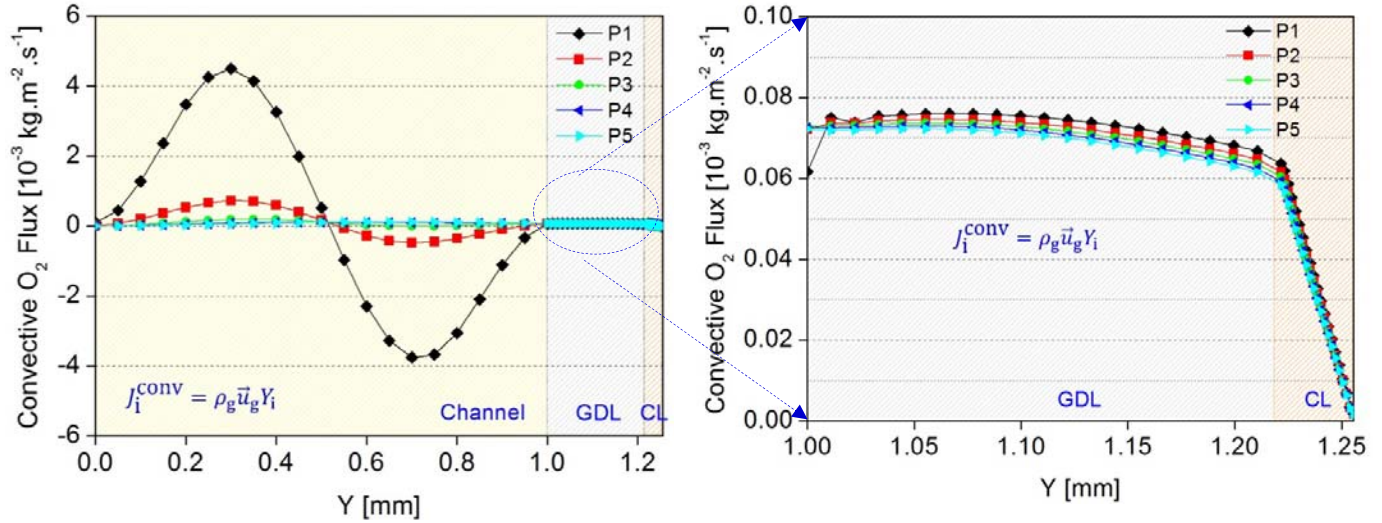
**Fig. 51.** Local (a) convective and (b) diffusive mass fluxes of oxygen in the y direction (through-plane direction) at the different stream-wise locations in the cathode channel, gas diffusion layer and catalyst layer under the average cell current

density of 0.76 A·cm$^{-2}$: P1-5 represent the locations of 10%, 30%, 50%, 70% and 90% of the channel length downstream of the channel inlet.

**Fig. 51** exhibits the y-component (through-plane) local convective and diffusive mass fluxes of oxygen at the different stream-wise locations in the cathode channel, GDL, and CL under the current density of 0.76 A·cm$^{-2}$. It is found that near the inlet, the y-component convective oxygen flux is significant, and this is mainly because the gas flow has not been fully developed yet, as can be seen in **Fig. 52**. In the GDL and CL, the convective oxygen flux is about one to two orders of magnitude lower than that in the channel; however, it is slightly affected by the stream-wise locations (see **Fig. 51 (a)**). The very small convective oxygen flux in the porous electrode (i.e., GDL and CL) is due to the very small gas permeability, which indicates a very large resistance for the convective flow in comparison with that in the flow channel, as shown in **Fig. 52** (a). On the other hand, the diffusive oxygen flux in the porous media seems less affected by the stream-wise locations as the oxygen concentration in the porous electrode does not change much along the stream-wise direction (see **Fig. 52** (b)), leading to similar local reaction rates (see **Fig. 52** (c)). Due to the similar reaction rates in the CL and the similar oxygen concentration in the channel, the local oxygen fluxes from channel to CL at different stream-wise locations is almost the same (see **Fig. 51**). It should be noted that in the flow channel, the y direction (through-plane) diffusive flux varies dramatically at different locations (see **Fig. 51** (b)), because the oxygen concentration in the channel has been reduced noticeably along the stream-wise direction as the electrochemical reaction proceeds (see **Fig. 52** (b)).

10% L    30% L    50% L    70% L    90% L

Anode

Cathode

y
z    x

0   2   4   6   8   10   12   14
Velocity [m/s]

10 m/s

(a) Velocity field

Cathode channel

Cathode gas diffusion layer

Cathode catalyst layer

0   0.03   0.06   0.09   0.12   0.15   0.18
Oxygen Mass Fraction

20 m/s
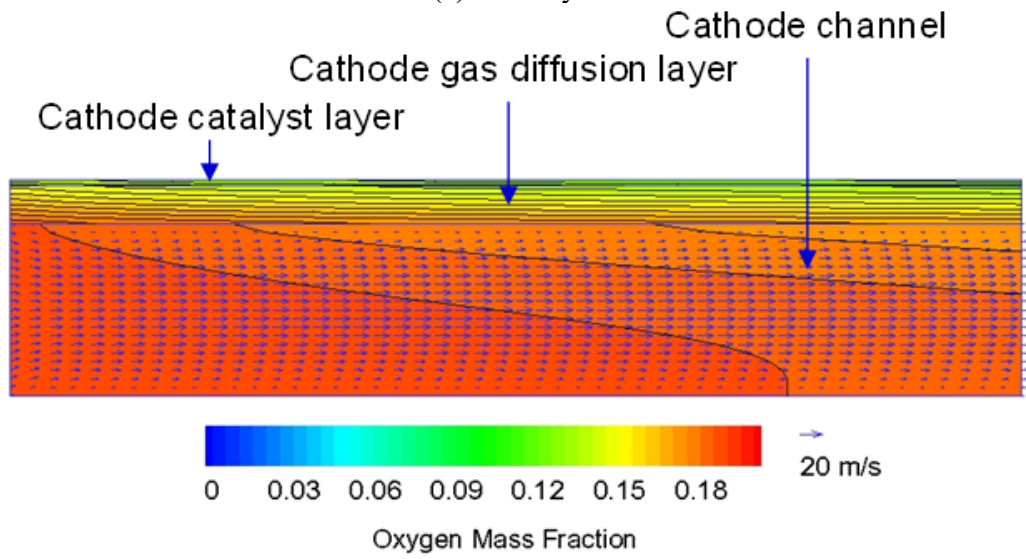
(b) Oxygen distribution

(c) Local reaction rates in cathode catalyst layer

**Fig. 52.** (a) Velocity field, (b) oxygen distribution and (c) local reaction rates at the average cell current density of 0.76 A·cm$^{-2}$: (cross-sections parallel to the y-z plane located at the 10%, 30%, 50%, 70% and 90% of the channel length downstream of the channel inlet).

## 6.3 Average Oxygen Flux

The average oxygen flux from the channel toward the reaction sites is of great significance for the PEM fuel cell operation. The major mass transport resistance comes from the porous media; therefore, it is of great significance to investigate the average oxygen mass flux in the porous electrode.



(a) 0.60V, 1.22 A·cm$^{-2}$         (b) 0.70V, 0.76 A·cm$^{-2}$

(c) 0.80V, 0.34 A·cm$^{-2}$           (d) 0.90V, 0.10 A·cm$^{-2}$
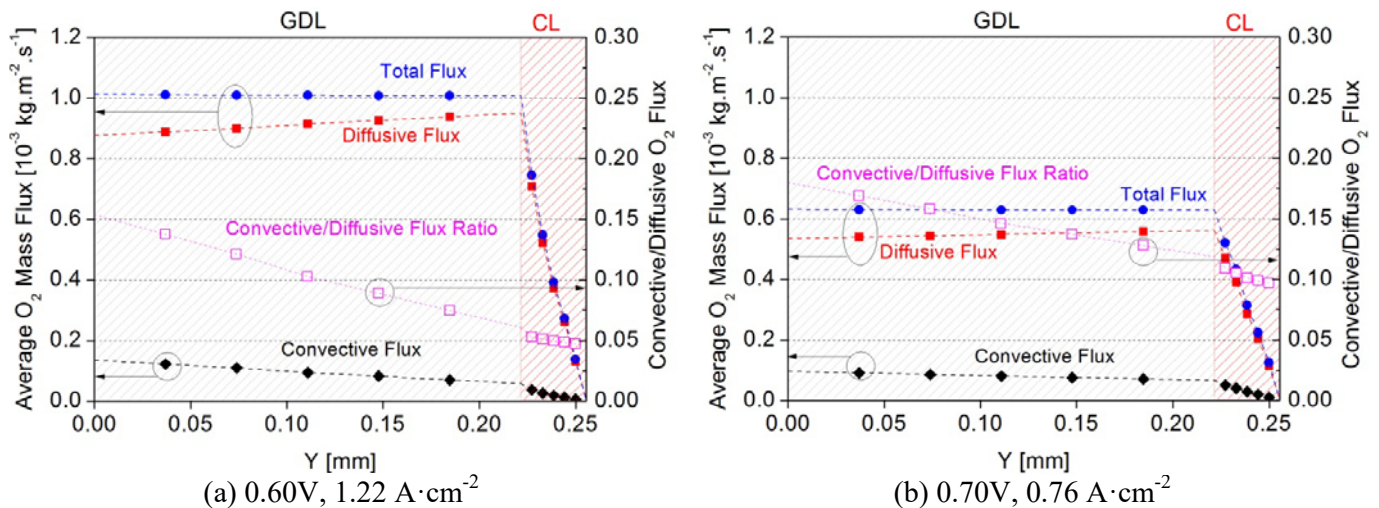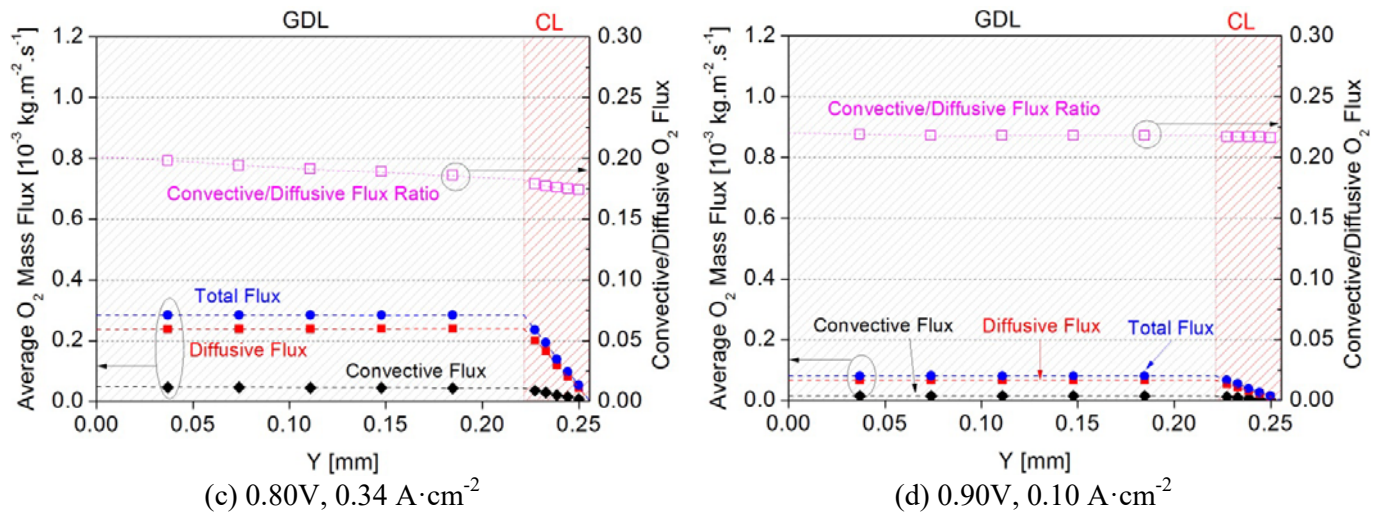
**Fig. 53.** Area-weighted average oxygen fluxes through the cross sections parallel to x-z plane in cathode gas diffusion layer and catalyst layer at the different average cell current densities of (a) 1.22 A·cm$^{-2}$, (b) 0.76 A·cm$^{-2}$, (c) 0.34 A·cm$^{-2}$ and (d) 0.10 A·cm$^{-2}$, respectively.

**Fig. 53** shows the area-weighted average oxygen mass fluxes through the cross sections parallel to x-z plane in the cathode GDL and CL at the various current densities. It is found that for a given current density, the total average oxygen flux in the GDL is constant along the y-direction toward the CL, while that in the CL is gradually reduced when the oxygen is approaching the membrane because the oxygen is consumed throughout the CL. The convective flux in the entire electrode is about 5-20% of the diffusive counterpart. Under the small current densities (e.g., 0.10 A·cm$^{-2}$), the total average flux in the GDL is relatively low ($8.07 \times 10^{-5}$ kg·m$^{-2}$·s$^{-1}$), and the ratio of the convective to the diffusive flux is maintained at a high level of ~22%, indicating that the convective mass transfer in the porous electrode is not negligible (see **Fig. 53** (d)). It can be seen from **Fig. 54** (d) and **Fig. 55** (d) that the oxygen concentration in both CL and GDL is relatively uniform at a high level (17.5-18.0%), thereby generating a small diffusive flux. Similarly, the pressure gradient in the porous CL (see **Fig. 48** (a)**)** and GDL (see **Fig. 49** (a)) is relatively small, generating a small convection in the porous media.

(a) 0.60V, 1.22 A·cm⁻²

(b) 0.70V, 0.76 A·cm⁻²

(c) 0.80V, 0.34 A·cm⁻²

(d) 0.90V, 0.10 A·cm⁻²
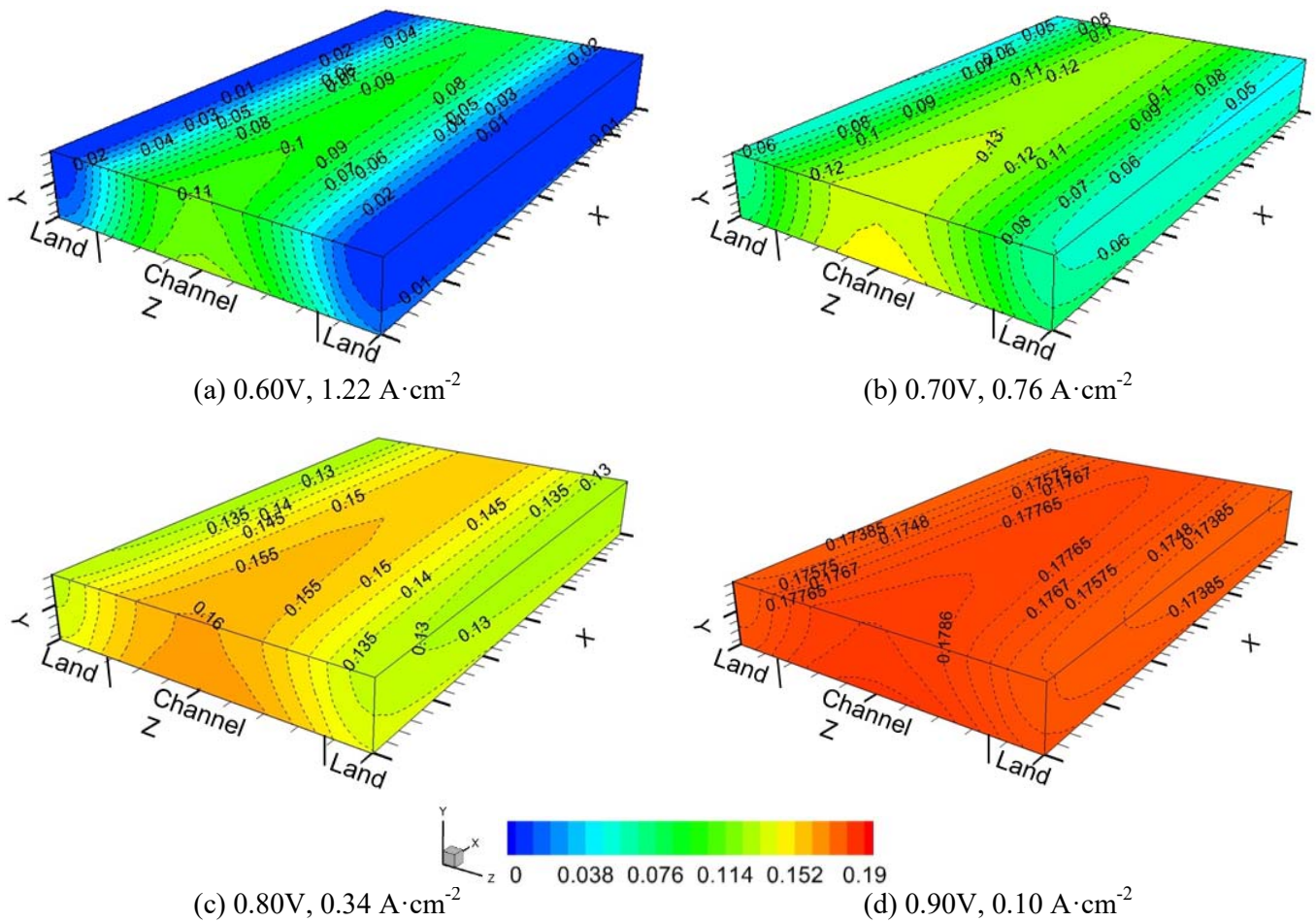
**Fig. 54.** Oxygen mass fraction in the cathode catalyst layer at the different current densities of (a) 1.22 A· Pressure cm⁻², (b) 0.76 A·cm⁻², (c) 0.34 A·cm⁻² and (d) 0.10 A·cm⁻², respectively.

However, as the current density is increased (e.g., 1.22 A·cm⁻²), the total flux in the GDL can be as high as $1.01 \times 10^{-3}$ kg·m⁻²·s⁻¹, and the convective flux is relatively small and is only about 5-14% of the diffusive flux, depending on the closeness to the membrane. It is interesting to find that the convective transport of the oxygen toward the membrane is more difficult in the CL at high current densities (see **Fig. 53** (a)), and the diffusive flux dominates in the GDL and CL. This is mainly because the oxygen concentration is extremely low in the CL (see **Fig. 54** (a) and **Fig. 55** (a)) due to the rapid electrochemical reactions, generating a large oxygen concentration between the CL-membrane interface and the GDL-channel interface. The results indicate that if measures can be taken to enhance the convection inside the

porous media, e.g., the design of baffle plates in the flow channels [166], the oxygen supply under high current densities can be potentially improved.



(a) 0.60V, 1.22 A·cm$^{-2}$

(b) 0.70V, 0.76 A·cm$^{-2}$

(c) 0.80V, 0.34 A·cm$^{-2}$

(d) 0.90V, 0.10 A·cm$^{-2}$
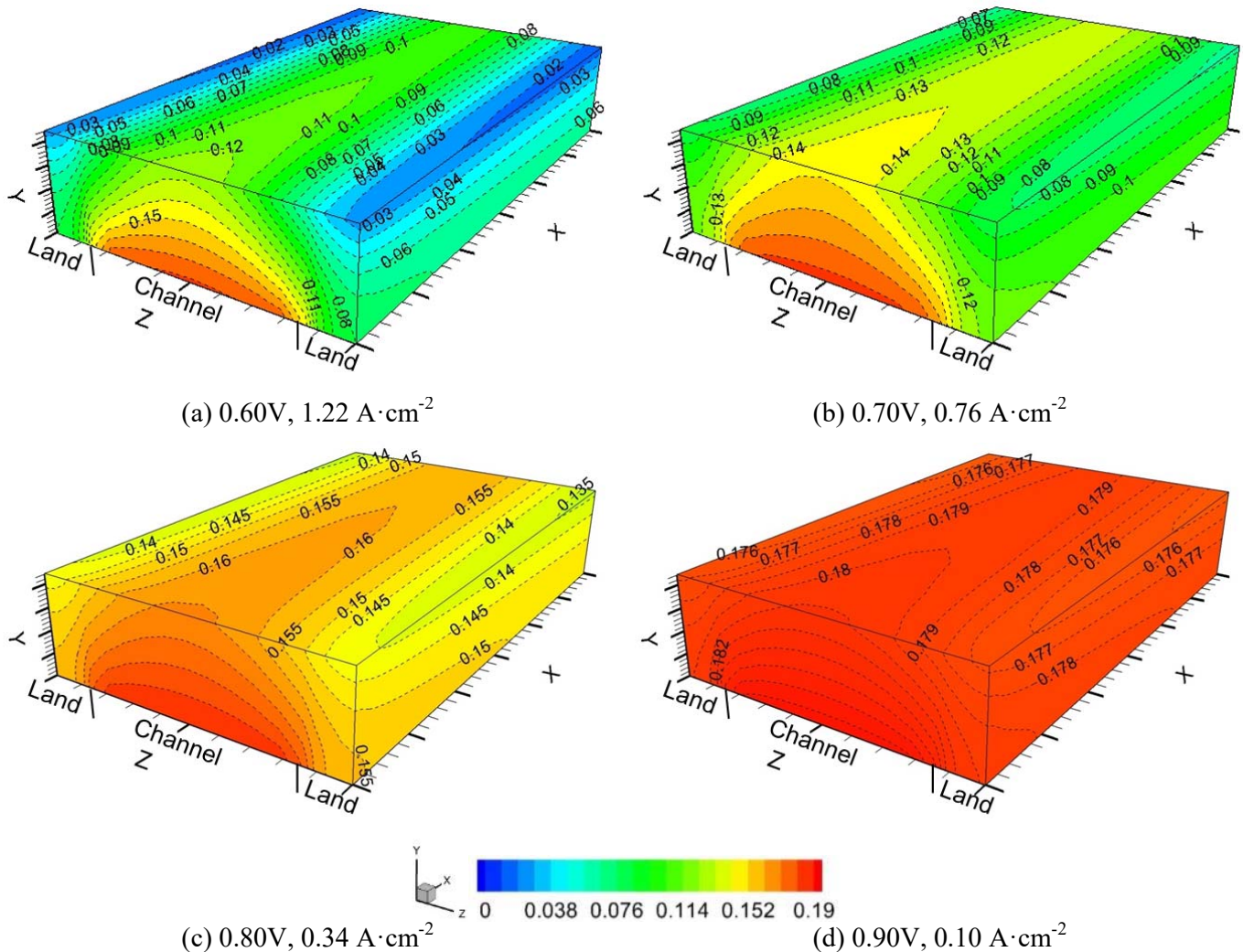
**Fig. 55.** Oxygen mass fraction in the cathode gas diffusion layer at the different current densities of (a) 1.22 A·cm$^{-2}$, (b) 0.76 A·cm$^{-2}$, (c) 0.34 A·cm$^{-2}$ and (d) 0.10 A·cm$^{-2}$, respectively.

## 6.4 Summary

In the present study, a three-dimensional numerical model for the polymer electrolyte membrane (PEM) fuel cells has been developed based on the electrochemical reactions and transport processes inside the associated catalyst layer (CL), gas

diffusion layers (GDL), and flow channel at the anode and cathode separated by the membrane. Governing equations of continuity, momentum, gas species transport, electronic and protonic potential, liquid and membrane water, and energy are coupled with chemical reaction kinetics by introducing various sources terms. The dimensions of the fuel cell components, the pore structure of the porous media (GDL and CL), and mass transport properties such as permeability and effective diffusibility are experimentally determined. These experimental parameters are introduced into the two-fluid model, and the simulation results are validated with the experimental current-voltage (I-V) curves (i.e., polarization curves). The experimental results indicate that permeability of the GDL and CL in the present study is $1.39 \times 10^{-13}$ and $2.18 \times 10^{-15}$ $m^2$, respectively, which are about 1-2 orders smaller than the reported data in the literature. The diffusibility of the GDLs and CLs is 0.094 and 0.014, which are much smaller than the values determined by the Bruggeman's correlation, which is widely used in the numerical simulation for PEM fuel cells. The simulation results based on these mass transport properties indicate that the local mass flux of oxygen is highly dependent on the average current density and the location inside the cell. Specifically, in the cathode electrode of the PEM fuel cell, the in-plane and stream-wise oxygen fluxes ($10^{-11} \sim 10^{-6}$ $kg \cdot m^{-2} \cdot s^{-1}$) are negligibly small in comparison with their through-plane counterpart ($\sim 10^{-3}$ $kg \cdot m^{-2} \cdot s^{-1}$). The average flux of convection can be as large as 20% of its diffusive counterpart at a small current density ($0.10$ $A \cdot cm^{-2}$), while the ratio of the convective to diffusive oxygen flux is reduced to as small as 5-14% under the large current density of 1.22 $A \cdot cm^{-2}$, indicating a potential for the performance improvement of the PEM fuel cells by enhancing the convection in GDL and CL.

# Chapter 7
# Conclusions and Future Work

In this research, a comprehensive understanding of the structure of catalyst layers (CLs) is investigated through experimental and numerical techniques. The experimental methods include the method of standard porosimetry (MSP), the Loschmidt Cell, permeability measurement, and cell performance testing. The MSP, which is established based on the phenomenon of the capillary equilibrium in porous media, is employed to characterize the structure of the CLs in terms of porosity, pore size distribution (PSD), pore surface area, mean pore size, and surface fractal dimension. The Loschmidt Cell, built based on the Fick's law of diffusion, is used to study the effective diffusion coefficient and the corresponding diffusion resistivity. The permeability measurement based on Darcy's law has been developed in this research to investigate the gas permeability and permeation resistivity. A commercially available automatic test station is used to test the fuel cell performance. With the measured parameters, the current two-fluid PEM fuel cell modeling has been improved, and a numerical study is performed to investigate the mass transport within the PEM fuel cells. The simulation work is focused on the convective and diffusive oxygen transport fluxes in the channels, gas diffusion layers (GDLs) and CLs.

## 7.1 Conclusions

In this research, experimental and numerical approaches are utilized to obtain a comprehensive understanding of the effect of CL fabrication process on the structure formation, the effect of CL structure on the CL macro-properties, and the effect of the structural and macro-properties on the mass transport phenomena and cell performance. The key conclusions from this research are

o   The structure of the CLs is determined by the fabrication process, and specifically, the catalyst loading, types of catalysts, and fabrication methods all have a decisive effect on the structure formation. For the constant Pt loading and the same type of

catalyst, the electrode prepared by the method of catalyst coated on membrane (CCM) presents a denser structure and larger geometric surface area than its counterpart prepared by the method of catalyst coated on GDL substrate (CCS). For the same electrode preparation method, as the Pt loading is increased, the electrodes tend to have smaller porosity but larger pore surface area.

o The presence of the CLs in the catalyzed electrodes is of great significance to the overall pore structure of the catalyzed electrodes. The pore size of the electrode has a wide range from a few nm to a few hundred μm. The pores smaller than 100 nm in the electrodes are increased with the increased Pt loading in comparison with the uncatalyzed GDL. These small pores contribute to 95.0-96.5% of the surface area even though their volume is less than 23% of the total pore volume.

o The effective diffusion coefficient of the GDLs, CLs, and electrodes can be measured by the Loschmidt Cell with an acceptable accuracy. The effective diffusibility of the GDLs, CLs, and electrodes is much smaller than the data reported in literature and the values determined by the Bruggeman's correlation (widely used in the current modeling studies) as a function of the porosity of each porous cell component.

o The gas permeability of the GDLs, CLs, and electrodes determined in the present thesis study is about 1-2 orders of magnitude smaller than the data widely employed for modeling in literature. In addition, a higher temperature results in a higher gas permeability value, although the enhancement is small within the temperature range tested (25–75 °C). Also, oxygen shows a slightly higher permeability value than air and nitrogen; however, the difference is within 5% for all cases because oxygen and nitrogen have similar molecular properties.

o The structure of the prepared CLs and electrodes by CCM and CCS methods has a significant impact on the mass transport properties and cell performance. The reduction in the porosity and the increase in the pore surface area due to the CCM methods are found to affect the mass transport negatively but the electrochemical performance positively in comparison of the CCS method. Such a trade-off relationship leads to significantly different cell performance characteristics. At high Pt loadings (e.g., 0.4 mg·cm$^{-2}$), the CCM and CCS electrodes yield comparable cell performance, while at low Pt loadings (e.g., 0.1 mg·cm$^{-2}$), the maximum power density of the CCS electrode deteriorates as much as 60% than that of CCM. Therefore, the method of catalyst coated on substrate (CCS) is not

suitable for the low-Pt-loading (e.g., 0.1 mg·cm$^{-2}$) electrodes unless the material penetration into the GDL void regions can be inhibited.

o The simulation results based on the 60% Pt/C catalysts with the Pt loading of 0.4 mg·cm$^{-2}$ indicate that the convective oxygen flux in the GDL and CL from the channel toward the membrane can be as large as 20% of the diffusive counterpart at the low current density (e.g., 0.10 A·cm$^{-2}$), while the ratio can be reduced to as low as 5-13% at the high current density region (e.g., 1.22 A·cm$^{-2}$). The results suggest that if measures can be taken to enhance the convection in the porous media under high current densities, the transport of oxygen to the reaction sites can be considerably improved.

## 7.2 Future Work

The experimental methods presented in this thesis can be further extended to characterize the CLs with various compositions by other fabrication techniques. The numerical methods can be continued if further *ex-situ* experimental data are collected. Future work for this research area can be summarized as follows:

o Many factors affect the structure of the CLs and the electrodes including the Pt loading, Pt/C, and fabrication methods, which is identified and quantitatively analyzed in the present thesis study. Some other parameters such as fabrication conditions, catalyst composition, novel catalyst or ionomer, and hot pressing may also significantly affect the structure of the CLs and hence the catalyzed electrodes. It would be interesting to investigate the effect of these parameters on the structure formation of the CLs.

o Fractal dimension of the CLs and electrodes has been identified as a good indicator of the complexity and uniformity of their structure. The fractal dimension theory has been identified as a good explanation of why the pore surface area of a specific porous material varies significantly due to the different measurement methods employed. It would be interesting to further investigate the relationship between the fractal dimension and the mass transport properties, such as the effective diffusion coefficient and permeability.

o The measured mass transport properties, such the effective diffusion coefficient and permeability, of the GDLs, CLs, and electrodes are much lower than the data reported and the values predicted by the empirical correlations in literature. It would be useful if a new empirical correlation can be developed specifically for the CLs, and the developed correlation will be useful for the numerical modeling of PEM fuel cells.

o Finally, if a comprehensive database of the pore structure characterization, mass transport properties, and cell performance can be established for different types of CLs, more numerical studies can be carried out. The mass transport and the cell performance can be better understood in the ultra-low-Pt-loading ($<0.1$ mg·cm$^{-2}$) PEM fuel cells, which is of great significance to the PEM fuel cell commercialization.

# References

[1]     Li X. Principles of Fuel Cells. New York: Taylor & Francis Group; 2006.

[2]     Zhao J, Shahgaldi S, Ozden A, Alaefour IE, Li X, Hamdullahpur F. Geometric pore surface area and fractal dimension of catalyzed electrodes in polymer electrolyte membrane fuel cells. Int J Energy Res 2018:1–9. doi:https://doi.org/10.1002/er.4260.

[3]     Zhao J, Shahgaldi S, Alaefour I, Yang S, Li X. Pore structure and effective diffusion coefficient of catalyzed electrodes in polymer electrolyte membrane fuel cells. Int J Hydrogen Energy 2018;43:3776–85. doi:10.1016/j.ijhydene.2018.01.019.

[4]     Ozden A, Shahgaldi S, Zhao J, Li X, Hamdullahpur F. Degradations in porous components of a proton exchange membrane fuel cell under freeze-thaw cycles : Morphology and microstructure effects. Int J Hydrogen Energy 2018:1–14. doi:10.1016/j.ijhydene.2018.10.209.

[5]     Zhao J, Shahgaldi S, Alaefour I, Xu Q, Li X. Gas permeability of catalyzed electrodes in polymer electrolyte membrane fuel cells. Appl Energy 2018;209:203–10. doi:10.1016/j.apenergy.2017.10.087.

[6]     Zhao J, Ozden A, Shahgaldi S, Alaefour IE, Li X, Hamdullahpur F. Effect of Pt loading and catalyst type on the pore structure of porous electrodes in polymer electrolyte membrane (PEM) fuel cells. Energy 2018;150:69–76. doi:10.1016/j.energy.2018.02.134.

[7]     Zhao J, Shahgaldi S, Li X, Liu Z (Simon). Experimental Observations of Microstructure Changes in the Catalyst Layers of Proton Exchange Membrane Fuel Cells under Wet-Dry Cycles. J Electrochem Soc 2018;165:F3337–45. doi:10.1149/2.0391806jes.

[8]     Shahgaldi S, Alaefour I, Zhao J, Li X. Impact of ionomer in the catalyst layers on proton exchange membrane fuel cell performance under different reactant flows and pressures. Fuel 2018;227:35–41. doi:10.1016/j.fuel.2018.04.076.

[9]     Xu Q, Zhang W, Zhao J, Xing L, Ma Q, Xu L, et al. Effect of air supply on the performance of an active direct methanol fuel cell (DMFC) fed with neat methanol. Int J Green Energy 2018;15:181–8.

doi:10.1080/15435075.2018.1431547.

[10] Ozden A, Shahgaldi S, Zhao J, Li X, Hamdullahpur F. Assessment of graphene as an alternative microporous layer material for proton exchange membrane fuel cells. Fuel 2018;215:726–34. doi:10.1016/j.fuel.2017.11.109.

[11] Shahgaldi S, Zhao J, Alaefour I, Li X. Investigation of catalytic vs reactant transport effect of catalyst layers on proton exchange membrane fuel cell performance. Fuel 2017;208:321–8. doi:10.1016/j.fuel.2017.07.035.

[12] Chang Y, Zhao J, Shahgaldi S, Qin Y, Yin Y, Li X. Modelling of mechanical microstructure changes in the catalyst layer of a polymer electrolyte membrane fuel cell. Int J Hydrogen Energy 2018:1–13. doi:10.1016/j.ijhydene.2018.10.157.

[13] U.S. Department of Energy Hydrogen and Fuel Cells Program. Record 17007: Fuel Cell System Cost - 2017 2017. http://www.hydrogen.energy.gov/program_records.html.

[14] Litster S, McLean G. PEM fuel cell electrodes. J Power Sources 2004;130:61–76. doi:10.1016/j.jpowsour.2003.12.055.

[15] Wang Y, Chen KS, Mishler J, Cho SC, Adroher XC. A review of polymer electrolyte membrane fuel cells: Technology, applications, and needs on fundamental research. Appl Energy 2011;88:981–1007. doi:10.1016/j.apenergy.2010.09.030.

[16] Kim S, Ahn BK, Mench MM. Physical degradation of membrane electrode assemblies undergoing freeze/thaw cycling: Diffusion media effects. J Power Sources 2008;179:140–6. doi:10.1016/j.jpowsour.2007.12.114.

[17] Lin Wang, Attila Husar, Tianhong Zhou HL. A parametric study of PEM fuel cell performances. Int J Hydrogen Energy 2003;28:1263–1272. doi:10.1016/S0360-3199(02)00284-7.

[18] Wu J, Yuan XZ, Martin JJ, Wang H, Zhang J, Shen J, et al. A review of PEM fuel cell durability: Degradation mechanisms and mitigation strategies. J Power Sources 2008;184:104–19. doi:10.1016/j.jpowsour.2008.06.006.

[19] Zhang J. PEM Fuel Cell Electrocatalysts and Catalyst Layers. London: Springer London; 2008.

[20] Taira H, Liu H. In-situ measurements of GDL effective permeability and

under-land cross-flow in a PEM fuel cell. Int J Hydrogen Energy 2012;37:13725–30.

[21] Park S, Popov BN. Effect of a GDL based on carbon paper or carbon cloth on PEM fuel cell performance. Fuel 2011;90:436–40. doi:10.1016/j.fuel.2010.09.003.

[22] Shojaeefard MH, Molaeimanesh GR, Nazemian M, Moqaddari MR. A review on microstructure reconstruction of PEM fuel cells porous electrodes for pore scale simulation. Int J Hydrogen Energy 2016;41:20276–93. doi:10.1016/j.ijhydene.2016.08.179.

[23] Li H, Tang Y, Wang Z, Shi Z, Wu S, Song D, et al. A review of water flooding issues in the proton exchange membrane fuel cell. J Power Sources 2008;178:103–17. doi:10.1016/j.jpowsour.2007.12.068.

[24] Park S, Popov BN. Effect of cathode GDL characteristics on mass transport in PEM fuel cells. Fuel 2009;88:2068–73. doi:10.1016/j.fuel.2009.06.020.

[25] Roohparvarzadeh S. Experimental Characterization of the Compressive Behaviour of Gas Diffusion Layers in PEM Fuel Cells. 2014.

[26] Ayyadurai SM, Choi Y-S, Ganesan P, Kumaraguru SP, Popov BN. Novel PEMFC Cathodes Prepared by Pulse Deposition. J Electrochem Soc 2007;154:B1063. doi:10.1149/1.2769264.

[27] Lamanna JM, Kandlikar SG. Determination of effective water vapor diffusion coefficient in pemfc gas diffusion layers. Int J Hydrogen Energy 2011;36:5021–9. doi:10.1016/j.ijhydene.2011.01.036.

[28] Serincan MF, Pasaogullari U. Mechanical behavior of the membrane during the polymer electrolyte fuel cell operation. J Power Sources 2011;196:1303–13. doi:10.1016/j.jpowsour.2010.06.045.

[29] Quick C, Ritzinger D, Lehnert W, Hartnig C. Characterization of water transport in gas diffusion media. J Power Sources 2009;190:110–20. doi:10.1016/j.jpowsour.2008.07.093.

[30] Das PK, Li X, Liu ZS. Effective transport coefficients in PEM fuel cell catalyst and gas diffusion layers: Beyond Bruggeman approximation. Appl Energy 2010;87:2785–96.

[31] Molaeimanesh GR, Saeidi Googarchin H, Qasemian Moqaddam A. Lattice

Boltzmann simulation of proton exchange membrane fuel cells – A review on opportunities and challenges. Int J Hydrogen Energy 2016;41:22221–45. doi:10.1016/j.ijhydene.2016.09.211.

[32] Friedmann R, Van Nguyen T. Optimization of the Microstructure of the Cathode Catalyst Layer of a PEMFC for Two-Phase Flow. J Electrochem Soc 2010;157:B260–5. doi:10.1149/1.3264628.

[33] Shahgaldi S, Ozden A, Li X, Hamdullahpur F. Cathode catalyst layer design with gradients of ionomer distribution for proton exchange membrane fuel cells. Energy Convers Manag 2018;171:1476–86. doi:10.1016/j.enconman.2018.06.078.

[34] Rong F, Huang C, Liu ZS, Song D, Wang Q. Microstructure changes in the catalyst layers of PEM fuel cells induced by load cycling. Part II. Simulation and understanding. J Power Sources 2008;175:712–23. doi:10.1016/j.jpowsour.2007.10.007.

[35] Passalacqua E, Lufrano F, Squadrito G, Patti A, Giorgi L. Nafion content in the catalyst layer of polymer electrolyte fuel cells: Effects on structure and performance. Electrochim Acta 2001;46:799–805. doi:10.1016/S0013-4686(00)00679-4.

[36] Arcot MP, Zheng K, McGrory J, Fowler MW, Pritzker MD. Investigation of catalyst layer defects in catalyst-coated membrane for PEMFC application: Non-destructive method. Int J Energy Res 2018;42:3615–32. doi:10.1002/er.4107.

[37] Ye L, Gao Y, Zhu S, Zheng JJP, Li P, Zheng JJP. A Pt content and pore structure gradient distributed catalyst layer to improve the PEMFC performance. Int J Hydrogen Energy 2017;42:7241–5. doi:10.1016/j.ijhydene.2016.11.002.

[38] Wilson M, Gottesfeld S. Thin-film catalyst layers for polymer electrolyte fuel cell electrodes. J Appl Electrochem 1992;22:1–7. doi:10.1007/BF01093004.

[39] Wee J-H, Lee K-Y, Kim SH. Fabrication methods for low-Pt-loading electrocatalysts in proton exchange membrane fuel cell systems. J Power Sources 2007;165:667–77. doi:10.1016/j.jpowsour.2006.12.051.

[40] Ticianelli EA, Derouin CR, Redondo A, Srinivasan S. Methods to Advance

Technology of Proton Exchange Membrane Fuel Cells. J Electrochem Soc 1983;135:2209–14. doi:10.1149/1.2096240.

[41] Cheng X, Yi B, Han M, Zhang J, Qiao Y, Yu J. Investigation of platinum utilization and morphology in catalyst layer of polymer electrolyte fuel cells. J Power Sources 1999;79:75–81. doi:10.1016/S0378-7753(99)00046-4.

[42] Rabat H, Brault P. Plasma sputtering deposition of PEMFC porous carbon platinum electrodes. Fuel Cells 2008;8:81–6. doi:10.1002/fuce.200700036.

[43] Saha MS, Gullá AF, Allen RJ, Mukerjee S. High performance polymer electrolyte fuel cells with ultra-low Pt loading electrodes prepared by dual ion-beam assisted deposition. Electrochim Acta 2006;51:4680–92. doi:10.1016/j.electacta.2006.01.006.

[44] Rong F, Huang C, Liu ZS, Song D, Wang Q. Microstructure changes in the catalyst layers of PEM fuel cells induced by load cycling. Part I. Mechanical model. J Power Sources 2008;175:699–711. doi:10.1016/j.jpowsour.2007.10.006.

[45] Chung CG, Kim L, Sung YW, Lee J, Chung JS. Degradation mechanism of electrocatalyst during long-term operation of PEMFC. Int J Hydrogen Energy 2009;34:8974–81. doi:10.1016/j.ijhydene.2009.08.094.

[46] Gode P, Jaouen F, Lindbergh G, Lundblad A, Sundholm G. Influence of the composition on the structure and electrochemical characteristics of the PEFC cathode. Electrochim Acta 2003;48:4175–87. doi:10.1016/S0013-4686(03)00603-0.

[47] Pollet BG, Goh JTE. The importance of ultrasonic parameters in the preparation of fuel cell catalyst inks. Electrochim Acta 2014;128:292–303. doi:10.1016/j.electacta.2013.09.160.

[48] Bonifácio RN, Paschoal JOA, Linardi M, Cuenca R. Catalyst layer optimization by surface tension control during ink formulation of membrane electrode assemblies in proton exchange membrane fuel cell. J Power Sources 2011;196:4680–5. doi:10.1016/j.jpowsour.2011.01.010.

[49] Hongsirikarn K, Mo X, Liu Z, Goodwin JG. Prediction of the effective conductivity of Nafion in the catalyst layer of a proton exchange membrane fuel cell. J Power Sources 2010;195:5493–500.

doi:10.1016/j.jpowsour.2010.03.074.

[50] Song JM, Cha SY, Lee WM. Optimal composition of polymer electrolyte fuel cell electrodes determined by the AC impedance method. J Power Sources 2001;94:78–84. doi:10.1016/S0378-7753(00)00629-7.

[51] Xiong L, Manthiram A. High performance membrane-electrode assemblies with ultra-low Pt loading for proton exchange membrane fuel cells. Electrochim Acta 2005;50:3200–4. doi:10.1016/j.electacta.2004.11.049.

[52] Saha MS, Paul D, Malevich D, Peppley B, Karan K. Preparation of Ultra-Thin Catalyst Layers by Piezo-electric Printer for PEMFCs Applications. ECS Trans 2009;25:2049–59. doi:10.1149/1.3210761.

[53] Lee SJ, Mukerjee S, Mcbreen J, Rho YW, Kho YT, Lee TH. Effects of Nafion impregnation on performances of PEMFC electrodes. Electrochim Acta 1998;43:3693–701. doi:10.1016/S0013-4686(98)00127-3.

[54] Gamburzev S, Appleby AJ. Recent progress in performance improvement of the proton exchange membrane fuel cell (PEMFC). J Power Sources 2002;107:5–12. doi:10.1016/S0378-7753(01)00970-3.

[55] Qi Z, Kaufman A. Low Pt loading high performance cathodes for PEM fuel cells. J Power Sources 2003;113:37–43. doi:10.1016/S0378-7753(02)00477-9.

[56] Sasikumar G, Ihm JW, Ryu H. Dependence of optimum Nafion content in catalyst layer on platinum loading. J Power Sources 2004;132:11–7. doi:10.1016/j.jpowsour.2003.12.060.

[57] Antolini E, Giorgi L, Pozio A, Passalacqua E. Influence of Nafion loading in the catalyst layer of gas-diffusion electrodes for PEFC. J Power Sources 1999;77:136–42. doi:10.1016/S0378-7753(98)00186-4.

[58] Barrio A, Parrondo J, Lombrana JI, Uresandi M, Mijangos F. Influence of manufacturing parameters on MEA and PEMFC performance. Int J Chem React Eng 2008;6.

[59] De Bruijn FA, Dam VAT, Janssen GJM. Review: Durability and degradation issues of PEM fuel cell components. Fuel Cells 2008;8:3–22. doi:10.1002/fuce.200700053.

[60] Huang DC, Yu PJ, Liu FJ, Huang SL, Hsueh KL, Chen YC, et al. Effect of dispersion solvent in catalyst ink on proton exchange membrane fuel cell

performance. Int J Electrochem Sci 2011;6:2551–65.
doi:10.1016/j.jiec.2008.10.002.

[61]    Jiao K, Li X. Water transport in polymer electrolyte membrane fuel cells. Prog
Energy Combust Sci 2011;37:221–91.

[62]    Hansen TW, Delariva AT, Challa SR, Datye AK. Sintering of Catalytic
Nanoparticles : Particle Migration or Ostwald Ripening ? Acc Chem Res
2013;46:1720–30.

[63]    Rouquerol J, Avnir D, Fairbridge CW, Everett DH, Haynes JH, Pernicone N, et
al. Recommendations for the characterization of porous solid. Pure Appl Chem
1994;66:1739–58.

[64]    Lastoskie C, Gubbins KE, Quirke N. Pore size distribution analysis of
microporous carbons: A density functional theory approach. J Phys Chem
1993;97:4786–96. doi:10.1021/j100120a035.

[65]    Volfkovich YM, Sosenkin VE, Bagotsky VS. Structural and wetting properties
of fuel cell components. J Power Sources 2010;195:5429–41.
doi:10.1016/j.jpowsour.2010.03.002.

[66]    Unsworth G, Dong L, Li X. Improved experimental method for measuring gas
diffusivity through thin porous media. Am Inst Chem Eng J 2013;59:1409–19.

[67]    Volfkovich YM, Sakars AV, Volinsky A a. Application of the standard
porosimetry method for nanomaterials. Int J Nanotechnol 2005;2:292–302.

[68]    Volfkovich YM, Bagotzky VS. The method of standard porosimetry. 1.
Principles and possibilities. J Power Sources 1994;48:327–38.

[69]    Volfkovich YM, Bagotzky VS. The method of standard porosimetry 2.
Investigation of the formation of porous structures. J Power Sources
1994;48:339–48.

[70]    Giesche H. Mercury porosimetry: A general (practical) overview. Part Part Syst
Charact 2006;23:9–19.

[71]    Drake LC. Pore-Size Distribution in Porous Materials. Ind Eng Chem
1949;41:780–5.

[72]    Abell A, Willis K, Lange D. Mercury Intrusion Porosimetry and Image
Analysis of Cement-Based Materials. J Colloid Interface Sci 1999;211:39–44.

[73]    Vol'fkovich YM, Sosenkin VE, Nikol'skaya NF, Kulova TL. Porous structure

and hydrophilic-hydrophobic properties of gas diffusion layers of the electrodes in proton-exchange membrane fuel cells. Russ J Electrochem 2008;44:278–85. doi:10.1134/S102319350803004X.

[74]   Zamel N, Li X, Becker J, Wiegmann A. Effect of liquid water on transport properties of the gas diffusion layer of polymer electrolyte membrane fuel cells. Int J Hydrogen Energy 2011;36:5466–78. doi:10.1016/j.ijhydene.2011.01.146.

[75]   Yan Z, Chen C, Fan P, Wang M. Pore Structure Characterization of Ten Typical Rocks in China. Electron J Geotech Eng 2015;20:479–94.

[76]   Gregg SJ, Sing KSW, Salzberg HW. Adsorption Surface Area and Porosity. J Electrochem Soc 1967;114:279C–279C.

[77]   Brunauer S, Emmett PH, Teller E. Adsorption of Gases in Multimolecular Layers. J Am Chem Soc 1938;60:309–19. doi:10.1021/ja01269a023.

[78]   Lee Y, Jeong J, Youn IJ, Lee WH. Modified liquid displacement method for determination of pore size distribution in porous membranes. J Memb Sci 1997;130:149–56.

[79]   Akshaya Jena KG. Liquid Extrusion Techniques For Pore Structure Evaluation Of Nonwovens. Int Nonwovens J 2003;12:45–53.

[80]   Dubinin MM, Plavnik GM. Microporous structures of carbonaceous adsorbents. Carbon N Y 1968;6:183–92.

[81]   Crank J. The mathematics of diffusion. New York: Oxford University Press; 1979.

[82]   Flückiger R, Freunberger SA, Kramer D, Wokaun A, Scherer GG, Büchi FN. Anisotropic, effective diffusivity of porous gas diffusion layer materials for PEFC. Electrochim Acta 2008;54:551–9. doi:10.1016/j.electacta.2008.07.034.

[83]   Zamel N, Li X. Effective transport properties for polymer electrolyte membrane fuel cells - With a focus on the gas diffusion layer. Prog Energy Combust Sci 2013;39:111–46.

[84]   Kong IM, Jung A, Kim YS, Kim MS. Numerical investigation on double gas diffusion backing layer functionalized on water removal in a proton exchange membrane fuel cell. Energy 2017;120:478–87. doi:10.1016/j.energy.2016.11.100.

[85]   Astrath NGC, Shen J, Song D, Rohling JH, Astrath FBG, Zhou J, et al. The
       effect of relative humidity on binary gas diffusion. J Phys Chem B
       2009;113:8369–74. doi:10.1021/jp900796w.

[86]   Chapman S, Cowling TG, Park D. The Mathematical Theory of Non-Uniform
       Gases. Am J Phys 1962;30:389–389. doi:10.1119/1.1942035.

[87]   Cussler EL. Multicomponent Diffusion. Elsevier; 2013.

[88]   Zamel N, Li X, Shen J. Correlation for the effective gas diffusion coefficient in
       carbon paper diffusion media. Energy and Fuels 2009;23:6070–8.

[89]   Mintani M. Geometric factor for diffusion in porous media. J Chem Eng Japan
       1984;17:441–3.

[90]   Marrero TR, Mason EA. Gaseous Diffusion Coefficients. J Phys Chem Ref
       Data 1972;1:3–118.

[91]   Shen J, Zhou J, Astrath NGC, Navessin T, Liu ZS, Lei C, et al. Measurement
       of effective gas diffusion coefficients of catalyst layers of PEM fuel cells with
       a Loschmidt diffusion cell. J Power Sources 2011;196:674–8.

[92]   Dong L. Accuracy Improvement for Measurement of Gas Diffusivity through
       Thin Porous Media. 2012.

[93]   Dullien FAL. Porous media: fluid transport and pore structure. New York:
       Academic Press; 1979.

[94]   Andisheh-Tadbir M, El Hannach M, Kjeang E, Bahrami M. An analytical
       relationship for calculating the effective diffusivity of micro-porous layers. Int
       J Hydrogen Energy 2015;40:10242–50. doi:10.1016/j.ijhydene.2015.06.067.

[95]   Satterfield, Charles N. Sherwood TK. The role of diffusion in catalysis.
       London: Reading, MA: Addison-Wesley; 1963.

[96]   Hirschfelder JO, Curtiss CF, Bird RB, Mayer MG. Molecular Theory of Gases
       and Liquids (Vol. 26). New York: Wiley; 1954.

[97]   Prausnitz JM, Benson PR. Effective collision diameters and correlation of some
       thermodynamic properties of solutions. Am Inst Chem Eng J 1959;5:301–3.
       doi:10.1002/aic.690050310.

[98]   Um S, Wang C, Chen K. Computational fluid dynamics modeling of proton
       exchange membrane fuel cells. J Electrochem Soc 2000;147:4485–4493.

[99]   Hong P, Xu L, Li J, Ouyang M. Modeling of membrane electrode assembly of

PEM fuel cell to analyze voltage losses inside. Energy 2017;139:277–88. doi:10.1016/j.energy.2017.07.163.

[100] Neale GH, Nader WK. Prediction of transport processes within porous media: Diffusive flow processes within an homogeneous swarm of spherical particles. Am Inst Chem Eng J 1973;19:112–119.

[101] Tomadakis MM, Sotirchos S V. Ordinary and transition regime diffusion in random fiber structures. Am Inst Chem Eng J 1993;39:397–412.

[102] Mezedur MM, Kaviany M, Moore W. Effect of pore structure, randomness and size on effective mass diffusivity. Am Inst Chem Eng J 2002;48:15–24.

[103] Bruggeman DAG. Berechnung verschiedener physikalischer Konstanten von heterogenen Substanzen. III. Die elastischen Konstanten der quasiisotropen Mischkorper aus isotropen Substanzen. Ann Phys 1937;421:160–78.

[104] Pollard WG, Present RD. On gaseous self-diffusion in long capillary tubes. Phys Rev 1948;73:762–74. doi:10.1103/PhysRev.73.762.

[105] Zeng Z, Grigg R. A criterion for non-darcy flow in porous media. Transp Porous Media 2006;63:57–69. doi:10.1111/j.1439-0523.2006.01169.x.

[106] Pant LM, Mitra SK, Secanell M. Absolute permeability and Knudsen diffusivity measurements in PEMFC gas diffusion layers and micro porous layers. J Power Sources 2012;206:153–60. doi:10.1016/J.JPOWSOUR.2012.01.099.

[107] Hussaini IS, Wang CY. Measurement of relative permeability of fuel cell diffusion media. J Power Sources 2010;195:3830–40.

[108] Ismail MS, Damjanovic T, Hughes K, Ingham DB, Ma L, Pourkashanian M, et al. Through-Plane Permeability for Untreated and PTFE-Treated Gas Diffusion Layers in Proton Exchange Membrane Fuel Cells. J Fuel Cell Sci Technol 2010;7:051016.

[109] Tomadakis MM. Viscous Permeability of Random Fiber Structures: Comparison of Electrical and Diffusional Estimates with Experimental and Analytical Results. J Compos Mater 2005;39:163–88.

[110] Ismail MS, Hughes KJ, Ingham DB, Ma L, Pourkashanian M. Effects of anisotropic permeability and electrical conductivity of gas diffusion layers on the performance of proton exchange membrane fuel cells. Appl Energy

2012;95:50–63.

[111] Springer DS, Loaiciga HA, Cullen SJ, Everett LG. Air permeability of porous materials under controlled laboratory conditions. Ground Water 1998;36:558–65.

[112] Klinkenberg LJ. The permeability of porous media to liquids and gases. Drill Prod Pract 1941:57–73.

[113] Chen Y, Shen C, Lu P, Huang Y. Role of pore structure on liquid flow behaviors in porous media characterized by fractal geometry. Chem Eng Process Process Intensif 2015;87:75–80. doi:10.1016/j.cep.2014.11.014.

[114] Yuan W, Tang Y, Yang X, Wan Z. Porous metal materials for polymer electrolyte membrane fuel cells - A review. Appl Energy 2012;94:309–29. doi:10.1016/j.apenergy.2012.01.073.

[115] Gostick JT, Fowler MW, Pritzker MD, Ioannidis MA, Behra LM. In-plane and through-plane gas permeability of carbon fiber electrode backing layers. J Power Sources 2006;162:228–38.

[116] Tseng C-J, Lo S-K. Effects of microstructure characteristics of gas diffusion layer and microporous layer on the performance of PEMFC. Energy Convers Manag 2010;51:677–84.

[117] Tomadakis MM, Sotirchos S V. Effective Kundsen diffusivities in structures of randomly overlapping fibers. Am Inst Chem Eng J 1991;37:74–86.

[118] Tomadakis MM, Sotirchos S V. Knudsen diffusivities and properties of structures of unidirectional fibers. Am Inst Chem Eng J 1991;37:1175–86.

[119] Bird RB, Stewart WE, Lightfoot EN. Transport Phenomena. New York: John Wiley & Sons; 2007.

[120] Rumpf HCH, Gupte AR. Einflüsse der Porosität und Korngrößenverteilung im Widerstandsgesetz der Porenströmung. Chemie Ing Tech 1971;43:367–375.

[121] Jiao K, Park J, Li X. Experimental investigations on liquid water removal from the gas diffusion layer by reactant flow in a PEM fuel cell. Appl Energy 2010;87:2770–7.

[122] Zamora H, Cañizares P, Rodrigo MA, Lobato J. Improving of micro porous layer based on advanced carbon materials for high temperature proton exchange membrane fuel cell electrodes. Fuel Cells 2015;15:375–83.

[123] Ferreira RB, Falcão DS, Oliveira VB, Pinto AMFR. 1D + 3D two-phase flow numerical model of a proton exchange membrane fuel cell. Appl Energy 2017;203:474–95. doi:10.1016/j.apenergy.2017.06.048.

[124] Vasile NS, Doherty R, Monteverde Videla AHA, Specchia S. 3D multi-physics modeling of a gas diffusion electrode for oxygen reduction reaction for electrochemical energy conversion in PEM fuel cells. Appl Energy 2016;175:435–50. doi:10.1016/j.apenergy.2016.04.030.

[125] Wang ZH, Wang CY, Chen KS. Two-phase flow and transport in the air cathode of proton exchange membrane fuel cells. J Power Sources 2001;94:40–50.

[126] Haghayegh M, Eikani MH, Rowshanzamir S. Modeling and simulation of a proton exchange membrane fuel cell using computational fluid dynamics. Int J Hydrogen Energy 2017;42:21944–54. doi:10.1016/j.ijhydene.2017.07.098.

[127] Holton OT, Stevenson JW. The Role of Platinum in Proton Exchange Membrane Fuel Cells. Platin Met Rev 2013;57:259–71. doi:10.1595/147106713X671222.

[128] Sohn YJ, Kim M, Yang TH, Kim K. Numerical analysis of convective and diffusive fuel transports in high-temperature proton-exchange membrane fuel cells. Int J Hydrogen Energy 2011;36:15273–82. doi:10.1016/j.ijhydene.2011.08.069.

[129] Pasaogullari U, Wang CY. Two-phase transport and the role of micro-porous layer in polymer electrolyte fuel cells. Electrochim Acta 2004;49:4359–69.

[130] Ye Q, Nguyen T Van. Three-Dimensional Simulation of Liquid Water Distribution in a PEMFC with Experimentally Measured Capillary Functions. J Electrochem Soc 2007;154:B1242. doi:10.1149/1.2783775.

[131] Le AD, Zhou B. A general model of proton exchange membrane fuel cell. J Power Sources 2008;182:197–222. doi:10.1016/j.jpowsour.2008.03.047.

[132] Qin Y, Du Q, Fan M, Chang Y, Yin Y. Study on the operating pressure effect on the performance of a proton exchange membrane fuel cell power system. Energy Convers Manag 2017;142:357–65. doi:10.1016/j.enconman.2017.03.035.

[133] Qin Y, Li X, Jiao K, Du Q, Yin Y. Effective removal and transport of water in

a PEM fuel cell flow channel having a hydrophilic plate. Appl Energy 2014;113:116–26. doi:10.1016/j.apenergy.2013.06.053.

[134] Ju H, Meng H, Wang CY. A single-phase, non-isothermal model for PEM fuel cells. Int J Heat Mass Transf 2005;48:1303–15. doi:10.1016/j.ijheatmasstransfer.2004.10.004.

[135] Wu H, Li X, Berg P. On the modeling of water transport in polymer electrolyte membrane fuel cells. Electrochim Acta 2009;54:6913–27. doi:10.1016/j.electacta.2009.06.070.

[136] Wu H, Li X, Berg P. Numerical analysis of dynamic processes in fully humidified PEM fuel cells. Int J Hydrogen Energy 2007;32:2022–31. doi:10.1016/j.ijhydene.2006.09.046.

[137] Wu H, Berg P, Li X. Steady and unsteady 3D non-isothermal modeling of PEM fuel cells with the effect of non-equilibrium phase transfer. Appl Energy 2010;87:2778–84. doi:10.1016/j.apenergy.2009.06.024.

[138] Wu H, Berg P, Li X. Non-isothermal transient modeling of water transport in PEM fuel cells. J Power Sources 2007;165:232–43. doi:10.1016/j.jpowsour.2006.11.061.

[139] Jiao K, Li X. Three-dimensional multiphase modeling of cold start processes in polymer electrolyte membrane fuel cells. Electrochim Acta 2009;54:6876–91. doi:10.1016/j.electacta.2009.06.072.

[140] Jiao K, Alaefour IE, Li X. Three-dimensional non-isothermal modeling of carbon monoxide poisoning in high temperature proton exchange membrane fuel cells with phosphoric acid doped polybenzimidazole membranes. Fuel 2011;90:568–82. doi:10.1016/j.fuel.2010.10.018.

[141] Jiang Y, Yang Z, Jiao K, Du Q. Sensitivity analysis of uncertain parameters based on an improved proton exchange membrane fuel cell analytical model. Energy Convers Manag 2018;164:639–54. doi:10.1016/j.enconman.2018.03.002.

[142] Baschuk J., Li X. Modelling of polymer electrolyte membrane fuel cells with variable degrees of water flooding. J Power Sources 2000;86:181–96. doi:10.1016/S0378-7753(99)00426-7.

[143] Baschuk JJ, Li X. A comprehensive, consistent and systematic mathematical

model of PEM fuel cells. Appl Energy 2009;86:181–93. doi:10.1016/j.apenergy.2007.12.004.

[144] Hwang DS, Park CH, Yi SC, Lee YM. Optimal catalyst layer structure of polymer electrolyte membrane fuel cell. Int J Hydrogen Energy 2011;36:9876–85. doi:10.1016/j.ijhydene.2011.05.073.

[145] Therdthianwong A, Ekdharmasuit P, Therdthianwong S. Fabrication and performance of membrane electrode assembly prepared by a catalyst-coated membrane method: Effect of solvents used in a catalyst ink mixture. Energy and Fuels 2010;24:1191–6. doi:10.1021/ef901105k.

[146] Thanasilp S, Hunsom M. Effect of MEA fabrication techniques on the cell performance of Pt-Pd/C electrocatalyst for oxygen reduction in PEM fuel cell. Fuel 2010;89:3847–52. doi:10.1016/j.fuel.2010.07.008.

[147] Peng X, Omasta T, Rigdon W, Mustain WE. Fabrication of High Performing PEMFC Catalyst-Coated Membranes with a Low Cost Air-Assisted Cylindrical Liquid Jets Spraying System. J Electrochem Soc 2016;163:E407–13. doi:10.1149/2.0981614jes.

[148] Xie J, More KL, Zawodzinski TA, Smith WH. Porosimetry of MEAs Made by "Thin Film Decal" Method and Its Effect on Performance of PEFCs. J Electrochem Soc 2004;151:A1841. doi:10.1149/1.1796991.

[149] Kim S, Kim J-H, Oh J-G, Jang K-L, Jeong B-H, Hong BK, et al. Mechanical Behavior of Free-Standing Fuel Cell Electrodes on Water Surface. ACS Appl Mater Interfaces 2016;8:15391–8. doi:10.1021/acsami.6b03854.

[150] Xie J, Garzon F, Zawodzinski T, Smith W. Ionomer Segregation in Composite MEAs and Its Effect on Polymer Electrolyte Fuel Cell Performance. J Electrochem Soc 2004;151:A1084. doi:10.1149/1.1756887.

[151] Shahgaldi S, Alaefour I, Unsworth G, Li X. Development of a low temperature decal transfer method for the fabrication of proton exchange membrane fuel cells. Int J Hydrogen Energy 2017;42:11813–22. doi:10.1016/j.ijhydene.2017.02.127.

[152] Ahn M, Cho Y-H, Jung N, Lim JW, Kang YS, Sung Y-E. Structural Modification of a Membrane Electrode Assembly via a Spray Coating in PEMFCs. J Electrochem Soc 2012;159:B145. doi:10.1149/2.011202jes.

[153]  Reshetenko T V., Kim HT, Krewer U, Kweon HJ. The effect of the anode loading and method of MEA fabrication on DMFC performance. Fuel Cells 2007;7:238–45. doi:10.1002/fuce.200600030.

[154]  Morrow NR, Harris CC. Capillary Equilibrium in Porous Materials. Soc Pet Eng J 1965;5:15–24.

[155]  Nimmo JR. Porosity and pore size distribution. Encycl Soils Environ 2004:295–303. doi:10.1016/B978-0-12-409548-9.05265-9.

[156]  Shelberg MC, Lam N, Moellering H. Measuring the Fractal Dimensions of Surfaces. Proc Sixth Int Symp Comput Cartogr Auto-Carto 1983;6:319–28.

[157]  Zeng Q, Luo M, Pang X, Li L, Li K. Surface fractal dimension: An indicator to characterize the microstructure of cement-based porous materials. Appl Surf Sci 2013;282:302–7. doi:10.1016/j.apsusc.2013.05.123.

[158]  Miller B, Tyomkin I. An Extended Range Liquid Extrusion Method for Determining Pore Size Distributions. Text Res J 1986;56:35–40.

[159]  von Kraemer S, Puchner M, Jannasch P, Lundblad A, Lindbergh G. Gas Diffusion Electrodes and Membrane Electrode Assemblies Based on a Sulfonated Polysulfone for High-Temperature PEMFC. J Electrochem Soc 2006;153:A2077–84. doi:10.1149/1.2335979.

[160]  Chan C, Zamel N, Li X, Shen J. Experimental measurement of effective diffusion coefficient of gas diffusion layer/microporous layer in PEM fuel cells. Electrochim Acta 2011;65:13–21. doi:10.1016/j.electacta.2011.12.110.

[161]  Cunningham RE, Williams RJJ. Diffusion in Gases and Porous Media. 1980. doi:10.1007/978-1-4757-4983-0.

[162]  He W, Yi JS, Nguyen T V. Two-phase flow model of the cathode of PEM fuel cells using interdigitated flow fields. AIChE J 2006;146:38–2064. doi:10.1002/aic.690461016.

[163]  Kulikovsky AA. Quasi-3D Modeling of Water Transport in Polymer Electrolyte Fuel Cells. J Electrochem Soc 2003;150:A1432–9. doi:10.1149/1.1611489.

[164]  Zhang G, Jiao K. Multi-phase models for water and thermal management of proton exchange membrane fuel cell: A review. J Power Sources 2018;391:120–33. doi:10.1016/j.jpowsour.2018.04.071.

[165] Kahveci EE, Taymaz I. Assessment of single-serpentine PEM fuel cell model developed by computational fluid dynamics. Fuel 2018;217:51–8. doi:10.1016/j.fuel.2017.12.073.

[166] Yin Y, Wang X, Shangguan X, Zhang J, Qin Y. Numerical investigation on the characteristics of mass transport and performance of PEMFC with baffle plates installed in the flow channel. Int J Hydrogen Energy 2018;43:8048–62. doi:10.1016/j.ijhydene.2018.03.037.

# Appendix I
# Uncertainty Analysis of Standard Porosimetry

The measurement uncertainty of the method of standard porosimetry (MSP) comes from two major sources: bias uncertainty and precision uncertainty. The main factors determining the measurement uncertainty are discussed in this section.

## (1) The $0^{th}$ order uncertainty

The $0^{th}$ order uncertainty is the design stage uncertainty, which is entirely due to the instrument resolution and random reading uncertainty.

(a) For the micrometer, the $0^{th}$ order uncertainty comes from two aspects:

The instrument uncertainty $(U_c)_m$

$$(U_c)_m = \pm 0.004 \text{ mm} \qquad \text{(95\% confidence)}$$

The random error from reading instrument $(u_o)_m$

$$(U_o)_m = \pm 1/2 * \text{resolution} = \pm 0.0005 \text{ mm} \qquad \text{(95\% confidence)}$$

The design stage uncertainty of the $(u_d)_m$

$$(U_d)_m = \pm\sqrt{(U_d)_m^2 + (U_d)_m^2} = \pm 0.00403 \text{ mm} \qquad \text{(95\% confidence)}$$

As can be seen, the majority of the $(u_d)_m$ is due to the micrometer accuracy, and the reading error is tiny.

(b) For the digital balance, the $0^{th}$ order uncertainty comes from three aspects:

The instrument linearity $(U_l)_b$

$$(U_l)_b = \pm 0.0003 \text{g} \qquad \text{(95\% confidence)}$$

The instrument repeatability $(u_r)_b$

$$(U_r)_b = \pm 0.0001 \text{g} \qquad \text{(95\% confidence)}$$

The random error from reading instrument $(u_o)_b$

$$(U_o)_b = \pm 1/2 * \text{resolution} = \pm 0.00005 \text{g} \qquad \text{(95\% confidence)}$$

The design stage uncertainty of the $(U_d)_b$

$$(U_d)_b = \pm\sqrt{(U_l)_b^2 + (U_r)_b^2 + (U_0)_b^2} = \pm 0.00032 \text{ g} \qquad \text{(95\% confidence)}$$

As can be seen, the majority of the $(U_d)_b$ is due to the digital balance linearity, and the reading error is tiny.

(c) Another uncertainty source is the PSD curve of the standard samples given by the manufacturer. By comparing with the given curve as shown in **Fig. 11**, the PSD of the test samples can be achieved. The uncertainty of the PSD curve of the test samples is affected by the uncertainty of the given curve. However, the uncertainty of the given

curve is not provided by the manufacturer. So this design stage uncertainty due to the PSD curve of the standard samples is not discussed in this section.

## (2) The 1$^{st}$ order uncertainty

According to the previous experiment conducted, time is not a factor of the measurement uncertainty. Thus, the 1$^{st}$ order uncertainty equals to the 0$^{th}$ order uncertainty.

## (3) The N$^{th}$ order uncertainty

The N$^{th}$ order uncertainty is the presented result uncertainty, which is related to the instrument calibration characteristics and often allows a direct comparison between the results of similar tests using different instruments or at different test facilities.

The uncertainty of the pore volumes and porosity, for example, is analyzed in this section.

(a) The pore volume

The pore volume can be calculated using the following equation,

$$V_{pore} = \frac{(m_{sat\_bs} - m_b) - (m_{dry\_bs} - m_b)}{\rho_{octane}} \tag{I.1}$$

where $\rho_{octane}$ is the density of the octane, $m_{sat\_bs}$ is the total mass of the saturated sample and clean bottle, $m_{dry\_bs}$ is the total mass of the dry sample and clean bottle, and $m_b$ is the mass of the clean bottle.

The uncertainty of the pore volume, $(U_v)_{rss}$, can be calculated by the following equation,

$$(U_v)_{rss} = \left[ \left( \frac{\partial V_{pore}}{\partial m_{sat}} \Delta U_m \right)^2 + \left( \frac{\partial V_{pore}}{\partial m_{dry}} \Delta U_m \right)^2 + \left( \frac{\partial V_{pore}}{\partial \rho_{octane}} \Delta U_\rho \right)^2 \right]^{\frac{1}{2}} \tag{I.2}$$

where $\Delta U_m = (U_d)_m$, and $\Delta U_\rho \approx 0$. The uncertainty of pore volumes of different CLs is calculated, and the results are shown in **Table 20**.

**Table 20.** Uncertainty of the pore volume of catalyst layers (CLs) for CCM method

| Pt loading | mg·cm$^{-2}$ | 0.1 | 0.2 | 0.3 | 0.4 |
|---|---|---|---|---|---|
| Pore volume | mm$^3$ | 2.2 | 4.0 | 5.6 | 7.1 |
| Uncertainty | mm$^3$ | ±0.1 | ±0.1 | ±0.1 | ±0.1 |
| Relative uncertainty | % | 5.1 | 2.9 | 2.0 | 1.6 |

(b) The porosity

The porosity of the sample can be calculated using the following equation,

$$\varepsilon = \frac{V_{\text{pore}}}{V_{\text{total}}} = \frac{V_{\text{pore}}}{\frac{1}{4}\pi d^2 \delta} \tag{I.3}$$

The uncertainty of the porosity $(U_\varepsilon)_{\text{rss}}$ can be calculated by the following equation,

$$(U_\varepsilon)_{\text{rss}} = \left[ \left( \frac{\partial \varepsilon}{\partial V_{\text{pore}}} \Delta U_{V_{\text{pore}}} \right)^2 + \left( \frac{\partial \varepsilon}{\partial d} \Delta U_d \right)^2 + \left( \frac{\partial \varepsilon}{\partial \delta} \Delta U_\delta \right)^2 \right]^{\frac{1}{2}} \tag{I.4}$$

After completing all the tests of samples in this experiment, the final $N^{\text{th}}$ order uncertainty can be calculated according to the above equations. The uncertainty of porosity for different CLs is calculated and shown in **Table 21**.

**Table 21.** Uncertainty of the porosity of catalyst layers (CLs) for CCM method

| Pt loading | mg·cm$^{-2}$ | 0.1 | 0.2 | 0.3 | 0.4 |
|---|---|---|---|---|---|
| Porosity | -- | 0.55 | 0.51 | 0.50 | 0.40 |
| Uncertainty | -- | ±0.04 | ±0.02 | ±0.01 | ±0.01 |
| Relative uncertainty | % | 7.31 | 4.14 | 2.91 | 2.30 |

# Appendix II
# Solutions for One-Dimensional Diffusion Problem

Developing the diffusion theory for a Loschmidt Cell is crucial to obtain the equivalent diffusion coefficient further to apply to the resistance network theory to calculate the effective diffusion coefficient of the tested porous media.

The diffusion process in the chamber follows Fick's law of diffusion given below:

$$\frac{\partial C_i}{\partial t} = D\left(\frac{\partial^2 C_i}{\partial x^2} + \frac{\partial^2 C_i}{\partial y^2} + \frac{\partial^2 C_i}{\partial z^2}\right) \tag{II.1}$$

where $C_i$ is the concentration of species i, $t$ is the diffusion time, $D$ is the diffusion coefficient and $x$, $y$ and $z$ are the space dimensions. $x$ and $y$ are the space dimensions along the diameter direction, and $z$ is the space dimension along the height of the chambers.

This problem is simplified to be one-dimensional and along the height direction. This assumption is valid since the height is much longer than the diameter of the diffusion region. Thus, the governing equation is simplified and re-written as:

$$\frac{\partial C_i}{\partial t} = D\frac{\partial^2 C_i}{\partial z^2} \tag{II.2}$$

There are various solutions to this simplified problem. A general solution of Fick's law for finite length tube and a solution for semi-infinite length tube are discussed in detail as shown below.

**(1) General Solution of Fick's law for a finite length**

According to the experimental procedures, at the beginning of the experiment, the bottom chamber is full of oxygen gas while the top chamber is full of nitrogen gas as shown in **Fig. 56**. Thus, the initial conditions are,

$$C_i = \begin{cases} C_i^t & for\ (0 < z < \frac{L}{2}, t = 0) \\ C_i^b & for\ (-\frac{L}{2} < z < 0, t = 0) \end{cases} \tag{II.3}$$

where $C_i^t$ and $C_i^b$ are the initial concentrations of species $i$ in the top and bottom chambers, respectively.
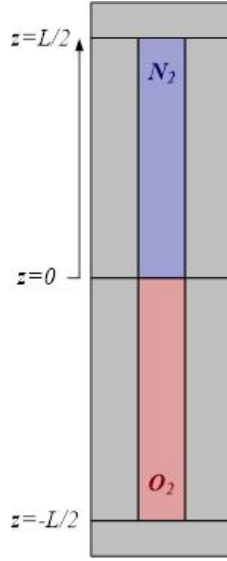
**Fig. 56.** Computational domain of the diffusion in a finite length tube.

Since no gasses can escape from the chambers to the outside environment, the insulation boundary conditions are,

$$\frac{\partial C_i}{\partial z}\big|_{z=\pm L/2} = 0 \; for \; (t > 0) \tag{II.4}$$

To solve the partial differential equation, a standard method of obtaining a solution is to assume that the variables are separable.

$$C_i = Z(z)T(t) \tag{II.5}$$

where $Z$ is a function of only $z$ and $T$ is a function of only $t$.

$$\frac{1}{T}\frac{dT}{dt} = \frac{D}{Z}\frac{d^2Z}{dz^2} \tag{II.6}$$

The left-hand side depends on $t$ only, while the right-hand side depends on $z$ only. Both sides, therefore, must be equal to the same constant, which is taken as $-\lambda^2 D$. Now we can obtain two ordinary differential equations:

$$\frac{1}{T}\frac{dT}{dt} = -\lambda^2 D \tag{II.7}$$

$$\frac{1}{Z}\frac{d^2Z}{dz^2} = -\lambda^2 \tag{II.8}$$

By solving these two ordinary differential equations constrained by the boundary conditions, the concentration is,

$$C_i = (A \sin \lambda z + B \cos \lambda z) e^{-\lambda^2 Dt} \tag{II.9}$$

where A and B are the integration constants. To satisfy the initial condition $C_i^t \neq C_i^b$, $A \neq 0$ and $B=0$ should be made. To satisfy the boundary condition, $\lambda = (2n+1)\pi/L$ for $(n=0,1,2,...)$. Thus, the above equation simplifies to

$$C_i = A \sin(\lambda z)e^{-\lambda^2 Dt} \tag{II.10}$$

Since the one-dimensional diffusion equation is a linear equation, the most general solution can is:

$$C_i = M + \sum_{n=0}^{\infty}[A_n \sin(\lambda_n z)]e^{-\lambda_n^2 Dt} \quad , \lambda_n = (2n+1)\pi/L \tag{II.11}$$

where $M$, $A_n$, and $\lambda_n$ are determined by the initial condition. Applying the initial condition results in the following:

$$C_i^t = M + \sum_{n=0}^{\infty}[A_n \sin(\lambda_n x)] \quad , \lambda_n = (2n+1)\pi/L \tag{II.12}$$

$$C_i^b = M + \sum_{n=0}^{\infty}[A_n \sin(-\lambda_n x)] \quad , \lambda_n = (2n+1)\pi/L \tag{II.13}$$

where $x$ is an arbitrary positive distance less than L/2. Thus,

$$M = \frac{C_i^t + C_i^b}{2} \tag{II.14}$$

$$C_i^t - C_i^b = 2\sum_{n=0}^{\infty}[A_n \sin(\lambda_n z)] \quad , \lambda_n = (2n+1)\pi/L \tag{II.15}$$

By multiplying both sides by $\sin(p\pi z/L)$ and integrating from 0 to $L$ using the relationships

$$\int_0^L \sin\left(\frac{p\pi z}{L}\right) \sin\left(\frac{m\pi z}{L}\right) dz = \begin{cases} 0, & m \neq p \\ \dfrac{L}{2}, & m = p \end{cases} \tag{II.16}$$

Thus, the term $A_n$ can be determined

$$A_n = \frac{C_i^t - C_i^b}{\pi} \frac{2}{2n+1} \tag{II.17}$$

where n=0, 1, 2…

The final general solution to this problem is

$$C_i = \frac{C_i^t + C_i^b}{2} + \frac{2(C_i^t - C_i^b)}{\pi}\sum_{n=0}^{\infty} \frac{1}{2n+1}\sin\left(\frac{(2n+1)\pi z}{L}\right)\exp\left(\frac{-D(2n+1)^2\pi^2 t}{L^2}\right) \tag{II.18}$$

where $n = 0, 1, 2…$This solution is regarded as the true values as long as $n$ is sufficiently large. However, this solution is not practical for curve fitting due to a large number of terms involving in the calculation. A solution for semi-infinite length is developed below to simplify the curve fitting algorithm.

**(2) Solution of Fick's law for semi-infinite length**

By analyzing the proposed problem, the diffusion rate of $O_2$ and $N_2$ is the same thus the $O_2$ concentration at the interface is regarded as constant. This analysis

is verified by **Eq. (II.18)** when $z = 0$. Considering the top half tube as a semi-infinite medium, $z > 0$, when the boundary condition keeps as a constant $O_2$ concentration $C_0$ = $(C_i^t + C_i^b)/2$, and the initial concentration is zero throughout the medium.
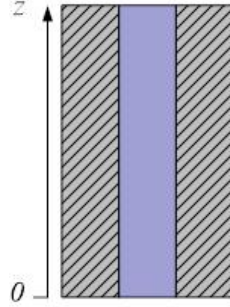


**Fig. 57.** Computational domain of the diffusion in a semi-infinite length tube.

The boundary conditions are,

$$C_i = \begin{cases} C_0, & for\ (z = 0) \\ 0, & for\ (z = +\infty) \end{cases} \tag{II.19}$$

Moreover, the initial condition is,

$$C_i = 0, for\ (z > 0\ and\ t = 0) \tag{II.20}$$

Multiplying both sides of Fick's diffusion equation by $e^{-pt}$ and integrating on $t$ from 0 to $\infty$ we obtain the following equations

$$\int_0^\infty e^{-pt} \frac{\partial C_i}{\partial t} dt = [C_i e^{-pt}]_0^\infty + p \int_0^\infty C_i e^{-pt} dt = p\overline{C} \tag{II.21}$$

$$\int_0^\infty e^{-pt} \frac{\partial^2 C_i}{\partial t^2} dt = \frac{\partial^2}{\partial z^2} \int_0^\infty C_i e^{-pt} dt = \frac{\partial^2 \overline{C}}{\partial z^2} \tag{II.22}$$

Since the term in the square bracket vanishes at $t = 0$ by applying initial conditions, and at $t = \infty$ through the exponential factor. Thus the initial Fick's diffusion equation reduces to,

$$D \frac{\partial^2 \overline{C}}{\partial z^2} = p\overline{C} \tag{II.23}$$

Applying the boundary condition we can have,

$$\overline{C} = \begin{cases} \int_0^\infty C_0 e^{-pt} dt = \dfrac{C_0}{p}, & z = 0 \\ 0, & z = \infty \end{cases} \tag{II.24}$$

Thus the solution of the ordinary differential equation is,

$$\overline{C} = \frac{C_0}{p} e^{-qz} \tag{II.25}$$

where $q^2 = p/D$.

Thus the following equation is established,

$$\frac{e^{-qz}}{p} = \int_0^\infty \frac{C_i}{C_0} e^{-pt} dt \tag{II.26}$$

The Laplace Transform (see Table 2.2 in Crank's book [81]) shows that the transform of the above equation is,

$$C_i = C_0 \text{erfc}\left(\frac{z}{2\sqrt{Dt}}\right) \tag{II.27}$$

Thus the above equation can be rewritten as,

$$C_i = \frac{C_i^b}{2} \text{erfc}\left(\frac{z}{2\sqrt{Dt}}\right) \tag{II.28}$$

**(3) Comparison of two solutions**

**Eq. (II.18)** best predicts the oxygen concentration change over time at a specific position in the chamber. However, to obtain the equivalent diffusion coefficient directly by using this equation is impractical since the calculation involves too many terms to get a high accuracy. Many researchers indicate that **Eq. (II.28)** is a good approximation [91] of the real values. When time is short, this equation shows excellent agreement with the 'finite-length' solution. A detailed comparison is shown below.

For most cases of this research, the probe location, diffusion coefficient, and experimental time are taken within a specific region as shown in **Table 22**. The comparison of the two solutions is made for this research.

**Table 22.** Parameters of diffusion for the uncertainty analysis of the Loschmidt Cell

| Parameters | Unit | Values |
|---|---|---|
| Probe location, $z$ | mm | 5-30 |
| Time, $t$ | s | 0-120 |
| Equivalent diffusion coefficient, $D$ | $m^2 \cdot s^{-1}$ | $(1-3) \times 10^{-5}$ |
| Chamber length, $L$ | cm | 42.5 |
| Oxygen concentration, $C$ | % | 0.2-50 |

In practice, we use m=0-10,000 to approximate the real results. By residual analysis of **Eq. (II.18)**,

$$C_i = \frac{C_i^t + C_i^b}{2} + \frac{2(C_i^t - C_i^b)}{\pi} \sum_{n=0}^{10,000} \frac{\exp\left(\frac{-D(2n+1)^2\pi^2 t}{L^2}\right)}{2n+1} \sin\left(\frac{(2n+1)\pi z}{L}\right) \quad \text{(II.29)}$$
$$+ \text{H.O.T.}$$

The higher order term of this equation is,

$$H.O.T. = \frac{2(C_i^t - C_i^b)}{\pi} \sum_{n=10,001}^{\infty} \frac{\exp(\frac{-D(2n+1)^2\pi^2 t}{L^2})}{2n+1} \sin\left(\frac{(2n+1)\pi z}{L}\right) \quad \text{(II.30)}$$

Furthermore, the H.O.T. of this equation,

$$|H.O.T.| < \frac{2C_i^b}{20{,}003\pi} \sum_{m=10,001}^{\infty} \exp(\frac{-D(2n+1)^2\pi^2 t}{L^2})$$

$$< \frac{2C_i^b}{20{,}003\pi} \frac{L}{2\pi\sqrt{Dt}} \int_{20{,}001\pi\sqrt{Dt}/L}^{\infty} e^{-x^2} dx$$

$$= \frac{C_i^b L}{20{,}003\pi^2\sqrt{Dt}} \text{erfc}(\frac{20{,}001\pi\sqrt{Dt}}{L})$$

Within the experimental range in this study, as shown in **Table 22**, the maximum error is,

$$\text{max error} = \max\left(\frac{|H.O.T.|}{C_i}\right) \approx 6.6e^{-22}$$

As can be seen, when m = 0-10,000 the error due to H.O.T. can be neglected. Furthermore, the relative error between **Eq. (II.28)** and **Eq. (II.18)** is less than $6.1e^{-12}$. Thus, it is reasonable to utilize **Eq. (II.28)** for curve fitting in this study because it is simpler and outputs excellent agreement with the theoretical values. Shen et al.'s work [91] supports this finding, and the maximum relative error between the semi-infinite-length solution and the general finite-length solution is negligible. Therefore, **Eq. (II.28)** is a valid approximation, and the semi-infinite-length solution is used in this experiment to process the $O_2$ concentration data to obtain the equivalent diffusion coefficient.

# Appendix III
# Uncertainty Analysis of Loschmidt Cell

The measurement uncertainty is analyzed to identify the accuracy of the experimental apparatus. For a well-calibrated experimental apparatus, the effective diffusion coefficient can be determined by analyzing **Eq. (3.25)** for semi-finite length diffusion problem. A traditional method for calculating the uncertainty of $D_{eff}$ is through a root-sum-square (RSS) method.

The uncertainty of effective diffusion coefficient measurements by a well-calibrated Loschmidt cell machine mainly comes from three major aspects: (1) $O_2$ concentration measurements over time at a specific probe location; (2) $D_{eq}$ calculation by curve fitting algorithm; (3) $D_{eff}$ calculation by resistance network analysis.

**(1) $O_2$ concentration measurements over time at a specific probe location:**

The $O_2$ concentration measurements are determined by an oxygen sensor as well as the measurement of probe location. According to the manufacturer, the accuracy of the oxygen sensor is $\pm 0.02\%$ $O_2$ @ 1% $O_2$ and $\pm 0.2\%$ $O_2$ @ 20% $O_2$. The $O_2$ concentration range of 5~30% is the most concerned in this study. Thus the instrument uncertainty ($0^{th}$ or design-stage uncertainty) of $\pm 0.2\%$ (assuming 95% confidential interval) will be used to do the uncertainty analysis for this experiment. A computer records the time of each measurement point, and the uncertainty is subtle compared to the time step of each measurement. Thus, the uncertainty in time recording is assumed to be zero for the following uncertainty analysis. In summary, this experiment requires a high-accuracy oxygen sensor.

**(2) $D_{eq}$ calculation by curve fitting algorithm:**

The dependence of different parameters on the equivalent diffusion coefficient can be predicted using the following equations:

$$D_{eq}^i = \frac{z^2}{4t}\left(\text{erfc}^{-1}\frac{2c_i}{c_b}\right)^{-2} \tag{III.1}$$

where $D^i_{eq}$ is the $i^{th}$ measurement of $O_2$ concentration in $m^2 \cdot s^{-2}$, $z$ is the distance of the probe from the surface of the sample in meters, $c$ is the corresponding gas concentration, and the subscript b means bottom chamber.

Ideally, if the probe location and oxygen concentration can be accurately measured at a specific diffusion time, the $D_{eq}$ can be determined by analyzing each single measurement point. In this case, each measurement of $O_2$ concentration at a

given moment has a unique impact on the $D_{eq}$ calculation, and this impact is evaluated by the root-sum-square method as described by the following equations.

$$u_{D_{eq}^i} = \left[ (\frac{\partial D_{eq}^i}{\partial z} \Delta z)^2 + (\frac{\partial D_{eq}^i}{\partial t} \Delta t)^2 + (\frac{\partial D_{eq}^i}{\partial C_i} \Delta C_i)^2 + (\frac{\partial D_{eq}^i}{\partial C_b} \Delta C_b)^2 \right]^{1/2} \qquad \text{(III.2)}$$

where

$$\frac{\partial D_{eq}^i}{\partial z} = \frac{z}{2t} \left( \text{erfc}^{-1} \frac{2c_i}{c_b} \right)^{-2}$$

$$\frac{\partial D_{eq}^i}{\partial t} = -\frac{z^2}{4t^2} \left( \text{erfc}^{-1} \frac{2c_i}{c_b} \right)^{-2}$$

$$\frac{\partial D_{eq}^i}{\partial c_i} = -\frac{z^2}{t} \left( \text{erfc}^{-1} \frac{2c_i}{c_b} \right)^{-3} \left( (\text{erfc}^{-1})' \frac{2c_i}{c_b} \right) \frac{1}{c_b}$$

$$\frac{\partial D_{eq}^i}{\partial c_i^b} = \frac{z^2}{t} \left( \text{erfc}^{-1} \frac{2c_i}{c_b} \right)^{-3} \left( (\text{erfc}^{-1})' \frac{2c_i}{c_b} \right) \frac{c_i}{(c_b)^2}$$

where $u$ is the uncertainty, and $\Delta$ means the design-stage uncertainty. Based on the previous analysis, $\Delta z = 4.3$ μm, $\Delta t = 0$ s, $\Delta c_i = 0.2\%$, and $\Delta c_b = 0$.

However, in practice, the equivalent diffusion coefficient is calculated from a set of measurements of oxygen concentration over time by curve fitting rather than being measured directly by the experiment equipment. Thus, the contribution of all the measurement points to the $D_{eq}$ is estimated by the root-mean-square (RMS) methods.

$$U_{D_{eq}} = \left[ \frac{1}{N} \sum_{i=1}^{N} \left( U_{D_{eq}^i} \right)^2 \right]^{1/2} \qquad \text{(III.3)}$$

where $N$ is the number of measurement points that are used for curve fitting to obtain $D_{eq}$.

### (3) $D_{eff}$ calculation by resistance network analysis

The uncertainty of the effective diffusion coefficient is also subject to the measurements of the thickness of CLs, the probe location and the equivalent diffusion coefficients in different experiment steps determine the accuracy of effective diffusion coefficients. The dependence of different parameters on the effective diffusion coefficient of substrates can be evaluated by the following equation,

$$D_{eff,sub} = \frac{l_{sub}}{\dfrac{z}{D_{eq,sub}} - \dfrac{z - l_{sub}}{D_{bulk}}} \qquad \text{(III.4)}$$

The uncertainty of the effective diffusion coefficient of the substrate, $U_{sub}$, is calculated by the root sum square method,

$$u_{\text{sub}} = \left[ \left(\frac{\partial D_{\text{eff,sub}}}{\partial l_{\text{sub}}} \Delta l\right)^2 + \left(\frac{\partial D_{\text{eff,sub}}}{\partial z} \Delta z\right)^2 + \left(\frac{\partial D_{\text{eff,sub}}}{\partial D_{\text{eq,sub}}} \Delta u_{D_{\text{eq,sub}}}\right)^2 + \left(\frac{\partial D_{\text{eff,sub}}}{\partial D_{\text{bulk}}} \Delta u_{\text{bulk}}\right)^2 \right]^{1/2} \quad \text{(III.5)}$$

where

$$\frac{\partial D_{\text{eff,sub}}}{\partial l_{\text{sub}}} = \frac{\dfrac{z}{D_{\text{eq,sub}}} - \dfrac{z}{D_{\text{bulk}}}}{\left(\dfrac{z}{D_{\text{eq,sub}}} - \dfrac{z - l_{\text{sub}}}{D_{\text{bulk}}}\right)^2}$$

$$\frac{\partial D_{\text{eff,sub}}}{\partial z} = \frac{-\dfrac{l_{\text{sub}}}{D_{\text{eq,sub}}} + \dfrac{l_{\text{sub}}}{D_{\text{bulk}}}}{\left(\dfrac{z}{D_{\text{eq,sub}}} - \dfrac{z - l_{\text{sub}}}{D_{\text{bulk}}}\right)^2}$$

$$\frac{\partial D_{\text{eff,sub}}}{\partial D_{\text{eq,sub}}} = \frac{l_{\text{sub}} z}{\left(\dfrac{z}{D_{\text{eq,sub}}} - \dfrac{z - l_{\text{sub}}}{D_{\text{bulk}}}\right)^2 D_{\text{eq,sub}}^2}$$

$$\frac{\partial D_{\text{eff,sub}}}{\partial D_{\text{bulk}}} = \frac{-l_{\text{sub}}(z - l_{\text{sub}})}{\left(\dfrac{z}{D_{\text{eq,sub}}} - \dfrac{z - l_{\text{sub}}}{D_{\text{bulk}}}\right)^2 D_{\text{bulk}}^2}$$

where $l$ is the thickness of the three corresponding samples.

The dependence of different parameters on the effective diffusion coefficient of catalyst layers can be estimated by the following equation,

$$D_{\text{eff,CL}} = \frac{l_{\text{CL}}}{\dfrac{z}{D_{\text{eq,total}}} - \dfrac{z}{D_{\text{eq,sub}}} + \dfrac{l_{\text{CL}}}{D_{\text{bulk}}}} \quad \text{(III.6)}$$

The uncertainty of the effective diffusion coefficient of the catalyst layers, $u_{cl}$, is calculated by the root-sum-square method,

$$u_{\text{CL}} = \left[ \left(\frac{\partial D_{\text{eff,CL}}}{\partial l_{\text{CL}}} \Delta l\right)^2 + \left(\frac{\partial D_{\text{eff,CL}}}{\partial z} \Delta z\right)^2 + \left(\frac{\partial D_{\text{eff,CL}}}{\partial D_{\text{eq,total}}} \Delta u_{D_{\text{eq,total}}}\right)^2 + \left(\frac{\partial D_{\text{eff,CL}}}{\partial D_{\text{eq,sub}}} \Delta u_{D_{\text{eq,sub}}}\right)^2 + \left(\frac{\partial D_{\text{eff,sub}}}{\partial D_{\text{bulk}}} \Delta u_{\text{bulk}}\right)^2 \right]^{1/2}$$

$$\text{(III.7)}$$

where

$$\frac{\partial D_{\text{eff,CL}}}{\partial l_{\text{CL}}} = \frac{\dfrac{z}{D_{\text{eq,total}}} - \dfrac{z}{D_{\text{eq,sub}}}}{\left(\dfrac{z}{D_{\text{eq,total}}} - \dfrac{z}{D_{\text{eq,sub}}} + \dfrac{l_{\text{CL}}}{D_{\text{bulk}}}\right)^2}$$

$$\frac{\partial D_{\text{eff,CL}}}{\partial z} = \frac{-\dfrac{l_{\text{CL}}}{D_{\text{eq,total}}} + \dfrac{l_{\text{CL}}}{D_{\text{eq,sub}}}}{\left(\dfrac{z}{D_{\text{eq,total}}} - \dfrac{z}{D_{\text{eq,sub}}} + \dfrac{l_{\text{CL}}}{D_{\text{bulk}}}\right)^2}$$

$$\frac{\partial D_{\text{eff,CL}}}{\partial D_{\text{eq,total}}} = \frac{l_{\text{CL}}z}{(\frac{z}{D_{\text{eq,total}}} - \frac{z}{D_{\text{eq,sub}}} + \frac{l_{\text{CL}}}{D_{\text{bulk}}})^2 D_{\text{eq,total}}^2}$$

$$\frac{\partial D_{\text{eff,CL}}}{\partial D_{\text{eq,sub}}} = \frac{-l_{\text{CL}}z}{(\frac{z}{D_{\text{eq,total}}} - \frac{z}{D_{\text{eq,sub}}} + \frac{l_{\text{CL}}}{D_{\text{bulk}}})^2 D_{\text{eq,sub}}^2}$$

$$\frac{\partial D_{\text{eff,CL}}}{\partial D_{\text{bulk}}} = \frac{l_{\text{CL}}^2}{(\frac{z}{D_{\text{eq,total}}} - \frac{z}{D_{\text{eq,sub}}} + \frac{l_{\text{CL}}}{D_{\text{bulk}}})^2 D_{\text{bulk}}^2}$$

Therefore, the uncertainty in the effective diffusion coefficient of catalyst layers can be determined.

Furthermore, the relative uncertainty of the $D_{\text{eff}}$ is a very complex function of the oxygen concentration, experimental time, probe location, thickness of catalyst layer, substrate material, and catalyst layer material.

$$RU = \frac{U_{D_{\text{eff,CL}}}}{D_{\text{eff,CL}}} = \text{Func}(c_i, t, z, l_{\text{CL}}, \text{Substrate, CL, etc.})$$

In this study, for a specific catalyst layer, the uncertainty analysis is conducted to select the substrate, to evaluate the experimental time, to optimize the probe location and to determine the number of sample stacking to minimize the measurement uncertainty. For illustrative purpose, a case study is conducted based on the experimental results provided by Shen et al. [91] which indicate the effective diffusion coefficient is $(1.47\pm0.05) \times 10^{-7} \text{m}^2\text{s}^{-1}$ under the temperature of 25 $^{\text{o}}$C and the pressure of 1 atm. The corresponding diffusibility of the CL is around 0.0073 which depends on the porous structure of the catalyst layers.

(a) Effect of Probe Location

Based on the information found in Shen et al.'s work as shown in **Table 23**, the experimental process is simulated using the analytical method and the relative uncertainty analysis is conducted based on the above discussion. The experimental time of one minute and the diffusibility and thickness of the substrate with 0.2 and 225 μm, respectively are used to do the uncertainty analysis.

**Table 23.** Parameters and experimental conditions taken from Shen et al.'s work for the uncertainty analysis of the Loschmidt Cell

| Parameters | Unit | Values |
|---|---|---|
| Temperature, $T$ | $^{\text{o}}$C | 25 |

| | | |
|---|---|---|
| Pressure, $p$ | atm | 1 |
| Thickness of CL, $l_{CL}$ | μm | 29 |
| Effective diffusion coefficient, $D_{eff,CL}$ | $m^2 \cdot s^{-1}$ | $(1.47 \pm 0.05) \times 10^{-7}$ |
| Diffusibility of CLs, $\varepsilon = D_{eff,CL}/D_{bulk}$ | -- | 0.0073 |

The relative uncertainty of the effective diffusion coefficient of CLs at different probe location is shown in **Fig. 58**. As can be seen, when probe location is less than 0.005 m, resistance network has a huge impact on the uncertainty, which means that the probe location is too close to the surface of the catalyst layers. However, when the probe location is larger than 0.020 m the measurement uncertainty is mainly determined by curve fitting algorithm which means the probe location is too far from the source of the diffusion, and it is difficult to detect the oxygen concentration change. Therefore, there exists an optimum range of probe location for a specific sample and system configuration. In this case, the probe location is fixed at 0.010 m away from the sliding gate.
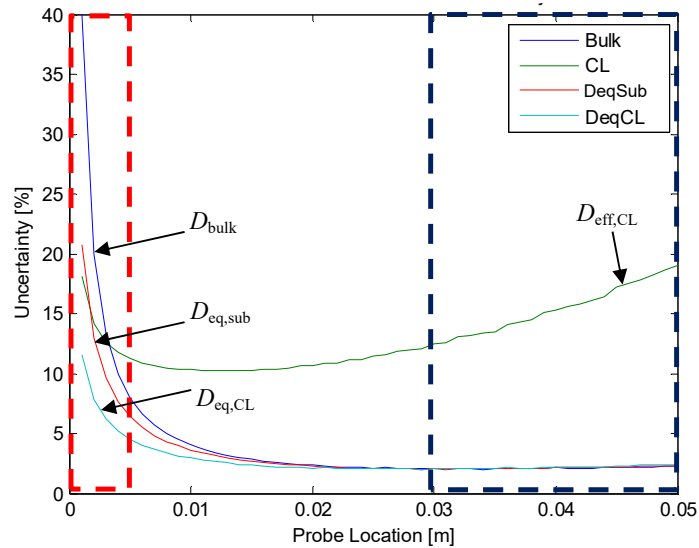


**Fig. 58.** Effect of probe location on the measurement uncertainty of the effective diffusion coefficient of catalyst layers (Cls), $D_{eff,CL}$.

(b) Effect of Data Point Selection

Based on the calculation, the relative uncertainty is still large at the probe location of 0.010 m. Further study indicates that the data points (measurement time

and concentration range) selected for curve fitting are also crucial to minimize the relative measurement uncertainty. **Eq. (III.2)** describes the parameters determining the equivalent diffusion coefficient before performing resistance network analysis.
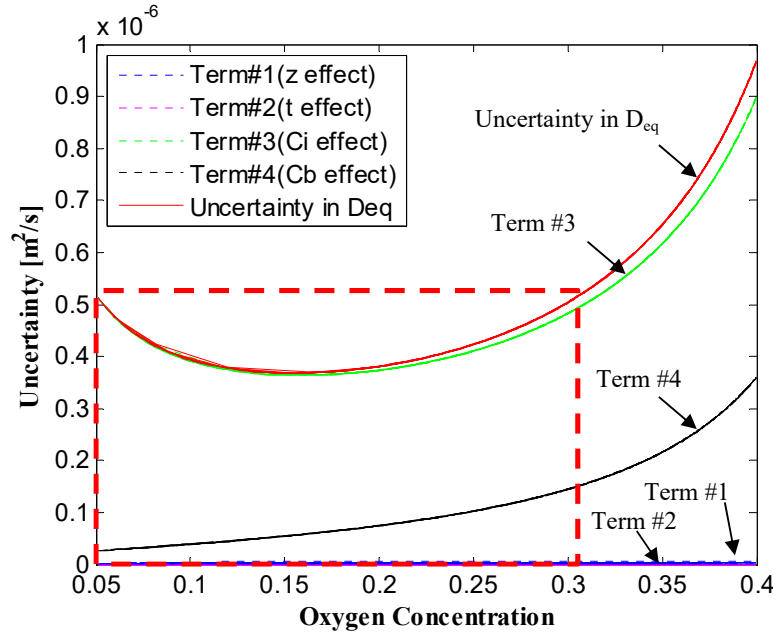


**Fig. 59.** Effect of data point selection on the measurement uncertainty of the equivalent diffusion coefficient of catalyst layers (CLs), $D_{eq}$.

**Fig. 59** shows the plot of the uncertainty vs. oxygen concentration. As can be seen, when the concentration is smaller than 5% or larger than 30%, the absolute uncertainty is much greater than those in the range of 5-30%. Thus, for the future experiment, the data point with an oxygen concentration of 5-30% will be used for curve fitting, further obtaining the equivalent diffusion coefficient. This finding is also true for different probe locations (0.005-0.020mm). At various probe location, 5-30% concentration associates with different experimental time. In this case, the experimental time is at most one minute due to the probe location of 10 mm.

By processing the data in this range, the relative uncertainty in the effective diffusion coefficient of CLs can further reduce to 6% which is sufficient for engineering problems.

(c) Effect of Instrument Selection

Under the same system configuration (e.g., probe location, chamber length and diameter, and $O_2$-$N_2$ gas pair) and the same data analysis procedure (e.g., data point

selection, curve fitting algorithm, and resistance network theory), the parameters of various instruments are investigated to ensure reasonable results.

As can be seen in **Table 24**, the results indicate that the measurement results can be very accurate and precise when high-quality instruments (i.e., oxygen sensor, length measurement instruments, and time recording) work for this experiment. However, the instrument cannot be unlimited improved due to the limited budget. In this case, the design-stage uncertainty of oxygen sensor is 0.2%, the design-stage uncertainty of micrometer is 4.3 *μm*, and the design-stage uncertainty in time recording is almost zero for the computer. With the current experimental instruments, the relative uncertainty can be as low as 6% for most cases which satisfied our requirement.

**Table 24.** Effect of instrument selection on the measurement uncertainty of the effective diffusion coefficient of catalyst layers (CLs), $D_{eff,CL}$

| Parameters | Value | Unit | Relative Uncertainty [%] |
|---|---|---|---|
| | 0.1 | % | 7.71 |
| Uncertainty of Oxygen Sensor | 0.2 | % | 9.18 |
| | 1.0 | % | 29.74 |
| | 1 | μm | 6.04 |
| Uncertainty of Micrometer | 4.3 | μm | 9.18 |
| | 10 | μm | 17.55 |
| | 0.01 | s | 9.18 |
| Uncertainty of Time Recording | 0.02 | s | 9.25 |
| | 0.1 | s | 11.25 |

(d) Effects of Sample and Substrate Specification

In practice, the thickness and effective diffusion coefficient of different CLs fabricated with different techniques vary widely. Based on our previous measurements and the data from Shen et al., the thickness of the catalyst layers ranges from 9-50 μm, and the diffusibility of the CL varies from 0.005-0.1. To examine the accuracy of the current system configuration, the current data analysis procedure, the current instruments, and the properties of CLs are investigated in this study, and the results are shown in **Fig. 60**.

As can be seen, the results indicate that within our predicted range, the relative uncertainty is within 10-15% for most cases. For some cases (e.g., thickness = 9 μm and $D_{eff} / D_{bulk}$ = 0.1), the relative uncertainty can be as large as 35%. Thus, some other measures should be taken to reduce the relative uncertainty such as sample stacking, adjusting the probe location, and applying a more accurate oxygen sensor.
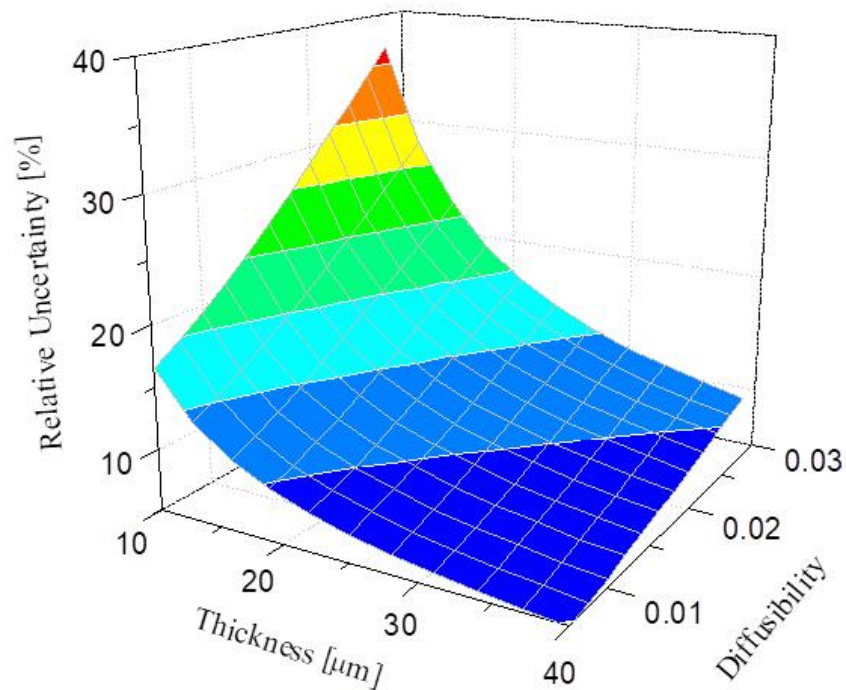


**Fig. 60.** Effect of material properties on the measurement uncertainty of the effective diffusion coefficient of catalyst layers (CLs), $D_{eff,CL}$.

(e) Effect of Sample Stacking

For some cases, the relative uncertainty can be as large as 20-35% which is still unacceptable in engineering problems. Sample stacking is a powerful method to reduce the relative uncertainty. As can be seen, when the number of sample stacking increases, the relative uncertainty reduces dramatically. However, the number of samples cannot be unlimited increased because if the samples are too thick by stacking, it will cause a sealing problem. Therefore, in this case, the number of samples is set to be 3 to reduce the measurement uncertainty meanwhile maintaining a low leakage level.

For the case of sample thickness of 10 μm and diffusibility of 0.03, by sample stacking from 3 pieces to 25 pieces, the relative uncertainty can be reduced from 39.21% to 12.25% as shown in **Fig. 61**. Thus, sample stacking is a potential way to reduce the measurement uncertainty.
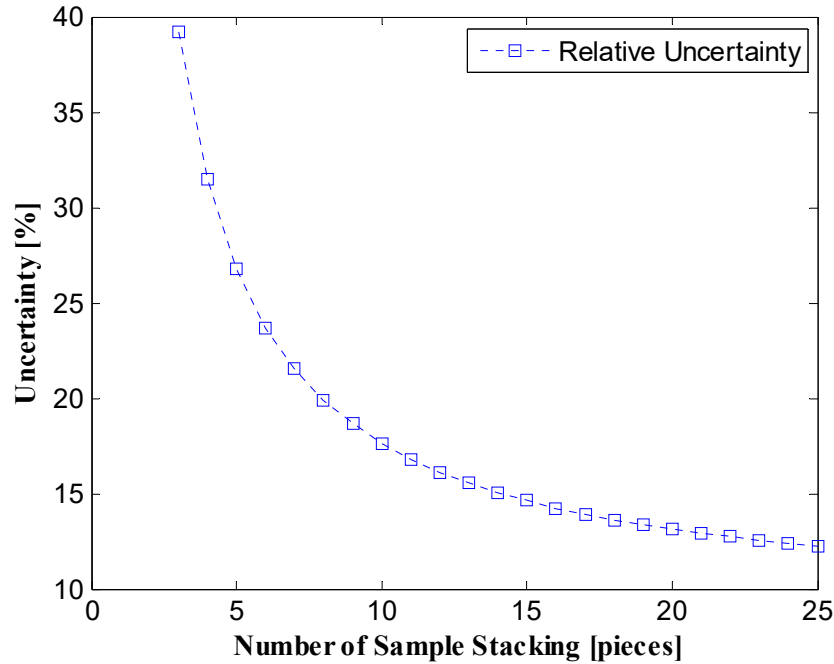


**Fig. 61.** Effect of sample stacking on the measurement uncertainty of the effective diffusion coefficient of catalyst layers (CLs), $D_{\text{eff,CL}}$.

The above uncertainty analysis is conducted according to an artificial specimen; in reality, each measurement should be analyzed based on the actual measurement results obtained from the experiment. The major parameters of the experimental setup and data analysis algorithm are determined based on the above discussion for the samples studied in this research to minimize the relative measurement uncertainty. Therefore, the probe location is 10 mm, the oxygen concentration of 5-30% is taken for curve fitting, and three pieces of samples are stacked together for each measurement. These parameters help maintain the measurement uncertainty within 12% for almost all current samples under study, and the experimental setup requires specific modifications if some samples are extremely thin (less than 10 μm).